



ΕΘΝΙΚΟ ΜΕΤΣΟΒΙΟ ΠΟΛΥΤΕΧΝΕΙΟ
ΣΧΟΛΗ ΑΓΡΟΝΟΜΩΝ & ΤΟΠΟΓΡΑΦΩΝ ΜΗΧΑΝΙΚΩΝ

Διερεύνηση συνδυασμένης χρήσης δεδομένων SAR
με ετερογενή τοπογραφικά δεδομένα μέσω
συνταύτισης μη συναρτησιακών καμπυλών

ΔΙΔΑΚΤΟΡΙΚΗ ΔΙΑΤΡΙΒΗ

Δήμητρας Ι. Βασιλάκη

Διπλωματούχου Αγρονόμου και Τοπογράφου Μηχανικού ΕΜΠ

ΑΘΗΝΑ
Αύγουστος 2013



Διερεύνηση συνδυασμένης χρήσης δεδομένων SAR
με ετερογενή τοπογραφικά δεδομένα μέσω
συνταύτισης μη συναρτησιακών καμπυλών

ΔΙΔΑΚΤΟΡΙΚΗ ΔΙΑΤΡΙΒΗ

Δήμητρας Ι. Βασιλάκη

Διπλωματούχου Αγρονόμου και Τοπογράφου Μηχανικού ΕΜΠ

Επιβλέπων Καθηγητής

Χ. Ιωαννίδης

Αναπληρωτής Καθηγητής ΕΜΠ

Συμβουλευτική Επιτροπή

Α. Γεωργόπουλος
Καθηγητής ΕΜΠ

Χ. Ιωαννίδης
Αναπληρωτής Καθηγητής ΕΜΠ

Β. Καραθανάση
Αναπληρώτρια Καθηγήτρια ΕΜΠ

Εξεταστική Επιτροπή

Α. Γεωργόπουλος
Καθηγητής ΕΜΠ

Ο. Γεωργούλα
Καθηγήτρια ΑΠΘ

Γ. Καρράς
Καθηγητής ΕΜΠ

Δ. Δελιαράογλου
Αναπληρωτής Καθηγητής ΕΜΠ

Χ. Ιωαννίδης
Αναπληρωτής Καθηγητής ΕΜΠ

Β. Καραθανάση
Αναπληρώτρια Καθηγήτρια ΕΜΠ

Λ. Γραμματικόπουλος
Καθηγητής Εφαρμογών ΤΕΙ-Α

Η παρούσα έρευνα έχει συγχρηματοδοτηθεί από την Ευρωπαϊκή Ένωση (Ευρωπαϊκό Κοινωνικό Ταμείο - ΕΚΤ) και από εθνικούς πόρους μέσω του Επιχειρησιακού Προγράμματος «Εκπαίδευση και Δια Βίου Μάθηση» του Εθνικού Στρατηγικού Πλαισίου Αναφοράς (ΕΣΠΑ) – Ερευνητικό Χρηματοδοτούμενο Έργο: Ηράκλειτος ΙΙ. Επένδυση στην κοινωνία της γνώσης μέσω του Ευρωπαϊκού Κοινωνικού Ταμείου.



European Union
European Social Fund



MINISTRY OF EDUCATION & RELIGIOUS AFFAIRS, CULTURE & SPORTS
MANAGING AUTHORITY

Co-financed by Greece and the European Union



Η έγκριση της διδακτορικής διατριβής από την Ανώτατη Σχολή Αγρονόμων και Τοπογράφων Μηχανικών του Ε.Μ. Πολυτεχνείου δεν υποδηλώνει αποδοχή των γνώμων του συγγραφέα (Ν. 5343/1932 Άρθρο 202).

RESEARCH ON THE SYNERGY OF SAR DATA
WITH HETEROGENEOUS DATA USING
FREE-FORM LINEAR FEATURES MATCHING



Dimitra I. Vassilaki
School of Rural and Surveying Engineering
National Technical University of Athens

Doctoral Dissertation

28 August 2013

Acknowledgements

This research has been co-financed by the European Union (European Social Fund - ESF) and Greek national funds through the Operational Program "Education and Lifelong Learning" of the National Strategic Reference Framework (NSRF) - Research Funding Program: Heracleitus II. Investing in knowledge society through the European Social Fund. Their support is fully appreciated.

The data sets over Kalamos, Greece, were provided by the School of Rural and Surveying Engineering, National Technical University of Athens. I am grateful for the kind offer. The data sets over the JRC's Maussane Test Site, France, were offered by the Joint Research Centre (JRC) - Institute for the Protection and Security of the Citizen (The WorldView-2 optical image (©DigitalGlobe [2010], all rights reserved; provided by European Space Imaging) and by the Intermap.

This research was conducted at the School of Rural and Surveying Engineering, National Technical University of Athens. I fully appreciate the provision of all necessary infrastructure and support and I am grateful to the dissertation supervisor and the members of the advisory and the examining committee.

Abstract

Modern high resolution satellite SAR data has now compatible resolution with existing remote sensing and geospatial data. In this light, the objective of this dissertation is two-fold: i) to research the potential of the combined use of high resolution satellite SAR data with heterogeneous (multimodal and multitemporal) remote sensing and geospatial data and ii) to research the use of linear features as an alternative (to solitary point) form of reference information for the co-registration of SAR data with heterogeneous data. This dissertation introduces general methods for automatically matching heterogeneous free-form linear features of the same (2D-2D, 3D-3D) or of different dimensionality (3D-2D), which can handle any geometry including the side looking geometry of the SAR sensors. It also introduces general methods for the direct georeferencing of TerraSAR-X SSC images and the geometric correlation and the radiometric merging of not geometrically corrected heterogeneous remote sensing and geospatial data. The general methods are then combined together and with other general methods and problems of surveying engineering in order to develop specific methods for the co-registration and the synergy of SAR data with unitemporal and multitemporal remote sensing, geodetic and geospatial data. The specific methods succeed to perform the co-registration (georeferencing) of not geometrically corrected SAR and remote sensing and geospatial data, the fusion of not geometrically corrected SAR and multispectral optical images in slant range SAR geometry and the rapid geometric correction of TerraSAR-X images using readily available global data sets. In contrast to previous research, the present dissertation considers: i) high resolution SAR data, ii) not geometrically corrected data, iii) linear features of arbitrary geometry, iv) terrain of arbitrary form, not necessarily flat, v) greater areas of the Earth's surface, not just small patches and vi) the metric exploitation of SAR data for topographic applications. At the time of writing of this dissertation none of the methods was available in the literature or in commercial or research software; they were all developed from scratch. The proposed methods and processes are validated and evaluated using numerous simulated and real world data sets and real world problems some of which are hardly solved with standard processes. In all cases the methods show very good performance and encourage further research on the use of linear features and on the synergy of SAR data with heterogeneous data.

Keywords: photogrammetry, geodesy, remote sensing, Synthetic Aperture Radar (SAR), optical images, geospatial data, multimodal, multitemporal, heterogeneous, georeferencing, registration/co-registration, matching, fusion, linear features, Iterative Closest Point (ICP) algorithm, Least Squares Adjustment (LSA)

Extended Abstract in Greek

Εκτεταμένη περίληψη στα Ελληνικά: Οι σύγχρονοι δορυφορικοί αισθητήρες SAR παρέχουν τη δυνατότητα αναγνώρισης λεπτομερειών της γήινης επιφάνειας όπως για παράδειγμα είναι οι δρόμοι και τα κτίρια. Η αναγνώριση τέτοιων λεπτομερειών δεν ήταν εφικτή στα δορυφορικά δεδομένα SAR της προηγούμενης γενιάς δεκτών, λόγω της σχετικά πολύ χαμηλότερης ανάλυσής τους. Αυτή η εξέλιξη στους δορυφορικούς αισθητήρες SAR έκανε για πρώτη φορά τα δεδομένα SAR συμβατά με άλλου τύπου τοπογραφικά δεδομένα, όπως είναι οι οπτικές εικόνες υψηλής ανάλυσης και οι χάρτες μεσαίας κλίμακας, με αποτέλεσμα τη δημιουργία διεθνούς ερευνητικού και πρακτικού ενδιαφέροντος για τη συνδυασμένη χρήση των δεδομένων SAR με άλλου τύπου τοπογραφικά δεδομένα.

Υπό το πρίσμα αυτών των εξελίξεων ο γενικός αντικειμενικός σκοπός της διατριβής είναι διττός: i) να διερευνήσει τη δυνατότητα συνδυασμένης χρήσης δεδομένων SAR υψηλής ανάλυσης με άλλου τύπου τοπογραφικά δεδομένα και ii) να διερευνήσει τη χρήση γραμμικών στοιχείων ακανόνιστης γεωμετρίας ως εναλλακτική (του μεμονωμένου σημείου) μορφή πληροφορίας αναφοράς για την αλληλοαναφορά και τη γεωαναφορά των δεδομένων SAR με άλλου τύπου τοπογραφικά δεδομένα. Η διερεύνηση αυτή αποσκοπεί στην αξιοποίηση της συμπληρωματικής (γεωμετρικής, φασματικής, χωρικής και χρονικής) φύσης των δεδομένων SAR στην υφιστάμενη τεχνολογία επισκόπησης και χαρτογράφησης της γήινης επιφάνειας. Η προηγούμενη σχετική έρευνα στο πεδίο αυτό δεν είναι ούτε εκτεταμένη ούτε συστηματική εξαιτίας του γεγονότος ότι μέχρι πρόσφατα δεν ήταν ευρέως διαθέσιμα δεδομένα SAR υψηλής ανάλυσης. Επιπλέον η χρήση γραμμικών στοιχείων ακανόνιστης γεωμετρίας έχει διερευνηθεί ελάχιστα.

Ειδικός αντικειμενικός σκοπός της διατριβής είναι η άρση των παραδοχών και περιορισμών που είχαν τεθεί σε προηγούμενες ερευνητικές εργασίες, ώστε η συνδυασμένη χρήση δεδομένων SAR να είναι εφικτή: i) για τα δεδομένα SAR υψηλής ανάλυσης, ii) για μη γεωμετρικά διορθωμένα δεδομένα, iii) με χρήση γραμμικών στοιχείων ακανόνιστης

γεωμετρίας, iv) για τυχαία μορφή γήινης επιφάνειας (όχι απαραίτητα επίπεδης), v) για ευρύτερες περιοχές της γήινης επιφάνειας (όχι μόνο μικρά τμήματα), και vi) για μετρική αξιοποίηση των δεδομένων SAR για τοπογραφικές εφαρμογές. Η άρση τέτοιου είδους παραδοχών είναι απόλυτως απαραίτητη προκειμένου για την ανάπτυξη γενικών μεθόδων που επιτρέπουν την εξαγωγή γενικών και ρεαλιστικών συμπερασμάτων για την ενσωμάτωση των δεδομένων των δεκτών SAR στην επισκόπηση και τοπογραφική αποτύπωση της γήινης επιφάνειας.

Στο πλαίσιο αυτό, η διατριβή εισάγει νέα γενική μέθοδο για την ολική συνταύτιση ζεύγους ετερογενών γραμμικών στοιχείων ακανόνιστης γεωμετρίας (μη συναρτησιακών καμπυλών), η οποία βασίζεται στο γενικό Επαναληπτικό Αλγόριθμο Πλησιέστερων Σημείων (Iterative Closest Point - ICP) σημαντικά τροποποιημένο για γραμμικά στοιχεία (με νέα μέθοδο υπολογισμού πλησιέστερων (ομόλογων/αντίστοιχων) κοινών σημείων μεταξύ γραμμικών στοιχείων). Ειδικότερα εισάγονται νέες μέθοδοι συνταύτισης γραμμικών στοιχείων στο επίπεδο (2Δ-2Δ), συνταύτισης γραμμικών στοιχείων στο χώρο (3Δ-3Δ) και συνταύτισης γραμμικών στοιχείων διαφορετικών διαστάσεων (3Δ-2Δ). Αυτές συνοδεύονται από νέες μεθόδους υπολογισμού αρχικής προσέγγισης βάσει στερεού μετασχηματισμού αλλά και βάσει μη στερεού μετασχηματισμού, χρησιμοποιώντας φυσικές ή στατιστικές ιδιότητες των γραμμικών στοιχείων. Εισάγεται και νέα γενική μέθοδος ολικής συνταύτισης δικτύου (πλήθους) ετερογενών γραμμικών στοιχείων ακανόνιστης γεωμετρίας που βασίζεται σε νέα μέθοδο αντιστοίχισης γραμμικών στοιχείων μεταξύ των δικτύων και ενιαίας επίλυσής τους με τη Μέθοδο Ελαχίστων Τετραγώνων (MET). Επίσης εισάγεται νέα και γενική μέθοδος άμεσης γεωαναφοράς εικόνων TerraSAR-X κεκλιμένης γεωμετρίας που βασίζεται σε νέα γεωμετρική αντιμετώπιση της διαδικασίας λήψης μετρήσεων SAR και αναλυτικής επίλυσης της γεωμετρίας λήψης, καθώς επίσης και μέθοδος αναλυτικού υπολογισμού τρόπου μετάδοσης του σφάλματος από τον τρισδιάστατο χώρο στη διδιάστατη εικόνα SAR. Τέλος εισάγεται νέα και γενική μέθοδος γεωμετρικής συσχέτισης - αναγωγής (της οποίας η ορθοαναγωγή είναι ειδική περίπτωση) μεταξύ μη γεωμετρικά διορθωμένης εικόνας και ετερογενών τοπογραφικών δεδομένων, καθώς και ραδιομετρικής συγχώνευσης ετερογενών εικόνων (συμπεριλαμβανομένων εικόνων SAR). Οι γενικές μέθοδοι της διατριβής τεκμηριώνονται και ελέγχονται με πλήθος προσομοιωμένων και πραγματικών δεδομένων σε πραγματικά προβλήματα και σε ορισμένες ιδιαίτερα απαιτητικές τοπογραφικές εφαρμογές.

Εκτός από νέες γενικές μεθόδους σε επίπεδο βασικής έρευνας, εισάγον-

ται νέες ειδικές μέθοδοι σε επίπεδο εφαρμοσμένης έρευνας. Οι γενικές μέθοδοι συνδυάζονται με μεθόδους, προβλήματα και δεδομένα από το ευρύτερο επιστημονικό πεδίο του Τοπογράφου Μηχανικού όπως είναι οι γεωδαιτικοί μετασχηματισμοί, τα μοντέλα γεωειδούς, τα παγκόσμια ψηφιακά μοντέλα επιφανείας, οι χαρτογραφικοί προβολικοί μετασχηματισμοί, ο τριγωνισμός Delaunay, η ραδιομετρική επεξεργασία εικόνων και οι μέθοδοι γεωμετρικής επεξεργασίας δισδιάστατων εικόνων που απεικονίζουν την τρισδιάστατη γήινη επιφάνεια. Συγκεκριμένα εισάγονται ειδικές μέθοδοι για την: i) Αλληλοαναφορά ή γεωαναφορά μη γεωμετρικά διορθωμένων εικόνων SAR με άλλου τύπου τοπογραφικά δεδομένα, ii) Αλληλοαναφορά ή γεωαναφορά μη γεωμετρικά διορθωμένων οπτικών εικόνων με δεδομένα SAR, iii) Αλληλοαναφορά μη γεωμετρικά διορθωμένων εικόνων SAR και οπτικών εικόνων, iii) Συγχώνευση/Σύντηξη μη γεωμετρικά διορθωμένων εικόνων SAR με οπτικές εικόνες και iv) Ταχεία γεωμετρική διόρθωση δορυφορικών εικόνων SAR του δέκτη TerraSAR-X μέσω άμεσης γεωαναφοράς και χρήσης παγκόσμιων μοντέλων επιφανείας και γεωειδούς. Οι ειδικές μέθοδοι τεκμηριώνονται και ελέγχονται με πραγματικά δεδομένα, και τεκμηριώνουν ακόμα περισσότερο τις γενικές μεθόδους από τις οποίες προήλθαν.

Οι ειδικές και γενικές μέθοδοι εφαρμόζονται σε τυχαία μορφή γήινης επιφάνειας και ευρύτερες περιοχές της γήινης επιφάνειας. Τα αποτελέσματα είναι συνεπή με την αναμενόμενη ακρίβεια και καταδεικνύουν τις δυνατότητες των σύγχρονων δεκτών SAR και τις δυνατότητες των γενικών και ειδικών μεθόδων που έχουν αναπτυχθεί στη διατριβή.

Λέξεις κλειδιά: φωτογραμμετρία, γεωδαισία, τηλεπισκόπηση, ραντάρ συνθετικού ανοίγματος/κεραίας (SAR), οπτικές εικόνες, τοπογραφικά δεδομένα, ετερογενή δεδομένα, γεωαναφορά, αλληλοαναφορά, συνταύτιση, συγχώνευση, γραμμικά στοιχεία, επαναληπτικός αλγόριθμος πλησιέστερων σημείων (ICP), μέθοδος ελαχίστων τετραγώνων (MET)

Contents

Contents	vi
Nomenclature	xiii
List of Figures	xiv
1 Introduction	1
1.1 Synergy of SAR and heterogeneous data	2
1.2 Co-registration of SAR and heterogeneous data	3
1.3 Co-registration methods	4
1.4 Linear features as reference information	6
1.5 Objective	8
1.6 Overview, contribution and organisation	10
2 Global matching of FFLFs	12
2.1 Analytical representation of linear features	13
2.2 General representation - FFLFs	15
2.3 Registration using homologous points	16
2.4 Registration using FAMRs	17
2.5 Registration using FFLFs matching	19
2.6 Computation of closest point pairs	20
2.7 FFLFs matching in two and three dimensions (2D-2D, 3D-3D) . .	23
2.8 Matching of FFLFs of different dimensionality (3D-2D)	24
2.9 Computation of initial approximation: The rigid approach	25
2.9.1 Translation approximation	26
2.9.2 Scale approximation	27
2.9.3 Rotation approximation	28
2.9.3.1 Rotation approximation using characteristic points	28
2.9.3.2 Rotation approximation using average azimuth .	29
2.9.3.3 Rotation approximation using exhaustive search .	29
2.9.3.4 Rotation approximation for 3D	30

2.9.4	Initial approximation for projection transformations (3D-2D)	31
2.10	Computation of initial approximation: The non-rigid approach . . .	31
2.10.1	Moment equations	32
2.10.2	Length equation	33
2.10.3	Least Squares Adjustment	34
2.10.4	Partial derivatives	35
2.11	Matching networks of FFLFs	36
2.11.1	Identification of FFLFs correspondences	38
2.11.1.1	End node approach	39
2.11.1.2	Centroid approach	39
2.11.1.3	Length approach	40
2.11.1.4	The average distance approach	41
2.11.1.5	The ICP approach	42
2.11.1.6	Hybrid approach	42
2.11.2	Partial Identification of FFLFs correspondences	43
2.11.3	Unified LSA	43
2.11.4	Pre-alignment	44
2.11.5	Computational aspects	45
2.11.6	3D-3D and 3D-2D networks	46
2.12	Overview and contribution	47
3	Co-registration, correlation and merging	49
3.1	GCLFs-based co-registration	50
3.2	Direct-georeferencing-based co-registration	51
3.2.1	Problem Formulation	52
3.2.2	Computation of the parameters $R_0, \Delta R, t_0, \Delta t_{Az}$	54
3.2.3	Computation of sensor's position with respect to time . . .	55
3.2.3.1	Available orbit data	55
3.2.3.2	Orbit approximation considering linear interpolation	56
3.2.3.3	Orbit approximation considering cubic interpolation: 2 time stamps	56
3.2.3.4	Orbit approximation considering cubic interpolation: more than 2 time stamps	57
3.2.4	Computation of point acquisition time	57
3.2.4.1	Computation of time t_P considering linear interpolation	58
3.2.4.2	Computation of time t_P considering cubic interpolation	58
3.3	Geometric correlation and radiometric merging	59
3.3.1	Geometric correlation	60

3.3.2 Radiometric merging	63
3.4 Overview and contribution	65
4 Validation and evaluation - simulated tests	67
4.1 Matching single pairs of 2D FFLFs with gross error	67
4.1.1 Transformation	67
4.1.2 Initial approximation	68
4.1.3 Tests	68
4.2 Matching single pairs of unrelated 2D FFLFs	70
4.3 Partial matching single pairs of 2D FFLFs	71
4.4 Matching single pairs of FFLFs of different dimensionality	72
4.4.1 Projective transformation	72
4.4.2 Test	73
4.5 Overview and contribution	73
5 Application to real world problems	
Validation and evaluation	76
5.1 Registration of 2D FFLFs Extracted from high resolution satellite imagery	76
5.1.1 Data sets	77
5.1.2 Application and results	77
5.2 Geospatial Data Integration using automatic global matching of FFLFs	81
5.2.1 Data sets	82
5.2.2 Application and results	82
5.3 Contour line matching	84
5.3.1 Data sets	84
5.3.2 Application and results	85
5.4 Multitemporal Geospatial Data Integration using automatic global matching of 3D FFLFs	86
5.4.1 Data sets	86
5.4.2 Transformation	87
5.4.3 Application and results	87
5.5 Registration of optical and SAR imagery by automatic free-form features global matching	89
5.5.1 Data sets	90
5.5.2 Projective transformations	91
5.5.3 Results	92
5.6 Enhanced initial approximation for ICP-based global matching of FFLFs in side-looking RADAR geometry	94
5.6.1 Data sets	95

5.6.2	Projective transformation	95
5.6.3	Preprocessing	100
5.6.4	Application and results	100
5.7	Multitemporal data registration through global matching of networks of 2D FFLFs	103
5.7.1	Data sets	104
5.7.2	Preprocessing	105
5.7.3	Application and results	106
5.8	Georeferencing of TerraSAR-X Images using Science Orbit Data	108
5.8.1	Data sets	108
5.8.2	Preprocessing	110
5.8.3	Application and results	110
5.9	Absolute orientation of old aerial photographs through ICP-based global matching of free-form linear features	111
5.9.1	Data sets	113
5.9.2	Transformation	113
5.9.3	Preprocessing	113
5.9.4	Application and results	113
5.10	Recovery of the geometry of historical aerial photographs associating self-calibration with ground control linear features	115
5.10.1	Projective transformations	117
5.10.2	Data sets	118
5.10.3	Preprocessing	120
5.10.4	Application and results	121
5.11	Overview and contribution	122
6	Specific methods	123
6.1	Georeferencing of not geometrically corrected SAR images to geometrically corrected unitemporal and multitemporal maps and optical images	123
6.1.1	Problem Formulation	126
6.1.2	Design of tests	127
6.1.3	Data sets	128
6.1.4	Error Propagation from Object Space to SAR Image Space	130
6.1.5	Application and results	131
6.1.6	Validation, evaluation and discussion of the results	134
6.1.7	Conclusions	141
6.2	Georeferencing of not geometrically corrected optical images to geometrically corrected SAR data	142
6.2.1	Test site and data sets	143
6.2.2	Overview and objective	147

6.2.3	Method	148
6.2.4	Measurement of the GCI	148
6.2.5	Computation of the georeferencing	149
6.2.6	Evaluation	150
6.2.7	Conclusions	152
6.3	Co-registration of not geometrically corrected optical and SAR im- agery over mountainous areas through automatic free-form features global matching	153
6.3.1	Projective transformations models	155
6.3.2	Two stage initial approximation	155
6.3.3	Data sets	156
6.3.4	Preprocessing	157
6.3.5	Geometric correction	158
6.3.6	Work flow of the test	158
6.3.7	Results	160
6.3.8	Conclusions	161
6.4	Fusion of optical and SAR images in slant range SAR geometry .	162
6.4.1	Data sets	165
6.4.2	Application and results	166
6.5	Rapid geometric correction of SAR images	169
6.5.1	Coordinate systems	170
6.5.2	The method	172
6.5.3	Computation of projection coordinates (f_1)	172
6.5.4	Computation of geodetic coordinates (Redfearn series) . .	174
6.5.5	Computation of orthometric elevation (DEM)	175
6.5.6	Computation of geometric elevations (geoid)	175
6.5.7	Computation of geocentric coordinates (f_2)	176
6.5.8	Computation of SSC image coordinates (direct georeferenc- ing)	177
6.5.9	Application of the method	177
6.6	Overview and contribution	183
7	Contribution, conclusions and outlook	185
	References	190

Nomenclature

Roman Symbols

ALOS Advanced Land Observing Satellite

ASI Italian Space Agency

ASTER Advanced Spaceborne Thermal Emission and Reflection Radiometer

B-spline Basis spline

CAD Computer-Aided Design

CE Circular Error

CGIAR Consultative Group on International Agricultural Research

CNES French National Centre for Space Studies

COSMO-SkyMed Constellation of small Satellites for the Mediterranean basin
Observation

CP Check Point

DEM Digital Elevation Model

DLR German Aerospace Centre

DLT Direct Linear Transform

DSM Digital Surface Model

EARSeL European Association of Remote Sensing Laboratories

EEC Enhanced Ellipsoid Corrected

EGG European Gravimetric Geoid Model

EGM	Earth Gravitational Model
EIGEN-6C2	European Improved Gravity model of the Earth by New techniques, Combined 2nd version
Envisat	Environmental Satellite
EO	Earth Observation
ERS	European Remote Sensing satellite
ETRS89	European Terrestrial Reference System 1989
FAMR	Feature of Analytic Mathematical Representation
FFLF	Free-Form Linear Feature
GCI	Ground Control Information
GCLF	Ground Control Linear Feature
GCP	Ground Control Point
GDAL	Geospatial Data Abstraction Library
GIS	Geographic Information System
GPS	Global Positioning System
HS	High Resolution SpotLight
ICGEM	International Center for Global Gravity Field Models
ICP	Iterative Closest Point
IEEE	Institute of Electrical and Electronics Engineers
ISPRS	International Society for Photogrammetry and Remote Sensing
LE	Linear Error
LSA	Least Squares Adjustment
NURB	Non-Uniform Rational Basis spline
PF	Polynomial Function
RADAR	RAdio Detection And Ranging

CONTENTS

RGB Red Green Blue

RMSE Root Mean Square Error

RPF Rational Polynomial Function

SAR Synthetic Aperture Radar

SRTM Shuttle Radar Topography Mission

SSC Single Look Slant Range Complex

TanDEM-X TerraSAR-X add-on for Digital Elevation Measurement

TIN Triangulated Irregular Network

List of Figures

2.1	Computation of closest points between point sets.	20
2.2	Computation of closest point pairs between FFLFs.	21
2.3	Speed up of computation of closest point pairs.	22
2.4	Exhaustive search algorithm.	30
2.5	The problem of global matching of networks of heterogeneous FFLFs.	37
2.6	Determination of FFLFs correspondences using arbitrary metric.	38
2.7	(a) Homologous end nodes, (b) common end nodes, (c) common start and end nodes.	39
2.8	Different FFLFs with same centroid.	40
2.9	(a) Non-uniform density of nodes, (b) Not homologous FFLFs which have a short identical part.	41
2.10	ICP for global matching networks of FFLFs.	44
2.11	ICP for global matching networks of FFLFs (3D-2D).	46
3.1	SAR imaging geometry.	52
3.2	Imaging geometry in range.	53
3.3	Imaging geometry in azimuth.	54
3.4	Linear orbit.	57
3.5	Geometric Fusion.	61
3.6	Geometric merging algorithm.	62
3.7	Radiometric Fusion.	65
4.1	Test S1.	68
4.2	Test S2.	69
4.3	Test S3.	69
4.4	Test S4.	70
4.5	Test S5.	70
4.6	Test S6.	71
4.7	Test S7.	72
4.8	Test S8 - 3D FFLF.	73
4.9	Test S8 - 3D-2D matching with no error.	74

LIST OF FIGURES

4.10 Test S8 - 3D-2D matching with artificial error.	74
5.1 Medium scale 40 years old paper map (left) and recent satellite optical image (right).	78
5.2 Map: road edges (yellow), road centreline (cyan).	78
5.3 Image: road edges (green), road centreline (magenta).	79
5.4 Image with Sobel filter: road edges (green), road centreline (magenta).	80
5.5 Matching results - Roughly pre-aligned Road centreline from map (cyan) and from satellite image (magenta) - Image to map transformed centreline.	80
5.6 Registration results - Recent satellite image registered to 40 years old map.	81
5.7 Study area on the vector data (left) and on the recent satellite optical image (right).	82
5.8 Data and matching results.	83
5.9 Integrated data.	83
5.10 Contour lines in maps of scale 1:50 000 and 1:5 000.	84
5.11 Contours line matching (2D-2D). Data (cyan, magenta) and results (black).	85
5.12 RMS error reduction.	86
5.13 Topographic map 1:50 000 (left) and 1:5 000 (left).	87
5.14 Matching results: Map 1:50 000 to map 1:5 000.	88
5.15 Matching results of profiles: Map 1:50 000 to map 1:5 000.	88
5.16 Topographic map (right) and optical image (left).	90
5.17 SAR image.	91
5.18 Matching results: SAR image to Map.	92
5.19 Matching results: optical image to Map.	93
5.20 Example 1: Map road centreline (in cyan).	96
5.21 Example 1: SAR road centreline (in orange).	97
5.22 Example 2: Map road centreline (in cyan).	97
5.23 Example 2: SAR road centreline (in orange).	98
5.24 Example 1: Polynomial initial approximation (blue dashed) using 4 moments.	98
5.25 Example 1: Polynomial initial approximation (blue dashed) using 4 moments and length equation.	99
5.26 Example 2: Polynomial initial approximation (blue dashed) using 4 moments.	99
5.27 Example 2: Polynomial initial approximation (blue dashed) using 4 moments and length equation.	100

LIST OF FIGURES

5.28	Convergence of the ICP-based matching with present method and the two stage method.	101
5.29	Example 1: Matched FFLFs.	102
5.30	Example 2: Matched FFLFs.	102
5.31	Map restituted in 1970: study area with the linear features used for the registration.	104
5.32	IKONOS satellite image captured in 2000: study area with the linear features used for the registration.	105
5.33	Registration using linear features: pre-aligned data and results. . .	106
5.34	Registration results: Recent satellite image overlaid to 30 years older map.	107
5.35	Archived maps.	109
5.36	SAR image and CPs' distribution.	109
5.37	The overlapping part of the historical image (yellow), the FFLFs (red) and the CPs (green).	112
5.38	Planar and vertical matching results.	114
5.39	Data sets: aerial photograph captured in 1945 (left), orthoimage made from aerial images collected in 2008 (right).	117
5.40	GCLFS (in red), CPs (in yellow) and GCPs (in cyan) on the historical photograph.	119
5.41	GCLFS on the historical photograph (in magenta), projected GCLFs from the orthoimage and the corresponding DEM using the computed transformation (in black).	121
6.1	Archived map.	124
6.2	Recent optical orthoimage.	125
6.3	SSC SAR image.	126
6.4	Roads are common in all data sets.	129
6.5	Matching results of Test A0. 3D GCLFs extracted from the old map (cyan), 2D GCLFs extracted from the SAR image (magenta), matched projection of the 3D GCLFs (black dashed). Figure 6.6 shows the road sections inside the green ellipses magnified (GCLF = ground control linear features).	131
6.6	Test A0: Road sections with wide temporal changes. 2D GCLFs (magenta), matched projection of the 3D GCLFs (black dashed). . .	132
6.7	Matching results of Test A1. GCLFs with wide temporal changes are excluded.	132
6.8	Matching results of Test A2. Only few GCLFs are used.	133
6.9	Test A1: Road sections with temporal changes. 2D GCLFs (magenta), matched projection of the 3D GCLFs (black dashed). . . .	133

LIST OF FIGURES

6.10 Matching results of Test B1. The 3D GCLFs are extracted from a recent orthoimage.	135
6.11 Matching results of Test B2. Only few GCLFs are used.	135
6.12 The CP distribution used for tests A (yellow) and B (red), shown on the SAR image.	136
6.13 Some of the CPs used for test B, shown on the SAR (left) and optical (right) image.	137
6.14 Test A2: CPs residuals in Range and Azimuth (pixels).	139
6.15 Test site and coverage of the satellite optical image (in red) and the aerial SAR data (in cyan).	144
6.16 3D roads centrelines overlaid on the geometrically corrected SAR image.	145
6.17 The interferometrically produced DSM.	146
6.18 The distribution of GCLFS and GCPs (in blue) and CPs (in green) over the test site. GCLFs and CPs (left), and GCPs and CPs (right).	151
6.19 Topographic map (right) and optical image (left).	156
6.20 SAR image.	157
6.21 Map: road edges (lines in red), road centreline (in cyan).	158
6.22 Optical: road edges (lines in green), road centreline (in magenta).	159
6.23 SAR image: road edges (line in green), road centreline (in orange).	159
6.24 Profile of road centreline, computed by the DTM.	159
6.25 Matching results: Optical image to Map.	160
6.26 Matching results: SAR image to Map.	161
6.27 The co-registered optical and SAR images geometrically corrected.	162
6.28 SAR image.	162
6.29 Optical image.	163
6.30 Shaded representation of TIN created by the contours of the map.	163
6.31 Metallic pillars. Left: map. Centre: optical image. Right: SAR image.	164
6.32 Metallic pillars. Left: SAR image. Right: fused SAR image.	167
6.33 Optical and SAR images fused in slant range geometry.	168
6.34 The geoid undulation.	171
6.35 Transformations of coordinate systems.	173
6.36 Geoid undulation over the country according to EGM2008.	176
6.37 The global SRTM DEM over the test site.	178
6.38 The global ASTER DEM over the test site.	179
6.39 The archived local DEM over the test site.	179
6.40 The recent local DEM over the test site.	180
6.41 The geometrically corrected image using the ASTER DEM.	181
6.42 The distribution of the CPs on the SSC TerraSAR-X image.	181

LIST OF FIGURES

6.43	Expected planar error according to the sensor's specifications (in black) and according to analytical equations (in red).	183
------	---	-----

Chapter 1

Introduction

The year 2007 marked the beginning of two independent satellite SAR projects, the COSMO-SkyMed (Covello et al. [2010]) and the TanDEM-X (Werninghaus and Buckreuss [2010], Breit et al. [2010]), as the COSMO-SkyMed-1, the COSMO-SkyMed-2 satellite sensors and the TerraSAR-X satellite sensor launched to orbit. The COSMO-SkyMed project was expected to launch to orbit a constellation of four identical sensors, while the TanDEM-X project was expected to launch two identical sensors designed to be used as a single-pass satellite interferometric mission. Both projects were based on X-band SAR sensors and were able to collect High Resolution (HR) SAR images. At the end of the same year another satellite, the Radarsat-2 satellite (Ali et al. [2004]) carrying a C-band SAR sensor, launched to orbit, following its predecessor Radarsat-1. This was the beginning of a small flotilla of high resolution satellite SAR sensors in Earth orbit. In 2010, the COSMO-SkyMed-3, the COSMO-SkyMed-4 and the TanDEM-X satellites also launched to orbit, completing the COSMO-SkyMed and the TanDEM-X projects. During the same period seven reconnaissance satellites, the SAR-Lupe constellation, the TechSAR and the RISAT-2 launched. In total, thirteen high resolution SAR sensors launched to orbit during the period 2007-2010 (Ioannidis and Vassilaki [2008]).

The HR imaging capability is probably the best characteristic among the wide range of innovative characteristics of these sensors (Covello et al. [2010]). The resolution of this new generation of SAR sensors is many times better than the resolution of the previous generation such as ERS-1 (1991), Radarsat-1 (1995), ERS-2 (1995) and Envisat (2002). The resolution of HR satellite SAR images is now 1 m, while previously the resolution generally varied from 10m to 30m. As a result, details of the Earth's surface such as roads and buildings that was hard or even impossible to identify on the previous generation of satellite SAR images, are now easy to identify (Eineder et al. [2009]). This ground-breaking development in satellite SAR sensors was the springboard of this dissertation.

Before the new generation, SAR sensors were well-known for their all-weather and day-and-night capabilities. It was also well known that they provide information about the properties of the targets, their 3D geometry and their evolution over time; an extended review of the SAR technology, the related methods and its applications can be found in Leberl [1991], Henderson and Lewis [1998] and more recently in Maitre [2010], Massonnet and Souyris [2010]. At the same period, it can not be overlooked that optical satellite images were well-established and in certain cases they had much better resolution. And certainly they are more descriptive as they are closer to the human eye perception, compared to the SAR images. Additionally, there was worldwide abundance of other existing geospatial data to be exploited, maintained and updated (Butenuth et al. [2007]).

The new generation of HR satellite SAR data had for the first time compatible resolution with existing remote sensing and geospatial data. As a result, a growing interest in the synergistic (combined and/or integrated) use of SAR data with heterogeneous (multi-source) remote sensing and geospatial data began to evolve. The interest was made evident by transnational cooperations of optical and SAR satellites (e.g. the CNES/ASI Orfeo program Taverna [2009], Galland et al. [2005]) and with the simultaneous existence of optical and SAR sensors in the same satellite (e.g. the ALOS satellite Shibasaki et al. [1997], Kimura and Ito [2000], Rosenqvist et al. [2007]). Related working groups began to appear in international scientific societies (e.g. ISPRS, EARSeL, IEEE) while research on this field gradually intensified (Section 1.1). In this light, the following primary question needed a clear answer:

“How can HR satellite SAR data be combined with heterogeneous remote sensing and geospatial data (multimodal and multitemporal)?”

The answer to this question, in the context of the-state-of-the-art shown in Sections 1.1–1.4, forms the objective of this dissertation, which is analysed in Section 1.5.

1.1 Synergy of SAR and heterogeneous data

The synergistic use of heterogeneous data sets offers enhanced capabilities for extracting information and optimised data updating, compared to the use of a single data type (Butenuth et al. [2007]). The synergistic use of SAR data with heterogeneous data has been, and is still being investigated for applications such as the detection and height estimation of buildings (Wegner et al. [2009], Thiele et al. [2009b], Wegner et al. [2011] and Wegner [2011]), the extraction of building outlines (Tupin and Roux [2003] and Sportouche et al. [2011]), the building

change detection (Vidal and Moreno [2011]), the earthquake damage detection (Stramondo et al. [2006] and Brunner et al. [2010] and Chini et al. [2009]), the floodplain inundation (Townsend and Walsh [1998]), the mapping of wetlands (Li and Chen [2005]), the monitoring of surface water quality (Zhang et al. [2002]), the stem volume estimation in boreal forest area / estimation of forest variables (Fransson et al. [2001], Holmström and Fransson [2003] and Moghaddam et al. [2002]), the crop management-identification (Moran et al. [1997], Blaes et al. [2005] and Okamoto and Kawashima [1999]), the snow and glaciers monitoring (Koskinen et al. [1999] and Trouve et al. [2007]) and the planetary mapping (Soderblom et al. [2007]), just to name a few.

Wegner [2011] classifies the ways to co-process (fuse) SAR data and heterogeneous data sets to:

1. *The co-registration of the data* (Toutin [1995], Dare and Dowman [2001], Inglada and Giros [2004], Hong and Schowengerdt [2005], Wegner [2007], Suri et al. [2009] and Suri and Reinartz [2010]).
2. *The pixel-based fusion* (Ehlers and Tomowski [2008] and Sörgel et al. [2008]).
3. *The feature-based fusion* (Schistad et al. [1996], Le Hegarat-Mascle et al. [1997], Macri-Pellizzeri et al. [2002], Waske and Benediktsson [2007]).
4. *The decision-based fusion* (Benediktsson et al. [1990], Serpico and Roli [1995], Briem et al. [2002], Waske and van der Linden [2008]).

This dissertation focuses at first on the co-registration¹ and later on the pixel-based (radiometric) fusion of HR SAR data with heterogeneous remote sensing and geospatial data. Both fields are quite new as HR SAR data was not available until recently, as it was presented earlier.

1.2 Co-registration of SAR and heterogeneous data

Whatever the type of data, the synergistic use prerequisites a good (or even perfect) co-registration. Inaccurate co-registration leads to poor or impossible merging and/or comparison of the data sets, which are the usual objectives of the combined use (Singh [1989], Townshend et al. [1992], Dai [1998], Habib and Al-Ruzouq [2005]).

Brown [1992] defines the co-registration as a mapping:

$$I_2(x, y) = g(I_1(f(x, y)))$$

¹The term “registration” also appears in the literature. The terminology of Newby [2012] and Zitova and Flusser [2003] is adopted here.

between two images $I_1(x, y)$ and $I_2(x, y)$ and tries to find the optimal 2D spatial-coordinate transformation f and optionally the 1D intensity transformation g , which make the best matching of the images.

Inglada and Giros [2004] defines the co-registration as a two step process. The first step determines the geometric transformation T which maximises the similarity between the reference image I and the secondary image J transformed by T :

$$S_c(I, T[J])$$

where S_c is a positive scalar function which measures the similarity between two images. The second step resamples the secondary image J by applying the transformation T .

There are many alternative definitions of the co-registration in the literature. They all agree that co-registration is ultimately the process of overlaying data sets of the same scene. The data sets to be co-registered are generally classified (Fonseca and Manjunath [1996], Zitova and Flusser [2003]) to:

1. Data sets collected from different viewpoints (*multiview analysis*).
2. Data sets collected at different times (*multitemporal analysis*).
3. Data sets collected using different sensors (*multimodal analysis*).
4. Images and models of the scene such as DEMs and maps (*scene-to-model analysis*).

In this dissertation the problem is considered in its general form and faces all the cases of the co-registration problem: the multimodal, the multitemporal, the scene-to-model and certainly the multiview analysis. In the era of the plurality of remote sensing and geospatial data types (both new and archived), it is necessary to face the problem of co-registration in its entirety, in order to be able to use HR satellite SAR data combined with the remote sensing and geospatial data which is available in the area of interest. After all, in real world practical cases, the type of available data varies widely.

1.3 Co-registration methods

The problem of the co-registration appears in many disciplines such as surveying, medicine, electrical and mechanical engineering. The solutions to this essentially common problem differentiate depending on the requirements of the corresponding discipline, as the data sets and the objectives usually vary widely. One discipline may be interested in the computational speed of the registration while

another may sacrifice speed for accuracy. Other disciplines face radiometrically monotonous images, while others face complex, rapidly varying images. In some disciplines such as surveying engineering, wide variations of the problem may occur within the same discipline. As a result a variety of co-registration methods have been developed (Brown [1992], Zitova and Flusser [2003]). Two broad categories of methods exist:

1. The *Area-based methods*.
2. The *Feature-based methods*.

Area-based methods deal with the images without attempting to detect distinct features. They use windows (rectangles) of predefined size or even whole images and work directly with the image intensity for the correspondence estimation during the registration process.

The limitations of the area based methods are: 1) the rectangular windows allow only translation or a small rotation between the images, otherwise they do not cover the same part of the scene if the images are deformed by more complex transformations, 2) “dull” windows containing smooth areas without prominent details will probably lead to incorrect matchings with other “dull” windows, 3) the matching of direct image intensities makes area based methods sensitive to the intensity changes introduced by noise, varying illumination and different sensor types (Zitova and Flusser [2003]).

Area-based methods are preferably applied when the images have not many prominent details (monotonous radiometry) and the distinctive information is provided by gray-levels or colours rather than local shapes and structure. A typical case is medical images which are not rich in details (Rezaie and Srinath [1984]).

Feature-based methods work with features (point, linear, region) which represent information of higher level. The features should be distinct, cover the whole image and be efficiently detectable either manually or automatically in both images. They should remain constant between the acquisition times of the two images. In contrast to area-based methods, they do not work with image intensity values, which makes them suitable for cases with varying illumination, complex scenes and/or multimodal acquisition.

Feature-based method are recommended if the images contain sufficient distinctive and easily detectable features. This is usually the case in remote sensing and computer vision applications, where typical images contain a lot of details such as towns, rivers, roads etc (Zitova and Flusser [2003]).

The only drawback of feature-based methods is that they depend on the feature detection method. Other than that they are very general and allow the co-registration of very heterogeneous data, even images with other data types

such as maps. They can also handle complex transformations such as the SAR physical model (Vassilaki [2012]). For all these reasons feature-based methods are popular in surveying engineering. Traditionally point features are used for the computation of the transformation whatever the data type (geodetic reference transformation, geospatial data integration, projective image transforms). However, research is gradually oriented in the exploitation of more complex features such as region features and linear features, as alternative or complementary to point features (Tommaselli and Marcato Jr. [2012]).

In this dissertation, feature-based methods are used as they: i) are of long lasting value in surveying engineering, ii) are able to handle very heterogeneous data, iii) are able to handle complex scenes of the Earth' surface, iv) can handle to complex transformations and distortions of the sensor. Moreover, initial results on feature-based methods on the combined use of SAR data with heterogenous remote sensing and geospatial data were very promising (Dare and Dowman [2001] and Karjalainen [2007]).

1.4 Linear features as reference information

Feature-based methods use point, line and region (which are essentially closed lines) features as matching primitives. For the co-registration of SAR data with heterogeneous data, region (Dare and Dowman [2001]) and line features (Li et al. [1995], Karjalainen [2007]) have been exploited as matching primitives, in order to work around the ambiguous identification of points on the fuzzy and speckled SAR images and to overpass the difficulty to reliably identify common points between the SAR images and other data types. For these reasons, this dissertation uses linear features such as road edges and coastline (line features) and building outlines (region features) as matching primitives, in order to exploit the complex features abundant in the man-made and physical environment.

Linear features have attracted the interest of the remote sensing, photogrammetric and geoscientific society during the last three decades. Linear features are investigated as a complementary or an alternative to the solitary point, which is the basis of all photogrammetric mathematical models. The advantages of linear features against points have been widely discussed in literature. Linear features carry strong and descriptive geometric information. They are abundant in the man-made and physical environment (building outlines, roads, pipelines, coastline etc). They are detected and matched more reliably than solitary points. And they tend to persist over time. Heikkila [1991], Schenk [2004] and Habib et al. [2004], among others, discuss on the advantages of linear features in detail.

Linear features have been investigated in various research studies. Straight lines, straight line segments and generally features of analytical mathematical

representation (FAMRs), such as circles, were the first choice features in the early transitional stage from classical point-based models to more complex features (Masry [2008], Haralick and Chu [1984], Mulawa and Mikhail [1988], Liu et al. [1990], Petsa and Patias [1994], Weng et al. [1992]). FAMRs are still an active field of research: Bartoli and Sturm [2005], Jaw and Perny [2008], Tommaselli et al. [2010], Ok et al. [2012]). On the other hand, geometric features of arbitrary shape (free-form/natural linear features - FFLFs) such as coastline and roads' centrelines, remain mostly un-investigated in photogrammetric processes (Forkert [1994]). State-of-the-art feature extraction algorithms handle FAMRs more efficiently and robustly than FFLFs, a fact that seems to discourage the exploitation of FFLFs. The free-form nature of FFLFs, which is described by consecutive nodes of no regularity, is not amenable to analytical mathematical modelling, making it difficult to incorporate FFLFs into photogrammetric processes. Nevertheless, a boost in the exploitation of FFLFs was performed in Habib et al. [2003a,b]. Their method is based on the Generalised Hough Transform (GHT), an algorithm for detecting arbitrary shapes, which was suitably reformed for incorporation into the photogrammetric mathematical models.

Recent advances in the field have revealed the Iterative Closest Point (ICP) algorithm as a method of exploiting FFLFs for image orientation analysis and geospatial data integration. ICP is a general algorithm initially developed for computer vision applications (Besl and McKay [1992], Zhang [1994], Chen and Medioni [1991]). It consists of four steps which are repeated until convergence:

1. Computation of closest point pairs.
2. Computation of the transformation.
3. Application of the computed transformation.
4. Check of convergence within a tolerance.

Although it has proved to be a very accurate and versatile algorithm for 3D point cloud matching, the ICP algorithm has not been investigated thoroughly for FFLFs matching. Zalmanson [2000] investigated the recovery of exterior orientation parameters of aerial images using ICP-based matching of curves that were approximated by parametric form. Butenuth et al. [2007] used the ICP algorithm to compute the coarse co-registration of geospatial data under the similarity transformation. Akav et al. [2004] investigated the recovery of relative orientation parameters using ICP-based matching of planar curves on synthetic data. In Lee and Yu [2009] the previous research was further developed and the ICP algorithm was used for bundle block adjustment, exploiting FFLFs which were approximated by natural cubic splines. Therefore, the ICP algorithm is

of growing significance for the exploitation of FFLFs in georeferencing and co-registration processes.

In this dissertation, the man-made or physical linear features (building outlines, roads etc) are represented as Free Form Linear Features (FFLFs) which is the most general case of linear features. The matching of FFLFs are done with ICP heavily customised to handle the random geometric nature of FFLFs.

1.5 Objective

In the light of the state-of-the-art which was presented in Sections 1.1–1.4, the objective of this dissertation is two-fold:

1. To research the potential of the combined use of high resolution satellite SAR data with heterogeneous data (multimodal and multitemporal remote sensing and geospatial data).
2. To research the use of linear features as an alternative to solitary points for reference information for the co-registration of HR satellite SAR data with heterogeneous data and vice-versa.

Both topics, either by themselves or in combination, are new since the identification of details was not possible in older SAR data. Additionally, the exploitation of linear features in general (for example in optical images) is still an active field of research. In contrast to the related research (Sections 1.1–1.4), this dissertation successfully faces:

1. HR satellite SAR data. It is much more informative and accurate than the previous generation, it has compatible resolution with existing remote sensing and geospatial data. Furthermore numerous innovative SAR satellite projects are ongoing and/or pending. The majority of the data used in this dissertation is experimental high resolution spotlight acquisitions.
2. Not geometrically corrected data. Off-the-shelf geometrically corrected data merely smooths image distortions, as off-the-shelf products are normally processed massively for the whole surface of the Earth. The accuracy of these products is affected by the (low) accuracy of the global DEM used. Furthermore, in order to correct the data, the data has already been registered, albeit with low accuracy global space methods. Thus, although the geometric correction facilitates the automation of the co-registration, which one might call unnecessary as it has already been done in order to correct the data, it is poised to be of low accuracy.

In order to take full advantage of the resolution and accuracy of the SAR data, which in certain cases also has high geolocation accuracy, the SAR data used in this dissertation is slant range complex data.

3. Linear features of arbitrary geometry. Feature-based matching is according to literature better than Area-based matching for the co-registration of not geometrically corrected SAR data with heterogeneous data. Point features, which are traditionally used for the co-registration of data, are identified poorly on SAR images, due to the speckled and fuzzy nature and the slant range geometry of the SAR images. On the other hand more complex, linear, features such as building outlines, roads and coastline appear quite clear on the SAR images. Linear features rarely have analytical mathematical representation due to their nature (coastline), unknown geometry (rural roads), complicated geometry (building outlines), or errors in construction. Thus linear features of arbitrary geometry are considered in this dissertation. Provision for the rare case that these linear features are of analytical mathematical representation (for instance a circular city square) is also made.
4. Terrain of arbitrary form, not necessarily flat. The assumption of flat terrain appears often in the literature as it simplifies the problem of the co-registration and facilitates its automation. Unfortunately it is an assumption which may be considered valid only for certain areas of the Earth's surface, and in most of these areas approximately. In the majority of the Earth's surface failure to take terrain into account leads to poor accuracy.
5. Greater areas of the Earth's surface, not just small patches. The assumption of small patches also appears often in the literature because it simplifies the problem of the co-registration and makes it computationally possible. However, satellite data is not just a few hundreds x few hundreds of pixels, but tens of thousands. Additionally, in real world practical cases the use of more than one data set is often necessary. After all aerial and satellite mapping methods, in contrast to in-situ methods, are expected to be useful for the mapping of larger areas of the Earth's surface.
6. The metric exploitation of SAR data for topographic applications. SAR data has been mostly used, in research and in practice, for thematic applications, as the previous generation of SAR data had low resolution and could not compete with other data of higher resolution and accuracy. Moreover the speckled and fuzzy nature of SAR images, the large distortions due to the side looking geometry and the complex physical model did not encourage the use of SAR data in the mapping process. In this dissertation

the new generation of high resolution SAR sensors and their overlooked high geolocation accuracy in combination with FFLFs is harnessed to make SAR data a valuable source of accurate metric information.

1.6 Overview, contribution and organisation

Chapter 1 describes the motivation, the objectives in the context of the state-of-the-art of the related research fields and the contribution of this dissertation to knowledge.

Chapter 2 presents the novel general methods for FFLF matching which were developed in this dissertation: i) global matching of single pairs of FFLFs, ii) global matching of networks (multiple pairs) of FFLFs, iii) Robust computation of closest points of FFLFs (ICP), iv) Robust initial approximation for rigid transformations and v) Robust initial approximation for non-rigid transformations. The method for matching single pairs of FFLFs uses the ICP algorithm to perform accurate and robust global matching of heterogeneous FFLFs of the same (2D-2D, 3D-3D) (Vassilaki et al. [2008b]) or of different dimensionality (3D-2D) (Vassilaki et al. [2008a], Vassilaki et al. [2009b]). The method assumes no prior knowledge of the relative position of the features due to two robust approaches for the computation of the initial approximation: the rigid approach which exploits physical properties of the FFLFs (Vassilaki et al. [2008c]) and the non-rigid approach which exploits statistical properties of the FFLFs (Vassilaki et al. [2010]). The method is general as it imposes no constraints on the transformation (or projective transformation) type, on the geometry of the features and on the dimensionality of the data sets. Additionally no prior knowledge of point correspondences between the FFLFs is assumed, due to the method for the automated computation of homologous points between two heterogeneous FFLFs (Vassilaki et al. [2012b]). The method for matching networks of FFLFs establishes corresponding FFLFs automatically with relational matching, and extends the feature-based ICP-based matching introduced previously to compute a single transformation for all FFLFs pairs. The method is general and can match heterogeneous networks of FFLFs of the same (2D-2D, 3D-3D) Vassilaki et al. [2009a] or of different dimensionality (3D-2D)(Vassilaki et al. [2011c], Vassilaki [2012]).

Chapter 3 introduces new general concepts and methods for the co-registration, the correlation and the merging of multimodal and multitemporal data: i) the concept of using FFLFs as GCI (GCLFs) (Vassilaki et al. [2011c], Vassilaki [2012], Vassilaki et al. [2012a]), ii) the concept of the co-registration of not geometrically corrected SAR images with other data types through 3D-2D projective scene-to-model co-registration (not simply 2D-2D image-to-image transformations) (Vassilaki et al. [2009b], Vassilaki et al. [2011a], Vassilaki [2012]), iii) a method for the

direct georeferencing of TerraSAR-X images using orbital data and other meta data provided by the operator and without using any kind of GCI (Vassilaki et al. [2011b]), iv) a method for the geometric correlation (Vassilaki et al. [2011a]) and v) a method for the radiometric merging of not geometrically corrected multimodal and multitemporal data (Vassilaki et al. [2011a]).

Chapter 4 presents the validation and the evaluation of the general methods presented in the previous two chapters. Numerous simulated tests (Vassilaki et al. [2008a], Vassilaki et al. [2012b]) show the capabilities and the robustness of the methods.

Chapter 5 presents the validation, the evaluation and the versatility of the general methods using and real world problems with real world data as tests (Vassilaki et al. [2008b], Vassilaki et al. [2008a], Vassilaki et al. [2008c], Vassilaki et al. [2009b], Vassilaki et al. [2009a], Vassilaki et al. [2010], Vassilaki et al. [2011c], Vassilaki et al. [2011b], Vassilaki et al. [2011a], Vassilaki [2012], Vassilaki et al. [2012b], Vassilaki et al. [2012a]).

In *Chapter 6* the general methods are combined together and with other methods, principles, problems and data of surveying engineering in order to develop specific methods for: i) the registration (or georeferencing) of not geometrically corrected SAR images to geometrically corrected unitemporal and multitemporal maps and optical images and the corresponding DEM (Vassilaki [2012]), ii) the registration (or georeferencing) of not geometrically corrected optical images to geometrically corrected SAR images and the corresponding DEM (Vassilaki et al. [2013b], Vassilaki et al. [2013a]), iii) co-registration of not geometrically corrected optical and SAR imagery (Vassilaki et al. [2009b]), iv) the pixel-based fusion of not geometrically corrected SAR and multispectral optical images in slant range SAR imaging geometry (Vassilaki et al. [2011a]), and v) the rapid geometric correction of slant range TerraSAR-X SSC images using global DEMs and global geoid models (Vassilaki et al. [2013d], Vassilaki et al. [2013c]). The specific methods are applied and evaluated to greater areas of the Earth's surface (50 to 100 Km²) with arbitrary terrain form, and general conclusions about the developed general and specific methods and the synergy of SAR data with other data types are drawn.

Finally in *Chapter 7* the contribution to knowledge and the conclusions are presented and the possible outlook is discussed.

Chapter 2

Global matching of FFLFs

Linear features and particularly the new concept of Free Form Linear Features (FFLF) are central in this dissertation. A linear feature is 1-dimensional feature of the man-made or the physical environment. Linear features are road centrelines and edges, railway, canals, dams, building outlines, field boundaries, plantation boundaries, country borders, the outline of harbours, docks, piers, bridges, bays, swimming pools, building blocks, squares, parks and any other object of the man-made infrastructure. Linear features are also channels, the banks of rivers, sierras, the coastline of lakes, reservoirs and the sea, geologic faults, cliff edges, and any physical breakline of the terrain. Linear features are abundant in the man-made and physical environment, and are easily identified due to their big, elongated shape. They are thus a valuable resource as Ground Control Information (GCI) for the georeferencing of optical images, SAR images and other data, and as matching primitives for the co-registration of various types of data.

Linear features are important in multitemporal georeferencing and registration, as they tend to persist over long periods of time. For example large portions of road centrelines may remain constant for several decades, and can be identified with little trouble between new and old data sources. In contrast, solitary points are very laborious to identify and in most cases their location is ambiguous.

In the case of SAR data, the identification of solitary points is also laborious and ambiguous due to the fuzzy and speckled nature of the SAR images. This is more so in the case of multimodal georeferencing and co-registration of SAR data with other data types, where reliable common points must be identified. In contrast, common linear features are more easily identified and their elongated shape permits much more precise extraction.

Linear features provide a continuous source of information. It is not uncommon for the matching of a large linear feature to produce thousands of homologous points as a byproduct. The sheer amount of geometric information leads to the robust computation of the Least Squares Adjustment (LSA) and ensures

the elimination of outliers. The weight of thousands of homologous points overwhelms the effect of outliers with even many tenths of meter error, and in fact linear features can be used to spot such outliers. The production of homologous points also makes the linear features interoperable with any existing point-based methods. Point-based software can be used with linear features either with little modifications, or no modifications at all. The former case involves the incorporation of the linear features matching into the existing software, but does not affect the point-processing code in any way. The latter case involves the input of the homologous points to the unmodified existing software.

Linear features are more complex to handle than solitary points. The representation of the linear features and the method of matching are given in the following paragraphs.

2.1 Analytical representation of linear features

Man-made linear features are usually realisations of some analytical mathematical model. The model is seldom simple such as a circular city square, or a straight line road. In the majority of cases a linear feature is defined as multiple instances of the same or different models. For example a rectangular city square is a set of four straight line segments, and a road centreline is a set of straight lines segments, circular arcs and clothoid arcs joined smoothly together. These features, which are in general curved, can be represented directly by the parameters of the mathematical models (Features of Analytical Mathematical Model - FAMRs), one set of parameters for every model. For example the equation of a straight line segments in 2D is given by:

$$Y = a + bX \tag{2.1}$$

There are several disadvantages of this representation:

- The parameters a, b do not have an intuitive geometric meaning. Their computation is often numerically unstable Press et al. [1992].
- The range where the model is valid must be included in the form of $X_1 \leq X \leq X_2$.
- The number of parameters is different for each distinct model (line, circle, clothoid). Many models have special cases, such as a vertical straight line segment. All these lead to complicated computer code.
- The model does not scale well to 3D; the form of the model is quite different in 3D.

-
- It must be ensured that two consecutive models are joined; the last endpoint of the previous model must be exactly the same as the first endpoint of the next model.

A FAMR is better represented by the coordinates of actual points through which the FAMR passes. The mathematical model, which remains the same, is now implicitly defined by the coordinates, which can be used to compute its parameters. For a straight line segment the representation becomes:

$$X_A, Y_A \quad X_B, Y_B \tag{2.2}$$

This representation remedies all the disadvantages:

- The coordinates X_A, Y_A and X_B, Y_B through which the FAMR passes have a very intuitive geometric meaning.
- The straight line segment begins at X_A, Y_A and ends at X_B, Y_B which is even more intuitive.
- All models are defined implicitly through the coordinates of a variable number of points. This homogenises different models and simplifies the computer code.
- The model scales well to 3D; the Z coordinate is added to every point.
- The coordinates ensure that the next segment begins where the last ends.

The curve which joins the coordinates is described by the mathematical models. In general the form of mathematical models of 2D FAMRs are different from the 3D models. For example the straight line segment model is given by Equation 2.1 in 2D, but in 3D it is given by:

$$\frac{X - X_A}{a} = \frac{Y - Y_A}{b} = \frac{Z - Z_A}{c} \tag{2.3}$$

where X_A, Y_A, Z_A is a point of the FAMR and a, b, c are non-unique parameters. Like Equation 2.1, Equation 2.3 has special cases, if any of the parameters a, b, c is zero, which result to complex computer code. In order to unify the form for the 2D and 3D space and eliminate special cases, a parametric form of the mathematical models is used:

$$\begin{aligned} X = X(t) = f(t), \quad Y = Y(t) = g(t), & \quad \text{for 2D} \\ X = X(t) = f(t), \quad Y = Y(t) = g(t), \quad Z = Z(t) = h(t), & \quad \text{for 3D} \end{aligned} \tag{2.4}$$

where $f(t), g(t), h(t)$ are the model parametric functions for each coordinate and t is the parameter which takes arbitrary values. Typically it takes values from

zero, which corresponds to the first point of the FAMR, to one, which corresponds to the last point of the FAMR, or from zero to the length of the curve, which gives the parameter a physical meaning. For example the parametric form of the linear segment of Equation 2.2 is:

$$\begin{aligned}
 X(t) &= X_A + \frac{X_B - X_A}{D_{AB}}t, \quad Y_A + \frac{Y_B - Y_A}{D_{AB}}t, & \text{for 2D} \\
 X(t) &= X_A + \frac{X_B - X_A}{D_{AB}}t, \quad Y_A + \frac{Y_B - Y_A}{D_{AB}}t, \quad Z_A + \frac{Z_B - Z_A}{D_{AB}}t, & \text{for 3D}
 \end{aligned} \tag{2.5}$$

where

$$\begin{aligned}
 D_{AB} &= \sqrt{(X_B - X_A)^2 + (Y_B - Y_A)^2}, & \text{for 2D} \\
 D_{AB} &= \sqrt{(X_B - X_A)^2 + (Y_B - Y_A)^2 + (Z_B - Z_A)^2}, & \text{for 3D}
 \end{aligned}$$

2.2 General representation - FFLFs

In the previous section the implicit assumption was made that man-made linear features are designed before they are constructed and that they are constructed according to the design. This is not always true as, for example, a circular city square may not be a perfect circle due to construction errors, but still perfectly functional for its purpose. Rural roads are often constructed without a particular design, perhaps following existing paths or field boundaries. Furthermore, physical linear features such as channels have generally arbitrary geometry. It is clear that these linear features do not adhere to any analytical mathematical model.

The best representation of such a feature is to measure all its, infinite number of, points. Since this is impossible, it is standard practice to measure a finite set of consecutive points of the feature (which from now on will be referenced as nodes) which best describe the feature according to the judgement of the engineer. And since the feature is one dimensional, these nodes must be joined with straight line segments or any other arbitrary interpolation function such as cubic splines, rational polynomial functions (RPF), non-uniform rational B-splines (NURB) etc. The set of nodes and the interpolation function together form the new concept of the Free Form Linear Feature (FFLF). The number and the density of nodes of a FFLF is arbitrary, and in fact the density of nodes is not uniform throughout the FFLF.

FFLFs are the most general form of linear features representation, as they include FAMRs as a special case, where the nodes are specific (for example the endpoints of the FAMR) and the interpolation function is the mathematical model of the FAMR. For example the straight line segment interpolation between the nodes of a FFLF is identical to Equation 2.5.

It must be emphasised that there is no unique representation of a man-made or physical linear feature as a FFLF. Two set of nodes which define two FFLFs, when joined may represent the same feature, but the sets can be completely different, as the location, the density and the number of the nodes will probably differ for each set (figure 2.2).

2.3 Registration using homologous points

Registration or co-registration is the computation of the relationship between the coordinate systems of two data sets. Georeferencing is a special case of registration where one of the coordinate systems is the object coordinate system. The relationship between the coordinates systems is in the form of mathematical relationship which is called a model. The models may be physical or empirical (Toutin [2004]). Physical models reflect the actual geometry and the mechanism of the sensor which acquires the data. Examples of physical models are the collinearity equations for aerial images and the similarity transformation for LIDAR data (Mikhail et al. [2001]). Physical models are naturally the most accurate models. Unfortunately they are also the most complex models, such as the physical model of the TerraSAR-X sensor (Vassilaki et al. [2011b]), and they typically require the nonlinear LSA in order to compute their parameters.

Empirical models are arbitrary mathematical transformations which are very loosely, if at all, related to the geometry and mechanism of the sensor, and express approximately the relationship between the data sets. Examples of empirical models are the affine transformation, polynomial functions, rational polynomial functions and the Direct Linear Transform (DLT). Empirical models are simpler from a computational point of view and typically require linear LSA. Empirical models are useful when the approximation error is less or at least not much larger than the apriori error of the data and in cases where the physical model of a sensor is unknown.

Both the physical and the empirical models are in the form of a mathematical formula, the parameters of which are typically unknown and are computed using available GCI (a notable exception is the TerraSAR-X sensor whose physical model parameters are known with high accuracy). For example the empirical model of the 2D affine transformation is:

$$\begin{aligned}x &= A_1X + A_2Y + A_3 \\y &= A_4X + A_5Y + A_6\end{aligned}\tag{2.6}$$

where X, Y and x, y are homologous points, meaning that point x, y in the image space corresponds to point X, Y in the object space. A_i are six unknown parameters to be computed. Assuming that the GCI is in the form of $N \geq 3$

pairs of homologous points, Equation 2.6 is applied for each pair and the system of equations is solved for the unknown parameters using the linear LSA:

$$\begin{aligned}
x_1 &= A_1X_1 + A_2Y_1 + A_3 \\
y_1 &= A_4X_1 + A_5Y_1 + A_6 \\
x_2 &= A_1X_2 + A_2Y_2 + A_3 \\
y_2 &= A_4X_2 + A_5Y_2 + A_6 \\
&\vdots \\
x_N &= A_1X_N + A_2Y_N + A_3 \\
y_N &= A_4X_N + A_5Y_N + A_6
\end{aligned} \tag{2.7}$$

or in matrix notation:

$$\begin{bmatrix} x_1 \\ y_1 \\ x_2 \\ y_2 \\ \vdots \\ x_N \\ y_N \end{bmatrix} = \begin{bmatrix} X_1 & Y_1 & 1 & 0 & 0 & 0 \\ 0 & 0 & 0 & X_1 & Y_1 & 1 \\ X_2 & Y_2 & 1 & 0 & 0 & 0 \\ 0 & 0 & 0 & X_2 & Y_2 & 1 \\ \vdots & \vdots & \vdots & \vdots & \vdots & \vdots \\ X_N & Y_N & 1 & 0 & 0 & 0 \\ 0 & 0 & 0 & X_N & Y_N & 1 \end{bmatrix} \begin{bmatrix} A_1 \\ A_2 \\ A_3 \\ A_4 \\ A_5 \\ A_6 \end{bmatrix} \tag{2.8}$$

or:

$$[B] = [A][X] \tag{2.9}$$

where $[B]$ contains image space coordinates, $[A]$ contains object space coordinates and $[X]$ is the matrix of the unknown parameters. Equation 2.9 is solved with the LSA:

$$[A^T][B] = [A^T][A][X] \quad \text{or} \quad [U] = [N][X] \quad \text{and} \quad [X] = [N^{-1}][B] \tag{2.10}$$

2.4 Registration using FAMRs

When the GCI is in the form of homologous FAMRs the computation of the parameters of the model is much more difficult. For simplicity let us assume that the homologous FAMRs are straight lines (not straight line segments) described by Equation 2.1, and specifically:

$$\begin{aligned}
y &= c + dx && \text{in the image space} \\
Y &= C + DX && \text{in the object space}
\end{aligned} \tag{2.11}$$

Substituting Equation 2.11 to 2.6:

$$\begin{aligned} A_4X + A_5Y + A_6 &= c + d(A_1X + A_2Y + A_3) \\ Y &= C + DX \end{aligned}$$

and combining these equations:

$$A_4X + A_5(C + DX) + A_6 = c + dA_1X + dA_2(C + DX) + dA_3$$

or:

$$(A_4X + A_5C + A_6) + (a_5D)X = (c + dA_2C + dA_3) + (dA_1X + dA_2D)X \quad (2.12)$$

Equation 2.12 is valid for arbitrary X and thus:

$$\begin{aligned} A_4X + A_5C + A_6 &= c + dA_2C + dA_3 \\ a_5D &= dA_1X + dA_2D \end{aligned} \quad (2.13)$$

Equation 2.13 can be solved for the six unknown parameters A_i using the linear LSA (at least 3 pairs of homologous FAMRs are needed). However this approach has several disadvantages:

- The parameters c, d, C, D are not the original measurements, but they are parameters computed (probably using LSA) by the original measurements (the coordinates) and thus they introduce error. If the FAMRs are represented by higher order functions instead of straight lines (for example second order polynomials) they introduce new error due to numerical instabilities Press et al. [1992].
- If the FAMRs are represented by higher order functions, Equation 2.13 will no longer be linear, even though the transformation is linear. This introduces the problem of guessing a first approximation for the nonlinear LSA and ensuring that it converges.
- In the most common case where the FAMRs are represented by piecewise functions, either linear or higher order, this approach can not be applied, because it is not known which segment of the image space FAMR corresponds to which segment of the object space FAMR. Worse, each FAMR may have different number of segments and each segment may span more than one segment of the other FAMR.

In order to overcome the problem of the FAMRs (or more generally the FFLFs) represented by piecewise functions, instead of the parameters c, d, C, D , global properties of the FFLFs can be used. This is entirely possible, and in section

2.9 and 2.10 the total length and other global properties of the FFLFs are used to compute (approximately) a simple empirical model. However the first two problems of the previous approach are not faced, and a new one is introduced: If both homologous FFLFs do not represent exactly the same portion of the actual physical or man-made feature, additional error is introduced.

2.5 Registration using FFLFs matching

A completely different and novel method developed in this dissertation is to use FFLFs to identify pairs of homologous points rather than compute the model parameters directly. For example if a pair of homologous FFLFs represent the same portion of the actual physical or man-made feature (global matching), the first points of the FFLFs are probably homologous. The last points of FFLFs are also probably homologous. Given enough pairs of homologous points, the parameters of the model can be easily computed as described in Section 2.3.

A method to systematically identify homologous points between two sets of points, (A) and (B), is the Iterated Closest Points algorithm or ICP (Besl and McKay [1992], Zhang [1994], Chen and Medioni [1991]). Typically the points of set (B) are the points of (A) transformed to another coordinate system, but it is not known which point B_j of set (B) corresponds to an arbitrary point A_i of set (A). According to ICP, point B_j is the point of set (B) which is closest to A_i (Figure 2.1). In other words, the distance between A_i and B_j is less than the distance between A_i and any other point of set (B). Repeating this matching procedure for all points of set (A), many pairs of homologous points are established and the transformation from (A) to (B) can be computed. For this method to succeed, the point sets (A) and (B) must be pre-aligned, meaning that point set (A) should be manually brought near point set (B) and approximately on the same scale and orientation.

Due to the approximate pre-alignment, some closest points computed by ICP, so far, may not be actually be homologous. For example using ICP point A_{n-1} is not found to be homologous to B_2 as it should. It is found to be homologous to B_1 , which is close to B_2 but nevertheless incorrect (Figure 2.1). It follows that the computed transformation may be approximate too. But if the points sets are sufficiently pre-aligned, the computed transformation, when applied to point set (A), is good enough to bring (A) closer to (B), essentially making the pre-alignment better. The closest points can then be re-established and a new and more accurate transformation can be computed, which will bring (A) even closer to (B), and the procedure is repeated until (A) and (B) match (converge).

ICP can not be applied to FFLFs, as FFLFs are generally represented by consecutive nodes of no regularity. Thus the outlines of the physical or man-made

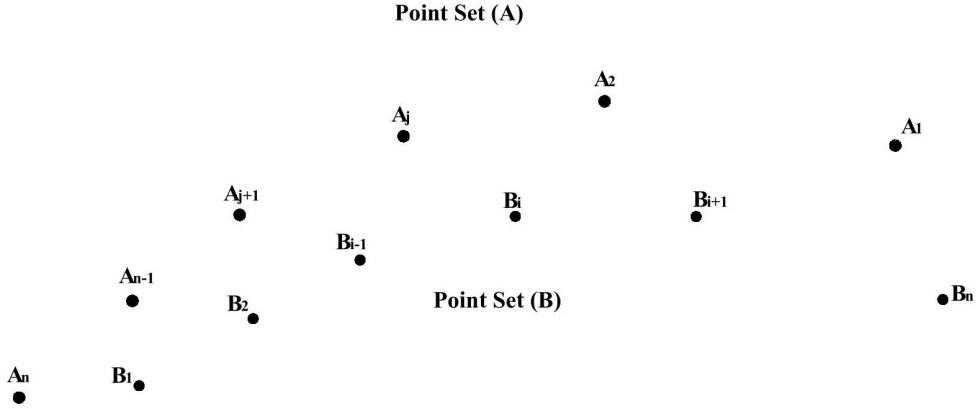


Figure 2.1: Computation of closest points between point sets.

object extracted by two data sources will probably be very different, meaning that the position and density of their nodes will vary substantially. This is especially true for the case of multimodal and multitemporal data sources where FFLFs are extracted with different processes from different kinds of data. The direct matching of their nodes is impossible, as the two FFLFs do not consist of corresponding nodes, neither in number nor in position (Figure 2.2).

A new method based on the Iterated Closest Points algorithm (ICP) Vassilaki et al. [2012b] was developed to match two FFLFs. The method systematically identifies homologous points between two FFLFs, (A) and (B). The FFLFs are assumed to be pre-aligned, meaning that they are moderately close together and approximately on the same scale. Then, the homologous point of an arbitrary node A_i on FFLF (A), is defined to be its nearest point on FFLF (B) which, almost certainly, is not a node of FFLF (B) but a point P on the curved line which joins the nodes of the FFLF (figure 2.2). In other words, the distance between A_i and P is less than the distance between A_i and any other point of FFLF (B), either a node or a point in the curved line which joins the nodes. Repeating this procedure for many points of FFLF (A), many pairs of homologous points are established and the model parameters can be computed. More details can be found in Sections 2.7 and 2.8.

2.6 Computation of closest point pairs

The robust computation of closest point pairs between 2 FFLFs is fundamental to all aspects of this dissertation. In general, FFLFs are represented by consecutive nodes of no regularity joined by straight line segments, or some other

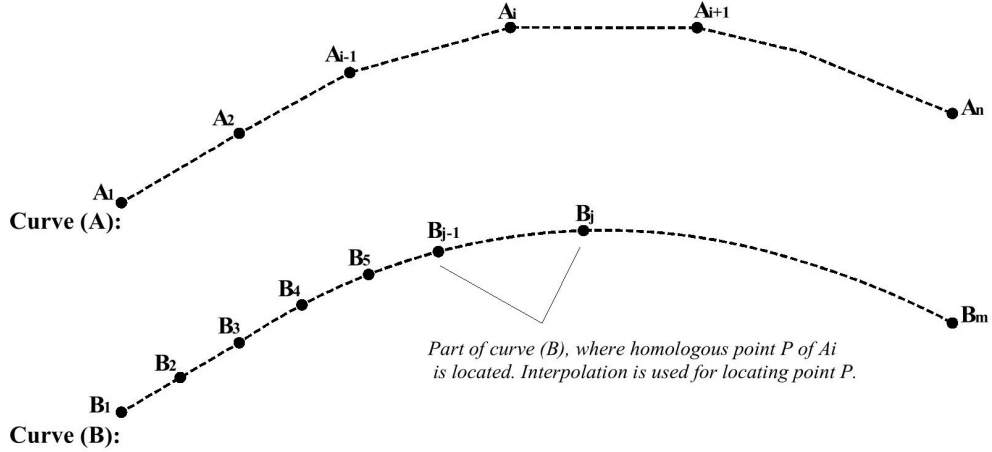


Figure 2.2: Computation of closest point pairs between FFLFs.

interpolation function such as cubic splines, NURBs, etc. In any case the original measurements, or information, are in the form of 2D or 3D node coordinates. The computation of the pairs of closest points between two heterogeneous FFLFs (A) and (B) is a proximity problem that could be stated as:

“Given a node A_N of a FFLF (A), find its minimum distance to another FFLF (B).”

For straight lines of infinite length, there are simple formulas which are based on the computation of a common perpendicular to the two lines. However, in the case of linear segments of finite length, the classical formulas for distance cannot be applied. In this case, the closest point may be located by minimising the function of the distance of node A_N to the curve interpolated between two consecutive nodes of FFLF (B), B_i and B_{i+1} (Figure 2.3). Care must be given to the fact that the minimum distance may be outside the curve segment $B_i B_{i+1}$. In a worse condition the minimum may be to the right of segment $B_{i-1} B_i$ and to the left of $B_i B_{i+1}$. It is also probable that, if the curve is not linear, the minimum cannot be computed analytically but some sort of iterative procedure must be employed, which may or may not converge. To overcome the difficulties, the problem may be restated as:

“Given a node A_N of a FFLF (A), find the point P of FFLF (B) whose distance to N is the minimum.”

If all the infinite points of FFLF (B) could be checked then the location of the closest point P would be straightforward. Clearly a computer cannot handle an infinite number of points. However the FFLF (B) can be split to a large set of consecutive interpolated points, each one very close to its previous and its next point. Then the distances of all these points to a node of FFLF (A)

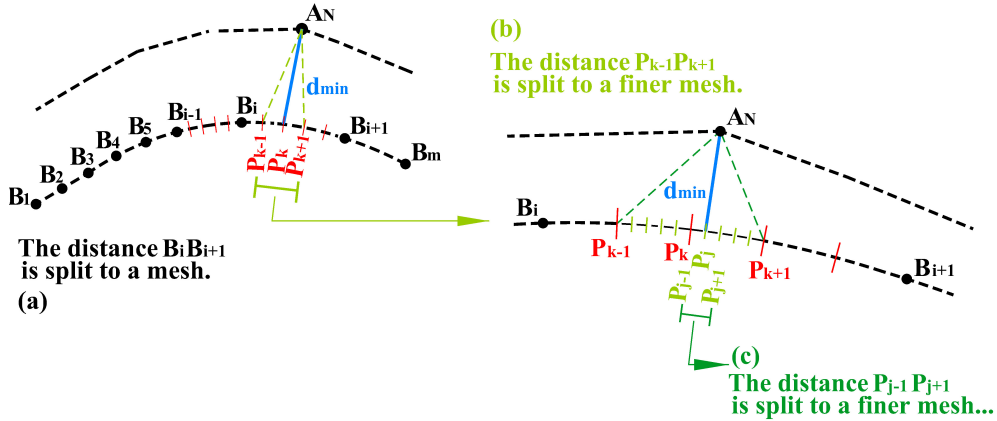


Figure 2.3: Speed up of computation of closest point pairs.

may be computed and P is the point with the least distance to node A_N . For this brute method to produce good results, the distance between two consecutive interpolated points must be very small, which leads to a large set of points. A statistically safe choice is a fraction (e.g., half) of the linear a priori error of the second FFLF, as less than that can not increase the accuracy of the nearest points. This approach has also the benefit that it is dimensionally agnostic; it works in both two and three dimensions unchanged.

In this dissertation global matching is examined but it is practically impossible to find two FFLFs that both represent exactly the same part of a physical linear feature (e.g., a road). One FFLF will be longer in one or both ends. In the case that FFLF (A) is shorter than FFLF (B), then every node of (A) corresponds to its closest point on (B) which is found as previously described; the part of (B) which exceeds (A) is automatically and effectively ignored. If FFLF (A) is longer, then the nodes that lie on the part of (A) that exceeds (B), correspond to exactly the first (or last) point of (B). These nodes are discarded; thus the part of (A) that exceeds (B) is ignored. This procedure works even when the overlap is small compared to the length of the FFLFs, as it is shown later in tests with simulated data.

The method, as described above, is computationally expensive but doable with modern computers. It is, however, relatively easy to speed up the process using a divide-and-conquer approach. FFLF (B) is split to a far smaller number of points than mentioned above, which implies a far bigger interpolation distance (than half the a priori error). In fact FFLF (B) may not be split at all (and thus represented by its original nodes) if linear interpolation is assumed between its nodes. However interpolation distance equal to one fifth of the average distance between the nodes is preferred in order to accommodate for non-linear interpolations between

the original nodes of the second FFLF (Figure 2.3). This discretisation suffices for up to 5th order polynomial interpolation which is enough for almost all cases and a good approximation for higher order cases (and anyway finer discretisation is computed in the next iteration). The closest point P to node A_N is located as described. Then the distance between the previous and next point of P is split to a finer mesh and a new closest point is located (Figure 2.3). The process is repeated until the interpolation distance is half of the a priori error of the second FFLF, as stated in previous paragraphs.

Further acceleration can be achieved by parallel computing. In Stamos et al. [2009] the closest point of every node A_N is computed concurrently by a different processor or core, as the computations are almost independent of each other. The parallelisation is implemented using the parallel framework of the upcoming Fortran 2008 standard and achieves almost linear speedup.

It must be emphasised that if the curve (FFLF) is defined by the nodes, then the interpolated points introduce no additional error because the curve has to be represented by some function joining the nodes. In this case the presented method makes no assumption of the interpolation function which links the nodes; the one suited to the problem involved may be used (linear, cubic splines, NURBs etc). On the other hand, in the rare case where the exact formula of the curve is known (FAMR), then this formula can be used to compute the points, so that no error is introduced.

2.7 FFLFs matching in two and three dimensions (2D-2D, 3D-3D)

The procedure to compute the closest point pairs is directly applied to the matching of FFLFs of the same dimensionality. Two FFLFs (A) and (B) are assumed to represent the same physical feature, for example a road. The FFLFs are related by an arbitrary transformation. For example FFLF (A) may be the ground coordinates of a road and (B) the stereo model coordinates of the same road, which are related with the 3D rigid transformation. The general outline of the method is described below:

1. Compute an initial approximation of the transformation between the FFLFs, as shown later.
2. Transform FFLF (A) using the initial transformation, so that the FFLFs are brought close together.
3. For each node of (A), determine its closest point on (B).

-
4. Compute the RMSE of the two FFLFs using the determined closest points.
 5. Use the determined closest node-point pairs to compute the parameters of the transformation between the FFLFs with the Least Squares Adjustment (LSA).
 6. Transform FFLF (A) using the transformation parameters, to bring (A) closer to (B).
 7. Repeat steps 3,4,5 and 6 until convergence, i.e. the RMSE stops decreasing.

As can be seen, the method is independent of the type of the transformation and can be used in both two and three dimensions. Specifically, steps 5 and 6 are specialised according to the transformation, as each transformation has its own formulas and parameters and may need linear or non-linear LSA. The different transformations may be implemented as derived classes of a general abstract class of transformations in an object oriented environment. Furthermore, step 3 computes a large number of homologous points, which guarantees compatibility of the proposed method with classical solitary point based methods and software.

One might argue that many point pairs are not independent measurements. For example a perfect circle, perhaps the outline of a circular city square, is defined by three parameters and thus the independent measurements are three even if the number nodes of the FFLF which represents the circular square is much larger. However in the common case that the circle has imperfections, the number of the independent measurements is larger and proportional to the number and the extent of the imperfections. If the FFLF is 3D and the elevation around the circular square is arbitrary, the number of independent measurements is also much larger. In general, it is standard practice to measure a finite set of nodes of a man-made or physical linear feature which best describe the feature according to the judgement of the engineer. Thus the nodes of a FFLF and the corresponding point pairs are in general independent measurements.

2.8 Matching of FFLFs of different dimensionality (3D-2D)

Two FFLFs (A) and (B) are assumed to represent the same physical feature. FFLF (A) is 3D and FFLF (B) is 2D. It is assumed that (B) is a projection of (A) of some arbitrary projection transformation. For example, FFLF (A) may be the ground coordinates of a road and FFLF (B) the 2D projection of the 3D road to an optical aerial image which are related by the central projection transformation. The general outline of the method is almost identical to the 2D

or 3D case but with the difference that the projection transformation cannot be inverted so that the correspondences between 3D nodes and projected 2D nodes must be saved:

1. Compute an initial approximation of the projection transformation between the FFLFs, as shown later.
2. Project 3D FFLF (A) to (A') using the initial projection transformation, so that the FFLFs (A') and (B) are close together, remembering which 3D node of (A) corresponds to which 2D node of (A').
3. For each 2D node of (A'), determine its closest point on (B) and, using the saved correspondence, make also pairs of 3D nodes of (A) and 2D points of (B).
4. Compute the RMSE using the determined closest points between FFLFs (A') and (B).
5. Use the determined closest node-point pairs of FFLFs (A) and (B) to compute the parameters of the transformation projection between (A) and (B) with the LSA.
6. Project 3D FFLF (A) to (A') using the projection parameters to bring (A') closer to (B) remembering which 3D node of (A) corresponds to which 2D node of (A').
7. Repeat steps 3,4,5 and 6 until convergence, i.e. the RMSE stops decreasing.

2.9 Computation of initial approximation: The rigid approach

The ICP algorithm requires a good initial approximation (pre-alignment) to converge, which means that the two FFLFs must be close enough to each other. The necessity of the initial approximation weakens the practicality of the ICP, or at least it makes ICP awkward to use, because the initial approximation must be given to the algorithm. However, if an approximation of the transformation between the FFLFs could be computed, this transformation could be used to move one FFLF close to the other, and trigger ICP convergence. The transformation between the FFLFs is dependent on the problem involved, and it is thus arbitrary. However, many 2D or 3D transformations in geoscience and remote sensing may be themselves approximated by the 2D or 3D similarity transformation respectively. This also works for projection transformations as shown below.

The similarity transformation, if computed, will bring the FFLFs close together; then the ICP will compute point pairs which can be used to compute the real, problem-dependent, transformation.

The similarity transformation in 2D consists of a translation, a rotation and a scale. Each of these may be approximated independently. For the 3D case the translation, the Z-axis rotation and the scale approximation is the same, while the X-axis and Y-axis rotations are approximated as zero. For the case of different dimensionality (3D-2D), an initial approximation of the projection is introduced and then the case is reduced to 2D-2D. In the next paragraphs various cases and methods are examined and proposed for the automated pre-alignment of the FFLFs to be matched. They intend to cover the case of global matching but they also work when the FFLFs do not have 100% overlap. Experimental results show that an overlap of 90% is sufficient to produce a good initial approximation.

2.9.1 Translation approximation

A good and robust approximation of the translation between FFLFs (A) and (B) is the vector distance of their centroids:

$$\Delta x = \bar{x}_B - \bar{x}_A \quad (2.14)$$

The centroid represents an average of the coordinates of the whole FFLF, and its error is less than the error of a single node. If the FFLF is given as a set of n nodes and some kind of interpolation is used for the points of the curve between the nodes, the x coordinate of its centroid is computed as:

$$\bar{x} = \frac{1}{S} \sum_{j=1}^{n-1} \int_{S_j} x(s) ds \quad (2.15)$$

$$S = \sum_{j=1}^{n-1} \int_{S_j} ds \quad (2.16)$$

where there are $n-1$ segments between the nodes, S is the length of the FFLF and, in general, the (interpolation) function $x(s)$ is different for each segment j . Similar formulas yield the y and z coordinates of the centroid. If the interpolation between the nodes is linear then the integrals can be computed analytically. The interpolation function $x(s)$ for segment j (the segment between nodes j and $j+1$) is:

$$x(s) = x_j + \frac{\Delta x}{S_j} s \quad (2.17)$$

where:

$$\Delta x = x_{j+1} - x_j \quad (2.18)$$

$$S_j = \sqrt{(x_{j+1} - x_j)^2 + (y_{j+1} - y_j)^2 + (z_{j+1} - z_j)^2} \quad (2.19)$$

where $z_j = 0$ for 2D case. The integral of $x(s)$ over the segments is:

$$\int_{S_j} x(s) ds = \int_{S_j} \left(x_j + \frac{\Delta x}{S_j} s\right) ds = x_j S_j + \frac{\Delta x}{S_j} \frac{S_j^2}{2} = S_j \frac{x_j + x_{j+1}}{2} \quad (2.20)$$

If the segments are also of equal length S_1 , then Equation 2.15 becomes:

$$\bar{x} = \frac{\sum_{j=1}^N \int_{S_j} x(s) ds}{\sum_{j=1}^N \int_{S_j} ds} = \frac{\sum_{j=1}^{N-1} (x_j + x_{j+1})/2}{S_1(N-1)} = \frac{1}{N-1} \left(\frac{x_1}{2} + \sum_{j=2}^{N-1} x_j + \frac{x_N}{2}\right) \quad (2.21)$$

If the interpolation between the nodes is nonlinear, analytic integration of Equation 2.15 is difficult if not impossible. Numerical integration using the trapezoidal rule is in effect Equation 2.21, where the curve has been approximated with a large number of interpolated points (not just the nodes), and N is now the number of interpolation points. If the number of points is large, and the interpolation distance constant, then a simpler numerical integration rule suffices:

$$\bar{x} = \frac{1}{N} \sum_{j=1}^N x_j \quad (2.22)$$

The interpolation of a large number of points implies a large computational cost and heavy memory usage. However, the matching method presented in this dissertation computes a large number of interpolation points as a byproduct which can be exploited for the evaluation of Equation 2.22. Thus the computational cost of Equation 2.22 is negligible and additionally Equation 2.22 is independent to the interpolation used.

2.9.2 Scale approximation

Assuming global matching, a good and robust approximation of the scale between the FFLFs is the ratio of their lengths. Since the lengths are properties which represent the whole FFLF, the error of their ratio is less than the error of the ratio computed by single segments.

$$\mu = \frac{S_B}{S_A} \quad (2.23)$$

Assuming N nodes, the length S of either FFLF can be computed as:

$$S = \sum_{j=1}^{N-1} S_j = \sum_{j=1}^{N-1} \int_{S_j} ds \quad (2.24)$$

If the interpolation between the nodes is linear then the integrals can be computed analytically by Equation 2.19. If the interpolation between the nodes is nonlinear then the analytic computation of the integrals of Equation 2.24 is difficult if not impossible. Numerical integration leads to the same Equation 2.24, where the FFLF has been approximated with a large number of interpolated points (not just the nodes), N is now the number of interpolation points and the integrals are computed numerically by Equation 2.19. Again, the interpolation points are computed as a byproduct of the matching algorithm and the computational cost of the numerical integration is negligible. Once again, Equations 2.23 and 2.24 are independent of the interpolation scheme used. The scale transformation is applied after the transfer so that the approximation of the transfer is independent of the scale (and rotation).

2.9.3 Rotation approximation

Three procedures for the calculation of the 2D rotation approximation are presented below using characteristic points, average azimuth and exhaustive search. It is assumed that the translation and scale have been applied, so that the FFLFs have the same centroid and the same length. The approximations to 3D rotations are also presented.

2.9.3.1 Rotation approximation using characteristic points

If the coordinates of the same (characteristic) node are known for both FFLFs, then the difference of their azimuths with respect to the common centroid is an approximation of the rotation between the FFLFs:

$$\phi = \text{atan2}(x_B - \bar{x}, y_B - \bar{y}) - \text{atan2}(x_A - \bar{x}, y_A - \bar{y}) \quad (2.25)$$

where atan2 is the azimuth function available in most computer languages, x_A, y_A and x_B, y_B are the coordinates of the same characteristic point in FFLF (A) and (B) respectively, and \bar{x}, \bar{y} is the common centroid. In global matching the first node and the last node of each FFLF are homologous and thus Equation 2.25 can be evaluated twice. The average of the two (similar) rotations can be used as a

good approximation of the rotation between the FFLFs in order to increase the robustness of the method.

2.9.3.2 Rotation approximation using average azimuth

Following the rationale of the previous paragraph the average azimuths of the whole FFLFs should be more robust. To sidestep the fact that azimuths near 0° and 360° are almost the same, the average unit direction vector is used instead:

$$t(\vec{s}) = [t_x(s), t_y(s)] = [\sin \alpha(s), \cos \alpha(s)] \quad (2.26)$$

$$\alpha(s) = \text{atan2}[x(s) - \bar{x}, y(s) - \bar{y}] \quad (2.27)$$

Then the average direction vector is computed as:

$$\vec{t} = (\bar{t}_x, \bar{t}_y) = \left(\frac{1}{S} \sum_{j=1}^{n-1} \int_{S_j} t_x(s), \frac{1}{S} \sum_{j=1}^{n-1} \int_{S_j} t_y(s) \right) \quad (2.28)$$

where the integrals can be computed numerically as in Equation 2.21, and the average azimuth as:

$$\bar{\alpha} = \text{atan2}[\bar{t}_x, \bar{t}_y] \quad (2.29)$$

The rotation is computed as the difference between the average azimuths of the FFLFs as in Equation 2.25.

However Equations 2.28 and 2.29 have a subtle weakness. If the FFLF is a perfect circle or a perfect straight line, then the sums of Equation 2.28 are exactly zero, which means that 2.29 is undefined. Even if the FFLF is not a perfect circle, but just a closed curve or a nearly closed curve, the sums will be near zero, which may lead to poor evaluation of Equation 2.29 due to numerical errors and/or random errors in the nodes and interpolated points. The same is true if a FFLF is almost a straight line. The average azimuth can be used in physical linear features that exhibit no regular geometry such as river banks and coast line, and man-made linear features like roads and railways in mountainous terrain.

2.9.3.3 Rotation approximation using exhaustive search

A completely different method of finding a good approximation to the rotation between the two FFLFs is to try every single rotation and choose the one which gives the least error. It is of course impossible to try all of the infinite rotation angles and thus the next best approach is to try all the rotation angles between 0° and 360° with a small step $\Delta\theta$. A good value for $\Delta\theta$ was experimentally

Exhaustive Search of rotation.

Let $e_{min}=10^{100}$

Let $\Delta\theta=3$

For $\theta=0$ to 360 with step $\Delta\theta$:

Transform FFLF A to A' using rotation j.

Compute homologous points between A' , B with ICP.

Compute error e.

If $e < e_{min}$:

$e_{min} = e$

$\theta_{min} = \theta$

End if.

End for.

Use θ_{min} as the initial approximation of the rotation.

End.

Figure 2.4: Exhaustive search algorithm.

determined to be 3° . For each rotation angle the matching error of the FFLFs must be computed. This implies that, for each rotation angle, the ICP algorithm must be employed to find homologous points between the FFLFs, and then the homologous points are used to compute the error. The algorithm is summarised in figure 2.4. This method is the most robust but it is complicated and time consuming.

2.9.3.4 Rotation approximation for 3D

In geoscience and remote sensing almost all data is captured by satellite or aerial sensors which exhibit small X-axis and Y-axis rotations. Experience has shown that these rotations can be successfully approximated as zero. This renders the 3D rotation matrix of the similarity transformation to:

$$R_{\kappa\varphi\omega} = R_{\kappa}R_{\varphi}R_{\omega} = R_{\kappa} \quad (2.30)$$

which affects only the x and y coordinates leaving the Z coordinate unchanged. Thus the rotation κ can be approximated with the same methods as in the 2D case.

2.9.4 Initial approximation for projection transformations (3D-2D)

In the case of matching data of different dimensionality, the transformation involved is, as already mentioned, an arbitrary (problem dependent) projection of 3D data to 2D data. Assuming again data captured by satellite or aerial sensors, the effect of the terrain on the data is small because the X-axis and Y-axis rotations are small and the sensors are usually at high flying height. Thus an orthogonal projection to the XY plane, which in effect discards the Z coordinate, followed by unknown 2D transformation, is a good approximation to the original projection. The unknown 2D transformation can itself be approximated by the similarity transformation as in the 2D case.

2.10 Computation of initial approximation: The non-rigid approach

In cases with severe distortions such as in the slant range geometry of SAR images, the similarity transformation cannot adequately approximate the geometry of the sensor because it represents a rigid transformation. A non-rigid transformation, the simplest of which is the 1st order polynomial or the affine transformation, is clearly advantageous:

$$x = aX + bY + c, \quad y = dX + eY + f \quad (2.31)$$

where x, y are the coordinates of FFLF (B) and X, Y are the coordinates of the FFLF (A). Like the similarity transformation, the affine transformation, if computed, will bring the FFLFs close together, and then the ICP will compute point pairs, which can be used to compute the real transformation (2D-2D, 3D-3D, and 3D-2D) following the rationale of the previous paragraph. Unlike the similarity transformation, the affine transformation does not relate to physical properties such as the translation, scale and rotation which can be computed independently. Instead, some characteristic properties which depend on the FFLF as a whole must be used, since there is no prior knowledge of the correspondences of points. If the two FFLFs represent the same physical feature (for example a road centreline), then a characteristic property of FFLF (B) must be equal to the same characteristic property of the FFLF (A):

$$P(x_1, y_1, \dots, x_n, y_n) = P(aX_1 + bY_1 + c, dX_1 + eY_1 + f, \dots, aX_m + bY_m + c, dX_m + eY_m + f) \quad (2.32)$$

The number m of nodes of the FFLF (A) is, in general, different from the number of nodes n of FFLF (B). In general, node x_i, y_i does not correspond to any of the nodes X_i, Y_i (and certainly $i \neq j$). At least six characteristic properties are needed to compute the six coefficients (a, b, c, d, e, f) of the affine transformation. More than six will ensure robust results.

The statistical moments can be used as characteristic properties of the FFLFs, as described below. They have been used in many pattern recognition problems, since they transform the complicated geometry of an object to practically distinct numbers. It should be noted that some moments are insensitive to scale and rotation (moment invariants with respect to projective transformation). These moments are not used here since the objective is to use the moments to compute the coefficients of the transformation, and not to eliminate it.

The physical interpretation of the moments used here, is the average and standard deviation for the first and second moment, while the third and the fourth moments indicate the skewness and the kurtosis of the variable respectively (Abramowitz and Stegun [1970], Press et al. [1992]).

In theory, the moments could be used to compute the parameters of any kind of transformation, such as the DLT or even the physical model of the SAR sensor. In practice, however, this is not possible because the equations of moments lead to non-linear LSA, which requires initial values of the parameters. Unfortunately, no such initial values are available for transformations other than the similarity, or the one proposed in this Section.

2.10.1 Moment equations

The k th moment of a continuous random variable about a value c is defined as:

$$\mu'_k = \int_{-\infty}^{\infty} (x - c)^k f(x) dx \quad (2.33)$$

where $f(x)$ is the probability density function. The k th moment of a discrete random variable f_j about c is given by

$$\mu'_k = \frac{1}{m} \sum_{j=1}^m (f_j - c)^k \quad (2.34)$$

The first moments about zero of x, y and coordinates of FFLF (B), which coincide with the centroid of the FFLF, are given by

$$\mu'_{x1} = \frac{1}{n} \sum_{i=1}^n x_i, \quad \mu'_{y1} = \frac{1}{n} \sum_{i=1}^n y_i \quad (2.35)$$

These moments should be equal to the moments of the transformed coordinates of FFLF (A):

$$\mu'_{X1} = \frac{1}{m} \sum_{j=1}^m (aX_j + bY_j + c), \quad \mu'_{Y1} = \frac{1}{m} \sum_{j=1}^m (dX_j + eY_j + f) \quad (2.36)$$

In order to avoid huge numbers which will degrade the numerical computations, the normalised central moments are used for the higher moments:

$$\mu_{xk} = \sqrt[k]{\frac{1}{n} \sum_{i=1}^n (x_i - \mu'_{x1})^k}, \quad \mu_{yk} = \sqrt[k]{\frac{1}{n} \sum_{i=1}^n (y_i - \mu'_{y1})^k} \quad (2.37)$$

These moments should also be equal to the corresponding moments of FFLF (A):

$$\begin{aligned} \mu_{Xk} &= \sqrt[k]{\frac{1}{m} \sum_{j=1}^m (aX_j + bY_j + c - \mu'_{X1})^k} \\ \mu_{Yk} &= \sqrt[k]{\frac{1}{m} \sum_{j=1}^m (dX_j + eY_j + f - \mu'_{Y1})^k} \end{aligned} \quad (2.38)$$

Another reason for the normalisation of the higher order moments is to express the moments in the same units (length units or meters). Thus, all the equations of moments have the same (implicit) weight when the LSA is applied; numerical experiments with no, or other, normalisations led to poorer results.

2.10.2 Length equation

Each moment applied to x and y coordinates provides two equations. Thus, the first three moments (k=1,2,3) provide six equations which should be sufficient to estimate the six unknown coefficients of the affine transformation, but they give poor results in some cases. Taking four moments, or eight equations, and applying the LSA leads to better results, but it still lacks an acceptable quality. This could be explained by the fact that the affine transformation equation of moments for the x coordinates, are completely independent of the y coordinates. However, x and y coordinates are coupled as they together define a FFLF. This coupling should be reflected in the equations. One way to achieve this is to exploit the fact that the correspondent FFLFs have the same length (global matching):

$$L(x_1, y_1, \dots, x_n, y_n) = L(aX_1 + bY_1 + c, dX_1 + eY_1 + f, \dots, aX_m + bY_m + c, dX_m + eY_m + f) \quad (2.39)$$

or equally:

$$\begin{aligned}
& \sum_{j=2}^n [(x_i - x_{i-1})^2 + (y_i - y_{i-1})^2]^{1/2} = \\
& \sum_{j=2}^m \left[[(aX_j + bY_j + c) - (aX_{j-1} + bY_{j-1} + c)]^2 + \right. \\
& \quad \left. [(dX_j + eY_j + f) - (dX_{j-1} + eY_{j-1} + f)]^2 \right]^{1/2} = \tag{2.40} \\
& \sum_{j=2}^m \left[[a(X_j - X_{j-1}) + b(Y_j - Y_{j-1})]^2 + [d(X_j - X_{j-1}) + e(Y_j - Y_{j-1})]^2 \right]^{1/2} = \\
& \sum_{j=2}^m L_j
\end{aligned}$$

Results derived from various tests made for this research, showed that the equations of three moments combined with the equation of the lengths greatly enhance the results. If four moments are used the results are slightly better, but five or more moments give no noticeable improvements.

2.10.3 Least Squares Adjustment

As there are at least seven non-linear equations for six unknowns, the system of equations must be solved using the non-linear LSA. This implies that the equations must be linearised and initial values for the unknown coefficients must be computed. The partial derivatives of Equations 2.36, 2.38 and 2.40 with respect to the unknown parameters are shown in the Section 2.10.4.

The matrix equation of the iterative non-linear LSA is $[A][dx] = [B]$, where $[A]$ is the design matrix which contains the partial derivatives of each equation with respect to each unknown parameter. $[dx]$ is the vector of the adjustment values of the unknown parameters. The vector $[dx]$ which is computed by the first iteration of LSA, is used to update the initial values of the unknown parameters $[X^0]$: $[X^1] = [X^0] + [dx]$. The procedure is repeated until convergence ($[dx] = 0$).

The initial values $[X^0]$ of the unknown parameters can be found indirectly using the similarity transformation:

$$\begin{aligned}
x &= X_o + \mu (X \cos \phi + Y \sin \phi) = (\mu \cos \phi)X + (\mu \sin \phi)Y + X_o \\
y &= Y_o + \mu (-X \sin \phi + Y \cos \phi) = (-\mu \sin \phi)X + (\mu \cos \phi)Y + Y_o
\end{aligned} \tag{2.41}$$

where X_o, Y_o is the translation, μ is the scale and ϕ is the rotation angle. It must be noted that in this case the similarity transformation is not used as an initial

approximation to the ICP algorithm, but only to compute the first values for the application of the non-linear LSA. Comparing the similarity and the affine transformations (Equation 2.41 and Equation 2.31), the following first values can be found:

$$a = \mu \cos \phi, \quad b = \mu \sin \phi, \quad c = X_0, \quad d = -\mu \sin \phi, \quad e = \mu \cos \phi, \quad c = Y_0 \quad (2.42)$$

The parameters X_0, Y_0, μ, ϕ of the similarity transformation can be determined as described in the rigid approach for the computation of the initial approximation (Section 2.9).

2.10.4 Partial derivatives

The partial derivatives of Equations 2.36, 2.38 and 2.40 are given here for completeness.

$$\frac{\partial \mu'_{X1}}{\partial a} = \frac{1}{m} \sum_{j=1}^m X_j = \bar{X} \quad , \quad \frac{\partial \mu'_{X1}}{\partial b} = \frac{1}{m} \sum_{j=1}^m Y_j = \bar{Y}$$

$$\frac{\partial \mu'_{X1}}{\partial c} = \frac{1}{m} \sum_{j=1}^m 1 = 1$$

$$\frac{\partial \mu'_{Y1}}{\partial d} = \bar{X} \quad , \quad \frac{\partial \mu'_{Y1}}{\partial e} = \bar{Y} \quad , \quad \frac{\partial \mu'_{Y1}}{\partial f} = 1$$

$$\frac{\partial \mu_{Xk}}{\partial a} = \frac{(\mu_{Xk})^{1-k}}{m} \cdot \sum_{j=1}^m (aX_j + bY_j + c - \mu'_{X1})^{k-1} (X_j - \bar{X})$$

$$\frac{\partial \mu_{Xk}}{\partial b} = \frac{(\mu_{Xk})^{1-k}}{m} \cdot \sum_{j=1}^m (aX_j + bY_j + c - \mu'_{X1})^{k-1} (Y_j - \bar{Y})$$

$$\frac{\partial \mu_{Xk}}{\partial c} = \frac{(\mu_{Xk})^{1-k}}{m} \cdot \sum_{j=1}^m (aX_j + bY_j + c - \mu'_{X1})^{k-1} (1 - 1) = 0$$

$$\frac{\partial \mu_{Yk}}{\partial d} = \frac{(\mu_{Yk})^{1-k}}{m} \cdot \sum_{j=1}^m (dX_j + eY_j + f - \mu'_{Y1})^{k-1} (X_j - \bar{X})$$

$$\frac{\partial \mu_{Yk}}{\partial e} = \frac{(\mu_{Yk})^{1-k}}{m} \cdot \sum_{j=1}^m (dX_j + eY_j + f - \mu'_{Y1})^{k-1} (Y_j - \bar{Y})$$

$$\frac{\partial \mu_{Y^k}}{\partial f} = \frac{(\mu_{Y^k})^{1-k}}{m} \cdot \sum_{j=1}^m (dX_j + eY_j + f - \mu'_{Y^1})^{k-1} (1-1) = 0$$

$$\frac{\partial L}{\partial a} = \sum_{j=2}^m \frac{1}{L_j} [a(X_j - X_{j-1}) + b(Y_j - Y_{j-1})] (X_j - X_{j-1})$$

$$\frac{\partial L}{\partial b} = \sum_{j=2}^m \frac{1}{L_j} [a(X_j - X_{j-1}) + b(Y_j - Y_{j-1})] (Y_j - Y_{j-1})$$

$$\frac{\partial L}{\partial d} = \sum_{j=2}^m \frac{1}{L_j} [d(X_j - X_{j-1}) + e(Y_j - Y_{j-1})] (X_j - X_{j-1})$$

$$\frac{\partial L}{\partial e} = \sum_{j=2}^m \frac{1}{L_j} [d(X_j - X_{j-1}) + e(Y_j - Y_{j-1})] (Y_j - Y_{j-1})$$

2.11 Matching networks of FFLFs

The man-made or physical linear features that are identified in two heterogeneous multitemporal data sets of the same area and are going to be matched, are generally non-continuous. The larger linear feature could be chosen and the match of the data sets could be based on the matching of a single pair of FFLFs. This is certainly possible and it often leads to sufficient accuracy. However one pair of FFLFs may not represent the data sets in their entirety, as it may be confined to a small region of the data sets. In multitemporal cases large portions of linear features which are present in the older data set are often not present, or are drastically altered, in the newer data set. In these cases multiple pairs of FFLFs must be matched and two unique problems, which are not present in single pair FFLFs matching, have to be faced:

- It is generally not known which of the FFLFs of the first data set corresponds to which FFLF of the second data set. Thus the correspondences of the FFLFs must be established before application of the ICP algorithm.
- All the pairs of FFLFs share a common transformation. Thus it is not possible to match each pair independently, since each matching would produce a different transformation. All the pairs should be matched simultaneously in order to produce a single and more accurate transformation.

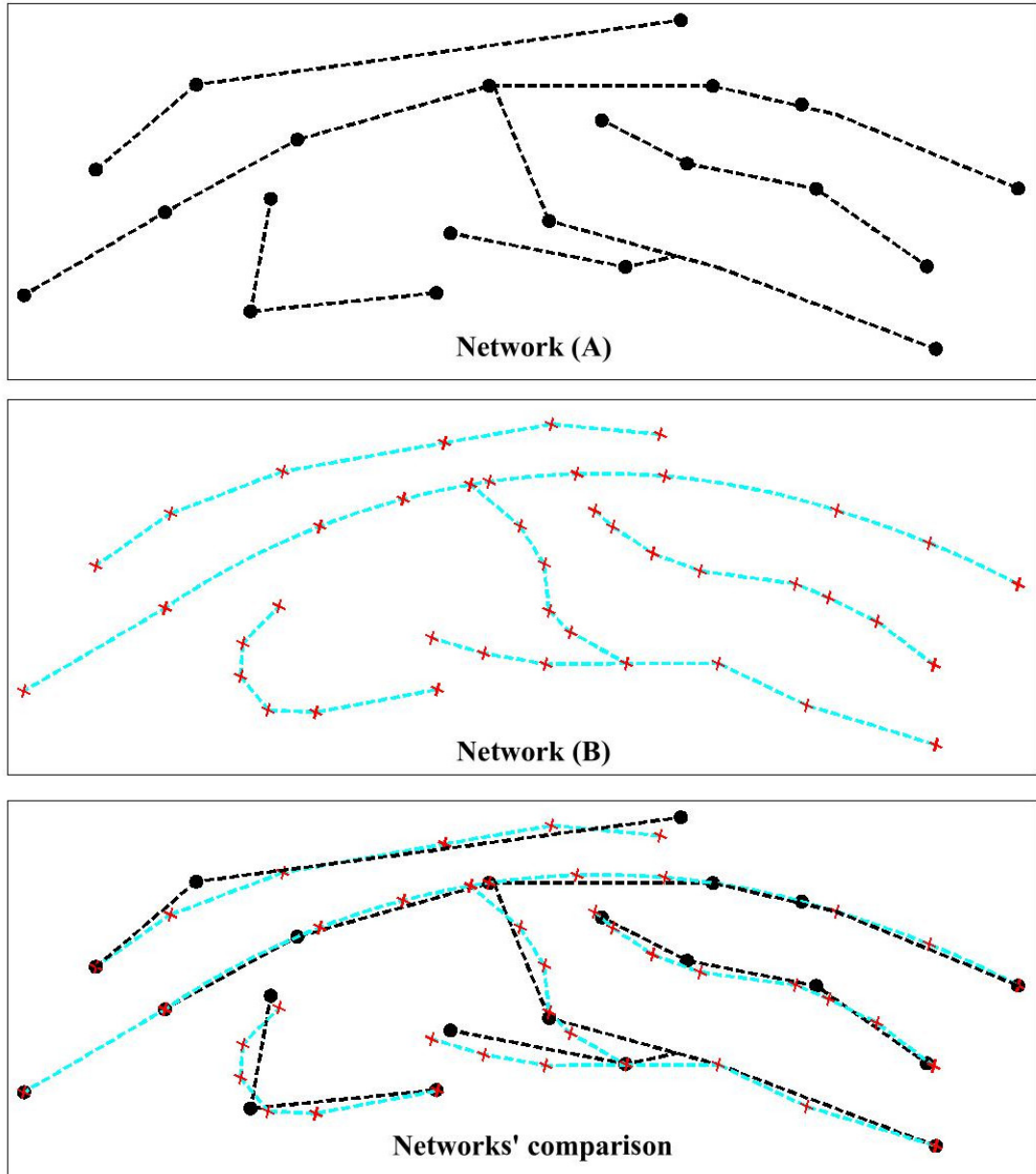


Figure 2.5: The problem of global matching of networks of heterogeneous FFLFs.

```

FFLFs correspondences:
For each FFLF (A) of the first network:
    For each FFLF (B) of the second network:
        Compute "distance" d of (A), (B).
        Save [d, (A), (B)] triplet to set T.
    End For.
End for.
Repeat while set T is not empty:
    Find the triplet d, (A), (B) of T with minimum d.
    Save (A), (B) as corresponding FFLFs.
    Erase all triplets of T which contain (A).
    Erase all triplets of T which contain (B).
End repeat.
End.

```

Figure 2.6: Determination of FFLFs correspondences using arbitrary metric.

2.11.1 Identification of FFLFs correspondences

In order to identify the FFLFs correspondences, it is assumed that the two data sets are initially pre-aligned. This is not a limitation of the proposed method, as the pre-alignment is a precondition for the convergence of the ICP algorithm. With this assumption the correspondences are easy to identify. A FFLF of the first data set corresponds to the FFLF of the other data set which is "closest" to it. However, the definition of "closest" is ambiguous for a FFLF which may span many other FFLFs (Figure 2.5). Different nodes of the same FFLF may be closest to nodes of different FFLFs. Clearly the "closeness" must refer to the FFLF as a whole. Six different approaches have been tested:

1. the end node approach
2. the centroid approach
3. the length approach
4. the average distance approach
5. the ICP approach
6. the Hybrid approach

Each approach uses a different metric of the "distance" of two arbitrary FFLFs. The pair of FFLFs which have the least metric are homologous. This means that

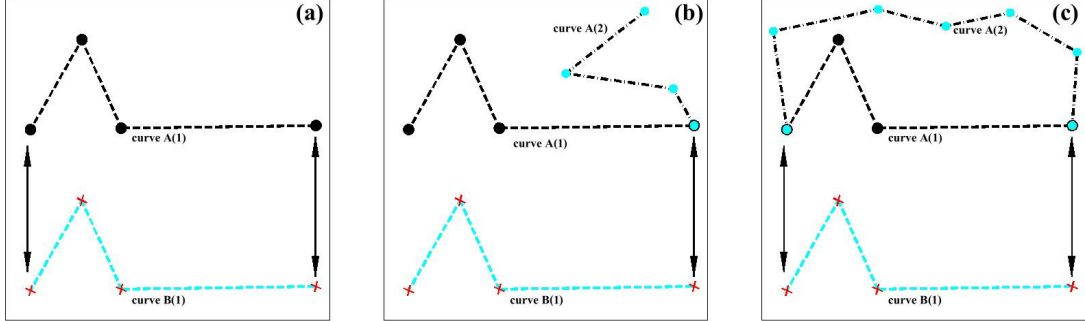


Figure 2.7: (a) Homologous end nodes, (b) common end nodes, (c) common start and end nodes.

a FFLF of the first data set is compared to every FFLF to the second data set (exhaustive search), which implies an execution time of $O(n^2)$ where n is the number of the different FFLFs. Quadratic execution time is prohibitive for large n , but the number of individual FFLFs is rather small, usually less than twenty and very rarely greater than a hundred. These numbers are within the capabilities of modern computers. The algorithm is shown in Figure 2.6.

2.11.1.1 End node approach

Let F be a characteristic point on FFLF A and let G be the same characteristic point in FFLF B. Then the distance between the points can be used as a (not very good) metric of the distance of the FFLFs:

$$\Delta_{AB} = \sqrt{(x_G - x_F)^2 + (y_G - y_F)^2} \quad (2.43)$$

In global matching, the first and last node of each FFLF have to be homologous (Figure 2.7a) and thus Equation 2.43 can be evaluated twice. The average of the two (similar) distances can be used as a better metric of the distance between the FFLFs. This metric is capable to avoid FFLFs which have one common point, such as when a road forks or when a road begins where the other ends (figure 2.7b). However it fails to distinguish between different FFLFs, in the rare case where two different FFLFs have the same ends (Figure 2.7c). The advantage of this approach is that it is very fast since it needs very few computations.

2.11.1.2 Centroid approach

Assuming global matching, a good metric of the distance of the FFLFs is the distance between the centroids of the two FFLFs:

$$\Delta_{AB} = \sqrt{(\bar{x}_B - \bar{x}_A)^2 + (\bar{y}_B - \bar{y}_A)^2} \quad (2.44)$$

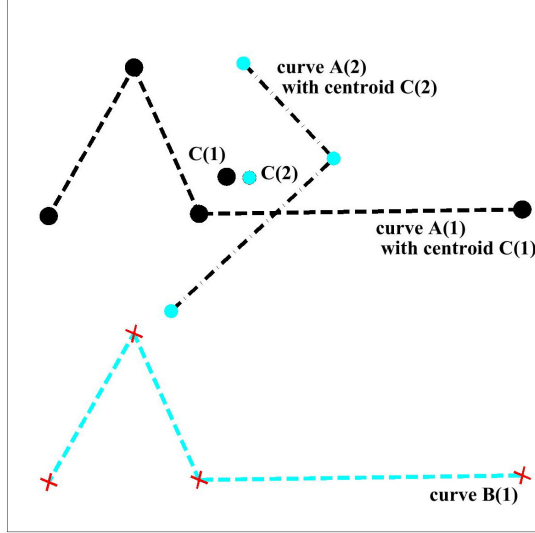


Figure 2.8: Different FFLFs with same centroid.

where \bar{x}_A, \bar{y}_A and \bar{x}_B, \bar{y}_B are the coordinates of the centroids of the two FFLFs which are computed as described in Section 2.9.1.

The centroids are quite insensitive to random errors in the nodes of each FFLF, as the errors tend to cancel out each other. Thus the centroid is the best single point representation of a FFLF. However this approach fails in the rare case when two totally different FFLFs have the same centroid, such as two intersecting roads (figure 2.8). The advantage of this approach is its robustness and the relatively small number of computations compared to the next approaches.

2.11.1.3 Length approach

Assuming that the FFLFs are roughly at the same scale, the lengths of two homologous FFLFs must be almost the same. Then the absolute difference of the lengths of the FFLFs can be used as metric of the distance of the FFLFs:

$$\Delta_{AB} = |S_B - S_A| \quad (2.45)$$

This approach obviously fails when two distinct FFLFs have the same length, case which is unlikely in the natural environment, but possible in urban areas. The advantage of this approach is that it is relatively fast; given that the lengths of the FFLFs are calculated once, the method needs few computations only.

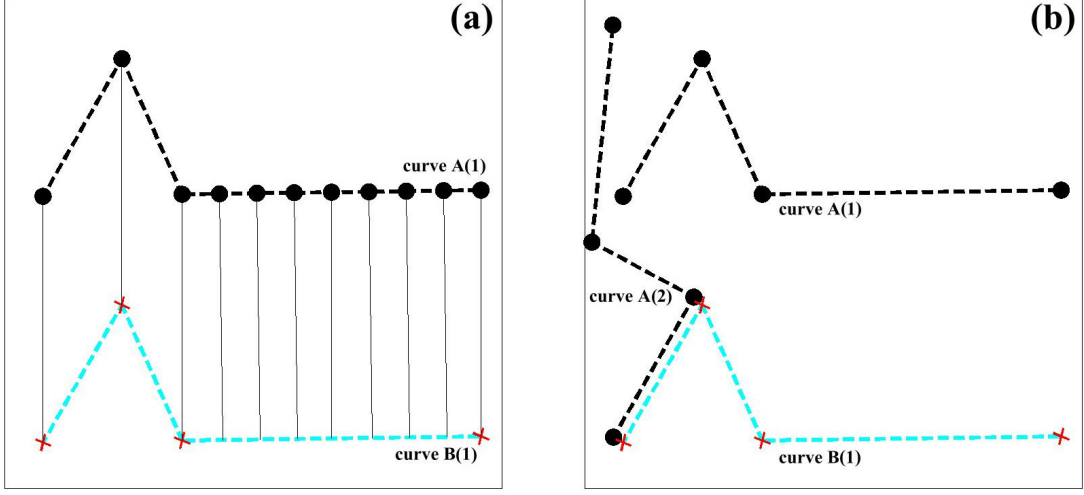


Figure 2.9: (a) Non-uniform density of nodes, (b) Not homologous FFLFs which have a short identical part.

2.11.1.4 The average distance approach

The first iteration of the ICP algorithm can be used to find the closest point of every node of a FFLF to the other FFLF. The average distance of the closest points is used as the metric of the distance between the FFLFs.

$$\Delta_{AB} = \frac{1}{N} \sum_{j=1}^N d_j = \frac{1}{N} \sum_{j=1}^N \sqrt{(x_{Bj} - x_{Aj})^2 + (y_{Bj} - y_{Aj})^2} \quad (2.46)$$

where N is the number of nodes and x, y are the coordinates of the nodes and their closest points.

In order to accommodate for non-uniform density of nodes (figure 2.9a) and assuming linear interpolation of the distance between nodes:

$$\Delta_{AB} = \frac{\sum_{j=1}^{N-1} (d_j + d_{j-1}) \frac{s_j}{2}}{\sum_{j=1}^{N-1} s_j} \quad (2.47)$$

where $s_j = \sqrt{(x_{A(j+1)} - x_{Aj})^2 + (y_{A(j+1)} - y_{Aj})^2}$ is the distance of consecutive nodes and the N nodes are in the overlapping (or common) part of the two FFLFs.

It must also be ensured that the common part of the FFLFs, where the ICP finds closest points, is big enough to be reliable. Otherwise, if only a small part of

the FFLFs is common and the FFLFs are identical along this part, the algorithm will erroneously accept them as homologous (Figure 2.9b). Experimentation has shown that setting a restrictive limit for the smallest acceptable common part, for example 75%, the correspondence of many pairs is not identified, even with a small rotation angle. On the other hand, if the limit is too permissive, for example 20%, the original problem is not solved.

The solution is to multiply the metric by a corrective coefficient, which is big when the common part is small and close to unity if the common part is big. The inverted ratio of the common length to the length of one of the FFLFs is the obvious choice, but experience showed this to be somewhat insensitive to small common parts. Thus the square of the inverted ratio is used:

$$\Delta_{AB}^* = \Delta_{AB} \left[\frac{S_A}{\sum_{j=1}^{N-1} s_j} \right]^2 \quad (2.48)$$

where S_A is the length of the first FFLF. The power of 2 ensures that for small common parts, for example 10%, the error will be multiplied by 100, so that the algorithm will choose a FFLF with bigger common part as homologous, if there is one. Otherwise, the FFLF with the small common part will be the homologous one, and the small common part would be probably due to poor pre-alignment.

2.11.1.5 The ICP approach

The full ICP algorithm (Section 2.7) can be used to match each FFLF of the first data set to every FFLF of the second data set. For many pairs the ICP will not converge, while for others the final RMS error will be large. The real homologous pair will be the one with the minimum RMS error.

The ICP approach is very robust, but it has the disadvantage that it is computationally very intensive.

2.11.1.6 Hybrid approach

The ICP approach is the best of the first four approaches presented above, because it leaves no doubt about the result. However it is also very time consuming and it would be advantageous to avoid it, or at least to use it as little as possible. Thus a hybrid approach is proposed. The distance between three characteristic homologous points is computed: the first node, the last node and the centroid (first and second approach). The absolute difference of the FFLF lengths is also computed (third approach). The biggest of these four values is used as a metric

of the distance of the FFLFs.

$$\Delta_{AB} = \max \left\{ \begin{array}{c} d_1 \\ d_N \\ \bar{d} \\ \Delta S \end{array} \right\} = \max \left\{ \begin{array}{c} \sqrt{(x_{B1} - x_{A1})^2 + (y_{B1} - y_{A1})^2} \\ \sqrt{(x_{BN} - x_{AN})^2 + (y_{BN} - y_{AN})^2} \\ \sqrt{(\bar{x}_B - \bar{x}_A)^2 + (\bar{y}_B - \bar{y}_A)^2} \\ |S_B - S_A| \end{array} \right\} \quad (2.49)$$

It is almost impossible that two distinct FFLFs B and C exist, for which the values of d_1 , d_N , \bar{d} , ΔS with FFLF A are identical. However in the unlikely case that it is so, the ICP approach can be used to determine which of the two FFLFs is really homologous to A.

2.11.2 Partial Identification of FFLFs correspondences

The method, as described so far, assumes global matching, implying that the number of FFLFs of each network is the same (N:N matching). The method, however, has partial matching capabilities which can be further exploited in future research. If the number of FFLFs of the two networks is different (N:M matching, N>M), the method finds the “closest” pair of FFLFs, marks these FFLFs as corresponding pair of FFLFs, and continues the same process for the remaining FFLFs (N-1:M-1 matching). In the end N-M single FFLFs are left, which are effectively ignored. The method proceeds with an ICP step, it brings the FFLFs even closer and it then re-evaluates the correspondence, as the “distance” between any pair of FFLFs is obviously changed. Furthermore, ICP automatically rejects two unrelated FFLFs marked to correspond if they do not overlap at all (Section 2.6).

2.11.3 Unified LSA

The ICP for a single pair of corresponding FFLFs between the two data sets, computes the closest points and the transformation using all the available data. Likewise, when there are multiple pairs of corresponding FFLFs, the transformation is common to all pairs and it is computed using all the data available (all the pairs). However, the closest points are not computed using the data of all the pairs, since it would be obviously an error to find closest points between unrelated FFLF. The computation of closest points is done independently for each pair of FFLFs. Then, the closest points of all the pairs of FFLFs are used to determine the parameters of a single transformation. The modified ICP algorithm for multiple pairs is summarised in figure 2.10.

```

ICP network global matching:
Repeat until convergence to minimum RMS error:
  For each pair (A,B) of FFLFs:
    For each node of FFLF (A):
      Determine the node's closest point on (B).
    End For.
  End for.
  Compute the global RMS error using determined closest points
    of all pairs.
  Use the determined closest points of all pairs to compute the
    parameters of the single transformation with the LSA.
  For each pair (A,B) of FFLFs:
    Transform FFLF (A) using the transformation parameters.
  End for.
End repeat.
End.

```

Figure 2.10: ICP for global matching networks of FFLFs.

2.11.4 Pre-alignment

The use of multiple pairs of FFLFs for the ICP increases the robustness of the method. If the pre-alignment is poor, then the ICP does not converge. However, it is conceivable that the ICP converges for one or two of the many pairs of corresponding FFLFs, where the pre-alignment is a little better by chance. This partial transformation, which is a good approximation to the global transformation, can be used to transform the rest of the pairs. This essentially improves the pre-alignment, making global ICP convergence possible.

If the data sets are not pre-aligned at all, then they need to be pre-aligned. Manual pre-alignment is generally awkward and cumbersome for multiple FFLFs. Especially in the case of 3D-2D matching (Section 2.11.6) of SAR images, it is rather difficult as the varying Z coordinate of the 3D FFLFs and the geometric distortions on the SAR image (2D FFLFs) makes their shapes incompatible. Manual move, scale and rotate operations, typically provided by CAD software, are not enough to cancel the elongated nature of the SAR projection. Instead, the 3D FFLFs must be projected to the image space of the 2D FFLFs using a good approximation of the unknown transformation parameters. Since all pairs of FFLFs share the same transformation, a good approximation of the projection of a single pair of FFLFs, automatically computed (Sections 2.9 and 2.10), can be used to project the 3D FFLFs network to the 2D image space, bringing the

data sets close together. The correspondence of the single pair of FFLFs is chosen manually by the user, so that in this sense the data sets are manually pre-aligned. However, apart from this, the procedure is fully automated.

2.11.5 Computational aspects

The matching of multiple pairs of FFLFs puts additional numerical burden to the ICP algorithm, which is already computational intensive. So, it is important to minimise the iterations needed by the multiple FFLFs matching, improving the pre-alignment. This could be achieved by performing the ICP individually to each one of the pairs at first, and then using the found closest points to initiate the matching of multiple pairs. In essence we would have less multiple ICP iterations at the expense of more individual ICP iterations.

Unfortunately this actually increases the computational cost and the computational time. For the analysis of the total number computations, M FFLFs, N nodes on each FFLF on the average, P parameters of the transformation, and J dimensions are assumed. For one individual ICP iteration, the dimensions of the matrices involved in LSA $[A][X] = [B]$, are respectively: $NJ \times P$, $P \times 1$ and $NJ \times 1$. Since M individuals ICP applications are done, M matrices $[A]$ and $[B]$ are created.

On the other hand, the dimensions of the matrices for one iteration of the global ICP, are respectively: $MNJ \times P$, $P \times 1$ and $MNJ \times 1$. Thus the computational cost for creating these matrices is equivalent for both approaches.

The solution of the matrix equations with LSA is typically done as:

$$[A^T][A][X] = [A^T][B] \Rightarrow [N][X] = [u] \quad (2.50)$$

where the dimensions of the final matrices $[N]$ and $[u]$ are respectively: $P \times P$ and $P \times 1$.

The number of arithmetic operations needed to perform the two matrix multiplications and the solution of the linear system of equations for one individual ICP are respectively (Press et al. [1992]): P^2NJ , PNJ and $P^3/6$. Since M individuals ICP applications are done, the total number of arithmetic operations is:

$$M(P^2NJ + PNJ + P^3/6) = P^2MNJ + PMNJ + MP^3/6 \quad (2.51)$$

In the case of global ICP, the number of the arithmetic operations is:

$$P^2MNJ + PMNJ + P^3/6 \quad (2.52)$$

As it can be seen, the ‘‘improvement’’ of the pre-alignment not only increases the complexity of the method, but it is also (slightly) slower, as the number of

3D-2D network global matching:

Compute an initial approximation of the projection transformation using one pair of FFLFs.

For each FFLF (A) of the first data set:
 Project FFLF (A) to A' using the projection.

End for.

Determine FFLFs correspondences.

Repeat until convergence to minimum RMS error:

 For each pair (A,B) of FFLFs:
 Project FFLF (A) to A' using the previous projection and save 3D-2D nodes association.

 For each node of FFLF A' :
 Determine the 2D node's closest point on (B).

 End For.

 End for.

 Compute the global RMS error using determined closest points of all 2D pairs.

 Use the saved association to produce 3D-2D pairs.

 Use all 3D-2D pairs to compute the parameters of the single projection transformation with the LSA.

End repeat.

End.

Figure 2.11: ICP for global matching networks of FFLFs (3D-2D).

operations is slightly less for the multiple ICP. Obviously, for each one of the two alternative procedures, the total number of operations depends also on the number of the iterations needed.

2.11.6 3D-3D and 3D-2D networks

The matching of networks of 3D FFLFs can be done as described in Sections 2.11.1 to 2.11.5 for the 2D case. The only difference is that the formulas which compute various distances should also take the z coordinate into account. For example equation 2.44 becomes:

$$\Delta_{AB} = \sqrt{(\bar{x}_B - \bar{x}_A)^2 + (\bar{y}_B - \bar{y}_A)^2 + (\bar{z}_B - \bar{z}_A)^2} \quad (2.53)$$

The matching of networks of different dimensionality (3D-2D) can also be done as described in Sections 2.11.1 to 2.11.5. The different dimensionality of the FFLFs (3D-2D) is handled through the method described in Section 2.8. The

3D nodes of the 3D FFLFs are projected to the 2D image space using a previous approximation of the projection parameters; the association of each 3D node and its 2D projection is saved. For each 2D node of the projected FFLFs, its closest point in the 2D FFLF is computed, producing 2D-2D pairs. The 2D-2D pairs are converted to 3D-2D pairs through the saved associations. The LSA is applied to the 3D-2D pairs to compute better approximation of the projections parameters. The steps of the complete matching algorithm are summarised in figure 2.11.

2.12 Overview and contribution

In this Chapter (*Chapter 2*) novel general methods were developed each of which provides several contributions to surveying engineering:

- The automated ICP-based method for global matching of single pairs of heterogeneous FFLFs of the same (2D-2D, 3D-3D) or of different dimensionality (3D-2D) which is accompanied by the automated computation of the initial approximation by using physical or statistical properties of the FFLFs.
- The automated method for global matching of networks (multiple pairs) of heterogeneous FFLFs of the same (2D-2D, 3D-3D) or of different dimensionality (3D-2D) which is accompanied by the automated identification of FFLFs correspondences and the unified Least Squares Adjustment for all the FFLFs of the networks.
- The robust and automatic computation of homologous points of a pair of FFLFs. The method is computationally intensive and can be accelerated by divide and conquer and/or parallel programming.
- The method to automatically compute the initial approximation required by the ICP algorithm. The method exploits physical properties of the whole FFLF such as the length and the centroid, to compute an initial similar transformation which brings the FFLFs close.
- The method to automatically compute the initial approximation required by the ICP algorithm, when the distortions of the sensor are severe and can not be approximated by rigid transformations. The method exploits statistical properties of the whole FFLF such as the average and higher order moments, to compute an initial 1st order polynomial transformation which brings the FFLFs close.

The methods are later tested, validated and evaluated using numerous simulated and real world data sets and real world problems (Chapters 4 and 5),

which can hardly be solved with standard methods. The general methods of this Chapter are also combined together, or combined with the general methods of the next chapter, or with other general methods, principles, problems and data of surveying engineering, in order to develop new specific methods (Chapter 6).

Chapter 3

Co-registration, correlation and merging

Co-registration of two data sets is the process of overlaying data sets of the same scene (Section 1.1). Common characteristic points or other features must be identified between the two data sets, and a mathematical relationship, or model (Section 2.3), between the characteristic features must be established. Using the model one data set is transformed and overlaid onto the other, or both data sets are transformed and overlaid onto another representation, as for example onto geometrically corrected images. In this dissertation at least one of the data sets is an image, the SAR image. The other data set may be also an image, for example an optical image, or something else, for example a map. The relationship between the data sets is three dimensional (3D-2D) as in the vast majority of the real-world cases the terrain is not flat. This is especially true for SAR images, where the side-looking geometry of the SAR sensor produces distortions which are greater than the distortions of an optical image. Thus, co-registration of SAR images with heterogeneous remote sensing and geospatial data is not a simple task:

1. The imaging technology of optical and SAR sensors is totally different as the former are passive sensors that record visible wave lengths while the latter are active sensors that record microwave lengths which can not be perceived by the human eye. Optical sensors record the backscattered physical light of the sun, while SAR sensors record the backscattered radiation which they themselves have transmitted.
2. The imaging geometry of optical and SAR sensors is totally different as the former is based on the principles of central projection in order to image the 3D world space on a 2D imaging plane, while the latter uses the side-looking slant range imaging geometry as projection principle.

-
3. The SAR imaging technology and geometry creates artifacts and distortions (speckle, layover, shadow etc) which are not present or they appear in different form on other data types.
 4. The three dimensional character of the model requires 3D information to compute its parameters. More 3D information is required to overlay the data sets to the same scene.

These fundamental differences in imaging technology and geometry affect severely the efficiency of otherwise robust correlation statistical methods, when applied to areas that suffer most from different sensor technology, such as mountainous areas and homogeneous sites like deserts or tundra (Reinartz et al. [2011]). The problem is intensified when multispectral optical images are considered and it is essentially unsolved when unprocessed (not geometrically corrected) high resolution multispectral optical and SAR images are considered. Ehlers [1991], Pohl and Genderen [1998], Simone et al. [2002], Zhang [2004], Wang et al. [2008], Goshtasby and Nikolov [2007] present extensive review of the related work.

This Chapter presents the co-registration of SAR and other data with linear features, and the georeferencing of certain space-borne SAR sensors which can be done without using any kind of Ground Control Information (GCI). A new method is introduced for the rigorous geometric correlation and radiometric merging of not geometrically corrected high resolution SAR and multispectral optical images. The concept of the method is to maintain the side-looking slant range geometry of the SAR image when it is combined with optical images. This concept is important as SAR images illustrate various details of the Earth's surface which are not illustrated on optical images and which are also lost when SAR images are geometrically corrected. As an example, metallic pillars appear as bright line segments in slant range SAR images while one can hardly distinguish them on an optical image. Furthermore, they degenerate to virtually single points when SAR images are geometrically corrected.

3.1 GCLFs-based co-registration

The co-registration of SAR images with 3D data sets such as maps requires that the 3D map coordinates of some characteristic features of the SAR image are known (Ground Control Information - GCI). The most common form of GCI is the solitary point (Ground Control Point - GCP), the fundamental feature of all photogrammetric processes. Numerous methods, data sets and tests have been presented over the years using GCPs (Toutin [2004], Dowman et al. [2012]). Repetition of this long-term research and practical knowledge would be redundant.

More complex features, such as straight lines and FFLFs can be exploited as an alternative/complementary form of GCI (Ground Control Linear Features - GCLFs). GCLFs are especially useful in the case of SAR images, whose fuzzy and speckled nature makes the identification of GCPs difficult and ambiguous. The same physical or man-made linear feature is identified on the SAR image (2D FFLF), and on the 3D data set (3D GCLF). The matching of the FFLF and the GCLF is performed as described in Section 2.8. Alternatively, networks of FFLFs and GCLFs can be used as described in Section 2.11.6. The matching produces a 3D-2D model which projects coordinates, or overlays, of the 3D data set to the SAR image.

The co-registration of SAR images with other images such as optical images requires additionally three dimensional information which is usually is in the form of 3D object coordinates of the Earth's surface (GCI). For each of the two images a physical or man-made linear feature is measured (2D FFLF), and the same feature is measured on the ground (3D GCLF) using perhaps a field survey such as GPS. The matching of the FFLF and the GCLF produces a 3D-2D model for each image which project 3D object coordinates of the ground to both images (georeferencing). The two projections of the same point or feature, are homologous and can be overlaid as described later in Section 3.3.2 along with the radiometric merging of images. The co-registration of images is thus indirect and it is done using GCI as intermediary.

In the case of the co-registration of images, GCLFs also provide the luxury and the elegance of using the same GCI to compute the georeferencing of both (heterogeneous) images. The reason is that linear features, in contrast to solitary points, tend to be identifiable in many types of data, and they tend to persist through time.

3.2 Direct-georeferencing-based co-registration

The georeferencing of certain space-borne SAR, such as the TerraSAR-X, can be done without using any kind of Ground Control Information (GCI). Particularly, the georeferencing of high resolution TerraSAR-X images can be done using merely the orbital data and the parameters of the processor. In other words it is possible to project a 3D point of the Earth's surface on a 2D SAR image, without using GCI. TerraSAR-X has three GPS receivers on-board which serve the mission and science operations of the sensor. Due to a GPS-based precise orbit determination strategy (Yoon et al. [2009]), the orbital path is offered to end users with a nominal accuracy up to 0.20 m (during periods with low solar activity much better accuracies have been reported), which is used to georeference the images.

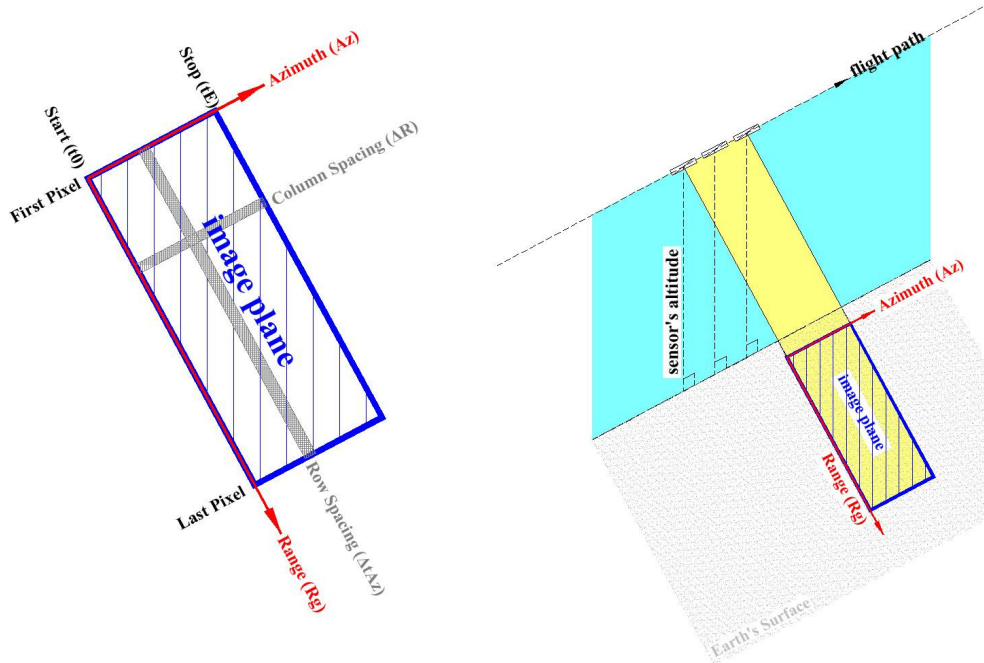


Figure 3.1: SAR imaging geometry.

3.2.1 Problem Formulation

A SAR image is essentially a 2D dimensional projection (x,y) of the 3D object space (X,Y,Z) . The two image dimensions have a straightforward physical meaning: the x-axis of the image represents the slant range (distance) (R) from the sensor to a target on the Earth's surface and the y-axis represents the time (t) , as the sensor moves following its orbit. Thus it could be said that a SAR image is essentially a diagram of range (distance) and time (Figure 3.1). Each point on the image space with the same x coordinate has the same slant range from the sensor, while each point with the same y coordinate has been measured at the same time. But as range is measured indirectly through time measurements, SAR image is ultimately a diagram of time versus time. Surprisingly enough, this diagram happens to illustrate a 2D projection of the 3D Earth's surface in a way that the human brain can comprehend.

Generally a point $P(X_P, Y_P, Z_P)$ of object space is projected to a point $p(x_p, y_p)$ on the SAR image. On the image, y_p is the translated and scaled time stamp t_P when the sensor measured point P , and x_p is the translated and scaled distance R_P from the sensor to point P at the time of the measurement t_P (Figures 3.2 and 3.3):

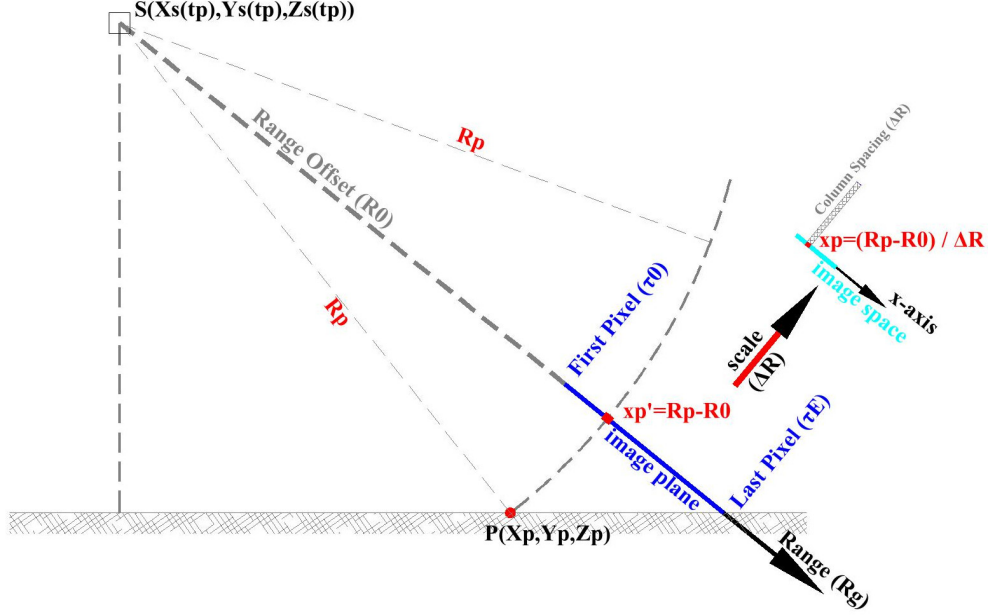


Figure 3.2: Imaging geometry in range.

$$x_P = \frac{R_P - R_0}{\Delta R}, \quad y_P = \frac{t_P - t_0}{\Delta t_{Az}} \quad (3.1)$$

The four translation and scale parameters R_0 , ΔR , t_0 , Δt_{Az} are unknowns to be computed. The distance R_P is computed as the distance of point P and the location S of the sensor at the time of the measurement.

$$R_P = \left| \vec{P} - \vec{S}(t_P) \right| \quad (3.2)$$

where:

$$\vec{P} = (X_P, Y_P, Z_P) \quad \text{and} \quad \vec{S}(t) = (X_S(t), Y_S(t), Z_S(t)) \quad (3.3)$$

Equation 3.3b describes the orbit of the SAR sensor which is unknown and must be determined. Time t_P can be computed by the geometry of the SAR sensor which, in the case of TerraSAR-X, states that the vector distance of point P and the SAR sensor is perpendicular to the SAR sensor's orbit at the time of the measurement (Leberl [1991], Toutin [2004], Maitre [2010]):

$$\vec{S}(t_P) \cdot \left(\vec{P} - \vec{S}(t_P) \right) = 0 \quad (3.4)$$

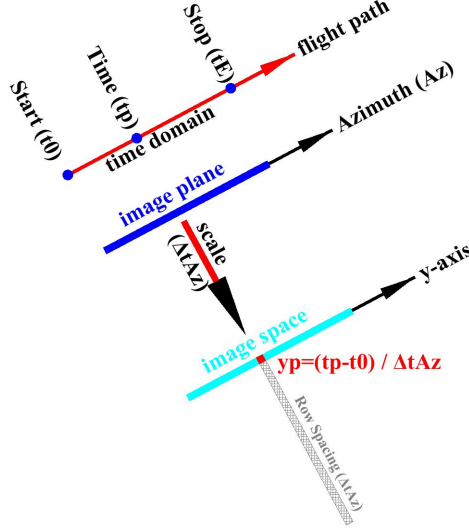


Figure 3.3: Imaging geometry in azimuth.

where the dot implies derivative with respect to time. Thus, the SAR projection is given by:

$$x_P = \frac{|\vec{P} - \vec{S}(t_P)| - R_0}{\Delta R}, \quad y_P = \frac{t_P - t_0}{\Delta t_{Az}} \quad (3.5)$$

where t_P is computed by Equation 3.4, and R_0 , ΔR , t_0 , Δt_{Az} plus the parameters implied in Equation 3.3b must be determined. In the following subsections, the computation of these parameters for TerraSAR-X images without using any kind of GCI is presented.

3.2.2 Computation of the parameters R_0 , ΔR , t_0 , Δt_{Az}

Most of the unknown parameters are given in the XML file that accompanies TerraSAR-X data (Fritz et al. [2007]):

- R_0 is the slant range offset and is given indirectly in the XML file. It can be computed as:

$$R_0 = \frac{c}{2} \tau_0 \quad (3.6)$$

where $c=299,792,458\text{m/sec}$ is the speed of light in vacuum and τ_0 is the two-way RADAR pulse travelling time for the first pixel of each row, given

in the following section of the XML file:

productInfo/sceneInfo/rangeTime/firstPixel

- t_0 is the time stamp when the image acquisition began, or when the first row of the image was acquired. It is given in a time/date format, which can be converted to seconds, in the following section of the XML file:

productInfo/sceneInfo/start/timeUTC

- ΔR is the column spacing in meters (the pixel size in the range direction) and it is given in the following section of the XML file:

productSpecific/complexImageInfo/projectedSpacingRange/slantRange

- Δt_{Az} is the row spacing in seconds (pixel size in the azimuth direction) and it is given in the following section of the XML file:

productInfo/imageDataInfo/imageRaster/columnSpacing

3.2.3 Computation of sensor's position with respect to time

The TerraSAR-X image is accompanied by accurate Science Orbit Data, with 3D nominal accuracy ± 0.20 m (Yoon et al. [2009]). During periods with low solar activity, much better accuracies (~ 0.03 m) have been reported (Breit et al. [2010]). The orbit of the sensor is given in the XML file as the position and the velocity vectors for twelve (12) or more time stamps.

In order to compute the position and the velocity in arbitrary time an interpolation must be used. The whole SAR image is acquired between 2 of the time stamps. Thus, the interpolation may be computed using these 2 stamps or more than 2 or all the stamps. In the following paragraphs various interpolations are examined.

3.2.3.1 Available orbit data

The number of time stamps N is given in the following section of the XML file (Fritz et al. [2007]):

platform/orbit/orbitHeader/numStateVectors

The position and the velocity data is given in the WGS84 geocentric coordinate system, in meters and meters/sec respectively. The time stamp (given in date/time format which can be converted to seconds), the position and the velocity are given as:

timeUTC, posX, posY, posZ, velX, velY, velZ

in the following section of the XML file:

platform/orbit

In order to compute the position and the velocity in arbitrary time an interpolation must be used. The whole SAR image is acquired between two of the time stamps. Thus, the interpolation may be computed using these two stamps.

3.2.3.2 Orbit approximation considering linear interpolation

Linear interpolation is given by the formulas:

$$\vec{S}(t) = \begin{bmatrix} X_S(t) \\ Y_S(t) \\ Z_S(t) \end{bmatrix} = \begin{bmatrix} a_0 + a_1 t \\ b_0 + b_1 t \\ c_0 + c_1 t \end{bmatrix} \quad (3.7)$$

The 6 unknown parameters can be easily computed using the 2 time stamps which encompass the duration of the image acquisition. It has the disadvantage that it does not take the available velocities into account.

3.2.3.3 Orbit approximation considering cubic interpolation: 2 time stamps

If the orbit of the sensor is approximated by a cubic spline, the velocity of the sensor is given by:

$$\vec{S}(t) = \begin{bmatrix} X_S(t) \\ Y_S(t) \\ Z_S(t) \end{bmatrix} = \begin{bmatrix} a_0 + a_1 t + a_2 t^2 + a_3 t^3 \\ b_0 + b_1 t + b_2 t^2 + b_3 t^3 \\ c_0 + c_1 t + c_2 t^2 + c_3 t^3 \end{bmatrix} \quad (3.8)$$

$$\vec{\dot{S}}(t) = \begin{bmatrix} \dot{X}_S(t) \\ \dot{Y}_S(t) \\ \dot{Z}_S(t) \end{bmatrix} = \begin{bmatrix} a_1 + 2a_2 t + 3a_3 t^2 \\ b_1 + 2b_2 t + 3b_3 t^2 \\ c_1 + 2c_2 t + 3c_3 t^2 \end{bmatrix} \quad (3.9)$$

where the dot implies velocity (derivative with respect to time). The 12 unknown parameters can be computed by the two time stamps t_{S_i} and $t_{S_{i+1}}$ which immediately encompass the duration of the image acquisition ($t_{S_i} < t_0 < t_{S_{i+1}}$), taking into account both the position and the velocity given in the XML file. The parameters for the X coordinate can be computed by solving the following Equations:

$$\begin{bmatrix} X_{S_i} \\ \dot{X}_{S_i} \\ X_{S_{i+1}} \\ \dot{X}_{S_{i+1}} \end{bmatrix} = \begin{bmatrix} 1 & t_{S_i} & t_{S_i}^2 & t_{S_i}^3 \\ 0 & 1 & 2t_{S_i} & 3t_{S_i}^2 \\ 1 & t_{S_{i+1}} & t_{S_{i+1}}^2 & t_{S_{i+1}}^3 \\ 0 & 1 & 2t_{S_{i+1}} & 3t_{S_{i+1}}^2 \end{bmatrix} \begin{bmatrix} a_0 \\ a_1 \\ a_2 \\ a_3 \end{bmatrix} \quad (3.10)$$

Similar equations can be solved for the parameters of Y and Z coordinates.

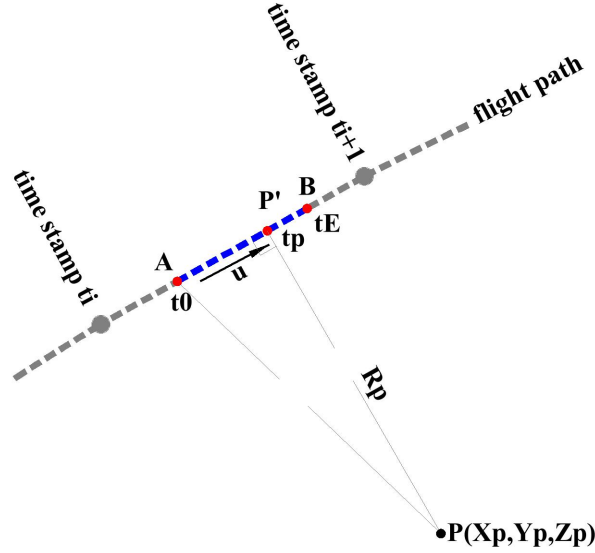


Figure 3.4: Linear orbit.

3.2.3.4 Orbit approximation considering cubic interpolation: more than 2 time stamps

Equations 3.8 and 3.9 can be applied to more than 2 time stamps, for example all the time stamps between i and j . For each time stamp two equations are produced which for the parameters of X coordinate lead to:

$$\begin{bmatrix} X_{S_i} \\ \dot{X}_{S_i} \\ X_{S_{i+1}} \\ \dot{X}_{S_{i+1}} \\ \vdots \\ X_{S_j} \\ \dot{X}_{S_j} \end{bmatrix} = \begin{bmatrix} 1 & t_{S_i} & t_{S_i}^2 & t_{S_i}^3 \\ 0 & 1 & 2t_{S_i} & 3t_{S_i}^2 \\ 1 & t_{S_{i+1}} & t_{S_{i+1}}^2 & t_{S_{i+1}}^3 \\ 0 & 1 & 2t_{S_{i+1}} & 3t_{S_{i+1}}^2 \\ \vdots & \vdots & \vdots & \vdots \\ 1 & t_{S_j} & t_{S_j}^2 & t_{S_j}^3 \\ 0 & 1 & 2t_{S_j} & 3t_{S_j}^2 \end{bmatrix} \begin{bmatrix} a_0 \\ a_1 \\ a_2 \\ a_3 \end{bmatrix} \quad (3.11)$$

Equations 3.11 can be solved with the LSA. Similar equations can be used for the Y and Z coordinate.

3.2.4 Computation of point acquisition time

The computation of the acquisition time t_P of an arbitrary point (Equation 3.4) is not straightforward. One procedure assuming linear orbit and one assuming cubic orbit are presented below.

3.2.4.1 Computation of time t_P considering linear interpolation

When the orbit of the sensor is considered linear, the velocity of the sensor is constant and its direction coincides with the orbit line (Figure 3.4). The unit vector along the straight line orbit is:

$$\vec{u} = \frac{\vec{S}(t_E) - \vec{S}(t_0)}{|\vec{S}(t_E) - \vec{S}(t_0)|} \quad (3.12)$$

The distance between A and P' can be found as the projection of the vector $A\vec{P}$ to the straight line orbit:

$$(AP') = A\vec{P} \cdot \vec{u} = \left(\vec{P} - \vec{S}(t_0) \right) \cdot \vec{u} \quad (3.13)$$

The time stamp t_P can be computed by a simple linear interpolation:

$$t_P = t_0 + (t_E - t_0) \frac{(AP')}{(AB)} = t_0 + (t_E - t_0) \frac{\left(\vec{P} - \vec{S}(t_0) \right) \cdot \vec{u}}{\left| \vec{S}(t_E) - \vec{S}(t_0) \right|} \quad (3.14)$$

3.2.4.2 Computation of time t_P considering cubic interpolation

The computation of t_P can also be achieved through a direct solution of Equation 3.4. If Equations 3.8 and 3.9 which describe the cubic interpolated orbit are applied to Equation 3.4 the dot product yields a polynomial equation with respect to t_P :

$$q(t_P) = k_0 + k_1 t_P + k_2 t_P^2 + k_3 t_P^3 + k_4 t_P^4 + k_5 t_P^5 = 0 \quad (3.15)$$

where:

$$\begin{aligned} k_0 &= X_P a_1 + Y_P b_1 + Z_P c_1 - a_0 a_1 - b_0 b_1 - c_0 c_1 \\ k_1 &= 2X_P a_2 - 2a_0 a_2 + a_1^2 + 2Y_P b_2 - 2b_0 b_2 + b_1^2 + 2Z_P c_2 - 2c_0 c_2 + c_1^2 \\ k_2 &= 3(X_P a_3 - a_0 a_3 + a_1 a_2 + Y_P b_3 - b_0 b_3 + b_1 b_2 + Z_P c_3 - c_0 c_3 + c_1 c_2) \\ k_3 &= 4a_1 a_3 + 2a_2^2 + 4b_1 b_3 + 2b_2^2 + 4c_1 c_3 + 2c_2^2 \\ k_4 &= 5(a_2 a_3 + b_2 b_3 + c_2 c_3) \\ k_5 &= 3(a_3^2 + b_3^2 + c_3^2) \end{aligned}$$

The analytical solution is not possible and so the Newton-Raphson numerical method is employed Press et al. [1992]. Given a previous poorer approximation, this method computes a better approximation to the solution:

$$\begin{aligned}
t_{P,N+1} &= t_{P,N} - \frac{q(t_{P,N})}{\dot{q}(t_{P,N})} \\
&= \frac{k_0 + k_1 t_{P,N} + k_2 t_{P,N}^2 + k_3 t_{P,N}^3 + k_4 t_{P,N}^4 + k_5 t_{P,N}^5}{k_1 + 2k_2 t_{P,N} + 3k_3 t_{P,N}^2 + 4k_4 t_{P,N}^3 + 5k_5 t_{P,N}^4} \quad (3.16)
\end{aligned}$$

As an initial approximation the value of t_P computed by Equation 3.14 can be used. In general Equation 3.15 may have 5 distinct solutions and Equation 3.16 generally converges to the one that is closer to the initial approximation. There is also the possibility that Equation 3.16 does not converge at all. For these reasons the procedure does not seem robust. However, in practice Equation 3.16 always converged to the correct solution in numerous tests, even when the initial approximation was purposely set to a completely different value.

3.3 Geometric correlation and radiometric merging

In order to overlay a SAR and another image, such as an optical image, for each pixel of the SAR image, the correspondent pixel position on the optical image must be found. Both images must be georeferenced as described in Section 3.1. Of course, the SAR image can be direct-georeferenced as described in Section 3.2. The georeferencing can be realised as a function which computes the image pixel coordinates x, y , given its 3D coordinates X, Y, Z in the object space (Earth's surface):

$$x^S = f_1(X, Y, Z), \quad y^S = f_2(X, Y, Z) \quad (3.17)$$

$$x^O = g_1(X, Y, Z), \quad y^O = g_2(X, Y, Z) \quad (3.18)$$

If the coordinates of a point P on the Earth's surface in the object space are known, then the pixel coordinates of its projections p^S to the SAR image and p^O to the optical image can be computed by Equations 3.17 and 3.18 respectively:

$$p^S = (x_P^S, y_P^S) = (f_1(X_P, Y_P, Z_P), f_2(X_P, Y_P, Z_P)) \quad (3.19)$$

$$p^O = (x_P^O, y_P^O) = (g_1(X_P, Y_P, Z_P), g_2(X_P, Y_P, Z_P)) \quad (3.20)$$

Equations 3.19 and 3.20 imply that points p^O and p^S are correspondent as they are the 2D projections of a single 3D point. This means that there is an indirect

relationship between the 2D image coordinates of the two images, which can be realised through points with known 3D object coordinates in object space.

In the theoretical case that a very dense mesh of 3D points were available, its projection would sufficiently span all the pixels of the optical and SAR image making the relationship global. However this is not the normal case. Usually the Earth's surface is approximated by a mathematical model (DEM, DTM, DSM), computed by comparatively sparse points, which more or less span the images. Thus correspondent points between the optical and the SAR image are limited by the sampling strategy used for the collection of the 3D points.

To overcome this limitation and achieve correlation of the optical and the SAR image at pixel level, an interpolation is developed which is based on the handling of triangular shapes of the Finite Element Method (Zienkiewicz [1988]) and the Boundary Element Method (Manolis and Beskos [1988]). The radiometric merging of the pixels of the multispectral optical image and the microwave SAR image is based on chromaticity theory (Niblack [1985]).

The proposed method is summarised as:

1. For each image type, independent recovery of its imaging geometry (georeferencing) is done.
2. A triangulation of the Earth's surface on the object space is established.
3. For each object space 3D point, its independent projections on the two image spaces (the optical and the SAR) are computed.
4. Correspondent pixels on each triangle are established.
5. The correspondent pixels are radiometrically merged.

3.3.1 Geometric correlation

As stated earlier, the mathematical representation of the Earth's surface with solitary points is not a common concept as it lacks practicality. Instead, grid-based and triangle-based modelling is usually employed Li and Chen [2005]. In any case, a network of planar triangles (equilateral or irregular) is readily available or can be computed.

The three vertices of each triangle on object space are projected, using Equations 3.19 and 3.20 on the SAR and the optical image, defining a projected triangle on each image (Figure 3.5). The region within the projected vertices is the projection of the region between the vertices in the object space. This projection is exact for optical sensors which abide to the collinearity equations and a good approximation for other sensors, as the triangles are comparatively small in relation

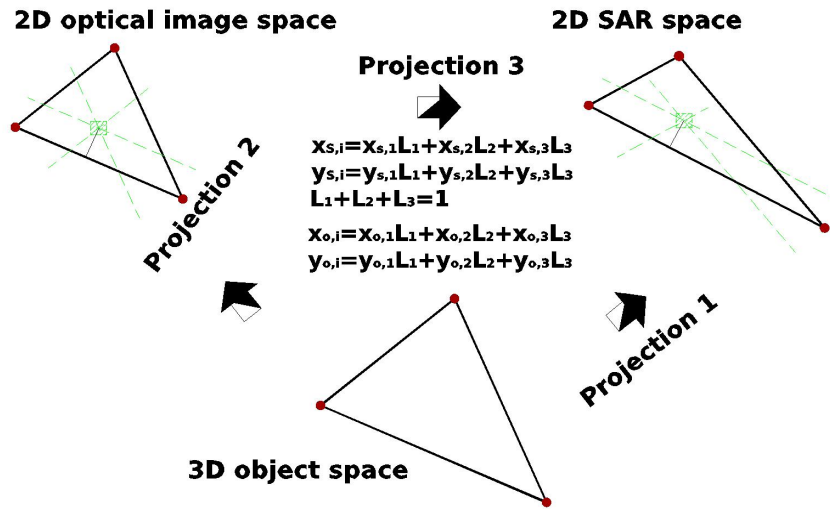


Figure 3.5: Geometric Fusion.

to the whole image. A point inside the triangle in the SAR image, whose relative position with respect to the triangle vertices is known (for example the centroid of the triangle), corresponds to a point inside the optical triangle with the same relative position with respect to the optical triangle vertices (for example the centroid of the optical triangle).

The relative positions of points that lie inside a triangle can be found using triangular local coordinates usually employed in the Finite Element Method and the Boundary Element Method in structural mechanics Li et al. [1985]. The pair of Cartesian coordinates (x,y) of a point Q inside the triangle is replaced by a triplet of triangular coordinates (L_1, L_2, L_3) by the following linear relation:

$$x = L_1x_1 + L_2x_2 + L_3x_3 \quad y = L_1y_1 + L_2y_2 + L_3y_3 \quad L_1 + L_2 + L_3 = 1.0 \quad (3.21)$$

where (x_1, y_1) , (x_2, y_2) , (x_3, y_3) are the Cartesian image coordinates of the three vertices of the triangle and (L_1, L_2, L_3) are the triangular local coordinates of point Q in the range 0.0 to 1.0. L_1 represents the relative distance between Q and the side 2-3 of the triangle which is opposite to vertex 1. It follows that $L_1 = 1.0$ if Q coincides with vertex 1 and $L_1 = 0.0$ if Q lies on side 2-3. Furthermore all points Q which lie on a line parallel to 2-3 have the same L_1 coordinate. Similar relationships hold for L_2 and L_3 . The local coordinates uniquely specify

Geometric merging.

For each triangle on the Earth's surface:

Project the three 3D object space vertices to the SAR image.

Create triangle on SAR image with the projected (pixel) 2D coordinates.

Project the three 3D object space vertices to optical image.

Create triangle on optical image with the projected (pixel) 2D coordinates.

For each pixel p^S in the SAR triangle:

Compute local coordinates L_i for point p^S .

Compute pixel p^O on the optical image using same L_i .

Points p^S and p^O are correspondent.

End for.

End For.

End.

Figure 3.6: Geometric merging algorithm.

the relative position of a point on the triangle with respect to its vertices. It follows that a point p^S on the triangle of the SAR image which is defined by local coordinates L_1, L_2, L_3 corresponds to a point p^O on the triangle of the optical image defined by the same local coordinates L_1, L_2, L_3 :

$$p^S = (x_P^S, y_P^S) = (L_1x_1^S + L_2x_2^S + L_3x_3^S, L_1y_1^S + L_2y_2^S + L_3y_3^S) \quad (3.22)$$

$$p^O = (x_P^O, y_P^O) = (L_1x_1^O + L_2x_2^O + L_3x_3^O, L_1y_1^O + L_2y_2^O + L_3y_3^O) \quad (3.23)$$

In order to find the correspondent point on the optical image given a specific point on the SAR image, the following procedure is used:

$$(x_P^S, y_P^S) \rightarrow (L_1, L_2, L_3) \rightarrow (x_P^O, y_P^O) \quad (3.24)$$

Equation 3.24 implies that the local coordinates L_1, L_2, L_3 are computed given the image pixel coordinates, or that Equations 3.21 are inverted:

$$\begin{bmatrix} x \\ y \\ 1 \end{bmatrix} = \begin{bmatrix} x_1 & x_2 & x_3 \\ y_1 & y_2 & y_3 \\ 1 & 1 & 1 \end{bmatrix} \begin{bmatrix} L_1 \\ L_2 \\ L_3 \end{bmatrix} \quad \text{or} \quad \begin{bmatrix} L_1 \\ L_2 \\ L_3 \end{bmatrix} = \begin{bmatrix} x_1 & x_2 & x_3 \\ y_1 & y_2 & y_3 \\ 1 & 1 & 1 \end{bmatrix}^{-1} \begin{bmatrix} x \\ y \\ 1 \end{bmatrix} \quad (3.25)$$

Equations 3.22, 3.23, 3.24 and 3.25 are applied to all pixels of all the triangles which are defined on the Earth's surface by a DTM or a DSM (or a triangulated DEM). The method is summarised as in Figure 3.6.

The method is very general as it can:

1. convert the optical image to the side-looking slant range geometry of the SAR image.
2. convert the SAR image to the projective geometry of the optical image.
3. convert the SAR or optical image to the XY – plane plane and thus geometrically correct the images.
4. convert object space data to the side-looking slant range geometry of the SAR image or to the projective geometry of the optical image, and thus make simulated SAR or optical images.
5. generally convert object space data, SAR data or optical data to arbitrary geometry, by converting the coordinates of the target triangle (x_P^S, y_P^S in Equation 3.24) by an arbitrary transformation.

3.3.2 Radiometric merging

Merging of a multispectral optical and a SAR image is the process of creating a new image which has the radiometric or spectral information of both. The new image may have the geometry of either the optical or the SAR image, or a new geometry such as the orthorectified geometry. As an interesting example, the imaging geometry of the SAR image is maintained, and the multispectral information (colour) of the optical image is merged with the intensity of the SAR image. The method is quite general as any multispectral image can be used, such as thermal image.

The colour of the optical image is completely unrelated to the gray shade of the SAR image, as the former records the visible wave lengths while the latter records microwave lengths which can not be perceived by the human eye. Furthermore, the optical image records the backscattered physical light of the sun, while the SAR image records the backscattered radiation which has been transmitted by the SAR sensor itself. Thus the fusion of optical and SAR images produces an image of higher quality since it combines the different information of the two images.

The colour can be thought of as the combination of two concepts. The first concept is the intensity or the brightness of the colour, and the second is the

chromaticity or the identification of the colour. Chromaticity is the property of the colour that lets us distinguish between two colours of the same brightness. The colour of the optical image pixels is given in (or can be converted to) the RGB space, where the colour is represented as a linear combination of three basic constituent colours (Red, Green, Blue). The intensity of each pixel colour is (or can be converted to) an integer number between 0 and 255 (R, G, B), where 0 is the darkest and 255 the brightest. The overall intensity of the pixel colour is the sum of the intensities of the constituent colours (R, G, B):

$$I = R + G + B \quad (3.26)$$

Then the chromaticity of the colour of the pixel is defined as:

$$R_c = \frac{R}{I}, \quad G_c = \frac{G}{I}, \quad B_c = \frac{B}{I} \quad \text{where} \quad R_c + G_c + B_c = 1 \quad (3.27)$$

Equation 3.27 shows that chromaticity is essentially two dimensional. However, the response of the human eye to colour is not linear with respect the wave length of the colour, and thus it perceives different colours with different intensities. The subjective (to the human eye) intensity of an RGB colour is (Niblack [1985]):

$$I = 0.299R + 0.587G + 0.114B \equiv I^* \quad (3.28)$$

Then the subjective chromaticity is found by Equation 3.27 where I is given by Equation 3.28.

The SAR image is available as grayscale colours, or as shades of gray. The intensity (I^*) of the gray shade of the SAR pixels is (or can be converted to) an integer between 0 and 255, where 0 is the darkest (black) and 255 the brightest (white). The overall intensity of the pixel is the intensity of the gray shade itself. The distribution of the (gray) intensities I^* of the SAR image pixels is what makes the SAR image appear what it is. In other words the information of the SAR image is encoded as the distribution of the intensities of its pixels. Thus, the intensities of the pixels should not be changed by the merging method. The merging method should only affect the chromaticity of the pixels. Each pixel of the new merged image can be computed as:

$$R^* = R_c I^*, \quad G^* = G_c I^*, \quad B^* = B_c I^* \quad (3.29)$$

where R_c, G_c, B_c is the chromaticity of the corresponding pixel in the optical image computed by Equations 3.27. From Equations 3.27, 3.28 and 3.29 we conclude that the intensity of the merged pixels is:

$$I = 0.299R^* + 0.587G^* + 0.114B^* = I^* \quad (3.30)$$

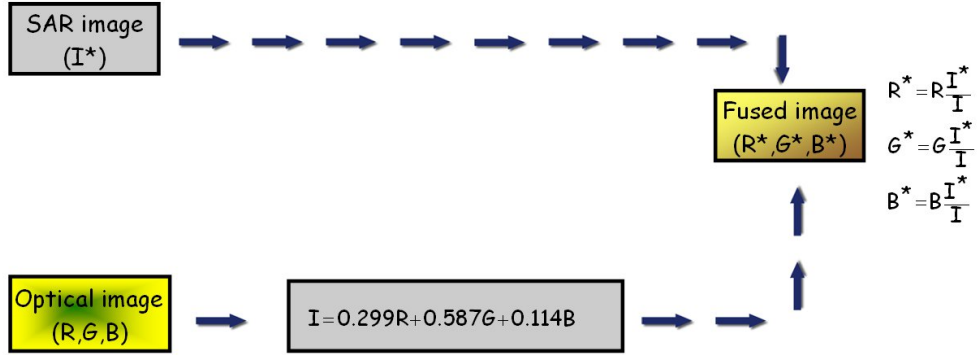


Figure 3.7: Radiometric Fusion.

which shows that Equation 3.29 does not affect the intensity of the SAR image, while it introduces the chromaticity of the optical image (Figure 3.7).

It must be noted that a pixel in the SAR image does not correspond to a single pixel in the optical image. The images are of different size (number of pixels in the x and y direction), and are probably rotated with respect to each other. Even if they are not, the resolution (pixels/m) of both images varies. Furthermore the way that the resolution varies is different for the optical and the SAR image, as they are based on completely different geometries. The inconsistencies could be remedied by geometrically correcting both images to the same resolution, size and position. However this would introduce error in both SAR and optical image by the geometric correction process. Furthermore, if the optical image were already geometrically corrected but of different resolution/position, more error would be introduced. The geometric correction of both images would also double the computational effort. In contrast, the present method does not alter the information of the SAR image (the pixel intensity) at all. The chromaticity of a SAR pixel is computed as the bicubic interpolation of the chromaticity of the pixels of the optical image, which surround the position of the projection of the SAR pixel to the optical image (Mikhail et al. [2001]).

3.4 Overview and contribution

In this Chapter (*Chapter 3*) the following novel concepts and methods were introduced, each of which provides one or more contributions to surveying engineering:

- The concept of using FFLFs as GCI (GCLFs).
- The concept of the co-registration of not geometrically corrected SAR im-

ages with other data types through 3D-2D projective scene-to-model co-registration (not simply 2D-2D image-to-image transformations).

- The direct georeferencing of TerraSAR-X images using orbital data and other meta data provided by the operator and without using any kind of GCI.
- The geometric correlation of not-geometrically-corrected heterogeneous images.
- The radiometric merging of not-geometrically-corrected heterogeneous images.

Chapter 4

Validation and evaluation - simulated tests

The methods presented in Chapters 2 and 3 are very general and can be adapted to a multitude of specific methods and practical problems. This Chapter illustrates the robustness of the methods with simulated data. FFLF matching has the ability to converge even if the FFLFs contains gross error or are completely unrelated. Simulated data shows that it converges to the best possible solution.

In all figures of this Chapter, the reference FFLF (B) appears with magenta colour, the secondary FFLF (A) (the FFLF which is going to be transformed) with cyan colour, the computed initial approximation with green colour and the result, which is FFLF (A) overlaid to (B), with black colour.

4.1 Matching single pairs of 2D FFLFs with gross error

The matching of 2D FFLFs as described in Section 2.7 is independent of the type of the transformation and in order to validate it, a transformation must be chosen.

4.1.1 Transformation

For illustration purposes, the 2D rigid similarity transformation (Equation 4.1) is employed for the matching of the simulated data sets using FFLFs as matching primitives. The 2D similarity transformation is not permissive, meaning that it can not stretch a FFLF to closely match the other, as for example the affine transformation may do. Thus the similarity transformation shows clearly any errors in the FFLFs.

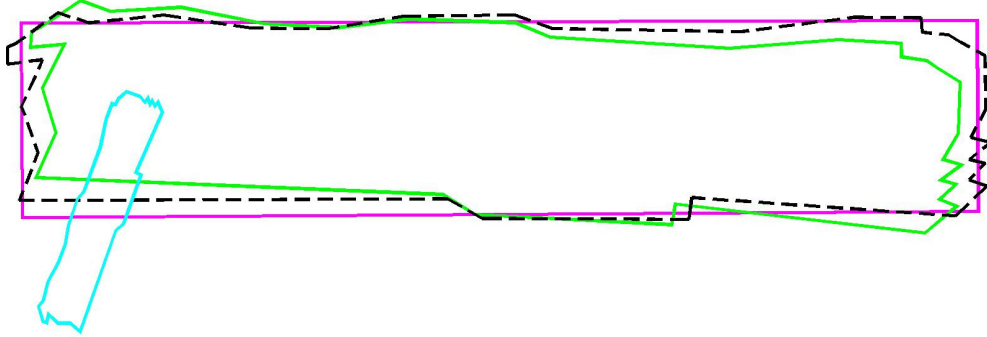


Figure 4.1: Test S1.

The 2D rigid similarity transformation considers two translations X_o, Y_o , a rotation ϕ and a scale μ between the data sets to be matched:

$$\begin{aligned} x &= X_o + \mu(X \cos \phi + Y \sin \phi) = (\mu \cos \phi)X + (\mu \sin \phi)Y + X_o \\ y &= Y_o + \mu(-X \sin \phi + Y \cos \phi) = (-\mu \sin \phi)X + (\mu \cos \phi)Y + Y_o \end{aligned} \quad (4.1)$$

Since the matching method computes a large number of interpolated points between the two FFLFs, the system of equations is overdetermined and the LSA is employed in order to solve it. The transformation is non-linear but can be turned into a linear one by setting $a = \mu \cos \phi$ and $b = \mu \sin \phi$:

$$\begin{aligned} x &= X_o + ax + by \\ y &= Y_o - bx + ay \end{aligned} \quad (4.2)$$

4.1.2 Initial approximation

The matching method needs an initial approximation (Section 2.9) when the FFLFs are not pre-aligned. The rigid approach (Section 2.9) is suitable for the 2D similarity transformation. The rotation is approximated with the exhaustive search approach (Section 2.9.3.3), as it is the most robust.

4.1.3 Tests

In tests S1, S2 and S3 (Figures 4.2, 4.3 and 4.1 respectively), FFLF (A) contains gross errors with respect to reference FFLF (B). The method made the best possible match (black and magenta). Furthermore, cyan FFLF (A) is transferred, rotated and scaled beyond recognition, but the initial approximation through the rigid approach brought it close enough (green) to trigger ICP convergence.

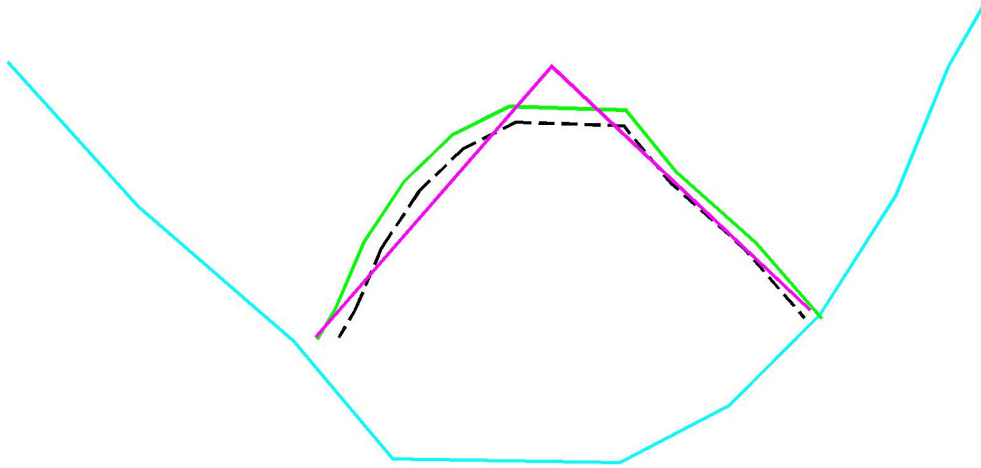


Figure 4.2: Test S2.

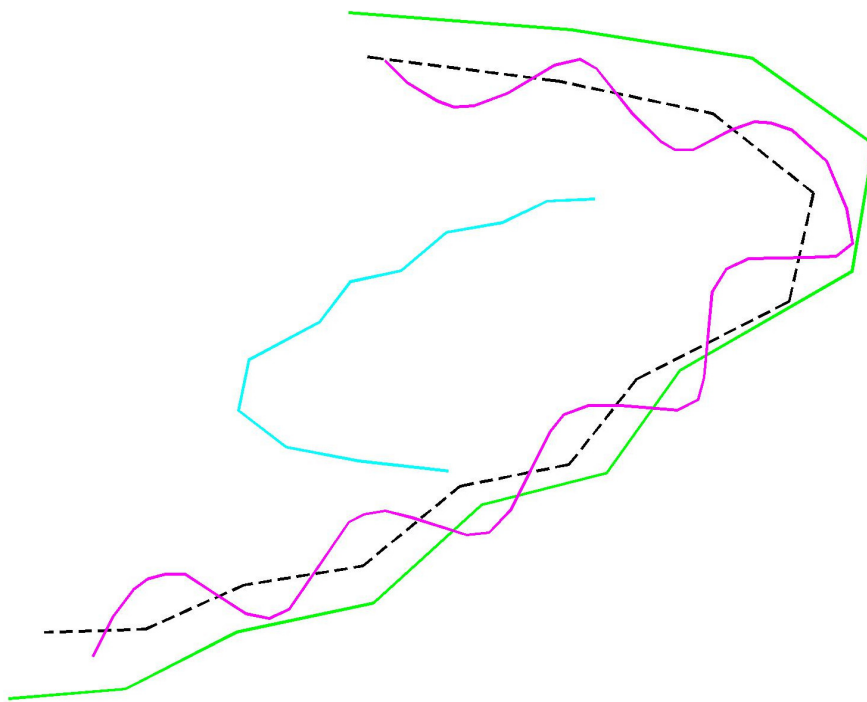


Figure 4.3: Test S3.

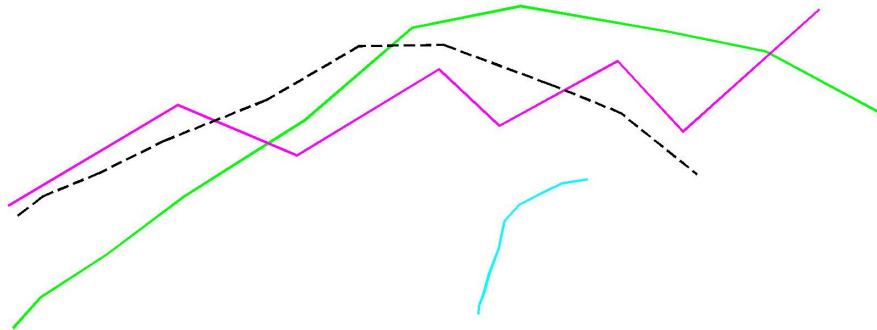


Figure 4.4: Test S4.

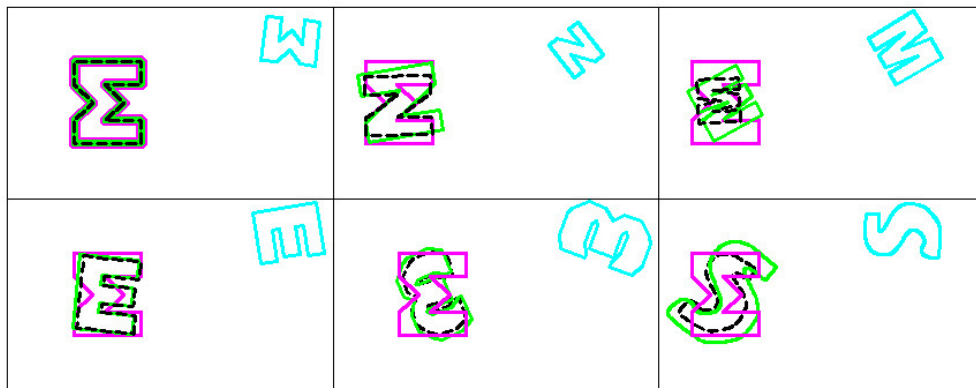


Figure 4.5: Test S5.

4.2 Matching single pairs of unrelated 2D FFLFs

Tests S4 and S5 (Figures 4.4 and 4.5 respectively) test the robustness of the method. The type of transformation is again the 2D similarity transformation (Section 4.1.1) and the initial approximation is done using the rigid approach (Section 4.1.2).

In test S4, FFLF (A) contains even greater error than in test S3, and in fact it is completely unrelated to reference FFLF (B), but the method managed to match them in the best possible way (black and magenta), as compared to manual matching tries.

In test S5, FFLFs which represent letters of the alphabet are matched. Letter Σ was matched successfully with itself (RMSE=0), while with other letters or digits (E, N, 3, M, ς) the method managed to converge and locate the slightest resemblance between them. The RMSE was much larger than zero, which hints

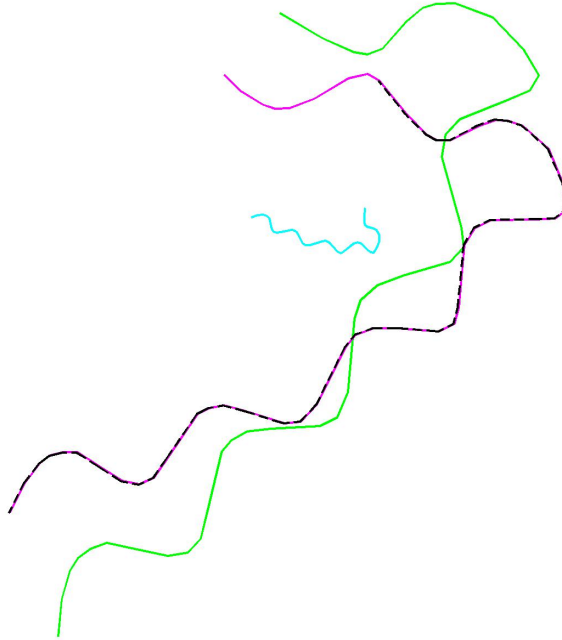


Figure 4.6: Test S6.

that the method could be used by computer vision.

4.3 Partial matching single pairs of 2D FFLFs

Tests S6 and S7 (Figures 4.6 and 4.7 respectively) test the robustness of the method when the overlap of the FFLFs is less than 100% (partial matching). The type of transformation is again the 2D similarity transformation (Section 4.1.1) and the initial approximation is done using the rigid approach (Section 4.1.2).

In test S6, FFLF (A) contains no error but overlaps about 90% with the reference FFLF (B). The overlap is sufficient for the initial approximation approach to bring the FFLFs close enough to trigger ICP convergence, and produce excellent partial matching.

In S7, the overlap of the FFLFs is too small, about 25%, for the initial approximation approach to work. However, when cyan FFLF (A) was brought manually near to the magenta reference FFLF (B), the method produced excellent partial matching.

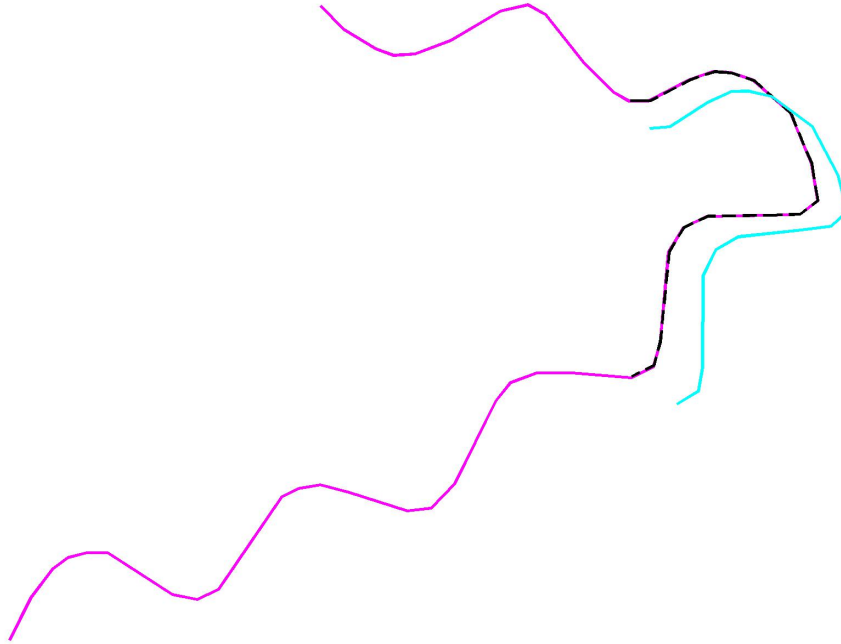


Figure 4.7: Test S7.

4.4 Matching single pairs of FFLFs of different dimensionality

The matching of 3D and 2D FFLFs as described in Section 2.8 is independent of the type of the projective transformation and in order to validate it, a projection must be chosen.

4.4.1 Projective transformation

For illustration purposes, the polynomial projection of the first order (Equation 4.3) is employed for the matching of the simulated data sets using FFLFs as matching primitives. Compared to other projections such as the rational polynomial projection, the first order polynomial projection is the least permissive, meaning that it does not stretch a FFLF too much, in order to match it with the other. Thus it shows more clearly any errors in the FFLFs.

$$\begin{aligned} x &= L_0X + L_1Y + L_2Z + L_3 \\ y &= L_4X + L_5Y + L_6Z + L_7 \end{aligned} \tag{4.3}$$

Since the matching method computes a large number of interpolated points be-

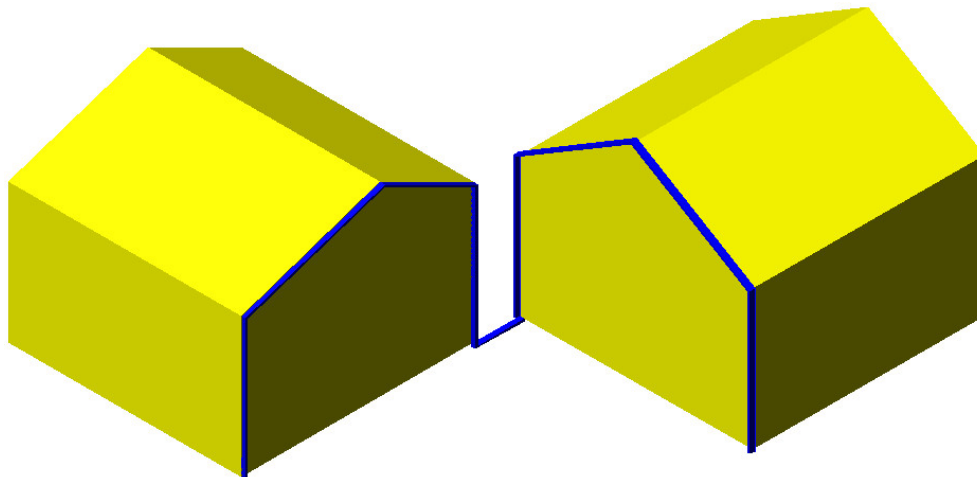


Figure 4.8: Test S8 - 3D FFLF.

tween the two FFLFs, the system of equations is overdetermined and the LSA is employed in order to solve it.

4.4.2 Test

In test S8 a simulated 3D FFLF and a simulated 2D FFLF were matched. The 3D FFLF is the outline of edges of two houses (Figure 4.8). The 2D FFLF was created by projecting the 3D FFLF using the Equation 4.3 for some values of the coefficients L_i , where x, y are the coordinates of the projected FFLF and X, Y, Z are the coordinates of the 3D FFLF. Both FFLFs were represented with 37 nodes. The length of the 3D FFLF is 24.2 m. A known first approximation of the coefficients L_i produced an initial approximation of the projected 3D FFLF (Figures 4.9 and 4.10).

The algorithm was run twice. In the first run the 2D reference FFLF had no errors. The results are presented in Figure 4.9, where it can be seen that the matching is perfect, as it was expected. In the second run, artificial random error of $\text{RMS}=0.20\text{m}$ was introduced in the projected coordinates. The results are presented in 4.10, where it can be seen that the matching is very good. The RMS error of the matching was 0.07m .

4.5 Overview and contribution

In this Chapter (*Chapter 4*) the general methods presented in Chapters 2 and 3 were tested with simulated data. The transformations (2D similarity and poly-

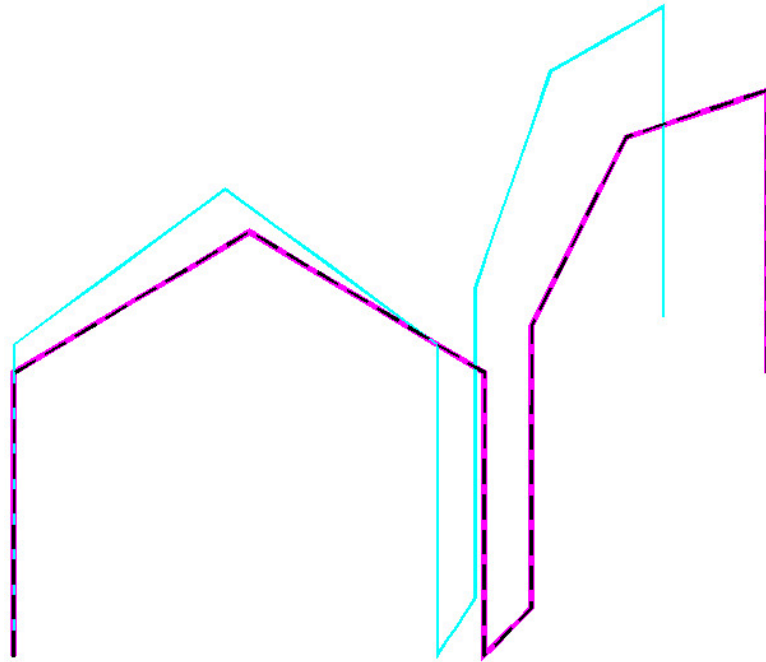


Figure 4.9: Test S8 - 3D-2D matching with no error.

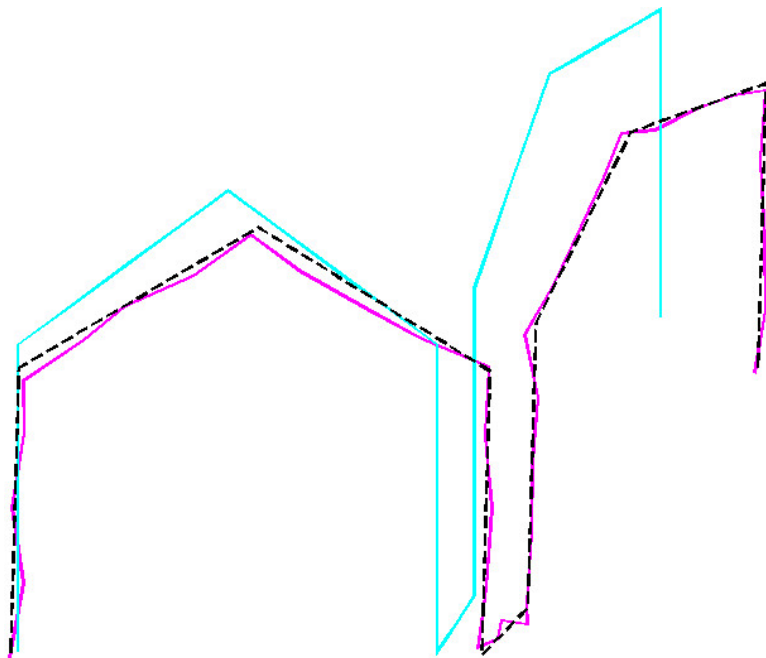


Figure 4.10: Test S8 - 3D-2D matching with artificial error.

nomial projection of first order) where chosen so that errors are not cancelled out by the adaptability of the transformations. The 2D-2D and 3D-2D matching as well as the initial approximation (rigid approach) were tested with simulated data designed to push the methods to the limits. The results showcase the robustness of the methods. The practicality of the methods was shown by testing the limited, but necessary partial matching capabilities of the methods.

Chapter 5

Application to real world problems Validation and evaluation

In this Chapter the general methods presented in Chapters 2 and 3 are applied to real world problems with real world data. Problems in the framework of 2D-2D, 3D-2D, 3D-3D FFLF matching of single pair or networks of FFLFs are solved. The general methods are subclassed (adapted) to the specific problems by choosing the dimensionality, the transformation model, the initial approximation method, single pair or network of FFLFs, and the correspondence method. The evaluation of the results of each problem is also the validation and evaluation of the general methods. The accuracy achieved in all problems is exceptional.

5.1 Registration of 2D FFLFs Extracted from high resolution satellite imagery

The process of image registration intends to geometrically match two or more images captured from different viewpoints (multiview analysis), at different time (multitemporal analysis), with different sensors (multimodal analysis), or to match images to existing models (scene-to-model registration). The applications are countless and cover computer vision, medical imaging, photogrammetry and remote sensing, inspection and quality control of manufactured parts, security monitoring. A lot of work has been done for automatic extraction of linear features from high resolution data, especially optical and RADAR imagery. At the same time, such linear features are gaining interest over point features in many photogrammetric procedures, such as orientations and triangulations, because man-made environment is rich of linear features, linear features can be detected more easily and more reliably than points and matching of linear features is often more reliable than point matching. In this Section a method for registering imagery

using linear features is presented. Since the automatic extraction of linear features is done independently for each image, registration based on linear features is independent to radiometric characteristics, bands and resolution. In fact it can be used with images captured from different sensors. This Section is orientated towards the registration of 2D FFLFs, such as roads, pipelines and railway lines, extracted from satellite images and/or topographic maps, for photogrammetric and remote sensing applications. The matching of the FFLFs is based on the Iterative Closest Point Algorithm and the Least Squares Adjustment (LSA). Implementation of the idea has been further incorporated in an open source CAD and has been tested with real world data of an urban area.

In this Section a recent high resolution satellite image is registered to a 40 years old archived topographic map. The 2D rigid similarity transformation (Equations 4.1 and 4.2) is employed for the registration of the data sets using FFLFs as matching primitives. The area of study is small part of the satellite image over a flat area and thus it is one of the very few cases where a 2D transformation can be used for the registration. The method implements, validates and evaluates the performance of the general ICP-based matching method (Section 2.7) for single pairs of FFLFs of the same dimensionality (2D-2D).

5.1.1 Data sets

The data sets of this study are:

1. a recent high resolution satellite QuickBird optical image with a pixel size of 0.63 m) (Figure 5.1).
2. a 40 years old medium scale (1:5 000) archived topographic map (Figure 5.1).

The study site is located in a sub-urban area of Athens, Greece, near the new international airport. For the connection of the airport with the city of Athens, a highway has been constructed as well as an expansion of the metropolitan and the sub-urban train. As a result, this area has had tremendous development for the last decade, and the available map and the image exhibit few common features. The main category of these common features are roads (Figure 5.1). These roads were used as matching primitives for the registration.

5.1.2 Application and results

The map was scanned with a 400 DPI resolution and it was imported to CAD software, where it was corrected from the errors due to the paper copy contractions/expansions, and it was transformed to the new national geodetic reference



Figure 5.1: Medium scale 40 years old paper map (left) and recent satellite optical image (right).

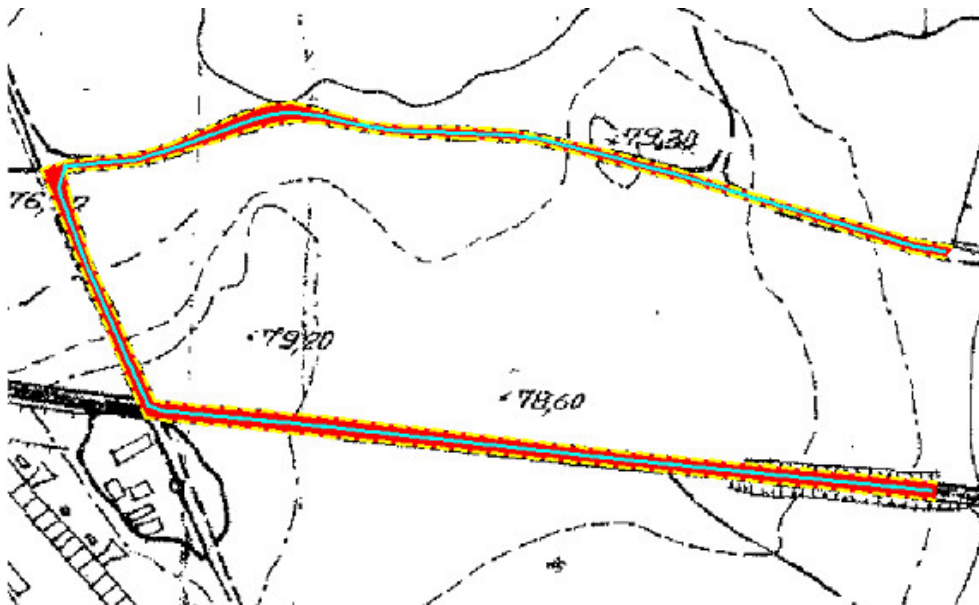


Figure 5.2: Map: road edges (yellow), road centreline (cyan).

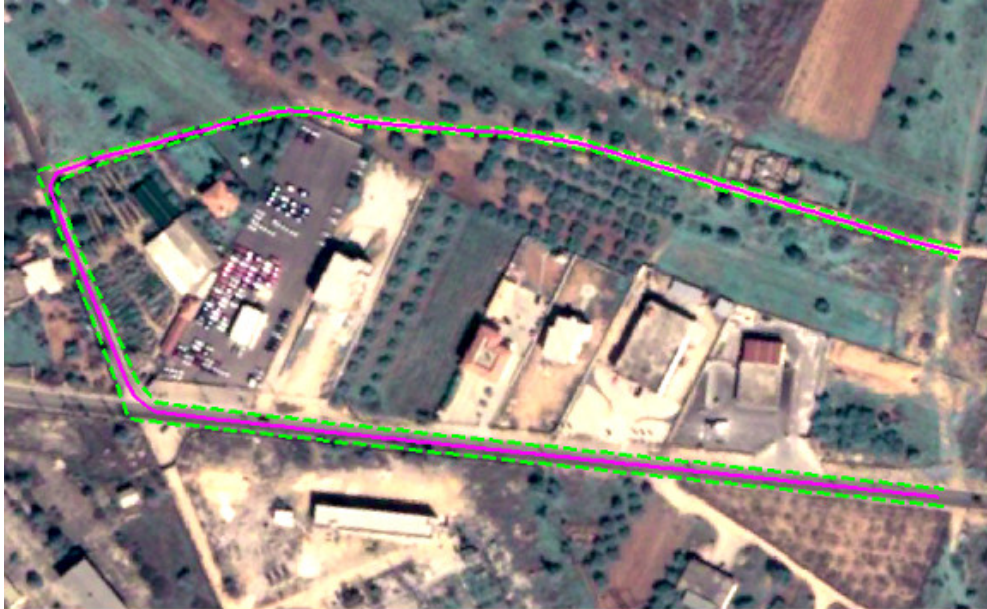


Figure 5.3: Image: road edges (green), road centreline (magenta).

system. The road edges extraction was done manually, by digitising the lines appeared on the map. Then the road centreline was calculated from the edges (Figure 5.2). The image was imported to CAD software too, where it was roughly georeferenced. The road edges extraction was done semi-automatically, by hand-digitising the lines appeared on the image after applying Sobel filter (Figures 5.3 and 5.4). Then the road centreline was calculated from the edges. Since the extraction of road centreline was done independently for the map and the satellite image, it was necessary to have a good initial estimation for the ICP algorithm. This information was acquired by using the same reference system for the map and for the image processing. Practically that means that before the extraction of FFLFs and the registration the map the image have to be roughly pre-aligned (Figure 5.5).

The results are shown in Figures 5.5 and 5.6. As it can be seen the centrelines are virtually indistinguishable. Eleven iterations of the ICP were done until convergence was achieved. The root mean square error (RMS) of the centrelines of the first iteration was 4.57 m and the final RMSE was 0.62 m. For stability reasons, it was assumed that convergence was achieved when 3 adjacent iterations gave the same RMSE. The results are excellent as the RMSE coincides with the expected error of the satellite image.



Figure 5.4: Image with Sobel filter: road edges (green), road centreline (magenta).

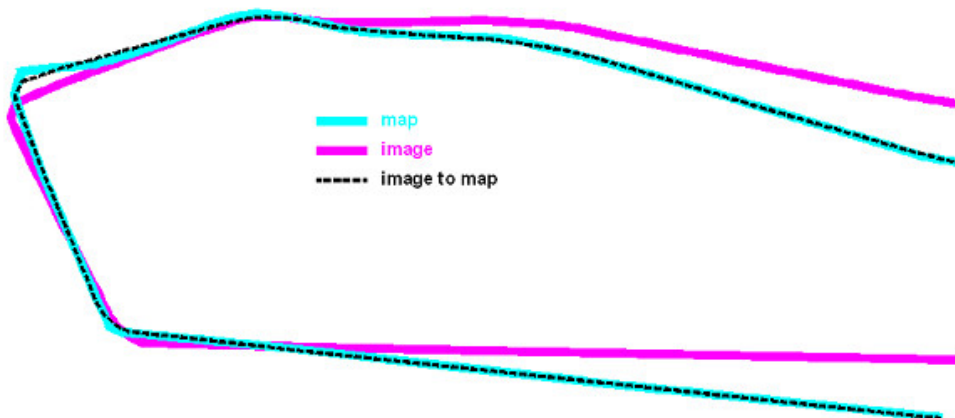


Figure 5.5: Matching results - Roughly pre-aligned Road centreline from map (cyan) and from satellite image (magenta) - Image to map transformed centreline.



Figure 5.6: Registration results - Recent satellite image registered to 40 years old map.

5.2 Geospatial Data Integration using automatic global matching of FFLFs

In this Section a method for geospatial data integration using linear features is presented. The matching of the FFLFs is based on the Iterative Closest Point (ICP) algorithm, with an extension for automated computation of the necessary initial approximation. The length is used for estimating the scale and the centroid is used for estimating the translations. For the estimation of the rotation three different approaches have been tested; the azimuth of characteristic points of the FFLF, the average azimuth angle of the whole FFLF, and an exhaustive search of all possible rotations.

The 2D rigid similarity transformation (Equations 4.1 and 4.2) is employed for the integration of 2D vector data and a geometrically corrected satellite image. The matching of 2D FFLFs is performed as described in Section 2.7. The method implements, validates and evaluates the performance of the rigid initial approximation for the ICP-based matching method of single pairs of FFLFs (Section 2.9), and three approaches for the rotation approximation (Sections 2.9.3.1, 2.9.3.2 and 2.9.3.3).



Figure 5.7: Study area on the vector data (left) and on the recent satellite optical image (right).

5.2.1 Data sets

The data sets of this test are:

1. a geometrically corrected satellite QuickBird optical image with a pixel size of 0.63 m (Figure 5.7).
2. vector data of scale 1:1 000 (Figure 5.7).

5.2.2 Application and results

Vector data is selected as the reference, master data. The data and the results are shown in Figure 5.8. The reference FFLF which is a road centreline extracted from the vector data, appears in cyan. The FFLF to be matched which is the road centreline extracted from the satellite image, appears in magenta. The initial approximation calculated by the use of the azimuth of characteristic points, by the use of the average azimuth and by the use of the exhaustive search appears in purple, green and orange respectively. The matched FFLF, considering 2D rigid similarity transformation, appears in black.

The RMSE of the matching of the first iteration is 7.25 m for the azimuth of characteristic points, 14.39 m for the average azimuth and 7.56 m for the exhaustive search. The final RMSE is 0.41 m for all three procedures which is a very accurate result considering the accuracy of the data sets. The integrated data is shown in Figure 5.9, where it can be seen that the matching is excellent.

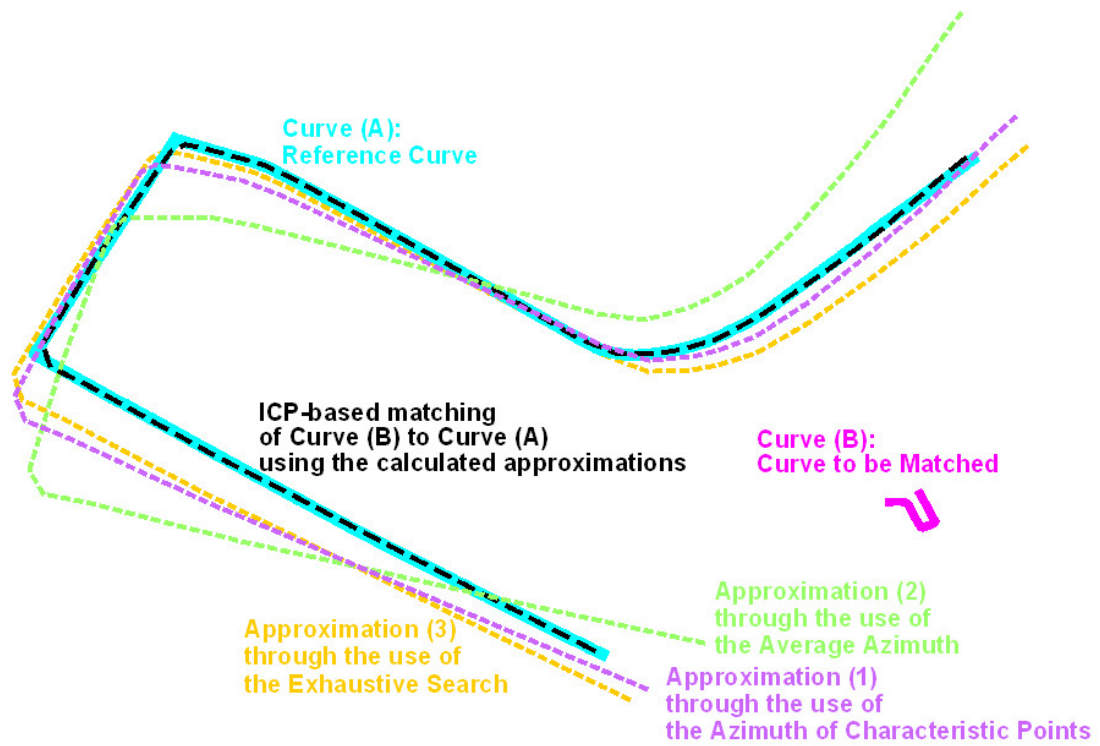


Figure 5.8: Data and matching results.



Figure 5.9: Integrated data.

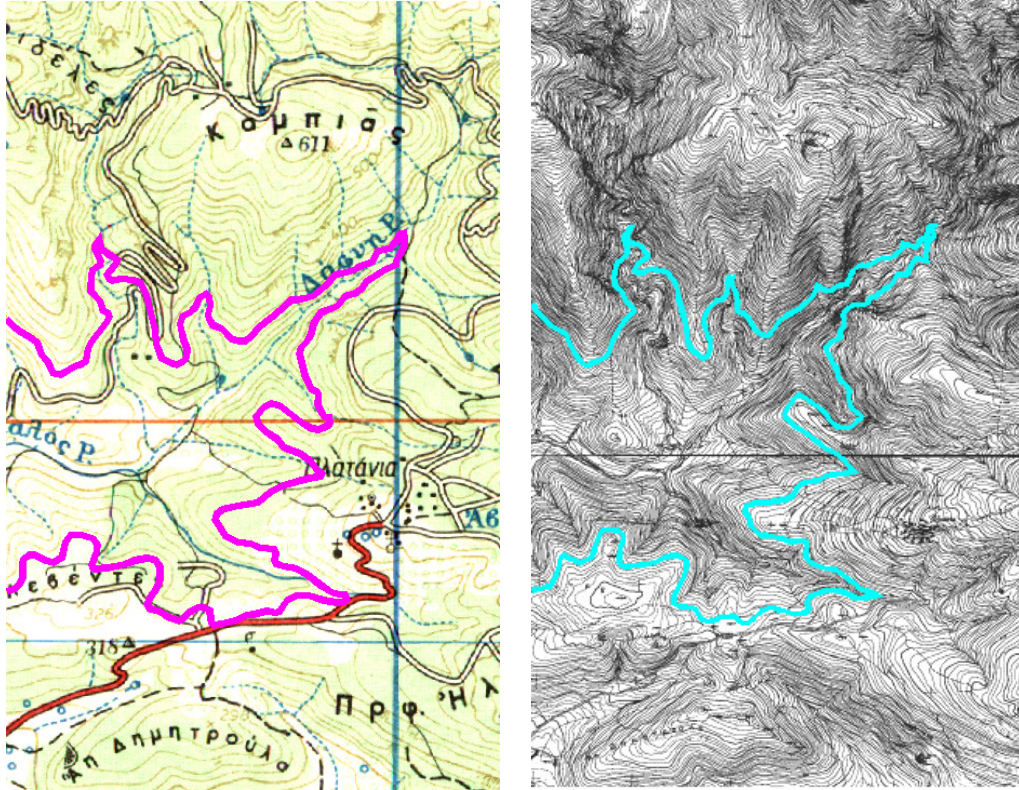


Figure 5.10: Contour lines in maps of scale 1:50 000 and 1:5 000.

5.3 Contour line matching

In this Section the contemporary problem of contour line matching (Reinoso [2011]) is faced by using two heterogeneous two-dimensional FFLFs which represent contour lines (Figure 5.10). The 2D rigid similarity transformation (Equations 4.1 and 4.2) is employed for the matching of two different maps. The method implements, validates and evaluates the performance of the ICP-based matching method of single pairs of FFLFs (Section 2.7).

5.3.1 Data sets

The data sets of this test are:

1. A small scale (1:50 000) topographic map (Figure 5.10). The accuracy of the map is about 15 m.
2. A medium scale (1:5 000) archived topographic map (Figure 5.10). The

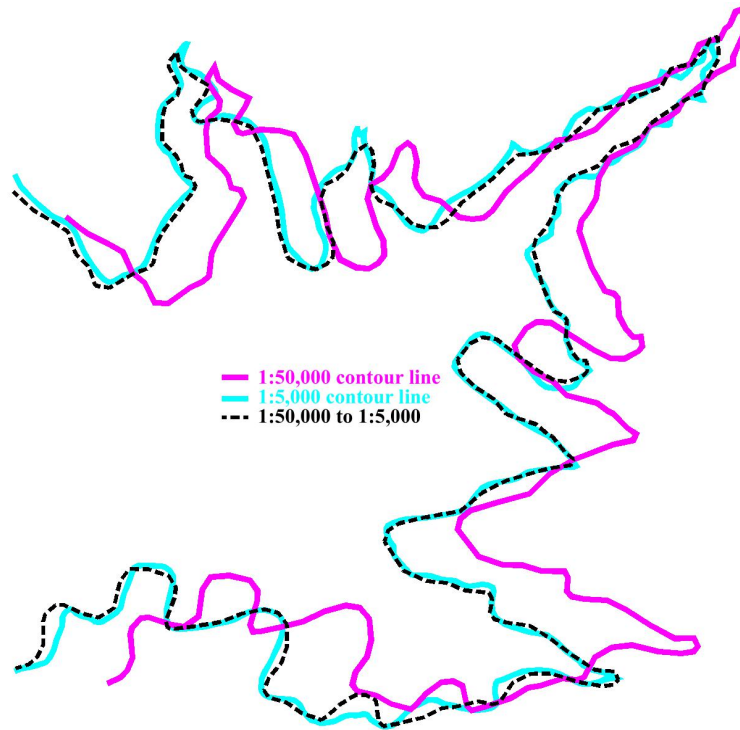


Figure 5.11: Contours line matching (2D-2D). Data (cyan, magenta) and results (black).

accuracy of the map is about 1.5 m.

5.3.2 Application and results

The magenta reference FFLF (B) was vectorised from the first map (1:50 000) and the cyan secondary FFLF (A) from the second map (1:5 000). FFLF (B) was represented with 407 nodes and (A) with 77 nodes. Their length is 10.2 Km. The differences between the two FFLFs are not visible in Figure 5.10 due to the small scale of the illustration, but they are evident in Figure 5.11 after the matching. FFLF (A) has much more detail than FFLF (B) especially where it is acutely sinuous.

The FFLFs were pre-aligned before matching. The results are presented in Figure 5.11 where it can be seen that the method produced the best possible match (black line). The RMS error of the matching was 15.97m which reflects the error of the small scale map. The error reduction in respect with the iterations can be seen in Figure 5.12.

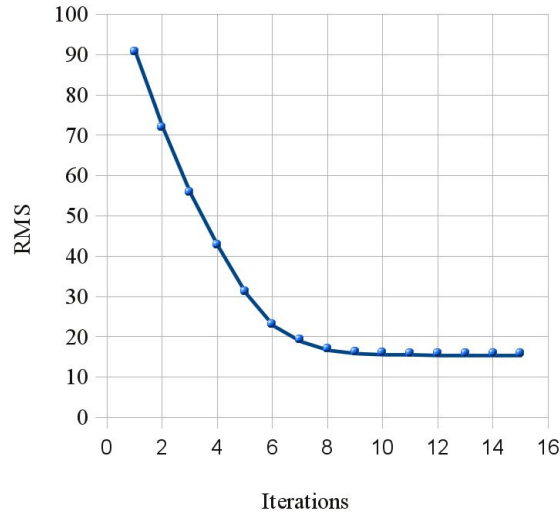


Figure 5.12: RMS error reduction.

5.4 Multitemporal Geospatial Data Integration using automatic global matching of 3D FFLFs

In this Section a method for integration of 3D geospatial data is presented. The 3D rigid similarity transformation (Equation 5.1) is employed for the integration of two maps of different scale compiled at different time. The method to match the FFLFs implements, validates and evaluates the performance of the ICP-based matching method of single pairs of 3D FFLFs (Section 2.7), and the initial approximation (Section 2.9) for 3D FFLFs (Section 2.9.3.4).

5.4.1 Data sets

The data sets of this test are:

1. A small scale (1:50 000) topographic map compiled in the 1980s (Figure 5.13). The planar accuracy of the map is about 15 m and the vertical accuracy 10 m.
2. A medium scale (1:5 000) archived topographic map compiled in the late 1960s (Figure 5.13). The accuracy of the map is about 1.5 m and the vertical accuracy 2 m.

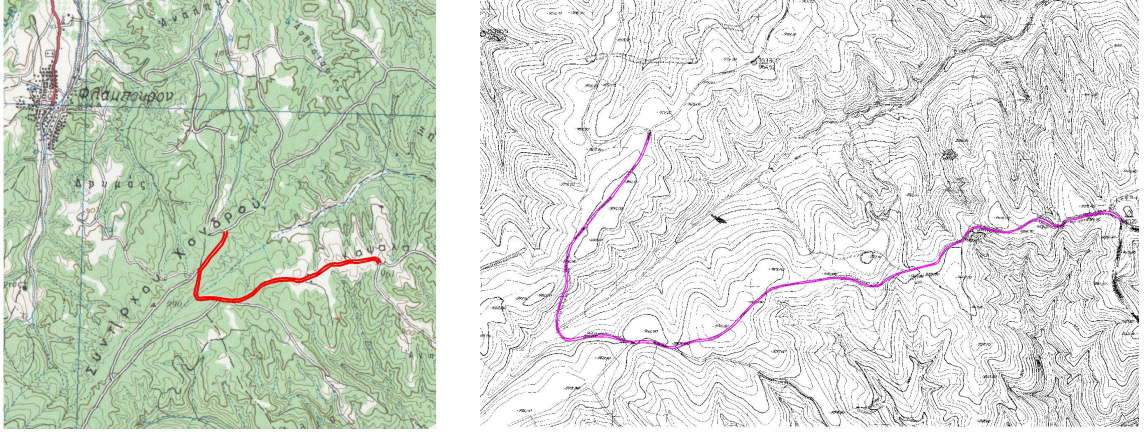


Figure 5.13: Topographic map 1:50 000 (left) and 1:5 000 (left).

5.4.2 Transformation

A 3D similarity transformation was used for the matching. It is a non-linear rigid transformation with seven unknown parameters; three translations X_o, Y_o, Z_o , three rotations ω, ϕ, κ and a scale μ :

$$\begin{bmatrix} x \\ y \\ z \end{bmatrix} = \begin{bmatrix} X_o \\ Y_o \\ Z_o \end{bmatrix} + \mu \cdot [R] \cdot \begin{bmatrix} X \\ Y \\ Z \end{bmatrix} \quad (5.1)$$

where the rotation matrix is given by:

$$\begin{aligned} [R] &= R_{\omega\phi\kappa} = [R_\omega] \cdot [R_\phi] \cdot [R_\kappa] = \\ &= \begin{bmatrix} 1 & 0 & 0 \\ 0 & \cos\omega & \sin\omega \\ 0 & -\sin\omega & \cos\omega \end{bmatrix} \cdot \begin{bmatrix} \cos\phi & 0 & -\sin\phi \\ 0 & 1 & 0 \\ \sin\phi & 0 & \cos\phi \end{bmatrix} \cdot \begin{bmatrix} \cos\kappa & \sin\kappa & 0 \\ -\sin\kappa & \cos\kappa & 0 \\ 0 & 0 & 1 \end{bmatrix} \end{aligned} \quad (5.2)$$

Since the matching method computes a large number of interpolated points between the two FFLFs, the system of equations is overdetermined and the non-linear LSA is employed in order to solve it.

5.4.3 Application and results

The cyan 3D FFLF (A) was extracted from the small scale map and represents a road of length 3.150 km. The magenta reference 3D FFLF (B) represents the same feature and was extracted from the medium scale map.



Figure 5.14: Matching results: Map 1:50 000 to map 1:5 000.

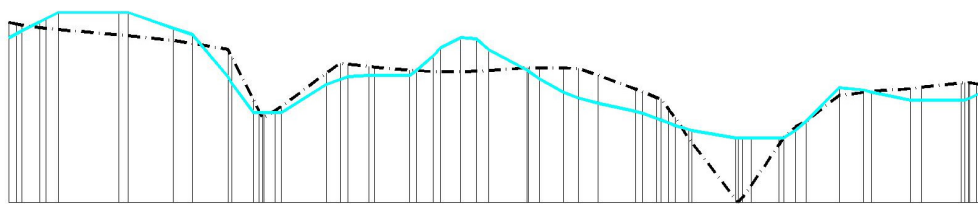


Figure 5.15: Matching results of profiles: Map 1:50 000 to map 1:5 000.

The initial approximation was computed through the rigid approach with an exhaustive search (green). The plan view and the profile view of the matched roads are shown in Figures 5.14 and 5.15 respectively. The planar RMSE of the matching was 12.6 m and the vertical error 6.7 m. The matching of the profiles is clearly the best possible one.

5.5 Registration of optical and SAR imagery by automatic free-form features global matching

Remote sensing and geoscience have undergone major improvements over the recent years. Sensors with various geometry, radiometric characteristics and resolution are now available and there is a growing demand for the complementary use of them, as well as for multi-temporal data registration and georeferencing. Under these circumstances, linear features are investigated as an alternative solution of classical point-based approaches. In this Section, a general method for the registration and the georeferencing of heterogeneous data, through FFLF matching is presented. The method has proved to be robust, efficient and accurate through tests with real data, heterogeneous, multimodal and multitemporal, such as optical and SAR images and linear maps.

Linear features have attracted the interest of the remote sensing, photogrammetric and geoscientific society during the last two decades. In contrast to solitary points, linear features carry strong and descriptive geometric information, which makes them a challenging research area for many fields and applications. The geometric exploitation of linear features has been investigated in photogrammetry and remote sensing for image orientation problems (Akav [2008], Changno and Bethel [2004], Dare and Dowman [2001], Habib and Al-Ruzouq [2004], Kubik [1988], Lee and Yu [2009], Mulawa and Mikhail [1988], Petsa [1995], Schenk [2004], Wang et al. [2008], Zalmanson [2000], Zielinski [1993]), and in geosciences for the integration of geospatial data (Butenuth et al. [2007], Kieler et al. [2009], Xiong and Sperling [2004]). It is also an active field of research in the fields of computer vision and medical imaging, among others (Huang et al. [2006], Maintz and Viergever [1998], Zitova and Flusser [2003]).

This Section contributes to this research framework of Earth sciences, by introducing a general, case independent, method for heterogeneous free-form features matching (Sections 2.7 and 2.9). Generality implies a method which can be applied to multimodal and multitemporal data, and facilitate the contemporary demand for the complementary use of different Earth Observation (EO) and GIS data types (Bellman and Hellwich [2006], Coulter et al. [2003], Inglada and Giros [2004], Le Moigne et al. [2002], Pohl and Genderen [1998], Sörgel et al. [2008], Butenuth et al. [2007]). The method is specialised to the registration of



Figure 5.16: Topographic map (right) and optical image (left).

recent optical and SAR satellite images to a small scale topographic map. Feature extraction is not discussed, as different kind of data still demand different approaches for the identification and the extraction of features.

5.5.1 Data sets

The method was implemented in Fortran, and for efficiency, convenience and user-friendliness, it was embedded into ThanCad (Stamos [2007]), a CAD program published under the GPL license. The method is tested with the following data sets:

1. A geocoded SAR image captured by the ALOS PALSAR satellite sensor. The resolution of the SAR image is 9 m and it was captured in 2007 (Figure 5.17).
2. An optical image captures by the ALOS PRISM sensor. The resolution of the optical image is 2.5 m and it was captured in 2007 (Figure 5.16).
3. A small scale (1:50 000) archived topographic map. The accuracy of the map is 15 m and it was compiled in 1987 (Figure 5.16).



Figure 5.17: SAR image.

The test area is in the greater north-eastern region of Athens, Greece. In the test, a 2D FFLF (5.2 km length) was extracted from the SAR image. The FFLF represents a shoreline, a physical feature with constant height. The FFLF was matched to the 2D FFLF representing the same feature, extracted from a small scale map. The test was repeated using the same feature extracted from the optical image. The FFLF extracted from the map was considered as the reference FFLF.

5.5.2 Projective transformations

The transformation between the object space and the optical or the SAR image is projective, but since the object space FFLF has constant elevation throughout its length, the 3D to 2D projective transformation degenerates to a 2D transformation. The first order 2D Rational PFs (RPFs) with common denominator (2D Direct Linear Transform: 2D-DLT) are employed for the registration of the data sets using FFLFs as matching primitives:

$$x = \frac{a_1X + a_2Y + a_4}{c_1X + c_2Y + 1}, \quad y = \frac{b_1X + b_2Y + b_4}{c_1X + c_2Y + 1} \quad (5.3)$$

The 2D-DLT has 8 unknown parameters and it is able to represent the non-



Figure 5.18: Matching results: SAR image to Map.

rigid nature of the SAR image. The matching method computes a large number of interpolated points between the two FFLFs, thus the system of equations is overdetermined and the LSA is employed in order to solve it. Equations 5.3 are non-linear but can be turned into linear ones by multiplying the two parts of the equations by the denominator.

5.5.3 Results

The data and the results of the matching are shown in Figures 5.18 and 5.19. The reference FFLF and the FFLF to be transformed (secondary), appear in red and cyan colour respectively. The initial approximation, which was computed through the rigid approach (Section 2.9), and the matched (final) FFLF using the selected transformation (or projection), appear in green dashed line and black dashed dot line, respectively. For illustration purposes the initial FFLFs (red and cyan) are shown together, though in reality their coordinates are completely unrelated. In

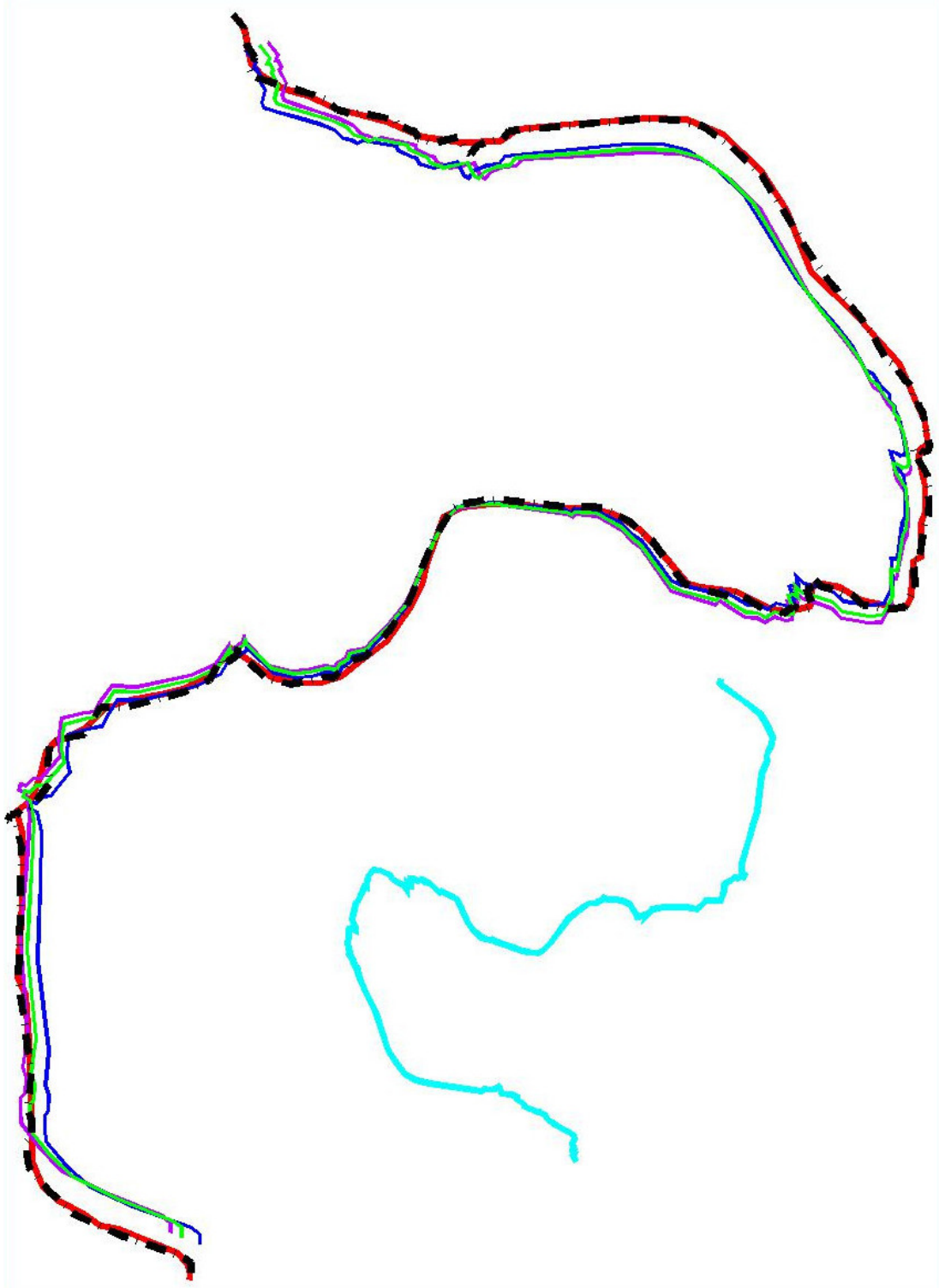


Figure 5.19: Matching results: optical image to Map.

Figure 5.18 the initial approximation is additionally computed by the use of the azimuth of characteristic points of Section 2.9.3.1 (blue dashed triple dot), and by the use of the average azimuth of Section 2.9.3.2 (magenta dashed double dot), as well as by the use of the exhaustive search of Section 2.9.3.3 (green dashed). All approximations triggered ICP convergence to the same result. The matching (dashed black) is exceptionally good as shown in Figures 5.18 and 5.19. The RMSE of the SAR image matching to the map is 12.6 m. The RMSE of the optical image matching to the map is 5.9 m.

It must be noted that the initial approximation of the SAR FFLF, computed through the rigid approach, is not very good and it only triggered ICP convergence because the problem is essentially 2D. In the case of projective transformations from 3D to 2D, the non-rigid approach (Section 2.10) should be used instead.

5.6 Enhanced initial approximation for ICP-based global matching of FFLFs in side-looking RADAR geometry

The exploitation of linear features in aerial and satellite image orientation analysis has attracted much interest, due to the advantages of linear features, as opposed to solitary points which are traditionally used in photogrammetric procedures. Linear features carry geometric information of higher quality, they can be extracted and matched more reliably, and they tend to be more stable during time. During the last decade, the Iterative Closest Point (ICP) algorithm has been introduced into various research projects, and, until recently, linear features were treated either as parametric curves, or as free-form/natural curves represented by cubic splines. Recent advances in the field show that ICP can handle linear features with an arbitrary mathematical representation, both for rigid and non-rigid transformations and for optical and SAR geometry. This Section presents an enhanced, more sophisticated single stage method for the computation of the first approximation which is one of the ICP requirements. The method is intended for ICP-based matching for the georeferencing of SAR images, using 3D linear features. The method uses the first order polynomial transformation, as an approximation to the arbitrary projection used in the SAR images. It exploits characteristic statistical properties of the FFLFs in order to compute the polynomial coefficients. Various tests performed with the Single look Slant range Complex image (SSC) captured by TerraSAR-X in High Resolution SpotLight mode (HS), show the superiority of the proposed method as opposed to the two-stage similarity initial approximation used in the past.

In this Section an enhanced, sophisticated single stage method for the com-

putation of the initial approximation for ICP-based global matching of FFLFs in side-looking RADAR geometry is presented. The method which uses the statistical moments and the length of the FFLFs as characteristic properties and which is described in Section 2.9.4, is validated and evaluated by two real world examples. The projective transformation 3D-DLT (Equations 6.11) are employed for the matching of 3D and 2D FFLFs (Section 2.8).

5.6.1 Data sets

The data sets of the tests are:

1. A recent high resolution spotlight TerraSAR-X SSC image with a pixel size of 1.0 m acquired in February 2009. The TerraSAR-X image is a High Resolution SpotLight (HS) image with single polarisation (HH); it is a Single look Slant range Complex image (SSC) (Figures 5.21 and 5.23).
2. a 40 years old medium scale (1:5 000) archived topographic map which was compiled in the 1970s with photogrammetric stereo-restitution (Figures 5.20 and 5.22).

The area of the tests is on the north east side of Athens. It is mountainous, contains some rural regions (villages and small towns) and is generally covered by sparse vegetation. During the recent forty years it has been subject to considerable development; new roads, buildings, and infrastructure in general. The terrain of the area is steep and the average slope is about 50%.

5.6.2 Projective transformation

The matching of 3D and 2D FFLFs as described in Section 2.8 is independent of the type of the projective transformation. Here, the 3D Direct Linear Transform (3D-DLT) with 11 unknown parameters is employed for the registration of the data sets using FFLFs as matching primitives:

$$x = \frac{a_1X + a_2Y + a_3Z + a_4}{c_1X + c_2Y + c_3Z + 1}, \quad y = \frac{b_1X + b_2Y + b_3Z + b_4}{c_1X + c_2Y + c_3Z + 1} \quad (5.4)$$

The matching method computes a large number of interpolated points between the two FFLFs, thus the system of equations is overdetermined and the LSA is employed in order to solve it. Equations 5.4 are non-linear but can be turned into linear ones by multiplying the two parts of the equations by the denominator.

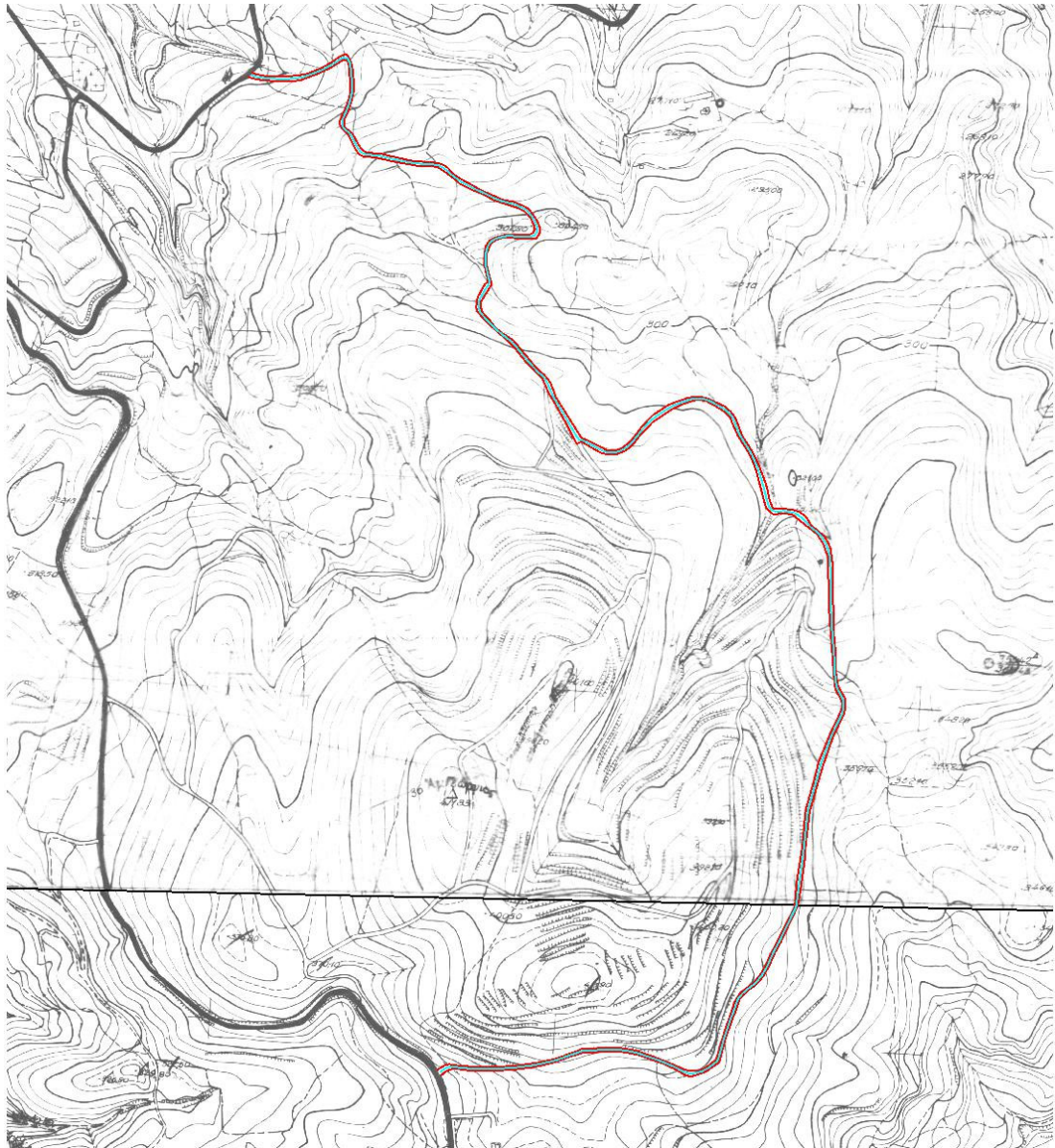


Figure 5.20: Example 1: Map road centreline (in cyan).



Figure 5.21: Example 1: SAR road centreline (in orange).

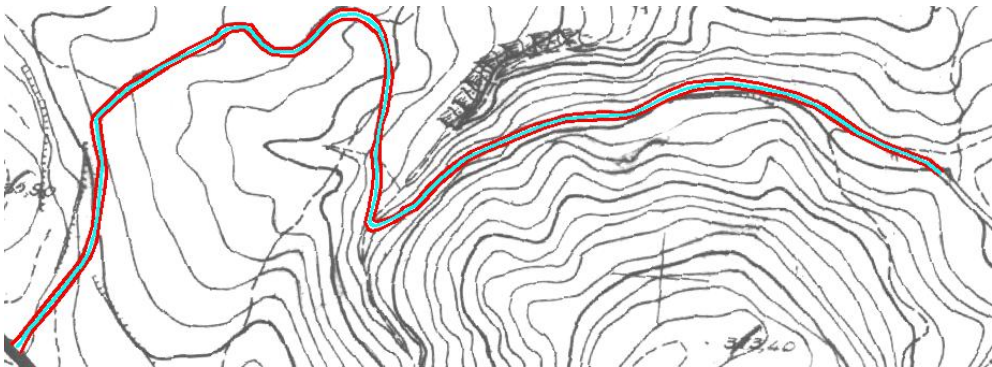


Figure 5.22: Example 2: Map road centreline (in cyan).

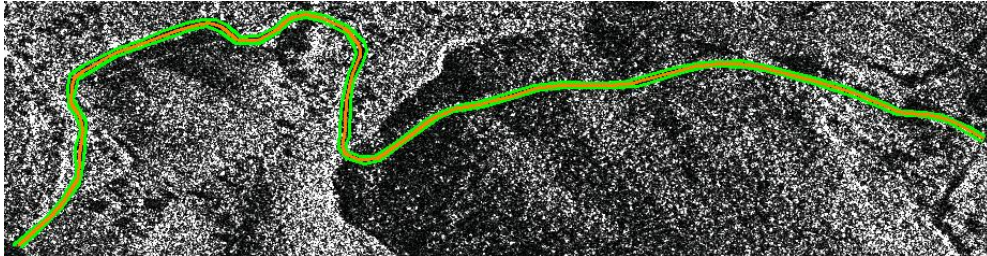


Figure 5.23: Example 2: SAR road centreline (in orange).

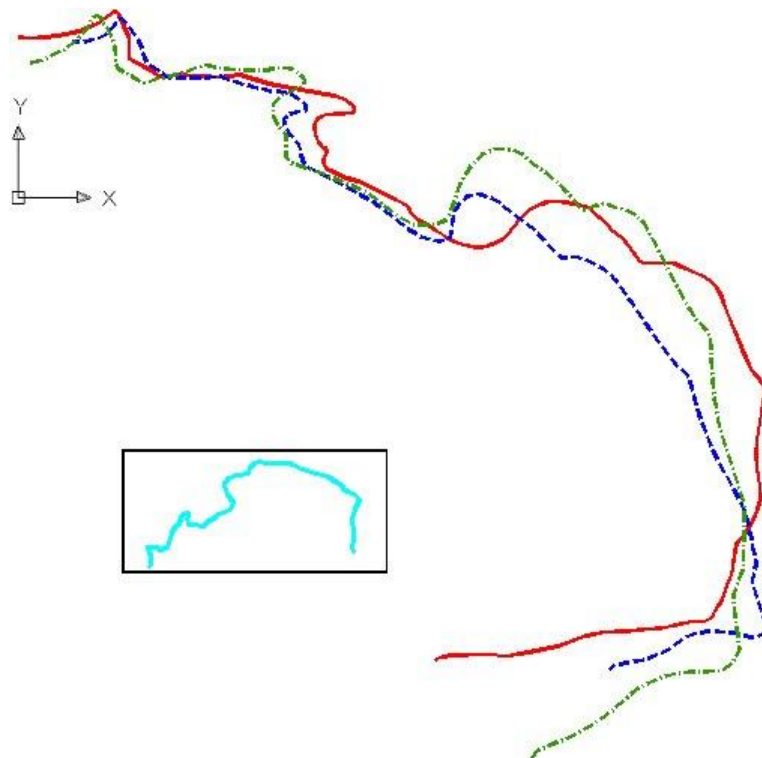


Figure 5.24: Example 1: Polynomial initial approximation (blue dashed) using 4 moments.

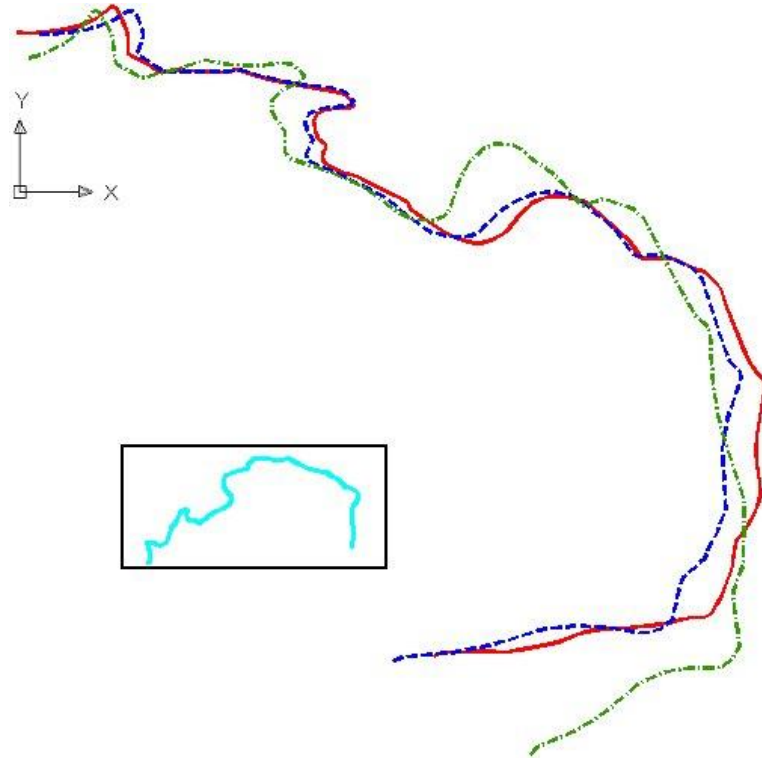


Figure 5.25: Example 1: Polynomial initial approximation (blue dashed) using 4 moments and length equation.

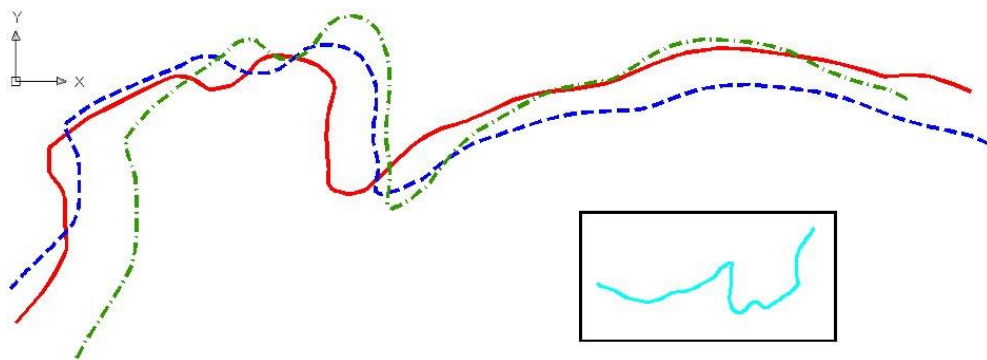


Figure 5.26: Example 2: Polynomial initial approximation (blue dashed) using 4 moments.

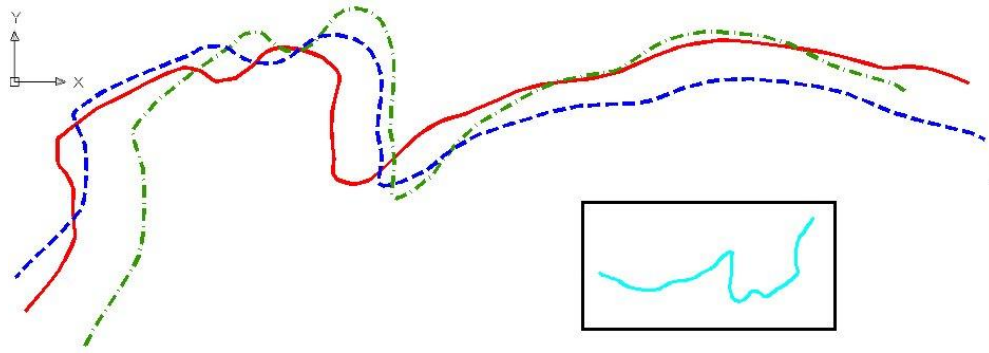


Figure 5.27: Example 2: Polynomial initial approximation (blue dashed) using 4 moments and length equation.

5.6.3 Preprocessing

Two real world examples were used in order to test the proposed method. For each of the two examples, a FFLF common to the two data sets was selected as a 3D linear feature. The FFLFs of both examples represent road centrelines (Figures 5.22 and 5.23). The 3D object coordinates refer to the Hellenic Geodetic Reference System 87 (HGRS87). The 2D SAR image coordinates refer to pixels. Thus, they are completely different and they do not fit on the same figure. For illustration purposes, a thumbnail of the 3D centreline is shown in the same figure with its 2D projections.

5.6.4 Application and results

The initial approximation of the projections of the 3D FFLFs were computed using 3–8 moment equations (Section 2.10.1), with or without the length equation (Section 2.10.2) of the non-rigid approach. A total of 12 cases were computed for each example. For each case, the RMSE of the initial approximation was computed performing a single ICP step between the initial approximation and the reference 2D FFLF on the SAR image.

The results showed that 4 moment equations gave less RMSE than 3 moment equations, but the difference of the errors was small and could not be identified in the scale of the figures. Moreover, 5 (or more) moment equations gave almost identical RMSE. For instance, in the first example:

- 3 moments and the length equations gave RMSE 44 pixels.
- 4 moments and the length equations gave RMSE 36 pixels.

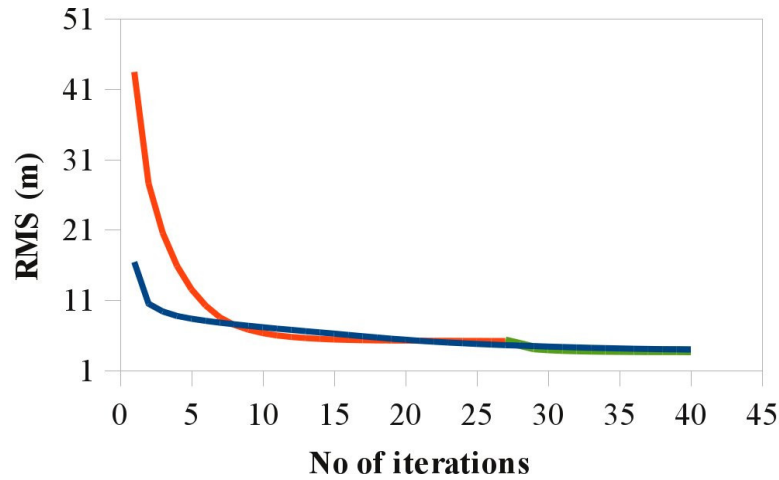


Figure 5.28: Convergence of the ICP-based matching with present method and the two stage method.

- 5–8 moments and the length equations gave RMSE no better than 33 pixels.

Thus, in the following figures the results of only two cases are shown for each example; 4 moment equations, with, and without, the length equation.

Figures 5.24 to 5.27 show the 2D SAR image coordinates. The flight (azimuth) direction is the y-axis on the figures, while the range direction is the x-axis. The distortion due to the SAR sensor of the road centreline is evident, if the SAR centreline (red) is compared to the object coordinates in the thumbnail (cyan).

In the first test (Figures 5.24 and 5.25), it is clear that the rigid nature of the similarity transformation (green-dashed) prevents it from modelling the SAR geometry as well as the polynomial transformation (blue-dashed). This is more evident in Figure 5.25, where the length equation pushes the polynomial initial approximation (blue-dashed) very close to the SAR centreline (red). In Figure 5.24, the 4 moment equations have brought the polynomial initial approximation (blue-dashed) near to the SAR centreline (red), but they have altered its length. Thus, it is impossible for the initial approximation to be close to the SAR centreline all over its whole length. The length equation remedies this side effect and brings the initial approximation (blue-dashed) very close to the SAR centreline (red), as it is shown in Figure 5.25. For illustration purposes the convergence of the ICP-based matching with the present method, versus the two stage method (Vassilaki et al. [2009b]) described in Section 6.3.2, is shown in Figure 5.28. The convergence with the present method appears with blue colour. The converge with the two stage method appears with red (1st stage) and green (2nd stage) colour.

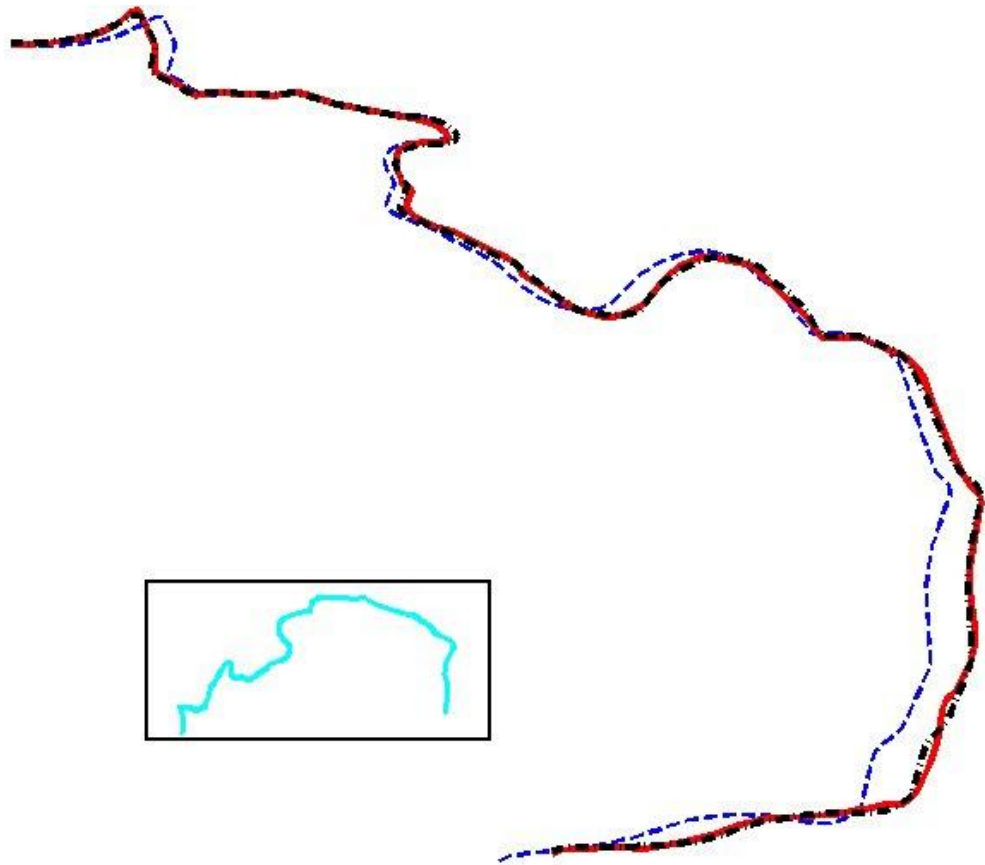


Figure 5.29: Example 1: Matched FFLFs.

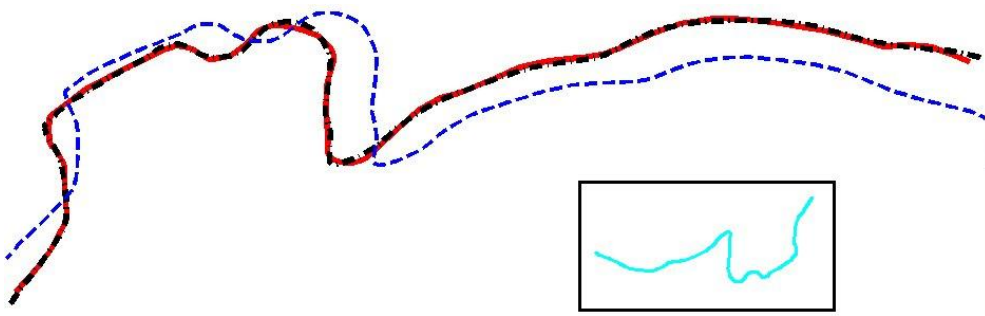


Figure 5.30: Example 2: Matched FFLFs.

In the second test (Figures 5.26 and 5.27), the polynomial initial approximation (blue-dashed) is better than the similarity initial approximation (green-dashed). This is also confirmed by the fact that ICP converges with the former but not with the latter approximation. In Figures 5.26, the 4 moment equations have brought the polynomial initial approximation (blue-dashed) near to the SAR centreline (red), but they have not altered its length as in the first example. Consequently, as it is shown in Figure 5.27, the length equation has little effect in this example. Nevertheless, it is needed in some cases, and its small computational cost justifies its use in all cases.

The initial approximation computed by 4 moments and length equations triggered ICP convergence and the FFLFs on the object space and the SAR image were matched. The matching is excellent as shown in Figures 5.29 and 5.30, where the FFLF in the object space is cyan, the FFLF in the SAR image is red, the initial approximation is blue-dashed, and the object space FFLF projected to the SAR image (matched FFLF) is black-dashed. The RMSE of the matched FFLFs is 3.7 m in the first example (Figure 5.29), and 1.4 m in the second test (Figure 5.30).

5.7 Multitemporal data registration through global matching of networks of 2D FFLFs

Multitemporal data registration, or accurate registration of images/data taken at different times, is a prerequisite procedure of significant importance in many applications concerning temporal change detection (Townshend et al. [1992], Dai [1998]), such as land cover change detection, coastline monitoring, deforestation, urbanisation, informal settlements detection, etc. A variety of change detection algorithms may be used (Chen et al. [2003]); image differencing (Castelli et al. [1998]), principal component analysis (Mas [1999]), change vector analysis (Lambin and Strahler [1994]), Markov random fields (Kasetkasem and Varshney [2002]), neural networks (Liu and Lathrop [2002]) are some of the tools that have been used.

The problem becomes more complicated when the geospatial data, that should be registered, are derived from different techniques and have various accuracies and resolutions. In recent years, the use of new instruments for surveying and mapping, such as SAR, LIDAR, GPS, and the application of novel techniques for the extraction of various products, has created the need for development of multitemporal heterogeneous data registration techniques.

In this Section a method for multitemporal heterogeneous data registration through global matching of networks of FFLFs based on the Iterative Closest Point (ICP) algorithm is presented. The method employs the 2D similarity trans-

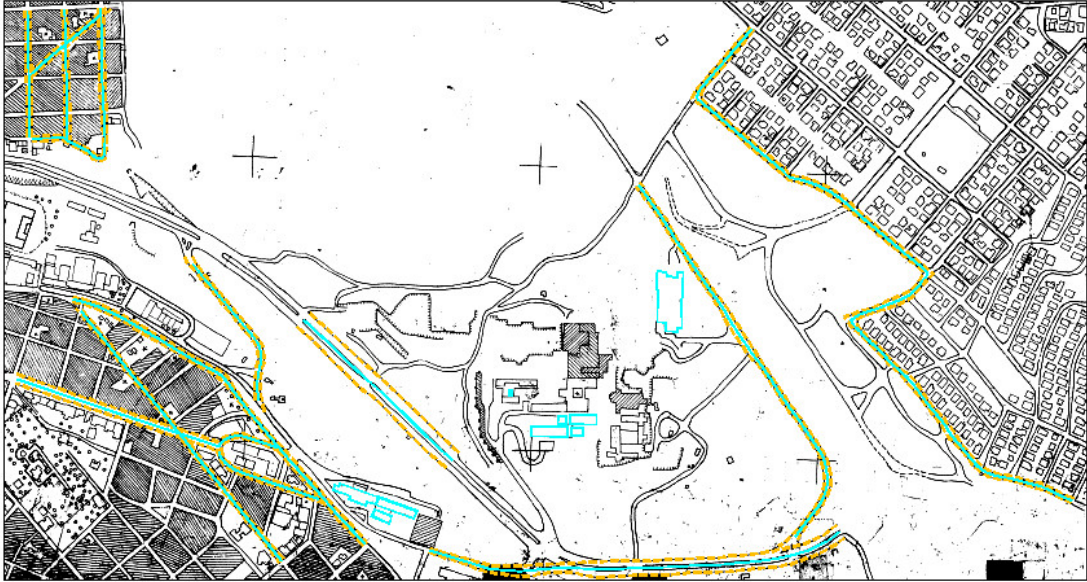


Figure 5.31: Map restituted in 1970: study area with the linear features used for the registration.

formation (Equations 4.1 and 4.2) for the matching of an optical orthoimage and a map. It implements, validates and evaluates the performance of the general ICP-based matching method for 2D networks of FFLFs (Section 2.11), and in particular the identification of FFLFs correspondences (Section 2.11.1), the unified LSA (Section 2.11.3) and minimisation of computational cost (Section 2.11.5).

5.7.1 Data sets

The data sets of this test are:

1. A geometrically corrected high resolution optical satellite image. It is an IKONOS image, with a pixel size of 1m, captured at 2000 (Figure 5.32).
2. A medium scale archived topographic map. The original map was in analogue form at a scale of 1:5 000 and it was compiled by stereo-restitution of aerial photographs, taken at 1970 or 30 years before the acquisition of the satellite image (Figure 5.31).

The study area exhibits wide temporal changes, as the most buildings of the campus and the road network were build after 1970. The available map and

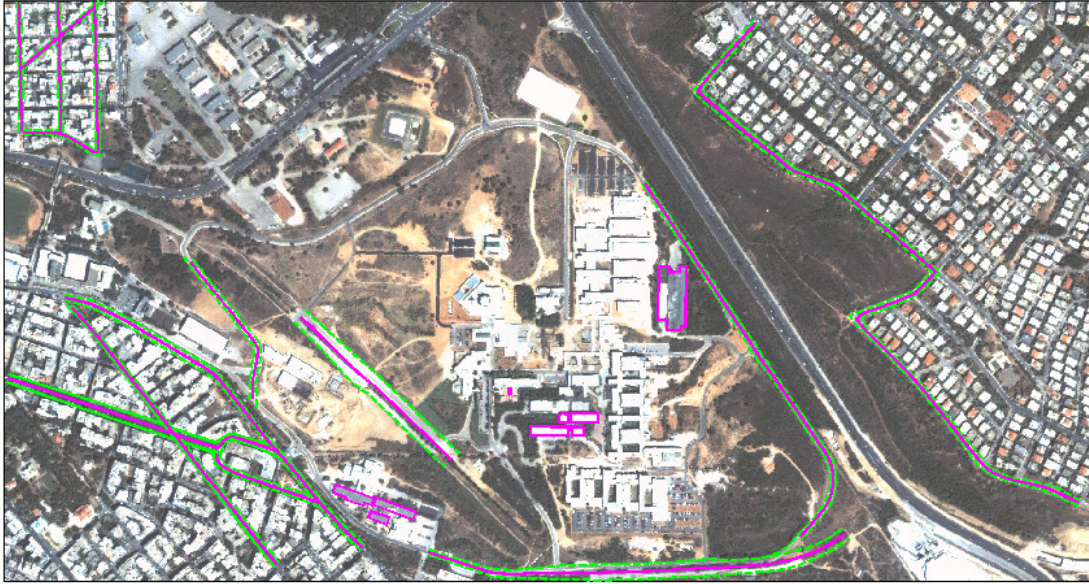


Figure 5.32: IKONOS satellite image captured in 2000: study area with the linear features used for the registration.

the image exhibit few common features. The most of these common features are roads. Some buildings can also be identified on both data (Figures 5.31 and 5.32).

5.7.2 Preprocessing

The registration of the two data was based on road centrelines and buildings' outlines. For the map, the road edges extraction and the buildings' outlines was done manually, by digitising the lines appeared on the map. Then the road centreline was calculated from the edges, through the use of skeletonisation techniques (5.31). For the orthoimage, the road edges and the buildings' outlines extraction were done semi-automatically, by hand-digitising the lines appeared on the image after applying Sobel filter. Then the road centreline was calculated from the edges, through the use of skeletonisation techniques (Figure 5.32). A preliminary registration was made by using a great number of linear features, which might be considered or seemed to be common. The selection of the features that were used finally for the application was made according to their statistical values in this solution.

Since the extraction of road centreline was done independently for the map and the satellite image, it was necessary to have a good initial estimation for the ICP algorithm. This information was acquired by using the same reference



Figure 5.33: Registration using linear features: pre-aligned data and results.

system for the map and for the image processing. Practically that means that before the extraction of FFLFs and the registration, the map and the image have to be roughly pre-aligned. Otherwise ICP does not converge.

5.7.3 Application and results

A network of 22 FFLFs were located and used for the registration, which include roads' centrelines and building outlines. In Figure 5.33 the reference network of FFLFs, which are extracted from the map, appears with cyan colour; the network to be matched, which is consisted of FFLFs from the satellite image, appears with magenta colour. For the identification of FFLFs correspondence the hybrid approach was applied (Section 2.11.1.6), which proved to give the best results. The correspondence of the 22 pairs of FFLFs (Section 2.11.1) was absolutely successful (Figure 5.34).

The matching procedure of the corresponding FFLFs was made by using the ICP algorithm; the 2D similarity transformation was used as a mathematical model for the transformation (Equation 4.1). Both techniques described in Section 2.11.5 were applied:

1. The one-step solution, using simultaneous ICP-based matching of all FFLFs.



Figure 5.34: Registration results: Recent satellite image overlaid to 30 years older map.

2. The two-steps solution; initially ICP-based matching separately for each pair of FFLFs, for improvement of the pre-alignment, and, afterwards, simultaneous matching of all FFLFs.

The final results were exactly the same in both techniques. The matched network of FFLFs appears with black dashed line in Figure 5.33. As it can be seen the centrelines are virtually indistinguishable. The final RMSE of the registration was 1.60 m, which is an excellent result; it is of the same order with the accuracy of the archived topographic map.

Comparing the results of the two techniques of Section 2.11.5 the following were observed:

1. The ICP algorithm for simultaneous matching of all 22 pairs of FFLFs converged in 23 iterations. The RMSE of the first iteration was 27.11 m and the RMSE of the last iteration was 1.60 m. In total (23x22=) 506 ICP iterations were necessary for the matching of all the 22 pairs of FFLFs.
2. In the case that the “improvement” of the pre-alignment was applied, the convergence of the simultaneous matching was made in 20 iterations, with RMSE of the first iteration 12.48 m and RMSE of the last iteration 1.60 m. The previous step of the “improvement” of the pre-alignment was made

in 3–50 iterations of the single pair ICP algorithm, applied to all pairs of FFLFs. In total 527 iterations were needed for the matching of 21 FFLFs. In one pair of FFLFs the ICP did not converge, probably due to poor initial approximation (in the procedure of simultaneous matching all 22 pairs of FFLFs participated). Thus, for the whole process (527+440=) 967 iterations of ICP algorithm were needed, which is almost double the number of those in the previous technique.

Consequently, the conclusion of Section 2.11.5 was verified. The adjustment with simultaneous matching of all pairs of FFLFs is preferable, as long as there are good initial approximations so that the ICP algorithm will converge.

5.8 Georeferencing of TerraSAR-X Images using Science Orbit Data

This Section focuses on the georeferencing of high resolution TerraSAR-X images using merely the orbital data and the parameters of the processor, as well as DLRs bulletins, without using any kind of Ground Control Information (GCI). In other words the aim of this Section is to project a 3D point of the Earth's surface on a 2D SAR image, without using GCI (Section 3.2). TerraSAR-X has three GPS receivers on-board which serve the mission and science operations of the sensor. Due to a GPS-based precise orbit determination strategy (Yoon et al. [2009]), the orbital path is offered to end users with a nominal accuracy up to 0.20 m (during periods with low solar activity much better accuracies have been reported), which is used to georeference the images.

The georeferencing is implemented as described in Section 3.2 and is evaluated using independent Check Points (CPs). Results are also compared with other methods applied to the same test site and with the same data sets.

5.8.1 Data sets

The data sets of this test are:

1. A whole scene of a High Resolution SpotLight (HS) TerraSAR-X image covering an area of about 50 km^2 (Figure 5.36) It is a basic image product, captured on February 2009 with the High Resolution SpotLight (HS) acquisition mode and it is of type Single Look Slant Range Complex (SSC). The incidence angle is 53° and the polarisation is single HH.
2. Archived medium scale topographic maps (1:5 000), which was compiled in 1970s with photogrammetric stereo-restitution (Figure 5.35). These maps



Figure 5.35: Archived maps.

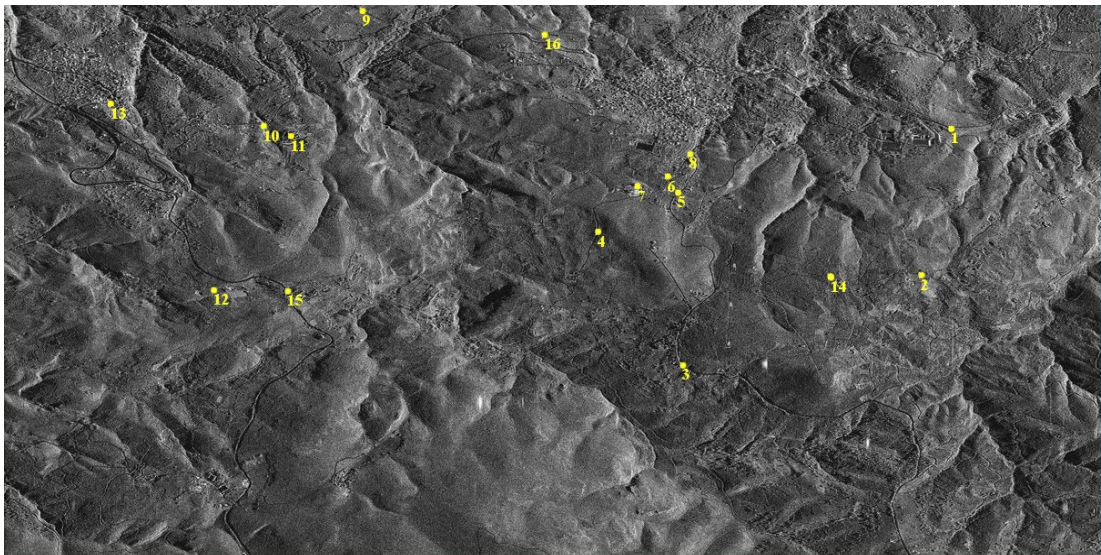


Figure 5.36: SAR image and CPs' distribution.

were selected because they cover the whole territory of Greece, are widely used as they are readily available and cost much less than a GPS survey. The horizontal and vertical accuracy of the maps is about 1.5 m and 2 m respectively.

The study area is located in the greater north-eastern region of Athens, Greece. The area has steep mountainous terrain and it is generally covered by sparse vegetation. Kalamos and Markopoulo Oropou, are two communities localised in the area.

5.8.2 Preprocessing

The archived maps were compiled in the old Greek reference system (HATT) which is using an Oblique Azimuthal Equidistant map projection and the Bessel ellipsoid. Thus transformation to the currently used reference system (HGRS87) which is using a Transverse Mercator map projection and is based on a shifted version of the GRS80 ellipsoid was done in order to compute the geocentric coordinates of the CPs in the WGS84 ellipsoid.

16 control points (CPs) were identified both in the maps and in the SAR image. An effort was made to distribute the CPs so that they cover the whole scene of the SAR image (Figure 5.36). This proved to be difficult as the map is much older than the SAR image. Almost all CPs are located on crossroads which makes their position more or less ambiguous. Some characteristic points of construction, such as building corners and fences, were also identified, but almost all proved to be unreliable, as most of the constructions had been rebuilt. Furthermore, the speckled nature of the SAR data made the location of the control points fuzzy.

5.8.3 Application and results

The 16 CPs measured on the maps were projected to the SAR image using the present method model and were compared to the ones measured on the SAR image. The orbit of the SAR sensor was approximated using 2, 4 and 12 time stamps (Sections 3.2.3.3 and 3.2.3.4). Table 5.1 shows the minimum, maximum and RMS errors in pixels using 2, 4 and 12 time stamps.

Table 5.2 shows a comparison between the proposed georeferencing method and methods using ground control linear features with 1st order 3D RPFs and 3D-DLT (Section 6.1) as well as ground control points with 1st order 3D RPFs and 3D-DLT (Vassilaki and Ioannidis [2010]). It is derived that the results using the present method are better than those computed using GCPs-based 1st order RPFs and DLT, and of the same accuracy with the results computed using Ground Control Linear Features.

Table 5.1: Results in pixels on 16 independent CPs, in the case of cubic interpolation assumption.

16 CPs	2 time stamps		4 time stamps		All 12 time stamps	
	dRg	dAz	dRg	dAz	dRg	dAz
Max error	11.3	7.7	11.3	7.6	12.1	6.4
Min error	1.1	0.2	1.1	0.1	0.3	0.7
RMSE	5.3	3.9	5.3	3.8	5.6	3.8

Table 5.2: Comparison with other methods; RMSE computed with 16 CPs.

Ground control information (GCI)	Projection transformation	RMSE x (Rg) (pixels)	RMSE y (Az) (pixels)
None	physical model	5.3	3.9
GCLFs	3D RPFs	4.4	3.8
GCLFs	3D DLT	4.2	3.7
GCPs	3D RPFs	7.2	3.6
GCPs	3D DLT	6.6	3.4

The results are especially good taking into consideration that (a) the check data (CPs) are derived from maps of an accuracy estimated to about 3 pixels, (b) the uncertainty of pixel identification in the SAR images is estimated to be >1 pixel, and (c) there are errors caused by the coordinate system transformation and ambiguities in the metadata.

5.9 Absolute orientation of old aerial photographs through ICP-based global matching of free-form linear features

In this Section a method for the absolute orientation of a stereomodel derived from small-scale old aerial photographs is presented. Archives of such images are maintained worldwide and are an objective witness to the evolution of the Earth's surface. They are useful in many interdisciplinary applications of environmental monitoring and boundary disputes. Their orientation is not a trivial task (Redweik et al. [2010]). Defects in the photographs due to their historic nature, the wide spatial changes on the Earth's surface over the years and the often small scale of the photographs make it hard, and in some cases impossible, to identify solitary ground control points.

The method implements, validates and evaluates the performance of the general ICP-based matching method (Section 2.7) and the initial approximation using

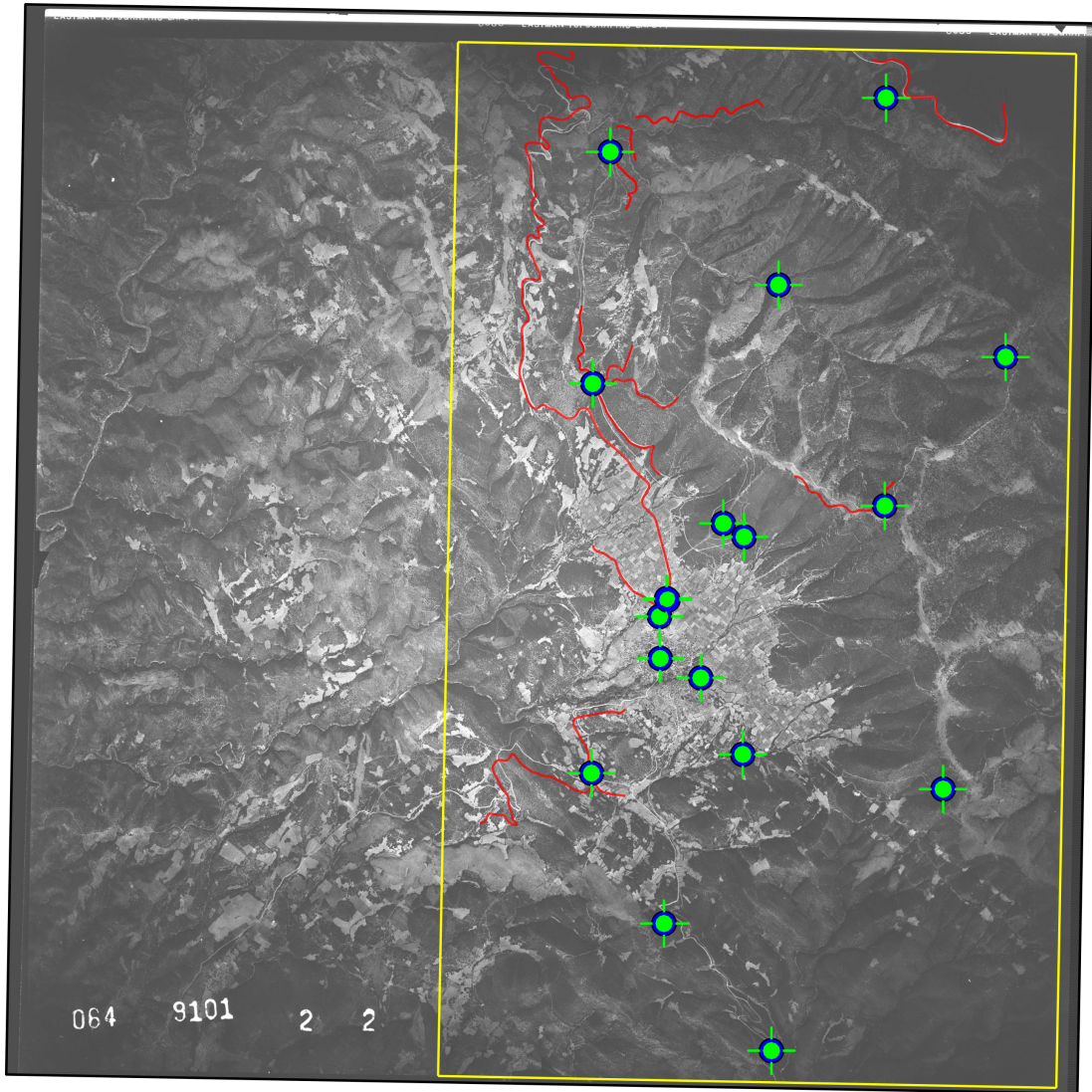


Figure 5.37: The overlapping part of the historical image (yellow), the FFLFs (red) and the CPs (green).

the rigid approach (Sections 2.9 and 2.9.3.4) for single pairs of 3D FFLFs (3D-3D). The potential of FFLFs to be used as an alternative form of ground control information is also shown.

5.9.1 Data sets

The data sets of this test are:

1. A stereopair of aerial photographs from the Greek archive of historical aerial photographs. The photographs were captured during 1945 and they are at a scale of 1:42 000.
2. Archived medium scale topographic maps of scale 1:5 000 compiled in the 1980s.

5.9.2 Transformation

The transformation between the 3D model coordinates of the stereomodel, and the object space is the 3D similarity transformation. It is a non-linear rigid transformation with seven unknown parameters; three translations X_o, Y_o, Z_o , three rotations ω, ϕ, κ and a scale μ (Equation 5.1).

5.9.3 Preprocessing

For the orientation of the stereopair of photographs 15 characteristic FFLFs, of a length of 0.4 to 7.4 km, such as road edges and creeks, have been used as ground control information. The FFLFs and 16 independent check points (CPs) were extracted from a map at a scale of 1:5 000. Relative orientation of the stereopair using a digital photogrammetric workstation (DPW) was accomplished and the digitisation of FFLFs in the 3D model coordinate system, which is an arbitrary system based on the coordinate system of the left image, followed. These FFLFs (Figure 5.37) were used to compute the centrelines of the features through skeletonisation techniques.

5.9.4 Application and results

The centrelines were used as ground control information and were matched using the 3D similarity transformation. The matching was done independently for each FFLF and it was carried out successfully despite the temporal changes they exhibit. The RMSE (X, Y) was 1.8 to 7.3 m and the RMSE in Z was 1.2 to 5.4 m. The matching of a typical FFLF is shown in Figure 5.38), where the reference FFLF is in magenta and the matched FFLF in black. The rough profile of the

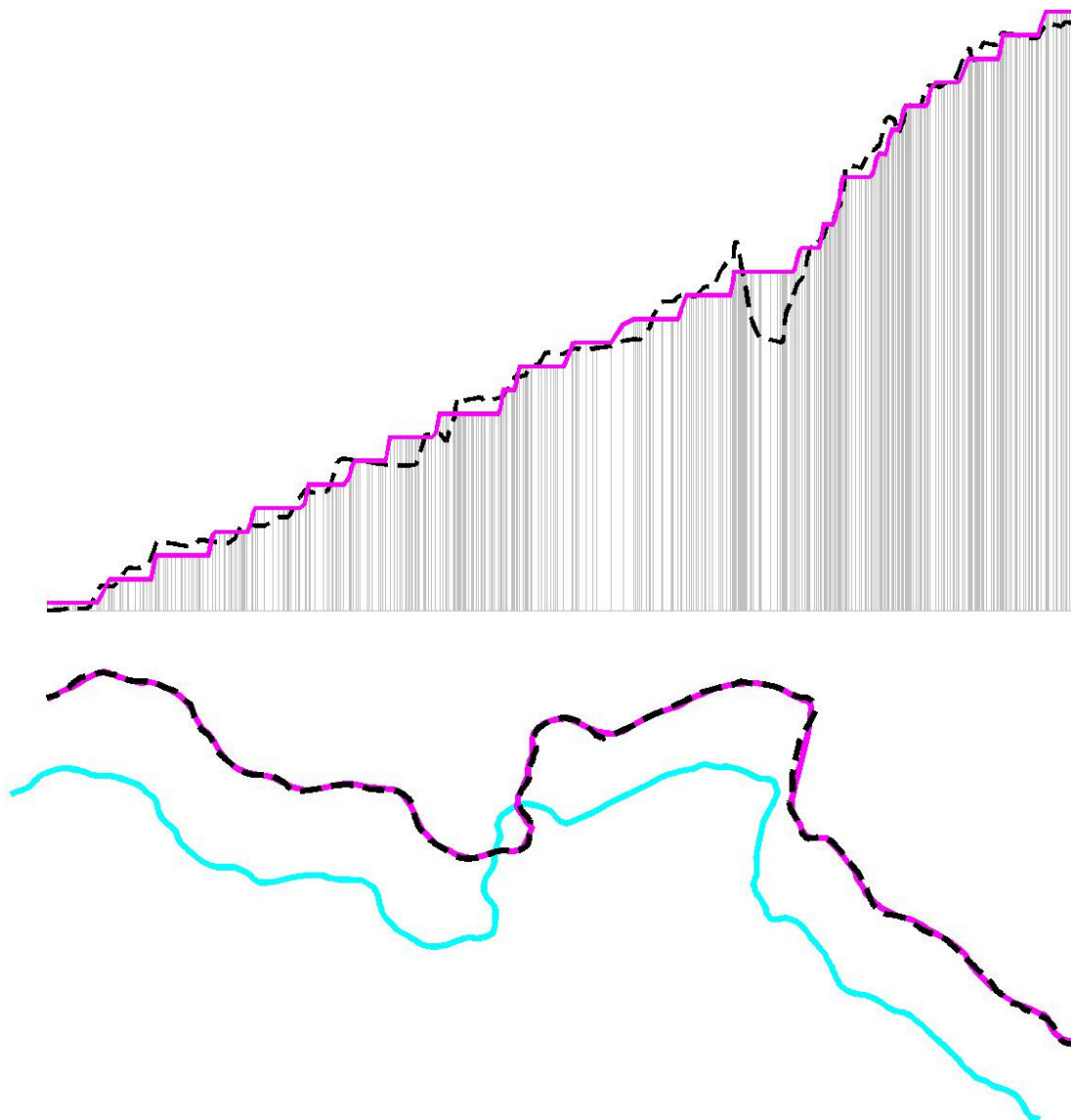


Figure 5.38: Planar and vertical matching results.

Table 5.3: Case study: RMSE (m) of 16 independent CPs.

GCI	X	Y	Z	XY	XYZ
Points	5.86	15.89	16.88	16.94	23.91
FFLFs	6.43	7.83	3.21	10.13	10.63

road centreline is due to the small scale of the map and the fact that the map does not have elevation information along the surface of the road. The centreline elevation was computed by the surrounding terrain.

The matching produced a total of 5475 homologous points between all the 3D model space FFLFs and the 3D object space FFLFs. These points were then used to compute the parameters of the absolute orientation (translations X_o, Y_o, Z_o , rotations ω, ϕ, κ and scale factor μ). The more advanced method of Section 2.11.3 could also have been used. The accuracy of the process was evaluated with 16 independent CPs (Table 5.3).

The parameters of the absolute orientation were also computed by aerial triangulation using 13 GCPs; their coordinates were extracted from the map of scale 1:5 000. The accuracy of the aerial triangulation was evaluated with the same 16 independent CPs (Figure 5.37, Table 5.3).

Comparative evaluation of the RMSE of the independent CPs (Table 5.3) shows that the proposed method is superior to the point-based method in difficult cases, as in this test. The robustness of the proposed method is shown in Figure 5.38 where a selection of the matching results, both in XY and Z, appear; despite segments with wide (temporal) changes, the method manages to converge to the best possible matching.

These conclusions are also confirmed by the application of the method to the georeferencing of contemporary high resolution satellite SAR images, where the identification of points is also difficult due to their fuzzy and speckled nature, as well as the side-looking imaging geometry of this type of image (Section 6.1).

5.10 Recovery of the geometry of historical aerial photographs associating self-calibration with ground control linear features

This Section addresses one of the hardest problems of multitemporal image analysis: the recovery of the imaging geometry, both the interior and the exterior, of historical aerial photographs, using ground control information from recent data, e.g., orthoimages and the corresponding DTM. Linear features of arbitrary geometry such as road edges are used as Ground Control Information instead of the

discrete points which are the regular case in image orientation analysis. In order to overcome the absence of the calibration report of the camera which collected the historical photographs two transformation models are used: the method of self-calibration method using the Collinearity Equations, and the Direct Linear Transformation. The time interval between the collection of the historical photographs and the recent data (orthoimages) is almost 65 years.

However, the recovery of the imaging geometry of historical images is a time-consuming and laborious process and it is hard to meet high standards of accuracy. A recent example is the Portugal's aerial images repository reclaim (Redweik et al. [2010]). The main reasons for these difficulties are (Vassilaki et al. [2012a]):

- The lack of camera calibration reports. It refers to the camera's geometric parameters, as documented in the camera calibration report. In the case of historical images, the camera's parameters may be partially available or they may even be lost during the years or never documented.
- The wide spatial changes occurred on the Earth's surface since the image capture and the present day. The time interval may be 60 or more years and thus it is hard to identify homologous points on the Earth's surface and on the photograph.

Moreover, characteristics inherent to the historical photographs, such as small image scale, old-fashioned radiometric characteristics, absence of FMC, use of reprints and deterioration due to the aging of the film and the storage conditions, make the identification of homologous points harder. Homologous points on the Earth's surface and on the photograph, namely Ground Control Points (GCPs), are necessary in order to recover the exterior geometry (exterior orientation) of the image at the time of the acquisition. Generally GCPs are collected through GPS ground survey. However this is seldom possible due to the large spatial changes. An alternative way to collect GCPs, is to identify homologous points on the photograph and on old maps, which are closer to the photograph, in time. In some cases historical field data may be available (Redweik et al. [2010]); its use may help but the field data, old by itself, does not necessarily guarantee adequate co-registration with contemporary remote sensing and geospatial data.

The objective of this Section is to investigate the use of linear features of arbitrary geometry as a source of ground control information, instead of the use of solitary points. Specifically, the problem is formulated to use linear features to recover the imaging geometry, both of the interior and exterior, of historical aerial photographs. The results are compared to those of the solitary points formulation, in terms of accuracy, reliability and workability.



Figure 5.39: Data sets: aerial photograph captured in 1945 (left), orthoimage made from aerial images collected in 2008 (right).

The method implements, validates and evaluates the performance of the general ICP-based matching method for networks of FFLFs of different dimensionality (Section 2.11.6), and in particular the identification of FFLFs correspondences in 3D-2D and the initial approximation (Sections 2.11.4 and 2.9.4). It showcases the generality of the matching method, as multiple projection transformations are used for the recovery of the geometry, one of which is highly non-linear, and the data sets differ greatly in acquisition time.

5.10.1 Projective transformations

In the case of historical photographs it is necessary to use transformation models which do not need the a priori knowledge of the interior orientation parameters (camera calibration report):

-
1. The photogrammetric resection with self-calibration using Collinearity Equations, with 9 unknown parameters:

$$\begin{aligned} x - x_0 &= -c \frac{(X - X_0)r_{11} + (Y - Y_0)r_{12} + (Z - Z_0)r_{13}}{(X - X_0)r_{31} + (Y - Y_0)r_{32} + (Z - Z_0)r_{33}} \\ y - y_0 &= -c \frac{(X - X_0)r_{21} + (Y - Y_0)r_{22} + (Z - Z_0)r_{23}}{(X - X_0)r_{31} + (Y - Y_0)r_{32} + (Z - Z_0)r_{33}} \end{aligned} \quad (5.5)$$

2. The 3D Direct Linear Transform (3D-DLT), with 11 unknown parameters:

$$x = \frac{a_1X + a_2Y + a_3Z + a_4}{c_1X + c_2Y + c_3Z + 1}, \quad y = \frac{b_1X + b_2Y + b_3Z + b_4}{c_1X + c_2Y + c_3Z + 1} \quad (5.6)$$

where x, y are the 2D image space coordinates of a point P, X, Y, Z are the 3D object space coordinates of the point P, c is the calibrated focal length (or camera constant), x_0, y_0 is the offset from the fiducial-based origin to the perspective centre origin (principal point), X_0, Y_0, Z_0 is the position of the centre of perspective (or camera station) in object space and r_{ij} are the elements of the rotation matrix $R_{\omega\varphi\kappa}$ (Equation 5.2) from the object space to the image space (Mikhail et al. [2001]). For the solution with the photogrammetric resection (Equation 5.5), the principle point may be considered that is identical with the centre of the photograph ($x_0 = y_0 = 0$) and that the radial distortion is insignificant, without significant impact on the accuracy. So, the remaining unknowns are 7 (c and the parameters of the exterior orientation $X_0, Y_0, Z_0, \omega, \varphi, \kappa$). In both models X, Y, Z and x, y are known for a large number of points provided by ICP.

5.10.2 Data sets

The data sets of this test are:

1. The diapositive of a grayscale aerial photograph (Figure 5.39) of scale 1:42 000 was captured in 1945. The diapositive was scanned using a photogrammetric flatbed scanner with 1200 DPI (about 21mm/pixel) resolution which is the regular resolution for scanning analogue photographs.
2. A recent medium scale (1:5 000) optical orthoimage with the corresponding DTM (Figure 5.39), which were created using aerial images collected in 2008. The pixel size of the orthoimage is 0.5 m while the pixel size of the DTM is 5 m. The planar accuracy of the orthoimage is 1.5 m and the vertical accuracy of the corresponding DTM is 2 m.

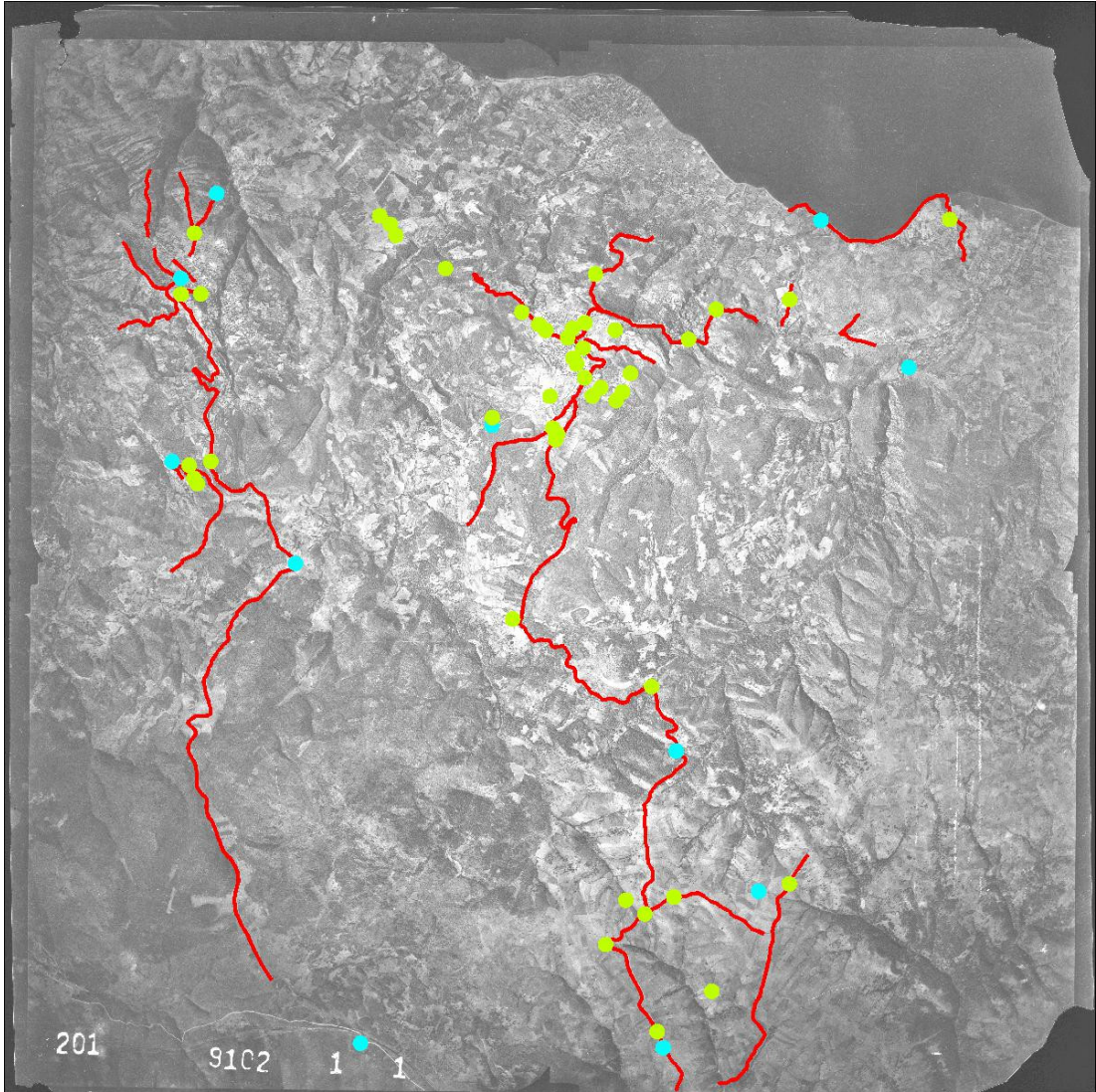


Figure 5.40: GCLFS (in red), CPs (in yellow) and GCPs (in cyan) on the historical photograph.

-
3. An archived medium scale topographic map of scale 1:5 000, compiled in 1970, which was used as an intermediate for the identification of common points between the aerial photograph and the orthoimage. The accuracy of the map is the same with the accuracy of the orthoimage and its corresponding DTM.

The data sets depict a region north-east of Athens which has steep mountainous terrain. The region is covered by typical southern Europe vegetation (thin) and two towns. A small part of the historical photograph is covered by the sea, and the average ground elevation is 270m. The large spatial changes between the data sets are evident in Figure 5.39, where the built up area of the orthophotograph is absent in the historical photograph.

5.10.3 Preprocessing

In order to use the proposed method to recover the imaging geometry of the historical photograph, twenty one homologous GCLFs of adequate length (0.5 Km to 12 Km) were identified between the historical aerial photograph and the recent orthoimage, most of which are road edges (Figure 5.40). For both data sets the road centre line was computed from the edges using skeletonisation techniques. The heights of the centre lines of the orthoimage were interpolated from the available DTM.

In order to evaluate the proposed method 46 independent Check Points (CPs) (Figure 5.40) were identified between the historical aerial photograph and the recent orthoimage. Additionally, 11 Ground Control Points (GCPs) were identified in order to check the proposed methods with the traditional solitary point based method (Figure 5.40). The identification of CPs and GCPs proved to be a quite laborious process with uncertain success. For the particular application, in order to increase the degree of success and reliability in determining more CPs and GCPs, an “interpolation-in-time” process was used. A topographic map compiled in 1970 was used as an intermediate between the historical photograph (1945) and the recent orthoimage (2008). Thus the 65 years time interval between the data sets was split to two time intervals: 25 years and 40 years. The “interpolation-in-time” process had also been used in former unpublished research of the author using blocks of aerial photographs: recent orthoimages were used for the orientation of blocks of aerial images of 1960 and then the oriented stereo-models of 1960 were used for the orientation of the historical photographs (1945). It is a quite laborious process, hard to be applied for operational cases, since various multimodal data sets have to be acquired and processed. In the current case, the topographic map was preferred because it is a standard accuracy mapping product.

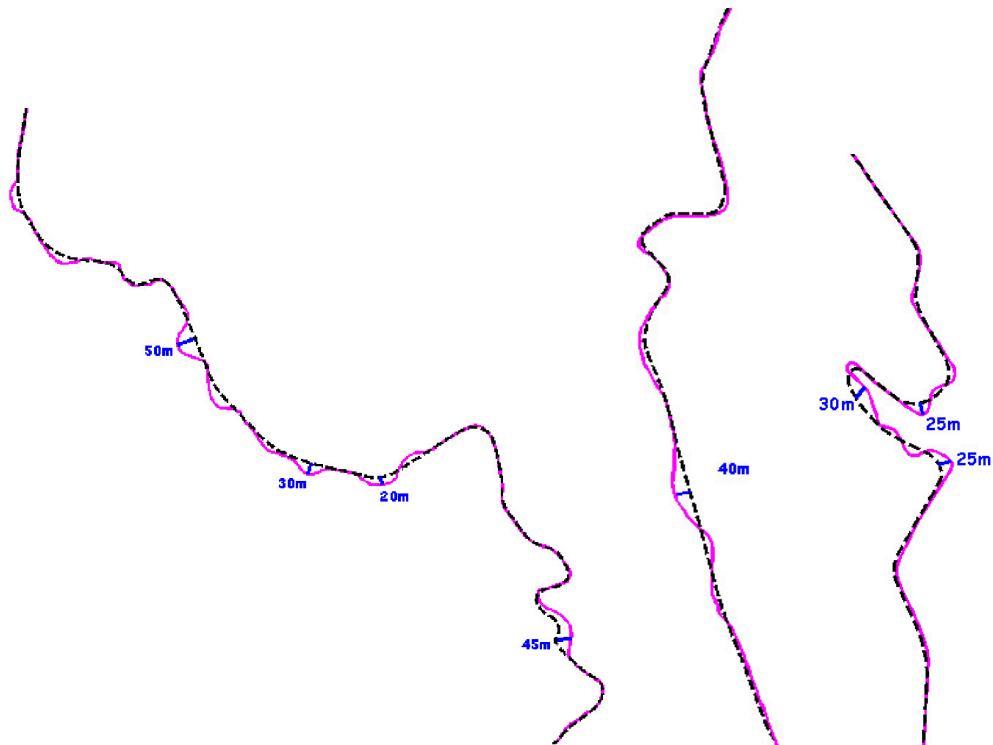


Figure 5.41: GCLFS on the historical photograph (in magenta), projected GCLFS from the orthoimage and the corresponding DEM using the computed transformation (in black).

5.10.4 Application and results

The computation of the image geometry with GCLFs was done twice: once using the Collinearity Equations and once using the 3D-DLT. The accuracy was evaluated using the 46 CPs. The results for the planar errors of CPs are: $RMSE(XY) = 6.5$ m using the Collinearity Equations and $RMSE(XY) = 6.2$ m using the DLT. These results are quite good as usually the accuracy achieved with this type of photographs is 10–15 m and sometimes even worse (20–25 m). In Figure 5.41, where some of the 3D-2D matching results are shown, the multitemporal nature of the data sets is evident.

The computation of the image geometry with GCPs was also done twice and the accuracy was evaluated using the same 46 CPs. The results for the planar errors of CPs are: $RMSE(XY) = 7.2$ m using the Collinearity Equations and $RMSE(XY) = 7.3$ m using the 3D-DLT. The results were computed by the especially sophisticated but also time-consuming procedure for the selection and identification of the GCPs, and are thus considered as the best possible results

using GCPs for the georeferencing of this historical photograph.

GCLFs achieve better accuracies than GCPs. The differences are approximately 1 m better than the “interpolation-in-time” process, and 4–9 m better than the usual cases. Furthermore, the identification of linear features which persist through the years, is straightforward, easier, more robust and much faster than the identification of solitary points. Thus GCLFs are preferable for the georeferencing of historical photographs.

5.11 Overview and contribution

In this Chapter (*Chapter 5*) the general methods presented in Chapters 2 and 3 were tested with real world problems and real world data. Each Section presents a problem which was addressed with a new method and achieved high accuracy as compared to other methods. Each Section is a contribution to the discipline of surveying engineering:

- Registration of 2D FFLFs Extracted from high resolution satellite imagery.
- Geospatial Data Integration using automatic global matching of FFLFs.
- Contour line matching.
- Multitemporal Geospatial Data Integration using automatic global matching of 3D FFLFs.
- Registration of optical and SAR imagery by automatic free-form features global matching.
- Enhanced initial approximation for ICP-based global matching of FFLFs in side-looking RADAR geometry.
- Multitemporal data registration through global matching of networks of 2D FFLFs.
- Georeferencing of TerraSAR-X Images using Science Orbit Data.
- Absolute orientation of old aerial photographs through ICP-based global matching of free-form linear features.
- Recovery of the geometry of historical aerial photographs associating self-calibration with ground control linear features.

Chapter 6

Specific methods

This Chapter presents methods specific to the objectives of the dissertation. They were developed by combining the general methods of Chapters 2 and 3 and general principles, methods and problems of surveying engineering. The general methods were specialised to handle multimodal and multitemporal data sets using a multitude of projective transformations. The high accuracy of the specific methods are tested with real world data.

6.1 Georeferencing of not geometrically corrected SAR images to geometrically corrected unitemporal and multitemporal maps and optical images

In this Section, 3D FFLFs are used as ground control information for the computation of the transformation from 3D object space to the 2D SAR image space. This is feasible due to the high resolution imaging capabilities of contemporary satellite SAR sensors which allow the identification of detailed structures. The computation of the transformation parameters is based on the general iterative closest point (ICP) based method for single free-form linear feature pair matching (Section 2.8), extended to simultaneously match multiple pairs of them (Section 2.11.6). The proposed method is tested with the georeferencing of a whole TerraSAR-X image, using multitemporal and unitemporal maps and optical images as a source of GCI. Linear features are shown to be a reliable form of ground control information.

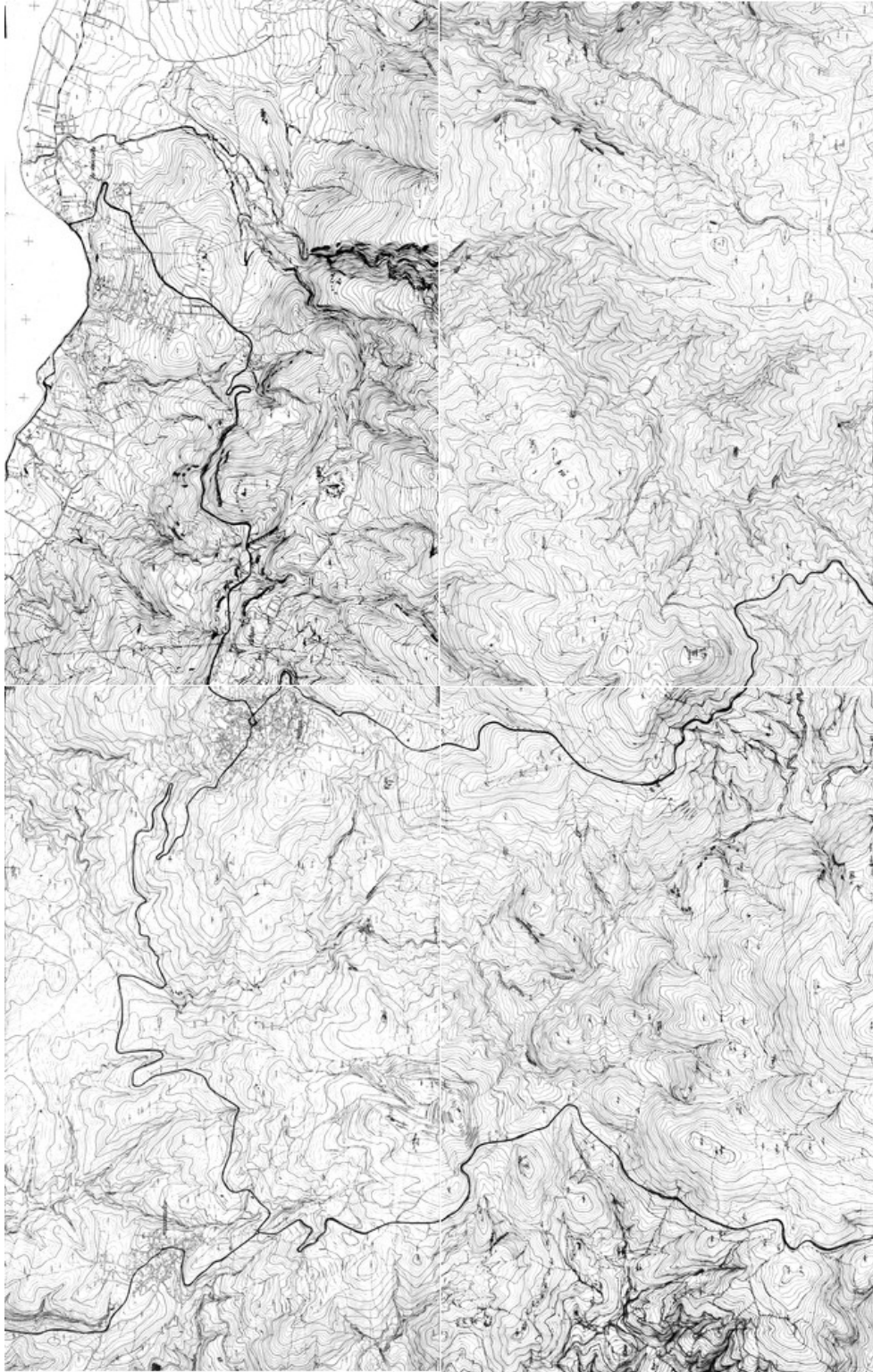


Figure 6.1: Archived map.



Figure 6.2: Recent optical orthoimage.

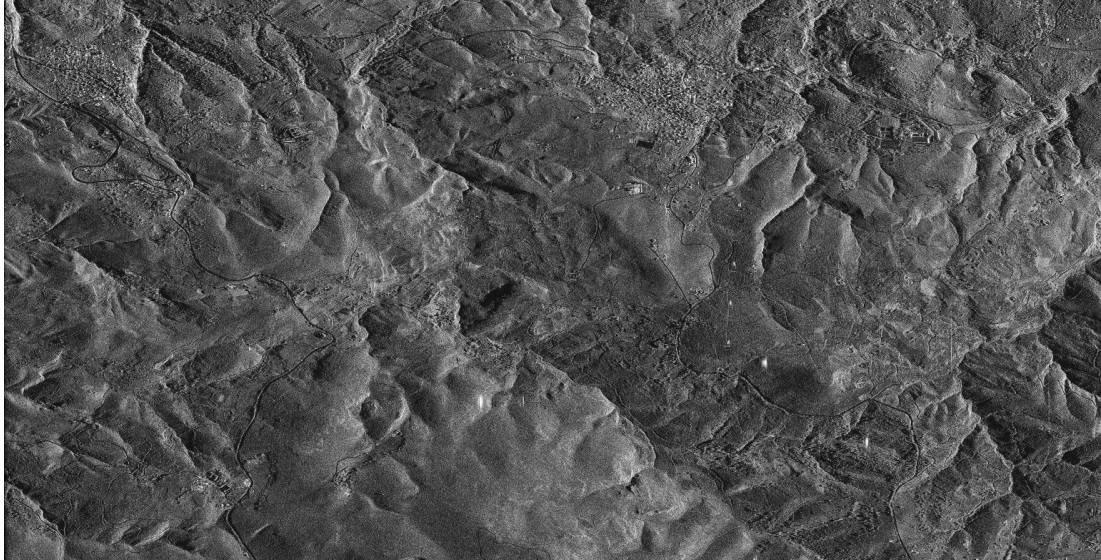


Figure 6.3: SSC SAR image.

6.1.1 Problem Formulation

A SAR image is a 2D projection (x,y) of the 3D object space (X,Y,Z) . The georeferencing process recovers the imaging geometry of the sensor at the time of acquisition, by the computation of the parameters of the transformation. Transformations are generally classified into empirical models and into physical sensor models (Section 2.3). Examples of empirical models are polynomial functions (PFs) and rational polynomial functions (RPFs), while physical sensor models are sensor dependent rigorous mathematical functions. In this Section the georeferencing is computed by using PFs and RPFs as transformation models, and the results are compared to those achieved using the physical model (Section 5.8). Although not widely adopted for SAR images (Toutin [2004], Dowman and Dollof [2000]), the use of empirical sensor models is still geometrically meaningful as it was recently explained by Zhang et al. [2011]. Traditionally the computation of the transformation parameters, either empirical or physical, requires solitary points with known 3D object-space and 2D image-space coordinates (ground control points, GCPs). In this Section the georeferencing parameters are computed using FFLFs with known 3D object-space and 2D image-space coordinates (GCLFs). In contrast to solitary points, the 3D information and the 2D information are in the form of a pair of two distinct heterogeneous FFLFs defined by their nodes (measured points). These nodes may vary widely as they are produced using different processes. Even though a corresponding pair of FFLFs represents

the same physical feature, generally no two nodes of the FFLFs correspond to the same physical point (Section 2.2). Homologous point pairs have to be computed (matched). The matching is complicated by the fact that the two FFLFs are of different dimensionality (Section 2.8). Furthermore, a single pair of FFLFs may not represent the entire data set, as it may be confined to a small region of the data. In this case, multiple pairs or a network of corresponding FFLFs are required (Section 2.11.6). The network of FFLFs increases the robustness but it introduces problems such as the FFLFs correspondence (Sections 2.11.1 and 2.11.2), simultaneous matching (Section 2.11.3) and pre-alignment (Section 2.11.4).

6.1.2 Design of tests

The experiments were designed to test both the robustness and the accuracy of the method. In the group “A” tests, the georeferencing of a TerraSAR-X image is done using GCI extracted from a 40 years old map. In the group “B” tests, the georeferencing of the same TerraSAR-X image is done using recently captured optical aerial images. Group A is a “crash test” of the proposed method and it may be of practical use in urgent situations when there is no time to collect up-to-date GCI (a day is enough for a satellite scene under the current method). Group B, where the data sets are compatible in terms of time, is a contribution to the operational georeferencing of TerraSAR-X images and their combined use with optical images.

Each group of experiments contains tests corresponding to four distinct projection models which are employed for the registration of the data sets using FFLFs as matching primitives:

1. The first order 3D-2D Polynomial Functions (PFs) with 8 unknown parameters:

$$x = a_1X + a_2Y + a_3Z + a_4, \quad y = b_1X + b_2Y + b_3Z + b_4 \quad (6.1)$$

2. The second order 3D-2D Polynomial Functions (PFs) (Toutin [2004]) with 16 unknown parameters:

$$\begin{aligned} x &= a_1X + a_2Y + a_3Z + a_4 + a_5X^2 + a_6Y^2 + a_7Z^2 + a_8XY \\ y &= b_1X + b_2Y + b_3Z + b_4 + b_5X^2 + b_6Y^2 + b_7Z^2 + b_8XY \end{aligned} \quad (6.2)$$

3. The 1st order Rational PFs (RPFs) with common denominator (3D Direct Linear Transform: 3D-DLT), with 11 unknown parameters:

$$x = \frac{a_1X + a_2Y + a_3Z + a_4}{c_1X + c_2Y + c_3Z + 1}, \quad y = \frac{b_1X + b_2Y + b_3Z + b_4}{c_1X + c_2Y + c_3Z + 1} \quad (6.3)$$

4. The 1st order 3D-2D RPFs with 14 unknown parameters:

$$x = \frac{a_1X + a_2Y + a_3Z + a_4}{c_1X + c_2Y + c_3Z + 1}, \quad y = \frac{b_1X + b_2Y + b_3Z + b_4}{d_1X + d_2Y + d_3Z + 1} \quad (6.4)$$

where X, Y, Z are the object coordinates and x, y are the SAR image space coordinates (slant range and azimuth, respectively). In any case the matching method computes a large number of interpolated points between the two FFLFs, thus the system of equations is overdetermined and the LSA is employed in order to solve it. Equations 6.1 and 6.2 are linear and the estimation of the unknown parameters is a straightforward process with LSA. Equations 6.3 and 6.4 are non-linear but can be turned into linear ones by multiplying the two parts of the equations by the denominator. The use of multiple projection models showcases the generality of the matching method.

6.1.3 Data sets

The study area is a sub-urban area in the greater north-eastern region of Athens, Greece. It has steep mountainous terrain with an average elevation of 270 m and it is generally covered by sparse vegetation. It also includes two small urban regions. The data used is:

1. A TerraSAR-X image (Figure 6.3).
2. An archived medium scale topographic map 6.1
3. A recent medium-scale optical orthoimage 6.2 with the corresponding digital terrain model (DTM).

The TerraSAR-X image is a single look slant range (SSC) imaging product captured in 2009 with the experimental 300 MHz high resolution spotlight (HS) imaging mode. The whole image, which covers an area of about 50 km² (5 km x 10 km), was used. The polarisation is HH and the scene centre incidence angle is 53°. The projected spacing values for range (ps_{Rg}) and azimuth (ps_{Az}) are 0.45 m and 0.87 m, respectively. The medium-scale archived topographic map was in analogue form at a scale of 1:5 000 and it was compiled by stereo-restitution from aerial photographs, captured in 1970. The map was converted to digital form by scanning and digitising; the contour lines of the map were converted to a DTM. The relative planar accuracy of the map is estimated at 1.5 m (σ_{PL}). The vertical contour interval is 4 m and the relative vertical accuracy is estimated at 2 m (σ_Z). The absolute planar accuracy is estimated at 2.5 m (σ_{PL}) and the vertical one at 4 m (σ_Z). The map is part of a series which cover the whole territory of Greece. They are readily available and they cost much less than a GPS survey.

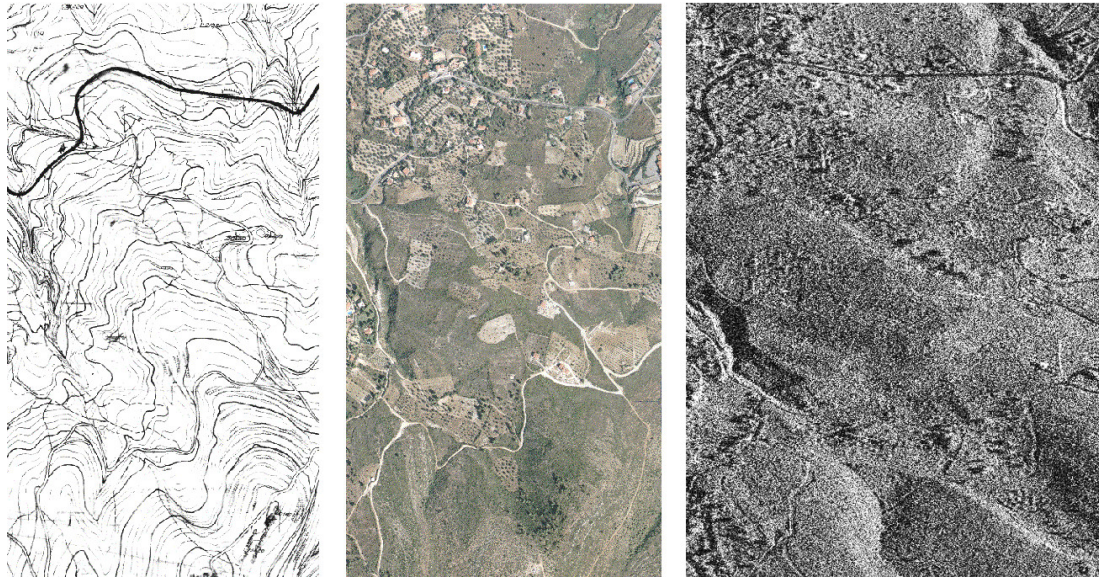


Figure 6.4: Roads are common in all data sets.

The area under study (Figure 6.4) changed widely during the 40 years between the two data collection phases (2009 and 1970). The area used to be an agricultural area but now exhibits a great variety of land uses, as it serves as a holiday resort near Athens. The map and the SAR image share few common features, as is the case in virtually all multitemporal data sets. Most of these common features are roads which, unfortunately, evolve through time. Many sections of the roads have changed considerably during the 40 years between data acquisitions, as it is shown in the next paragraphs.

The maps are topographic maps (not illustration or small scale maps) of scale 1:5 000 and thus there are no (significant) generalisations. Furthermore, most of the used roads are more than 6 m wide, which means that their width is over 1 mm in the map, and thus, the roads are clearly visible. The medium-scale optical orthoimage and the corresponding DTM were available with pixel sizes of 0.5 m and 5 m, respectively. The orthoimage was produced from aerial images collected in 2008. The orthoimage and the corresponding DTM are of the same nominal accuracy as the paper map, probably because they were also compiled to meet the specifications for mapping at a scale of 1:5 000.

6.1.4 Error Propagation from Object Space to SAR Image Space

The 3D error of the data sets must be expressed in terms of the 2D SAR image space, since this Section deals with the projection (in the mathematical sense) of the 3D object space to the 2D SAR image space. The error propagation of the object space to the SAR image space assumes that a point $P(X,Y,Z)$ measured on a map contains a planar error σ_{PL} and a vertical error σ_Z inherited from the accuracy of the map. There is no reason to assume that the σ_{PL} error is different in any particular direction so that $\sigma_X = \sigma_Y = \sigma_{PL}/\sqrt{2}$. The directions x, y are taken as the range and azimuth directions of the SAR sensor, respectively. The error σ_Y (m) is also the expected SAR image error in the azimuth direction of the SAR image. The σ_Z, σ_X errors lead to SAR image error in the range direction, which is more complicated due to the slant range geometry of the SAR sensor. The slant distance (S_D) from the sensor (X_0, Y_0, Z_0) to the point (X, Y, Z) is given by Equation 6.5 where $k = Z/Z_0 \ll 1$ and ϕ is the mean incidence angle of all points in the SAR image. The error of the slant distance is then computed by Equation 6.6. As the pixel spacing is different in the range (ps_{Rg}) and azimuth (ps_{Az}) direction of the SAR image, the error in pixels is computed by Equation 6.7).

$$\begin{aligned} S_D &= f(Z, X) = \sqrt{(Z_0 - Z)^2 + (X_0 - X)^2} \\ &\approx \sqrt{(Z_0 - Z)^2 + Z_0^2 \tan^2 \phi} = Z_0 \sqrt{(1 - k)^2 + \tan^2 \phi} \end{aligned} \quad (6.5)$$

$$\begin{aligned} \sigma_{S_D}^2 &= \left(\frac{\partial f}{\partial Z} \right)^2 \sigma_Z^2 + \left(\frac{\partial f}{\partial X} \right)^2 \sigma_X^2 \\ &= \frac{(Z_0 - Z)^2}{(Z_0 - Z)^2 + (X_0 - X)^2} \sigma_Z^2 + \frac{(X_0 - X)^2}{(Z_0 - Z)^2 + (X_0 - X)^2} \sigma_X^2 \\ &\approx \frac{Z_0^2 (1 - k)^2}{Z_0^2 [(1 - k)^2 + \tan^2 \phi]} \sigma_Z^2 + \frac{Z_0^2 \tan^2 \phi}{Z_0^2 [(1 - k)^2 + \tan^2 \phi]} \sigma_X^2 \\ &\approx \frac{1}{1 + \tan^2 \phi} \sigma_Z^2 + \frac{\tan^2 \phi}{1 + \tan^2 \phi} \sigma_X^2 \\ &= \cos^2 \phi \sigma_Z^2 + \sin^2 \phi \sigma_X^2 \Rightarrow \sigma_{S_D} \approx \sqrt{\cos^2 \phi \sigma_Z^2 + \sin^2 \phi \sigma_X^2} \end{aligned} \quad (6.6)$$

$$\sigma_{Rg, pix} \approx \frac{1}{ps_{Rg}} \sqrt{\cos^2 \phi \sigma_Z^2 + \sin^2 \phi \sigma_X^2}, \quad \sigma_{Az, pix} \approx \frac{1}{ps_{Az}} \sqrt{\frac{\sigma_{PL}^2}{2}} \quad (6.7)$$

The planar relative error ($\sigma_{PL}=1.5$ m) and the vertical relative error ($\sigma_Z=2$ m) of the 3D object space map are propagated to 1.4 m in the SAR range direction

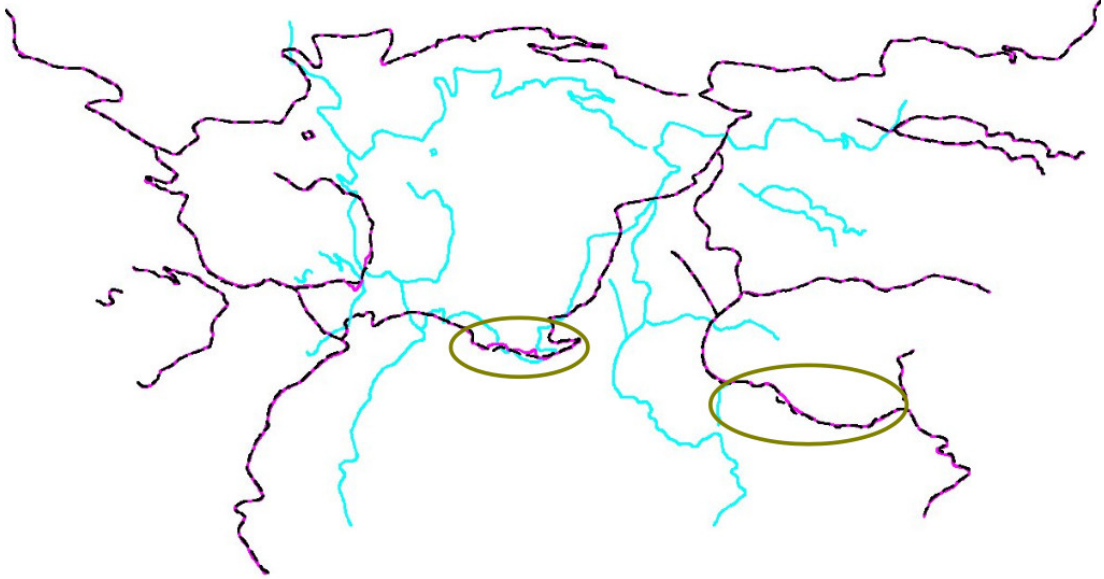


Figure 6.5: Matching results of Test A0. 3D GCLFs extracted from the old map (cyan), 2D GCLFs extracted from the SAR image (magenta), matched projection of the 3D GCLFs (black dashed). Figure 6.6 shows the road sections inside the green ellipses magnified (GCLF = ground control linear features).

($\sigma_{Rg,pix}$) and 0.9 m in the SAR azimuth direction ($\sigma_{Az,pix}$), while the planar absolute error ($\sigma_{PL}=2.5$ m) and the absolute vertical error ($\sigma_Z=4$ m) are propagated to 2.7 m in the SAR range direction ($\sigma_{Rg,pix}$) and 1.7 m in the SAR azimuth direction ($\sigma_{Az,pix}$). These values are valid for the specific SAR image of this Section and are used later for evaluation purposes.

6.1.5 Application and results

In all tests, the extraction of 2D road edges was done manually by digitising the lines in the map or in the optical image and in the SAR image. Most of the roads digitised are paved, as they appear better in the SAR images (Eineder et al. [2009]). The road centre lines were obtained from the edges using skeletonisation techniques. The road centre line is preferred to road edges as control FFLF, because it is more accurate than the edges and it fully represents the geometry of the road. For all the tests, a preliminary georeferencing was computed using a single pair of corresponding FFLFs that was identified manually (Section 2.11.4). The computed transformation parameters were used to bring the network of FFLFs close together. The contour lines of the map were also digitised. Then they were



Figure 6.6: Test A0: Road sections with wide temporal changes. 2D GCLFs (magenta), matched projection of the 3D GCLFs (black dashed).

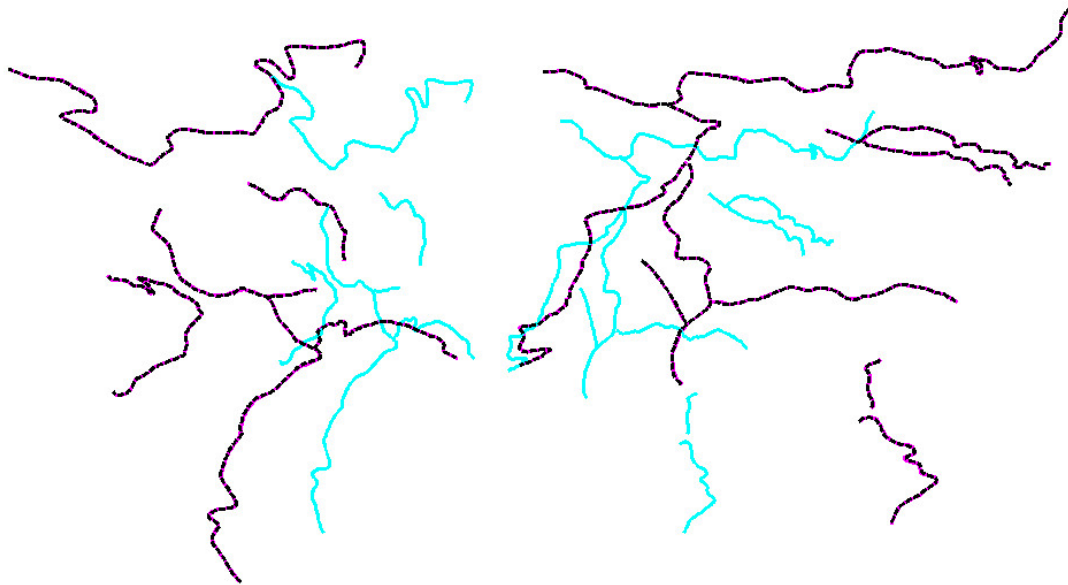


Figure 6.7: Matching results of Test A1. GCLFs with wide temporal changes are excluded.

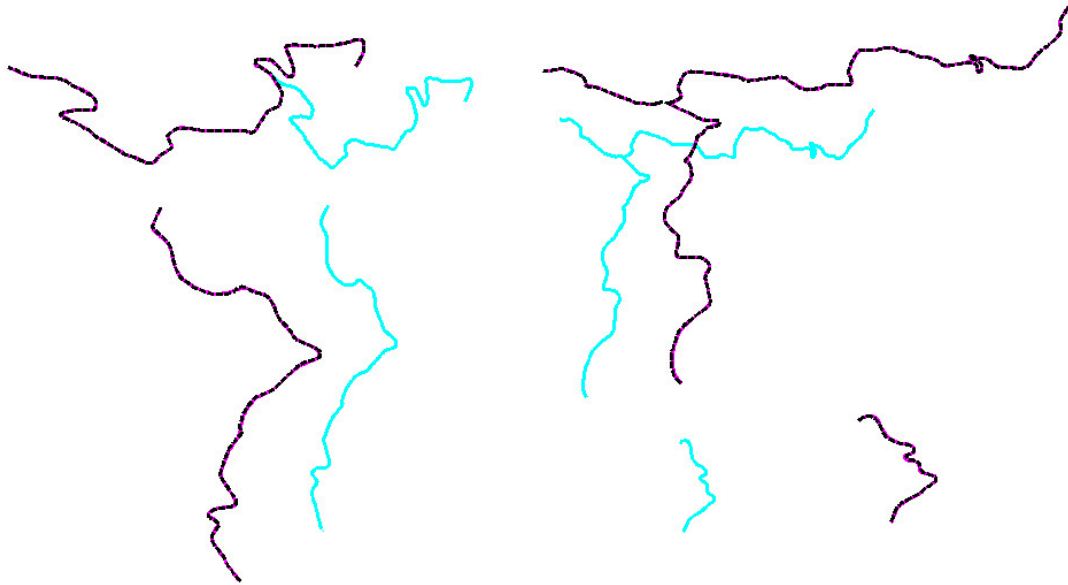


Figure 6.8: Matching results of Test A2. Only few GCLFs are used.

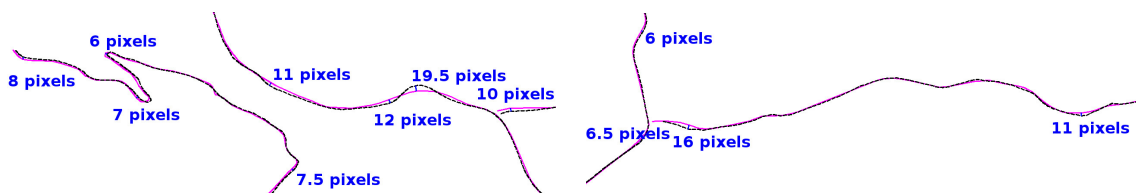


Figure 6.9: Test A1: Road sections with temporal changes. 2D GCLFs (magenta), matched projection of the 3D GCLFs (black dashed).

converted to Triangulated Irregular Network (TIN) via Delaunay triangulation, which was used as DTM in order to extract elevation information of the road centrelines.

In tests A, the length of the road centre lines varies from a few hundred meters to 8.5 km (Figures 6.5, 6.7 and 6.8). The height profiles of the road centre line are in general rough, due to the scale of the map and the fact that the map does not have elevation information along the surface of the road. The centre line elevation, interpolated in the DTM, was determined by the heights of the surrounding terrain. Three different cases were tested.

- In the first case (A0) the centre lines of 14 roads were used as ground control linear features (GCLFs). The whole lengths of the roads were used, regardless of the temporal changes that were identified.
- In the second case (A1) the same 14 centre lines as in (A0) were used, but the sections of the roads which exhibited large temporal changes were eliminated manually as identified by (A0).
- In the third case (A2) the centre lines of 4 roads, which span the whole scene of the SAR image, were used as GCLFs. The matching results are shown in Figures 6.5, 6.7 and 6.8.

The 3D GCLFs which were extracted from the map appear in cyan colour, the SAR 2D GCLFs appear in magenta colour, and the matched projection of the 3D GCLFs using the proposed method appear with a black dashed line. It must be noted that the coordinates of 3D GCLFs (cyan) and 2D GCLFs (magenta) were too different to fit into the same figure and thus the 3D GCLFs are shown scaled/translated for illustration purposes. In Figure 6.6 characteristic sections of the roads with wide temporal changes are presented for case A0. In Figure 6.9 characteristic sections with temporal changes are presented for case A1.

In tests B, the length of the road centre lines varies from 1.5 to 12 km (Figures 6.10 and 6.11). Two different cases were tested.

- In the first case (B1) the centre lines of 9 roads were used as GCLFs.
- In the second case (B2) the centre lines of 3 roads, which span the whole scene of the SAR image, were used as GCLFs.

The matching results are shown in Figures 6.10 and 6.11.

6.1.6 Validation, evaluation and discussion of the results

The accuracy of the computed georeferencing was checked with independent check points (CPs). In test A, 16 CPs were extracted from the medium scale old map

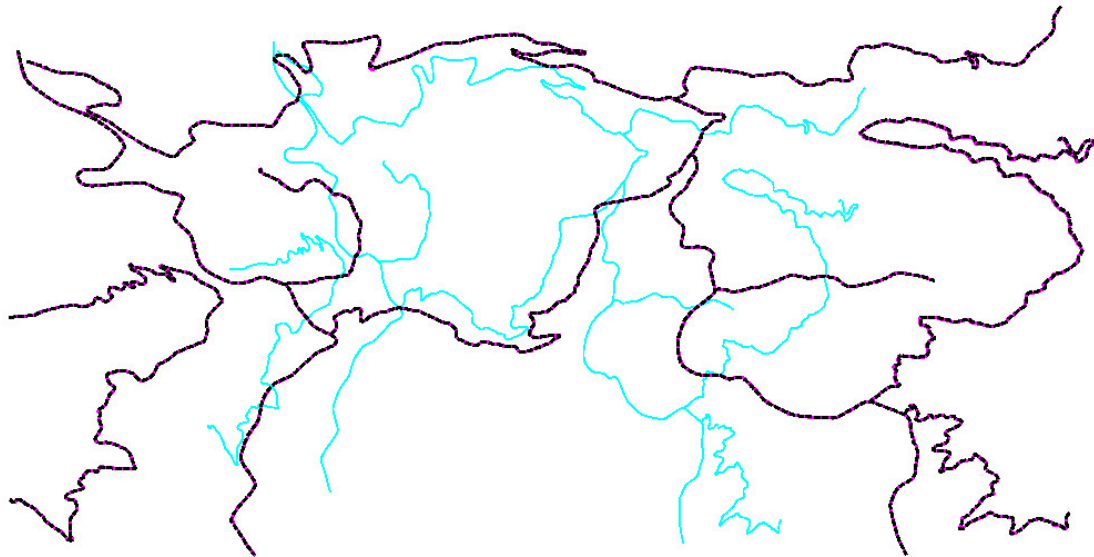


Figure 6.10: Matching results of Test B1. The 3D GCLFs are extracted from a recent orthoimage.

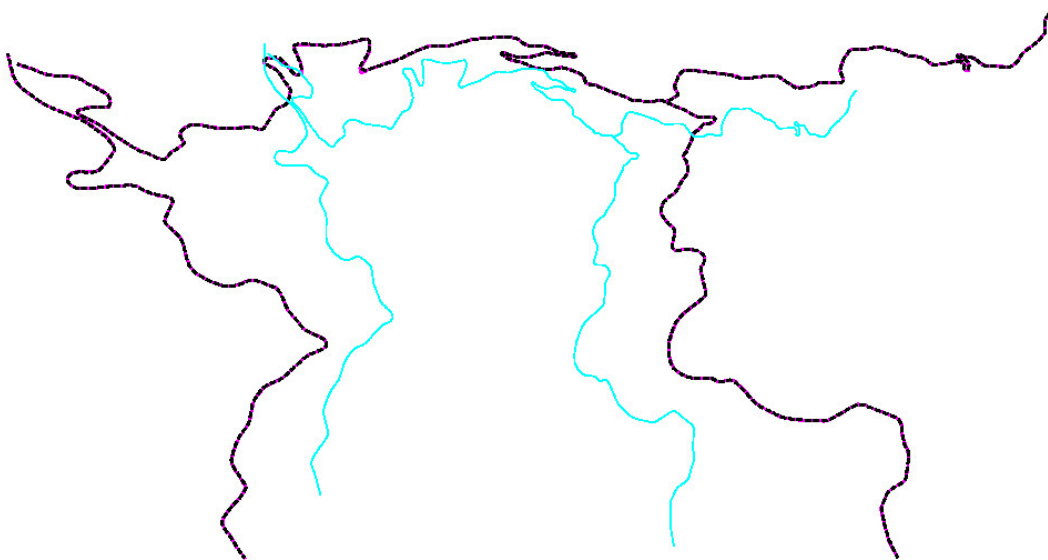


Figure 6.11: Matching results of Test B2. Only few GCLFs are used.

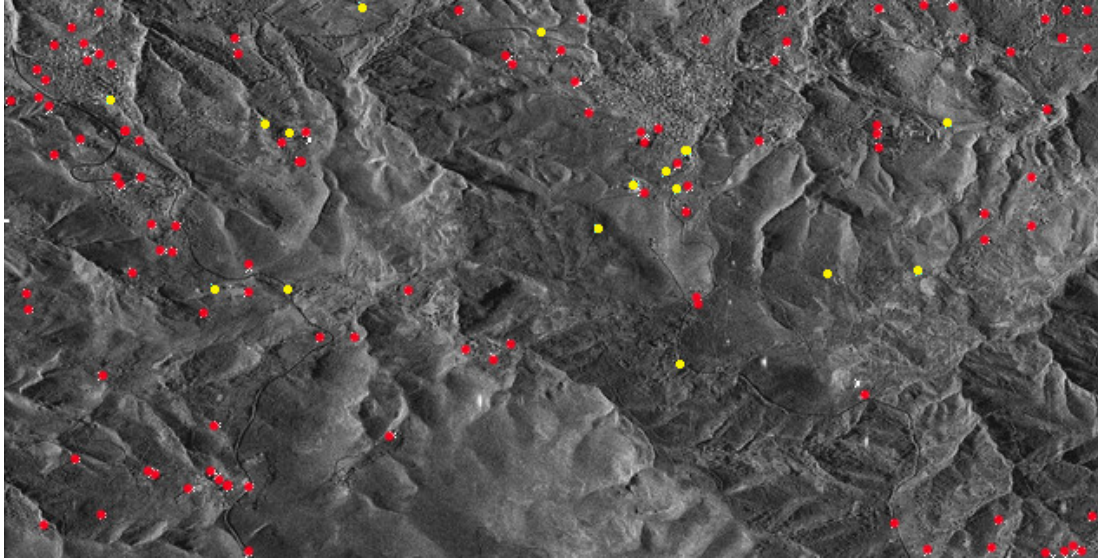


Figure 6.12: The CP distribution used for tests A (yellow) and B (red), shown on the SAR image.

and were also identified in the SAR image. Figure 6.12 shows the distribution of the CPs and Table 6.1 shows the RMSE (root-mean-square error) (in m) for the four computed transformation models (1–4). The RMSE is the root-mean-squared differences between the image coordinates of the CPs and the image coordinates of the CPs computed from their object coordinates using the computed transformation model. It is noticeable that the RMSE of the CPs is almost the same regardless of the transformation model used. The differences (1.1 m at most) are not statistically significant as they are less than the accuracy of the maps (1.4 m in range and 0.9 m in azimuth directions) and the uncertainty of the point location on the SAR image is larger than 1 pixel. It is also noticeable that the method is insensitive to temporal changes, given the abundance of GCLFs found in all cases (A0, A1 and A2). The method manages to match robustly and efficiently data which contain sections with gross temporal changes, producing low RMSE.

In the first case (A0) the GCLFs contain gross errors in various segments with temporal changes, but they cancel out. In fact, the method can also be used to identify the erroneous segments and exclude them from the matching, but this remains a subject of future research. The erroneous segments were removed manually in the second case (A1). After running tests A0, the distance of some segments of the matched roads were far larger than the rest. The length of these segments was small compared to the length of the roads. If the difference

Table 6.1: RMSE of the transformation models using CPs (meters). The error is dominated by the a-priori error of the GCI and/or CPs.

Test	GCI:GCLFs								GCI:none	
	1st order PFs		2nd order PFs		DLT		RPFs		Physical model	
	dRg	dAz	dRg	dAz	dRg	dAz	dRg	dAz	dRg	dAz
A0	1.9	3.4	2.4	4.1	2.6	3.7	2.3	4.5	2.4	3.5
A1	1.8	3.1	2.2	3.2	1.9	3.2	2.0	3.3		
A2	2.1	3.9	2.2	4.1	1.8	4.1	2.0	3.4		
B1	1.3	2.4	1.1	2.9	1.3	2.5	1.2	2.7	2.3	2.6
B2	1.3	2.6	1.2	3.5	1.5	2.8	1.3	2.9		



Figure 6.13: Some of the CPs used for test B, shown on the SAR (left) and optical (right) image.

Table 6.2: CPs RMSE (pixels), in Range and Azimuth.

Test	1st order PFs		2nd order PFs		DLT		RPFs	
	dRg	dAz	dRg	dAz	dRg	dAz	dRg	dAz
1	5.9	5.6	7.4	6.0	5.1	5.2	3.7	5.5
2	3.6	3.5	2.9	2.6	1.7	3.8	-0.1	2.9
3	-3.5	5.1	-4.6	4.5	-3.0	5.6	-2.6	4.9
4	-7.0	5.5	-7.7	4.0	-6.8	5.5	-7.2	4.5
5	-0.5	-2.4	-1.3	-3.5	-0.9	-2.8	-1.8	-3.0
6	1.8	-1.0	0.8	-1.9	1.4	-1.5	0.4	-1.4
7	1.7	4.6	0.9	3.5	1.5	4.3	0.7	4.1
8	0.8	3.3	-0.5	2.8	0.1	2.7	-1.2	3.2
9	-5.0	4.2	-8.8	6.0	-6.7	4.1	-7.8	6.9
10	4.2	-1.9	4.9	-2.0	4.1	-2.1	4.5	-1.8
11	-3.8	-4.8	-3.6	-4.5	-2.9	-5.1	-1.9	-4.6
12	-0.1	-2.9	1.2	-4.0	0.8	-2.6	1.5	-4.7
13	-4.5	3.1	-2.2	4.2	-5.0	3.1	-4.0	3.8
14	3.9	-0.2	1.4	-1.7	2.6	0.2	1.1	-1.2
15	5.7	2.2	5.7	1.1	7.5	2.7	8.7	0.4
16	-4.5	-1.9	-8.4	-0.8	-5.9	-2.2	-7.5	0.0
RMSE	4.1	3.6	4.8	3.7	4.2	3.7	4.4	3.8

was greater than a threshold (more than 3 times the average difference of the rest) and the length of the segment was greater than 5 times this threshold, the segment was excluded manually. Case A1 tends to give the best RMSE. In the last case (A2) the number of GCLFs is only 4, but they cover adequately the whole scene, and give almost the same RMSE as (A0).

In addition, for illustration purposes, Table 6.2 and Figure 6.14 show the residual in pixels of each CP using the 4 models, for the test A2.

In tests B, 108 CPs were extracted from the optical image and the corresponding DTM and were also identified on the SAR image. The abundance of solitary points which can be identified both on the optical and the SAR image offered the opportunity to collect a great number of CPs in order to improve the reliability. Features such as roads, pools, big buildings and field boundaries are identified clearly on both image types. Metallic objects appear brightly on the SAR image but it was impossible to identify them on the optical image. Built-up areas appear clearly in the optical image, but their interpretation in the SAR image was hard due to the layover and shadow effects. The elevation of features above the terrain surface could not be determined as only ground elevation information was available. Thus, the majority of CPs are corners of pools, field boundaries,

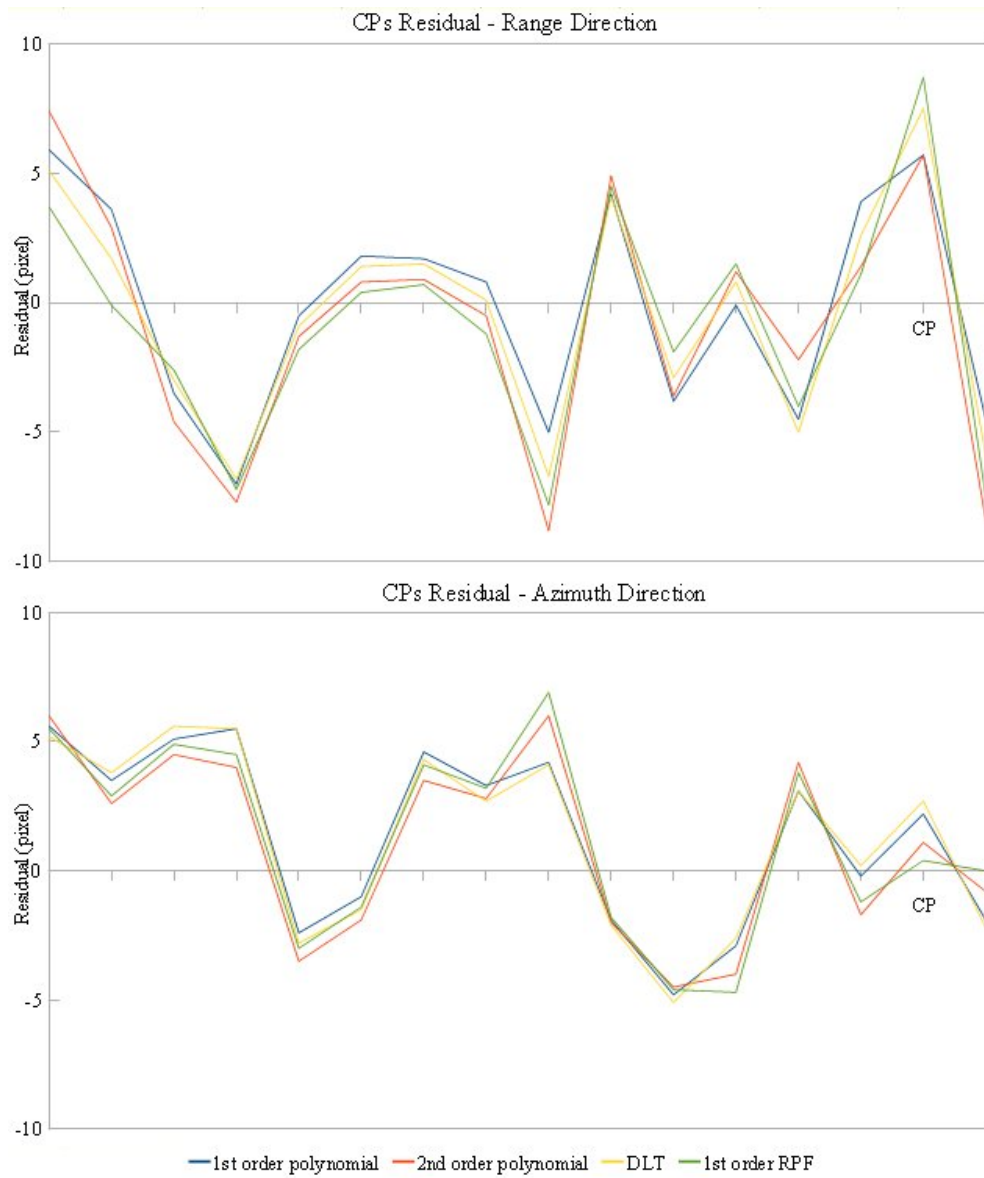


Figure 6.14: Test A2: CPs residuals in Range and Azimuth (pixels).

and characteristic points of roads. Figure 6.12 shows the distribution of the CPs, Figure 6.13 shows some of the CPs in detail and Table 6.1 shows the RMSE (in m) for the four computed transformation models (1–4).

The conclusions of tests A are verified in tests B:

1. The RMSE of the CPs is almost the same regardless of the transformation model used.
2. The RMSE is not sensitive to the number of GCLFs, if they cover adequately the scene.

It should also be noted that the RMSE is very close to the relative accuracy of the orthoimage and the corresponding DTM, computed in Section 6.1.4 (1.4 m and 0.9 m in the SAR range and azimuth directions, respectively).

The results computed with the present method (GCLFs) tend to be of better quality than those computed by solitary point based approaches. In Vassilaki and Ioannidis [2010] a terrain dependent approach was applied to the data sets of tests A using the 3D DLT (11 parameters) and the 1st order 3D RPF (14 parameters) transformations. The RMSE of independent CPs was about 3.2 m in range and about 3.0 m in azimuth direction. About the same results were later achieved by Crespi et al. [2010], who used a terrain independent approach to georeference a SpotLight COSMO-SkyMed image, using 3rd order 3D RPFs (78 parameters, 20 of which proved to be statistically significant). In Nonaka et al. [2008] a digital map at a scale of 1:2500 was used in order to evaluate the accuracy of the geometrically corrected EEC SpotLight TerraSAR-X products. The accuracy revealed to be better than 5 m in a flat area while it degraded to more than 10 m in mountainous areas.

Comparing the RMSE computed with the present method (GCLFs with empirical models) to those computed with the SAR physical model (without GCI), one might erroneously conclude that the present method is better. However, in both cases the error of the GCI and/or the CPs (map, orthoimage, uncertainty of the point location in the SAR image) dominates the (much smaller) error of the sensor. Furthermore, the empirical models reflect the relative accuracy of the GCI, while the physical model reflects the absolute accuracy of the GCI which is worse than the relative one. In Section 5.8, where the physical model was used with the data sets of tests A, the RMSE of the independent CPs is 2.4 m in range and 3.5 m in the azimuth direction. The absolute accuracy of the map, computed in Section 6.1.4, was 2.7 m and 1.7 m in the SAR range and azimuth directions, respectively. The RMSE in range is close to the one to be expected, but in azimuth it is somewhat larger. The overall 2D errors (geometric mean of range and azimuth), which are 4.2 m and 3.2 m for our results and the expected accuracy, respectively, are also relatively close. The relatively large RMSE values

in azimuth require further investigations. In test B the RMSE of the 108 CPs computed using the physical model is 2.3 m in range and 2.6 m in the azimuth direction. This is close to the absolute accuracy of the orthoimage and the corresponding DTM (the same as in test A) in range and also closer in azimuth than in test A. Again, the overall 2D error is close to the one expected (an overall RMSE of 3.4 m vs. an expected accuracy of 3.2 m). Thus, the results computed with the present method are of the same quality as the ones computed by the physical model without GCI.

6.1.7 Conclusions

The pixel location accuracy of TerraSAR-X images has been validated in the past by its operator and by independent researchers, with dedicated projects which demand the installation of corner reflectors on strategic places on the Earth's surface and the acquisition of data sets appropriate for this purpose. Although the accuracy was proven to be well below 1 m, the use of corner reflectors either as control or as check points is generally not desirable and/or feasible in everyday operational cases of research and practice, even more so in emergency situations.

The objective of this Section was to evaluate the performance of linear features as GCI for the operational georeferencing of TerraSAR-X images from map and optical images. Research conducted so far, in a sub-urban mountainous area, shows that contemporary satellite SAR sensors and the proposed method is promising with respect to robustness and accuracy: 1) linear features with large temporal changes, due to the 40 years time interval between the data acquisitions, are matched robustly and lead to a reliable recovery of the imaging geometry of the sensor (RMSE on independent CPs: 1.9 m in range and 3.2 m in azimuth), 2) linear features extracted from an optical image and the corresponding DTM are a reliable form of GCI (RMSE on independent CPs: 1.3 m in range and 2.5 m in azimuth).

The RMSE differences between the models (PFs, DLT, RPFs) are inconclusive as all models approach the accuracy of the map. The use of more accurate check points is needed for further evaluation. Automated extraction of the linear features is also expected to serve the goal of further refinement. However the latter will be not a trivial task because the road surfaces may be paved or not, and the material of the pavement may vary across a road's surface due to additional lanes. E.g. the deceleration lane may be paved, semi-paved or not paved at all. These facts differentiate the appearance of a road surfaces in the optical and the SAR images and make it hard to identify the differences, even for the human eye.

6.2 Georeferencing of not geometrically corrected optical images to geometrically corrected SAR data

The high resolution imaging modes of modern SAR sensors has made SAR data compatible with optical images. SAR data offers various capabilities which can enhance the geometric correction process of optical images (accurate, direct and ground-independent georeferencing capabilities and global DEM products). In this section an evaluation of SAR data as source of ground control information for the georeferencing of optical images is presented. The georeferencing of optical images using SAR data is in fact a co-registration problem which involves multimodal, multitemporal, and multiresolution data. And although 2D transformations have proved to be insufficient for the georeferencing process, as they can not account for the distortions due to terrain, quite a few approaches on the registration of optical to SAR data using 2D-2D transformations can still be found in the literature. In this Section the performance of 2D-2D transformations is compared to the 3D-2D projective transformation over a greater area of the Earth's surface with arbitrary terrain type. Two alternative forms of ground control information are used: points and FFLFs. The accuracy of the computed results is obtained using independent CPs and it is compared to the geolocation accuracy specification of the optical image, as well as to the accuracy of exhaustive georeferencing done by third parties.

State-of-the-art SAR sensors offer high resolution images which are comparable with high resolution optical images. They offer accurate, direct and ground-independent georeferencing capabilities and global DEM products. These capabilities combined can theoretically provide Ground Control Information (GCI) for the georeferencing of optical images. The idea of collecting GCI from air or space is quite attractive as it enhances the 'remote sensing' nature of optical images, making them independent of ground surveys which are usually necessary for the collection of the GCI. It is useful both for cases where direct georeferencing of optical images is not available and for cases where the direct georeferencing is not accurate enough.

In order to be able to extract GCI from SAR data and use it for real world operational cases, it is necessary that the SAR and optical images have also comparable accuracy. Currently, the geolocation accuracy specification defined by the operators of the sensors, as well as the pixel size of optical and SAR images, imply that the accuracy is indeed comparable. However, various results in the literature show that this is quite an unclear issue, which demands further research and experimentation:

-
1. The identification of points, the common form of GCI, is still quite ambiguous on SAR images, due to their speckled nature, slant range geometry and radiometric properties. Furthermore it is hard to guarantee that in real world practical cases, the existing methods will succeed to extract the same points on optical and on SAR images. As it is often reported in the literature, the accurate identification of homologous points on optical and SAR images is hard even for the human eye perception in real world images. This ambiguity is gradually faced using feature-based matching of more complex features (Dare and Dowman [2001], Karjalainen [2007], Hong and Schowengerdt [2005], Vassilaki [2012]) which can be identified more reliably on optical and SAR images than the points.
 2. Accuracy results on the co-registration of optical and SAR data vary. Dare and Dowman [2001] reported co-registration accuracy of 1.5 pixel for low terrain height variations, Hong and Schowengerdt [2005] reported co-registration accuracy of 0.6–3 pixels for reasonably flat terrain, Vassilaki et al. [2009b] reported 1 pixel for small image patches over hilly terrain. Reinartz et al. [2011] reported co-registration accuracy of 2–6 pixels for the co-registration of a satellite optical image to a geometrically corrected satellite SAR image over urban areas with moderate terrain. Vassilaki [2012] reported roughly the same accuracy as Reinartz et al. [2011] for the co-registration of a whole satellite slant range SAR image to a geometrically corrected aerial optical image, on mountain terrain with direct georeferencing (Vassilaki et al. [2011b]).

Accuracy results reported in literature should not be interpreted comparatively, as different methods, data sets, terrain and land use, under different objectives were processed. The only safe conclusion is that the state-of-the-art methods achieve roughly 1 pixel accuracy for the co-registration of small patches of data, which are geometrically corrected, or/and over flat areas. However, the accuracy of co-registration of real world, not geometrically corrected, data over greater areas of the Earth’s surface with arbitrary terrain type (not necessarily flat) remains an open issue.

This Section contributes to this research framework by presenting the an evaluation of SAR data as source of GCI. In the following subsections, the objectives of the study are presented, the test site and the data sets, and the methods and the tools which are used. The results of the study are presented and discussed.

6.2.1 Test site and data sets

The test site is JRC’s Maussane Terrestrial Test Site which is located near Maussane-les-Alpilles in South France. The area exhibits numerous land uses

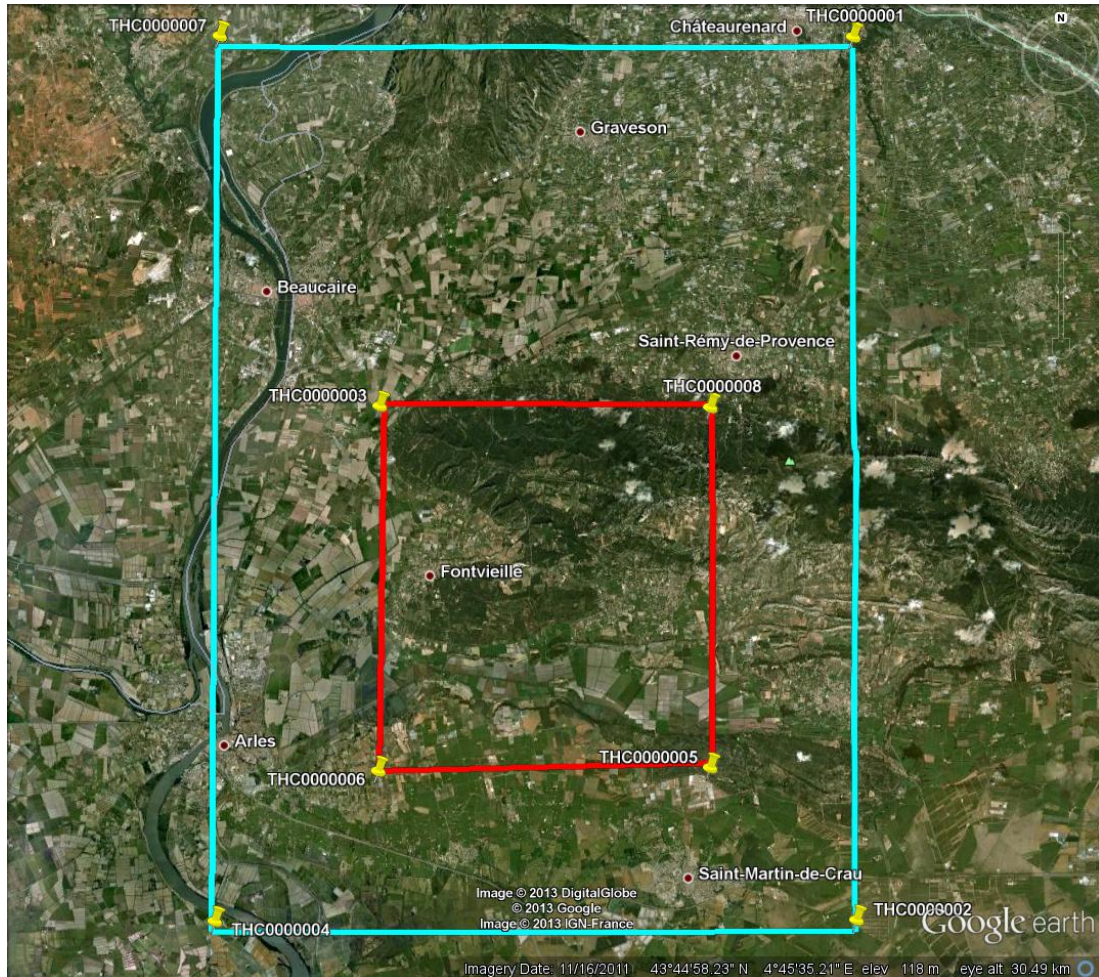


Figure 6.15: Test site and coverage of the satellite optical image (in red) and the aerial SAR data (in cyan).

(forest areas, olive groves, small urban areas, water bodies) and terrain variations (mountains, plains and water bodies). The area used in this Section spans $4^{\circ} 40'$ to $4^{\circ} 50'$ E and $43^{\circ} 39'$ to $43^{\circ} 46'$ N (Figure 6.15) and is about 100 Km^2 .

The SAR data over Maussane test site was collected in 2009 and consists of geometrically corrected aerial SAR images (Figure 6.16), DSM (Figure 6.17) and DTM which were interferometrically produced, and the 3D road network (Figure 6.16) which was extracted by the geometrically corrected SAR images and the DSM/DTM (Mercer [2007], Zhang et al. [2010], Intermap [2013]). The geometrically corrected SAR images have 1.25 m pixel size and according to the general accuracy specifications their horizontal absolute accuracy is 4 m (CE90%). The DSM/DTM are posted at 5 m and according to the general accuracy specifications

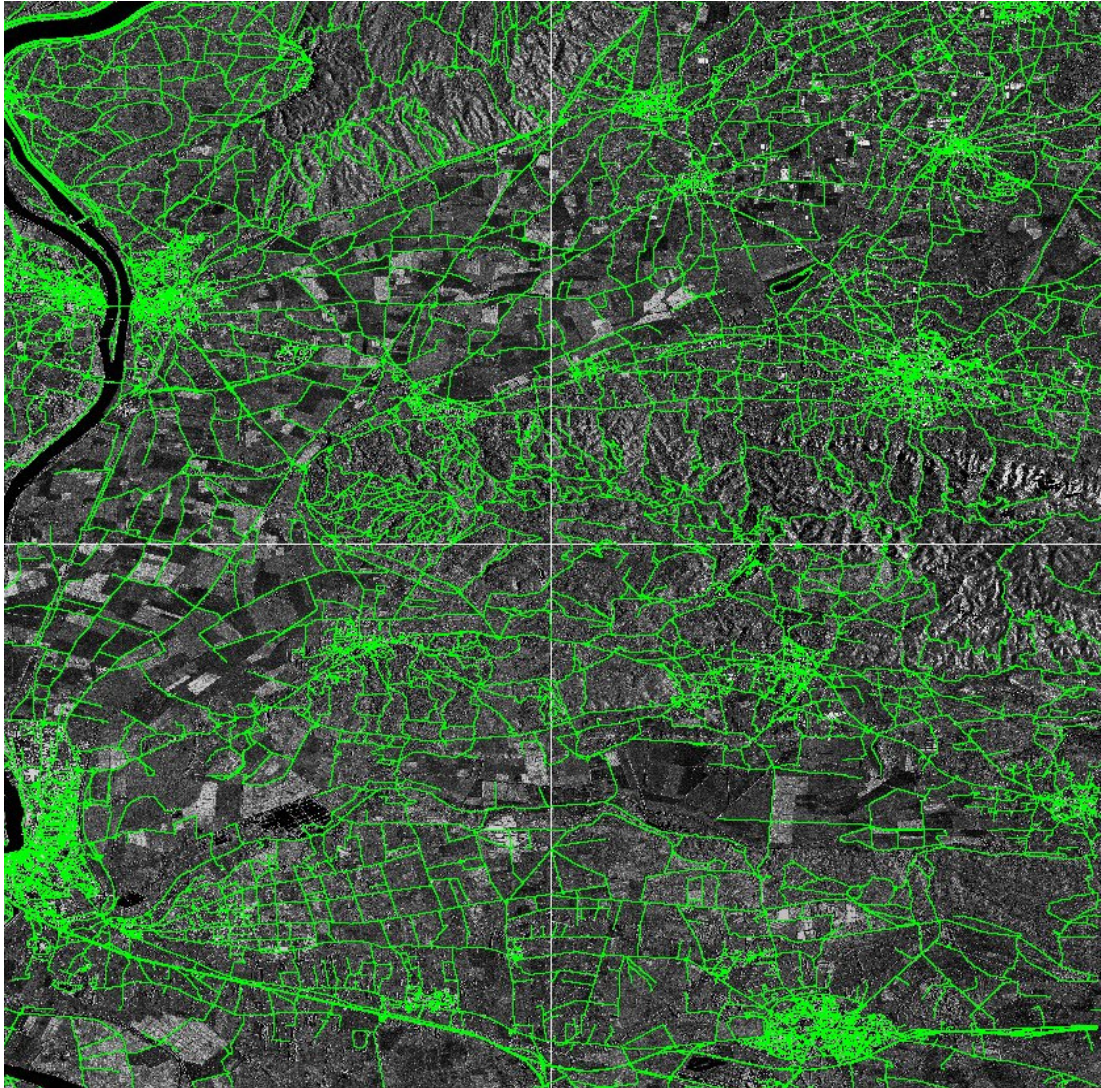


Figure 6.16: 3D roads centrelines overlaid on the geometrically corrected SAR image.

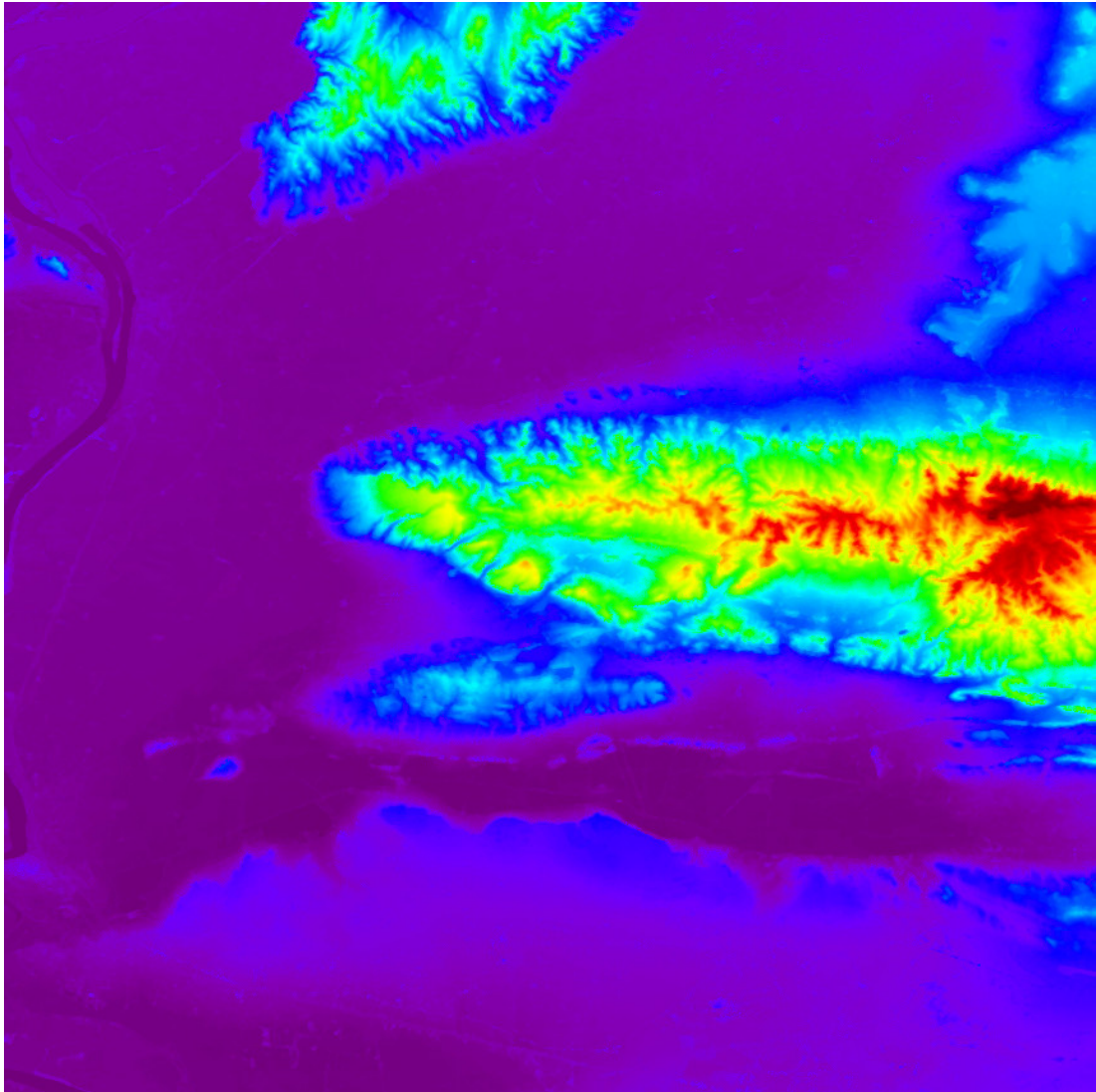


Figure 6.17: The interferometrically produced DSM.

the vertical accuracy is < 1 m (LE90%) for the 40% of the coverage area, 1–3 m (LE90%) for the 40% of the coverage area and > 3 m (LE90%) for the rest 20% of the coverage area. The planar geometry of roads' centrelines was extracted from the geometrically corrected SAR images and the elevation of the centrelines was determined from the interferometrically produced DTM/DSM. The accuracy of the 3D road network meets the accuracy of the initial SAR data. The planar coordinates (geographic latitude/longitude) are available in the horizontal geodetic datum ETRS89 (European Terrestrial Reference System 1989). The orthometric elevation is provided in the EGG07 (European Gravimetric Geoid model 2007) vertical geoid model.

The optical image was collected in 2010 and it is a level 2A standard satellite imagery. The nominal spatial resolution of the panchromatic imaging mode is 50 cm, and 2 m for the multispectral (8 spectral bands) imaging mode (Digital Globe [2013]). The general geolocation accuracy specification of the optical image is 6.5m (CE90%), with predicted performance in the range of 4.6 to 10.7 m (CE90%), excluding terrain and off-nadir effects. The geolocation accuracy specification of the optical image using GCPs is 2.0 m CE90% (Digital Globe [2013]). The off-nadir view angle is 36° , the cross-track view angle is 34.7° and the in-track view angle is -10.4° for the specific image used in this Section (Nowak Da Costa and Walczynska [2011]).

6.2.2 Overview and objective

The significance of using GCI for the geometric correction of optical images has been noted, analysed, researched and discussed exhaustively in the related literature. The most common form of GCI is the point, the fundamental feature of all photogrammetric processes. Numerous methods, data sets and tests have been presented over the years using GCPs (Toutin [2004], Dowman et al. [2012]. Repetition of this long-term research and practical knowledge would be redundant.

The general objectives of the study (Section 1.5) are:

1. To contribute to the evaluation of SAR data as source of GCI for the georeferencing of optical images.
2. To benchmark the performance of two alternatives forms of GCI: Ground Control Linear Features (GCLFs) and Ground Control Points (GCPs).

The accuracy of the georeferencing (either using GCLFs or GCPs) is computed using manually collected independent check points (CPs). The accuracy of the georeferencing is compared to the geolocation accuracy specification of the optical image, as well as to the accuracy of the exhaustive georeferencing done by third

parties. The test area is the well-known JRC's Maussane test site near Maussane-Alpilles in France.

The georeferencing process establishes the relationship of the 2D image space with the 3D object space. 3D-2D projection transformation models (empirical or physical) are used for this purpose (Toutin [2004], Dowman et al. [2012]). Although literature abounds with fully justified conclusions on the general unsuitability of 2D-2D projective transformations for the georeferencing process, 2D-2D transformations (even simple 2D rigid and affine ones) are still used for the development of methods for the co-registration of optical and SAR images. Arbitrary assumptions such as of flat terrain, small image patches and geometrically corrected images, enable such methods to compute good results.

The specific objective of this Section is to test the performance of the 2D-2D projective transformations applied to the georeferencing of a level 2A satellite optical image using SAR data (in other words the co-registration of optical and SAR data), over greater areas of the Earth's surface (not just small image patches), with terrain of arbitrary form (not necessarily flat). Two different transformation models are used in this Section: 1) 2D-2D and 2) 3D-2D 1st order polynomial functions (PFs). Two different forms of GCI are used: 1) GCPs and 2) GCLFs.

6.2.3 Method

The significance of using GCI for the geometric correction of optical images has been noted, analysed, researched and discussed exhaustively in the related literature. The most common form of GCI is the point, the fundamental feature of all photogrammetric processes. Numerous methods, data sets and tests have been presented over the years using GCPs (Toutin [2004], Dowman et al. [2012]). Repetition of this long-term research and practical knowledge would be redundant.

More complex features, such as straight lines and Free Form Linear Features (Section 2.2) can be exploited as an alternative/complementary form of GCI. The matching of networks of FFLFs of different dimensionality (Section 2.11.6) are used here. The initial approximation is computed as described in Sections 2.11.4 and 2.9.4. A common projective transformations is computed for all pairs of FFLFs of the networks (Section 2.11.3).

6.2.4 Measurement of the GCI

160 common points were identified between the optical and the SAR image. They were measured in the 2D optical image space (pixels) and in the 3D object space (meters) of the SAR image. The elevation of the points measured on the SAR image was interpolated from the available interferometrically produced DEM (DSM). Some of the points were used as GCPs in order to compute the

transformation models, and the remainder of the points were used as CPs in order to evaluate the computation. As the optical and the SAR image were unitemporal and the SAR image was geometrically corrected, it was not very hard to identify common regions and characteristics. On the other hand, the fuzzy and speckled nature of the SAR image made the identification and measurement of single points ambiguous. The computation of the transformation model (Section 6.2.5) and its application to project 3D points to the optical image, revealed a few gross errors and point ambiguities, which either could not be resolved and thus new points were measured, or led to re-measurement of the picked points. The procedure was then iterated many times. In general the measurement of the common points between the optical and the SAR image was a very laborious process.

Additionally 23 FFLFs were identified between the optical and the SAR image. The SAR data was accompanied by the vectors of the centrelines of the roads (3D Road Vectors) Zhang et al. [2010] and thus no extraction of roads was necessary on the SAR data (Figure 6.16). Common roads between the SAR data and the optical image were identified and then the edges of the roads were extracted manually on the optical image. The centrelines of the roads on the optical image space were computed with skeletonisation techniques. Although it was possible to identify a multitude of common roads between the optical and the SAR image, just a few of them were sufficient to ensure full GCI coverage of the optical image. The road centrelines were then used as matching primitives. The FFLFs with known 2D optical image space coordinates and known 3D object space node coordinates (readily available from the geometrically corrected SAR image and the DEM) were then used as GCLFs in order to compute the transformation model. Some editing (mostly merging) was needed to group the 3D roads according to the 2D roads. In general the measurement of common FFLFs was a straightforward and swift process.

6.2.5 Computation of the georeferencing

For both forms of GCI, 2D-2D and 3D-2D transformation models were used to georeference the optical image. The transformation models used are the following 1st order polynomial functions (PFs):

1. The 2D-2D 1st order PFs, with 6 unknown parameters:

$$\begin{aligned} x &= a_1X + a_2Y + a_3 \\ y &= b_1X + b_2Y + b_3 \end{aligned} \tag{6.8}$$

2. the 3D-2D 1st order PFs, with 8 unknown parameters:

$$\begin{aligned}x &= a_1X + a_2Y + a_3Z + a_4 \\ y &= b_1X + b_2Y + b_3Z + b_4\end{aligned}\tag{6.9}$$

Four combinations of GCI and transformation models were used for the computation of the georeferencing of the optical image:

1. 2D-2D PFs and GCPs.
2. 2D-2D PFs and GCLFs.
3. 3D-2D PFs and GCPs.
4. 3D-2D PFs and GCLFs.

In the first and the third case 11 points which span the optical image were used as GCPs (Figure 6.18) for the computation of the correspondent transformation model. In the second and the fourth case 23 FFLFs which span the optical image were used as GCLFs (Figure 6.18) for the computation of the correspondent transformation model. As a byproduct of the georeferencing process, the 23 GCLFS also produced automatically 91788 common 3D-2D points between the two data sets (2D optical image space and 3D object space of the SAR image). These points can be exploited by any standard photogrammetric/remote sensing software which does not have GCLFs capabilities.

6.2.6 Evaluation

The RMSE of the four cases was computed using manually collected independent CPs. From the 160 common points between the optical and the SAR image (Section 6.2.4), 11 points were used as GCPs (Section 6.2.5) and the remaining 149 points (in green in Figure 6.18) were used as CPs. The RMSE is shown in Table 6.3.

The accuracy of the four cases was evaluated using: i) the geolocation accuracy specification of the optical image which is 6.5 m (CE90%), with predicted performance in the range of 4.6 to 10.7 m (CE90%), excluding terrain and off-nadir effects, ii) the geolocation accuracy specification of the optical image with registration to GCPs which is 2.0 m (CE90%) and iii) the accuracy computed independently by JRC using GCPs and CPs measured with GPS (Nowak Da Costa and Walczynska [2011]) and exhaustive testing of mathematical models as implemented in numerous standard software. The computed accuracy (Table 6.3) shows that:

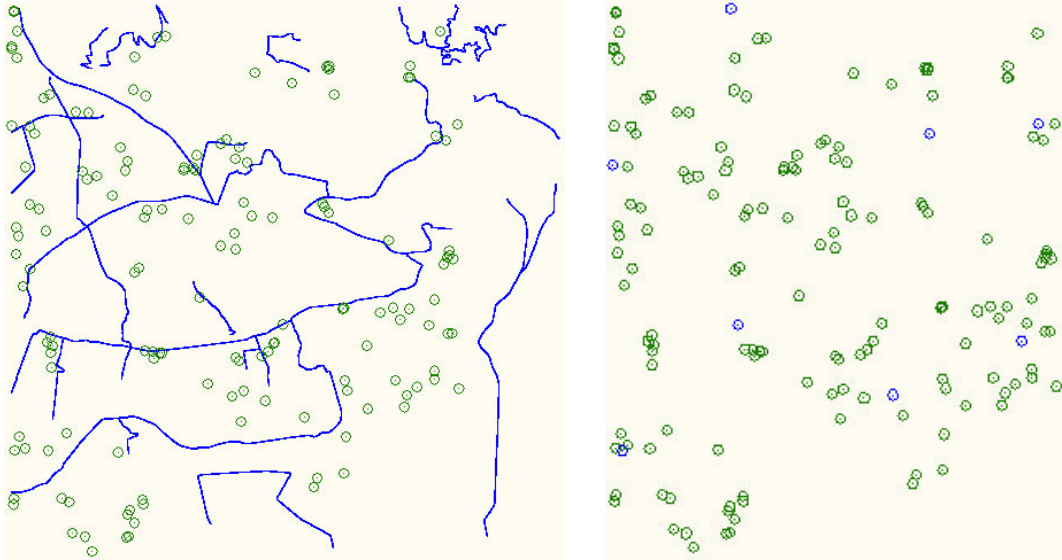


Figure 6.18: The distribution of GCLFs and GCPs (in blue) and CPs (in green) over the test site. GCLFs and CPs (left), and GCPs and CPs (right).

Model	GCI	X (m)	Y(m)	Planar (m)
2D-2D PFs	GCPs	32.3	14.6	35.4
	GCLFs	37.8	35.0	51.5
3D-2D PFs	GCPs	2.5	2.7	3.7
	GCLFs	2.5	2.4	3.5

Table 6.3: The CPs RMSE using 1st order 2D-2D and 3D-2D PFs for the two different forms of GCI (GCPs and GCLFs).

-
1. The 2D-2D transformations lead to far worse accuracy (several tens of meters) than the geolocation accuracy specification defined by the operator of the sensor (6.5 m), for both forms of GCI (GCPs and GCLFs). Furthermore, since a level 2A satellite optical image was used in this Section, the accuracy is expected to be even worse in the case of basic imagery products (for instance level 1A). Thus the 2D transformations should be abandoned for real world practical cases over greater areas of the Earth's surface with arbitrary terrain.
 2. The two forms of GCI (GCPs and GCLFs) used in this Section lead to the same accuracy (3.5 m), probably because it reflects the accuracy of the CPs themselves, namely 4 m planar and 1–2 m vertical accuracy. However, it should be noted that the measurement of the common points between the optical and the SAR image was a laborious process and thus the georeferencing using GCLFs is considered superior.
 3. The computed accuracy (3.5 m) does not (and can not) meet the geolocation accuracy specification with registration to GCPs (2 m). More accurate GCI (for example measured with GPS) should be used for this purpose (Nowak Da Costa and Walczynska [2011]). However, the computed accuracy (3.5 m) is better than the geolocation accuracy specification without GCPs (6.5, with predicted performance in the range of 4.6 to 10.7 m), more so because the geolocation accuracy specification does not include terrain and off-nadir effects, while the test region and data include both effects.

6.2.7 Conclusions

In this Section an evaluation of SAR data as source of GCI, under realistic conditions, was presented. More specifically GCPs and GCLFs were collected from geometrically corrected SAR images and the corresponding interferometrically produced DEM. They were used to compute the georeferencing of a level 2A satellite optical image over a greater areas of the Earth's surface (not just a small patch), with arbitrary terrain type (not necessarily flat). Both 2D-2D and 3D-2D transformation models were used and the accuracy was evaluated using independent CPs. The accuracy of the 2D-2D models was unacceptable to the point that they should not be used at all. The accuracy of the 3D-2D models reached the accuracy of the CPs themselves, which suggests that more accurate GCI will probably lead to better accuracy, and that SAR data has compatible accuracy with optical images. Further research and experimentation on the subject is thus encouraged.

6.3 Co-registration of not geometrically corrected optical and SAR imagery over mountainous areas through automatic free-form features global matching

An algorithm, for automatic global matching of heterogeneous free-form features (natural features) between the 3dimensional object space and the 2dimensional image space, taking into account the non-rigid nature of the projection transformation is presented in this Section. The algorithm is based on the the well-known Iterative Closest Point (ICP) algorithm. The algorithm is tested for the co-registration of high resolution TerraSAR-X and optical imagery of a mountainous site in the North East of Athens. The registration is based on free-form road centreline matching. Ground Control Linear Features (GCLFs) and DTM information is obtained from old existing maps of the area, while road centrelines are calculated from road edges using skeletonisation techniques. The geometric correction is done with the developed techniques and the results are encouraging.

Recent advances in SAR sensors, such as the unprecedented resolution of TerraSAR-X's and COSMO-Skymed's sensors, have conceptualised the complementary use of optical and SAR satellite data. SAR and optical data present many differences and similarities simultaneously. Although, in the past, the similarities led to the competition for the exclusive use of SAR or optical data, today their differences, and thus their mutual usefulness and effectiveness are fully appreciated. The concept of complimentary use of SAR and optical data is illustrated by the cooperation of optical and SAR satellites, (e.g. CNES/ASI Orfeo program), by the installation of both optical and SAR sensors on the same satellite (e.g. ALOS system), as well as by the compilation of scientific studies which end up in some specific applications of their combined use (Bellman and Hellwich [2006], Raouf and Lichtenegger [1997], Crosetto [1998], Honikel [1998], Karkee et al. [2006], Tupin [2006], Sörgel et al. [2008], Orsomando et al. [2007], Wegner et al. [2008]).

SAR and optical data registration is a prerequisite procedure of significant importance in many applications, such as image fusion, stereo formation and change detection. Although a lot of work has been done in the field of image registration (Zitova and Flusser [2003]), it remains an active field of research, especially for multimodal and multitemporal cases (Inglada and Giros [2004]), as the ones examined in this Section.

The new generation of space-borne sensors, described before, offers the capability of the identification of terrain features, such as roads' surfaces, especially paved ones (Eineder et al. [2009]), that was impossible to distinguish with sensors

of the previous generation.

Feature Based Photogrammetry states that linear features exhibit certain advantages over the classical, point based, approach for the orientation processes. Major advantages of linear features against points are (Mikhail [1993], Zalmanson [2000], Habib and Kelley [2001], Akav et al. [2004], Wang et al. [2008]):

1. Man-made and physical environment is rich of linear features (roads, pipelines, coastline).
2. Linear features can be detected more reliably.
3. The matching of linear features is more reliable.
4. Linear features consist a continuous control of information.
5. The identification of common linear features is more robust than node identification in multimodal and multitemporal registration, because experience tells that identification of common nodes is difficult and rare, and when a common pair of nodes is found (for example a crossroad), their exact relative position is often questionable.

This Section focuses on the joint use of optical and SAR images, and takes advantage of the linear features and the high resolution of the new space-borne SAR sensors. A feature-based matching method for the registration of not geometrically corrected optical and SAR images is presented. Applications were made on mountainous areas, which are not thoroughly investigated so far.

The method is based on the Iterative Closest Point (ICP), and matches heterogeneous FFLFs from the 3dimensional object space to the 2dimensional image space (Section 2.8). In order to converge, the ICP needs a good initial approximation which weakens its practicality, or at least it makes it awkward to use, as an initial approximation must be given to the method manually. Thus the automated computation of a good initial approximation of Section 2.9.4 is used.

The philosophy of the method, ignoring temporarily the algorithmic implementation, is that the microwave nature of SAR sensors in combination with the side-looking geometry, makes the identification of homologous free-form features much easier and less ambiguous, than the identification of solitary point features, which are traditionally used for the georeferencing and registration procedures. And that the same Ground Control Information is used for the georeferencing of SAR images and the georeferencing of the optical images, which leads to better co-registration of the images and less time and cost for the procedure.

The method is tested with the registration of recent high resolution optical and SAR satellite images to a 40 years old archived topographic map is presented.

Various projective transformations are employed for the registration of the data sets using FFLFs as matching primitives. Both images were geometrically corrected for illustration purpose (Section 3.3.1).

6.3.1 Projective transformations models

The matching of 3D and 2D FFLFs as described in Section 2.8 is independent of the type of the projective transformation. Here, three different 3D-2D projective transformation models (Equations 6.10 to 6.12) are employed for the registration of the data sets using FFLFs as matching primitives:

1. The 1st order 3D-2D Polynomial Functions (PFs) with eight unknown parameters:

$$x = a_1X + a_2Y + a_3Z + a_4, \quad y = b_1X + b_2Y + b_3Z + b_4 \quad (6.10)$$

2. The 1st order Rational PFs (RPFs) with common denominator (3D Direct Linear Transform: 3D-DLT), with 11 unknown parameters:

$$x = \frac{a_1X + a_2Y + a_3Z + a_4}{c_1X + c_2Y + c_3Z + 1}, \quad y = \frac{b_1X + b_2Y + b_3Z + b_4}{c_1X + c_2Y + c_3Z + 1} \quad (6.11)$$

3. The 1st order 3D-2D RPFs with 14 unknown parameters:

$$x = \frac{a_1X + a_2Y + a_3Z + a_4}{c_1X + c_2Y + c_3Z + 1}, \quad y = \frac{b_1X + b_2Y + b_3Z + b_4}{d_1X + d_2Y + d_3Z + 1} \quad (6.12)$$

In any case the matching method computes a large number of interpolated points between the two FFLFs, thus the system of equations is overdetermined and the LSA is employed in order to solve it. Equations 6.10 are linear and the estimation of the unknown parameters is a straightforward process with LSA. Equations 6.11 and 6.12 are non-linear but can be turned into linear ones by multiplying the two parts of the equations by the denominator.

The use of multiple projection transformations showcases the generality of the matching method (Section 2.8).

6.3.2 Two stage initial approximation

The computation of the initial approximation uses the rigid approach (Section 2.9.4), for single pairs of FFLFs of different dimensionality (3D-2D). While this is sufficient for the case of optical images, it is not generally sufficient for the non-rigid nature of the geometry of the SAR sensor. The initial approximation does

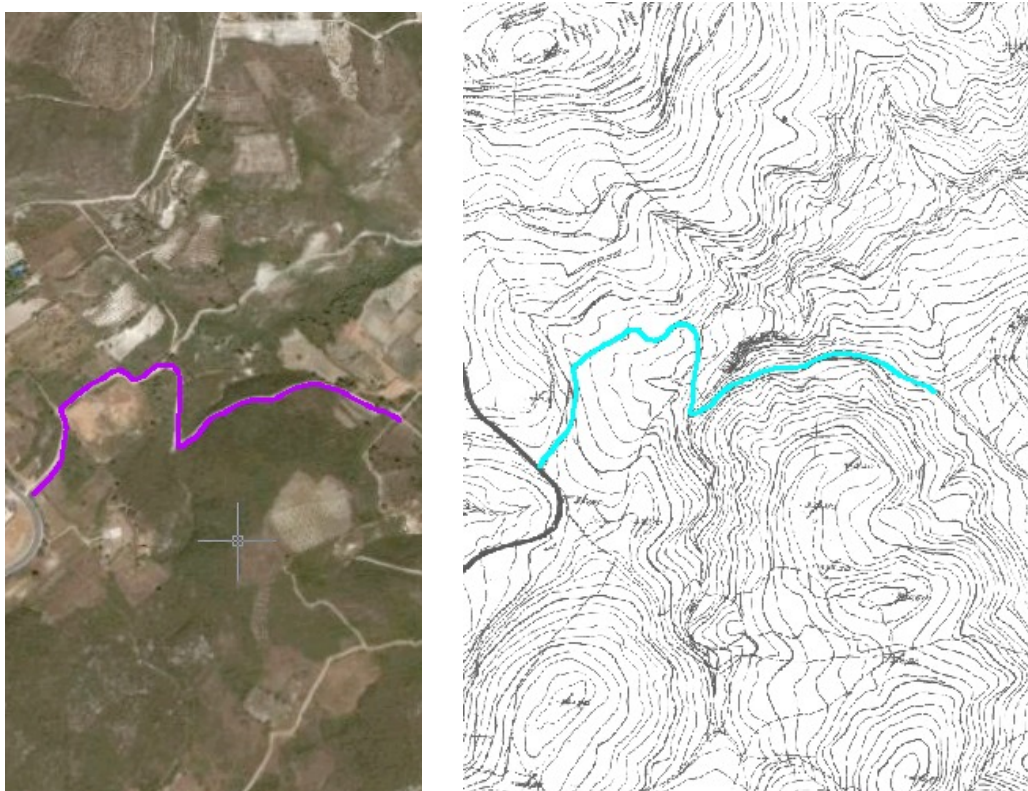


Figure 6.19: Topographic map (right) and optical image (left).

not trigger ICP convergence when 3D-DLT and 1st order RPF is used. However, the 1st order polynomial is the most stable projection, and the ICP does converge using it. The result can be used successfully as an initial approximation to 3D-DLT and 1st order RPF.

Thus a two stage initial approximation is established for higher order projective transformations applied to SAR images. The 1st order polynomial is computed, and then this is used as a better initial approximation for the higher order projective transformation.

6.3.3 Data sets

The data sets of this test are:

1. A recent high resolution spotlight TerraSAR-X SSC image with single polarisation (HH); it is a Single look Slant range Complex image (SSC). The SAR image was captured on February 2nd, 2009. The range resolution is 0.45 m and the azimuth line resolution is 0.87 m (Figure 6.20).

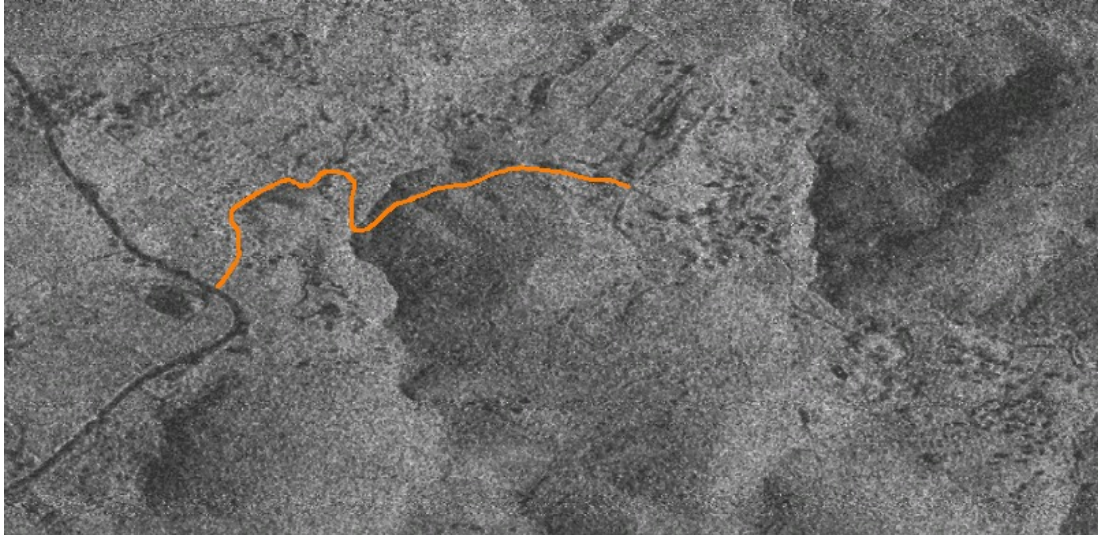


Figure 6.20: SAR image.

2. An optical image downloaded from Google Earth (Figure 6.19). The optical image was captured by DigitalGlobe.
3. A 40 years old medium scale (1:5 000) archived topographic map (Figure 6.19).

The application area is in the greater north-eastern region of Athens, Greece, and it has steep mountainous terrain of mean elevation of 270 m (Figures 6.19 and 6.20).

6.3.4 Preprocessing

TerraSAR-X's datafile (XML, cos) was converted to common standard format TIFF using software ERDAS v9.3. The GDAL library could be used for the same job. The SAR image was converted to intensity, while keeping the slant range geometry of the original image. Then the image was flipped horizontally because it was the mirror of the optical image. No conversion was done to the optical image. The map was scanned with 400 DPI resolution and it was imported to CAD software, where it was corrected from the errors due to the contractions/expansions of the paper medium, and it was transformed to the new national geodetic reference system.

The road which was used as a linear feature of the matching, is shown in Figures 6.21 – 6.23. The road edges extraction was done manually, by digitising the lines appeared on the data. The road centreline was obtained from the edges

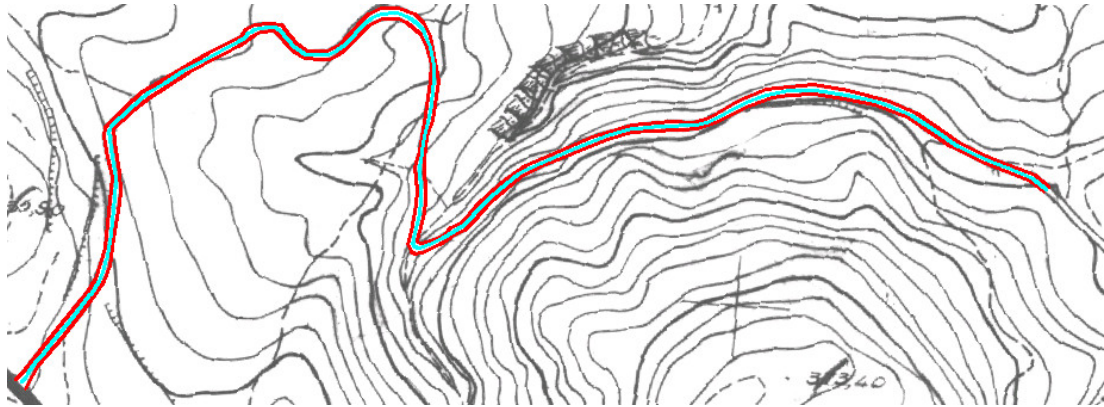


Figure 6.21: Map: road edges (lines in red), road centreline (in cyan).

using skeletonisation techniques (Figures 6.21, 6.22, 6.23). The length of the road is about 950 m. The road centreline is preferred to road edges as control FFLF, because it has less error than the edges and it fully represents the geometry of the road.

The contour lines of the map, were digitised and converted to Triangulated Irregular Network (TIN) via Delaunay triangulation, which was used for the geometric correction. The TIN was also used as DTM in order to extract elevation information of the road.

The rough profile of the road centreline is due to the small scale of the map and the fact that the map does not have elevation information along the surface of the road. The centreline elevation was computed by the surrounding terrain (Figures 6.21 and Figures 6.24).

6.3.5 Geometric correction

The geometric correction of both images, which was done for illustration purpose, was done using the method described in Section 3.3.1. The necessary TIN was obtained by the map digitising the contour lines. The type of the projective transformation used for the geometric correction of both images was the RPFs.

6.3.6 Work flow of the test

The computational steps taken for the test may be summarised as follows:

1. Preprocessing (SAR, map).
2. Extraction of road edges (SAR, optical, map).



Figure 6.22: Optical: road edges (lines in green), road centreline (in magenta).

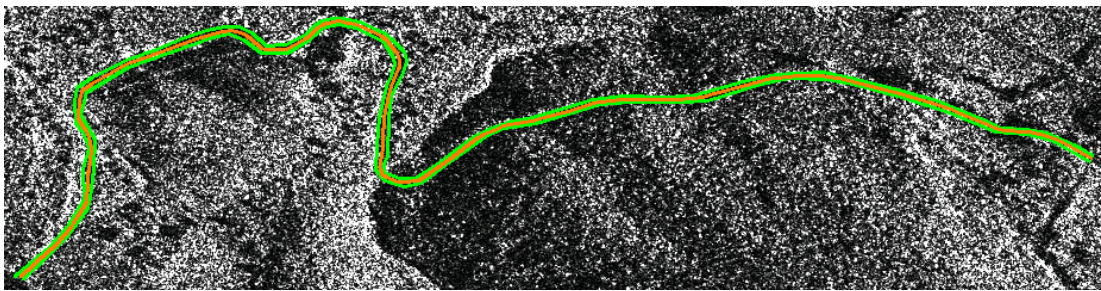


Figure 6.23: SAR image: road edges (line in green), road centreline (in orange).

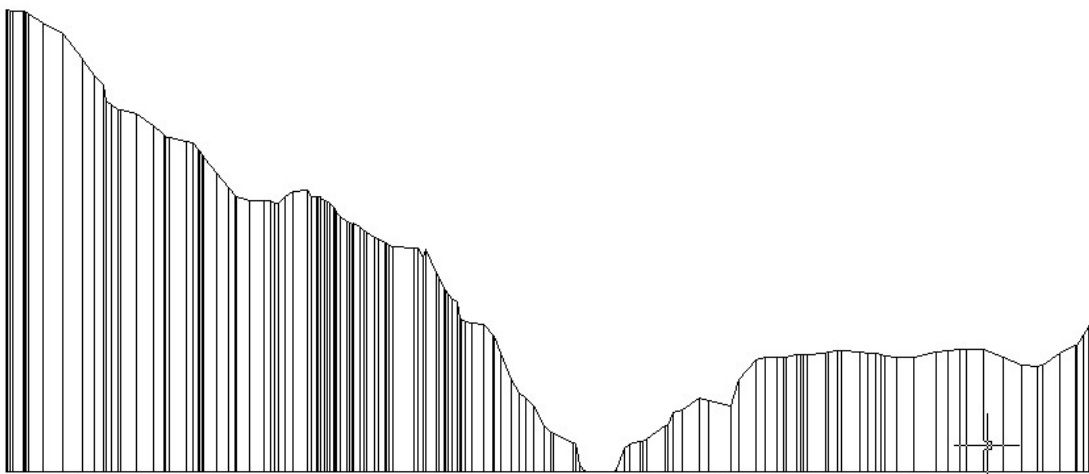


Figure 6.24: Profile of road centreline, computed by the DTM.

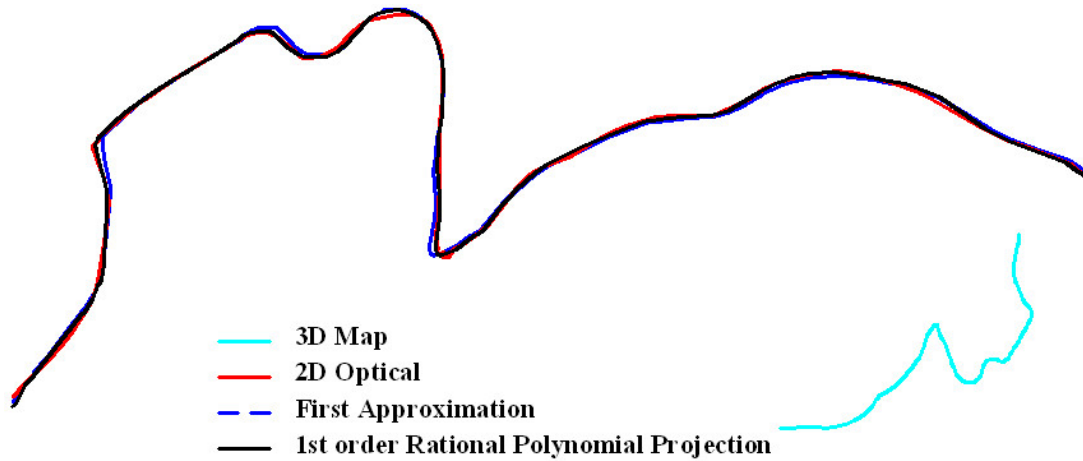


Figure 6.25: Matching results: Optical image to Map.

3. Calculation of road centreline (SAR, optical, map).
4. SAR to map matching, using 3D road centreline and its 2D projection.
5. SAR geometric correction, using the TIN obtained by the map and the projection computed in step iv.
6. Optical to map matching, using 3D road centreline and its 2D projection.
7. Optical geometric correction, using the TIN obtained by the map and the projection computed in step vi.
8. SAR to optical overlay, for illustration purposes.

6.3.7 Results

The results of the matching are shown in Figures 6.25 and 6.26 for the optical image and for the SAR image respectively. For illustration purposes the initial FFLFs are shown together, though in reality their coordinates are completely unrelated. The figures show the 3D FFLF from map (in cyan), the 2D FFLF from SAR/optical (in red), the initial approximation as computed by the rigid approach (in blue dashed), the matched 3D FFLF to 2D using similarity transformation (light blue dashed dot), the matched 3D FFLF to 2D using 1st order RPFs (in black). The matched 3D FFLF using 1st order PFs and 3D-DLT are too close to the one using RPFs to be shown in the Figures.

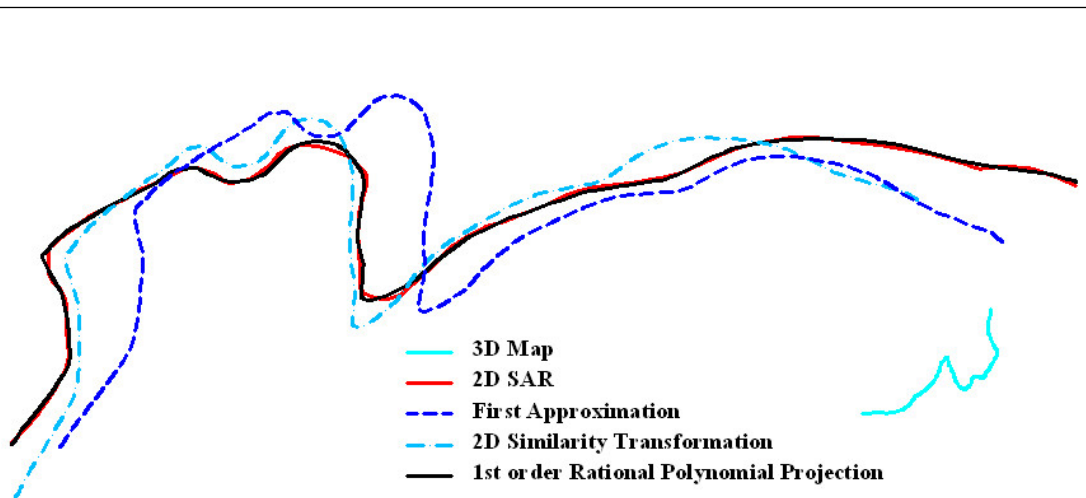


Figure 6.26: Matching results: SAR image to Map.

Table 6.4: RMSE of the matching processes for the SAR and the optical image.

Transformation/projection projection	SAR to map RMSE(m)	Optical to map RMSE(m)
Initial approximation	13.61	3.20
2D Similarity	8.15	2.29
1st order Polynomial	1.61	1.49
3D-DLT	1.42	1.39
1st order RPFs	1.39	1.08

As shown in Figures 6.25 and 6.26 the matching of the FFLFs is successful. The RMSE between the matched FFLFs is shown in Table 6.3.7 for various projection types. The achieved matching accuracy using the projective transformations (3D-2D) is more than satisfactory, considering that the horizontal and vertical accuracy of the topographic map is of 1.5 m and 2 m respectively. The 2D transformations lead to poor results as the terrain is not flat. A combination of the geometrically corrected images in chess board pattern is shown in Figure 6.27.

6.3.8 Conclusions

In this Section, a method for automatic global matching of heterogeneous free-form linear features between the 3dimensional object space and the 2dimensional image space was presented. The method is based on ICP and handles any non-rigid projection type. The method uses linear features which are much easier

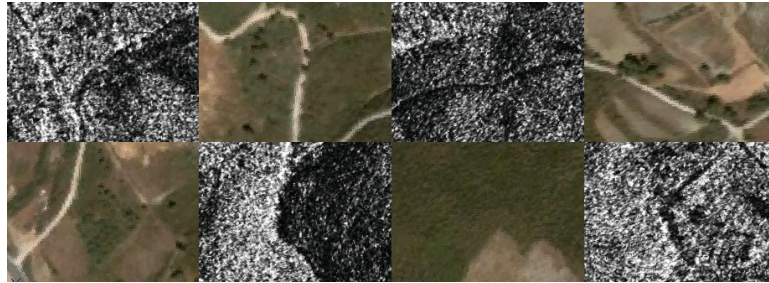


Figure 6.27: The co-registered optical and SAR images geometrically corrected.

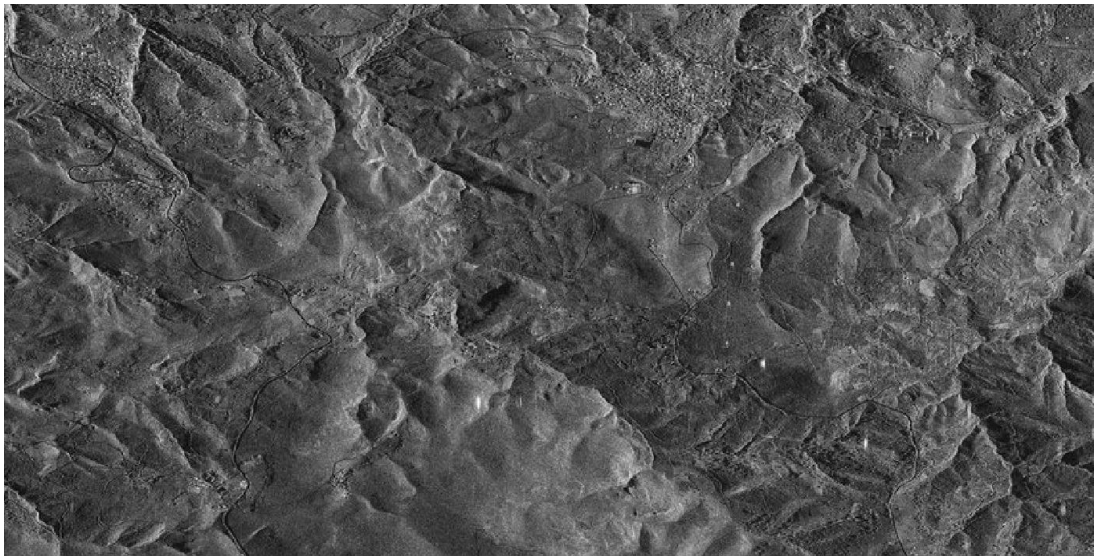


Figure 6.28: SAR image.

to locate and more robust than solitary points, especially for the speckled SAR images. The method produces very good results, as was illustrated in a typical mountainous site of Greece.

6.4 Fusion of optical and SAR images in slant range SAR geometry

Recent advances in the field of space-borne SAR sensors came up with sensors able to collect high resolution satellite SAR images with GSD at the order of 1m. Such detailed illustration of the Earth's surface makes it possible to identify



Figure 6.29: Optical image.

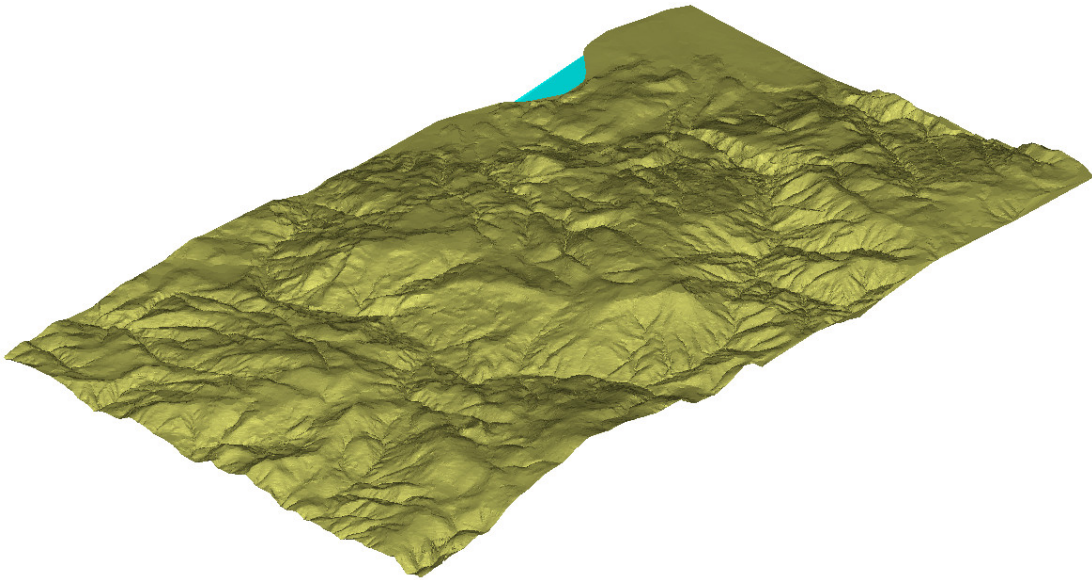


Figure 6.30: Shaded representation of TIN created by the contours of the map.

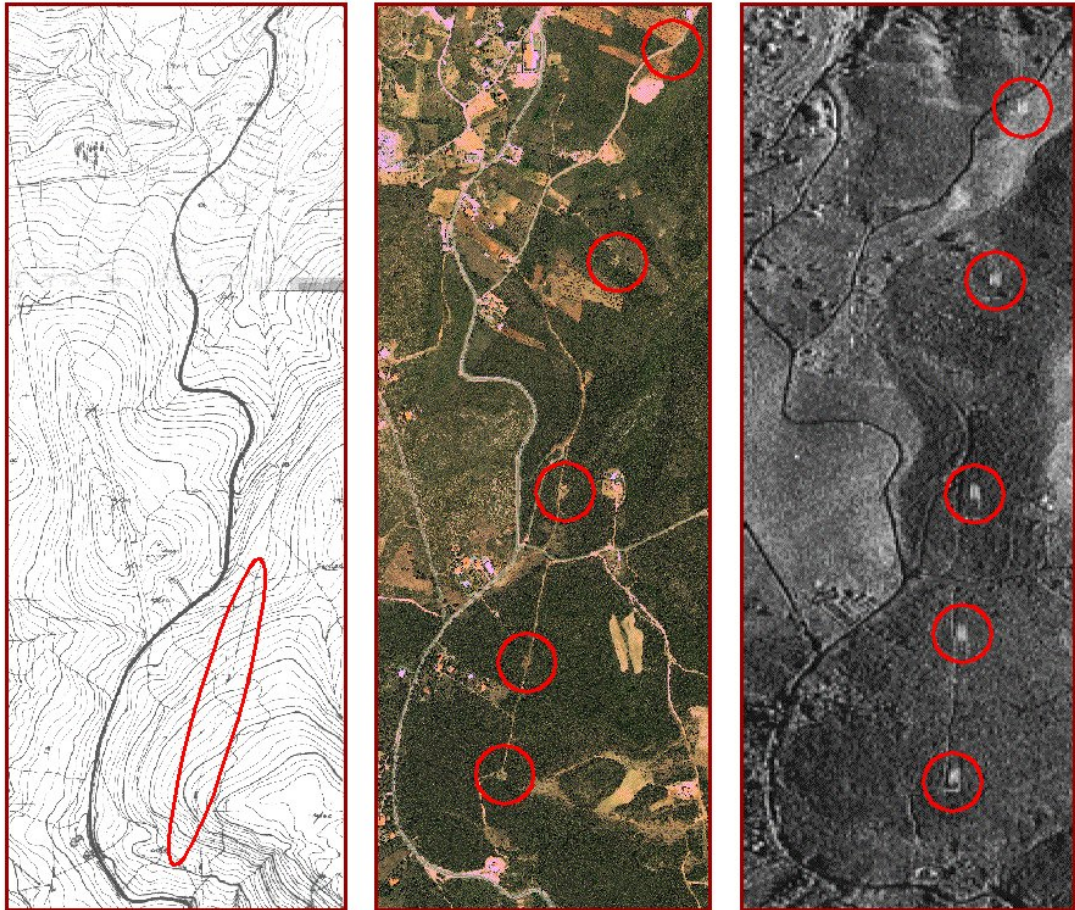


Figure 6.31: Metallic pillars. Left: map. Centre: optical image. Right: SAR image.

physical and man-made features that was hard or even impossible to identify in the previous generation of SAR images. This makes optical and SAR images compatible by means of resolution and offers various possibilities of a combined use of these two different and potentially complementary data types. SAR and optical data have many differences and similarities. Although, in the past, the similarities led to the competition for the exclusive use of SAR or optical data, today their differences, and thus their mutual usefulness and effectiveness, are fully appreciated. The concept of complimentary use of SAR and optical data is illustrated by the cooperation of optical and SAR satellites (e.g., CNES/ASI Orfeo program) and by the installation of both optical and SAR sensors on the same satellite (e.g., ALOS satellite). This Section focuses on the fusion of high resolution optical and SAR images.

The fusion of optical and SAR images has been investigated in various research studies. It combines the complementary information collected by the two different types of sensors, in order to produce geospatial products of higher quality (Ehlers [1991], Pohl and Genderen [1998]). A fusion process normally uses geometrically corrected images where it is more straightforward to correlate the two data sets. Two geometrically corrected images, an optical and a SAR, are merged to form a new image that contains the spectral information of both. Unfortunately, the geometric correction process inherently causes loss of the specific geometric information provided by the side-looking SAR geometry. For example, objects such as metallic pillars which appear as bright line segments in slant range geometry, degenerate to single points in geometrically corrected SAR images. Furthermore, the geometric correction process introduces unavoidable loss in the radiometric quality and the accuracy of both images.

In contrast to previous research studies which are based on the fusion of geometrically corrected images, here the a method for the fusion of optical and SAR images in slant range SAR geometry is proposed. The method maintains the geometric properties of SAR images and the intensity of the back-scattered radiation, while it enhances them with the descriptive optical colours.

The method implements, validates and evaluates the performance of the general method for geometric and radiometric merging of images (Section 3.3).

6.4.1 Data sets

The data sets of this test are:

1. A TerraSAR-X image which is a basic image product, captured in February 2009 with the High Resolution SpotLight (HS) acquisition mode and it is of type Single Look Slant Range Complex (SSC). The incidence angle is 53° and the polarisation is single HH (Figure 6.28).
2. A QuickBird optical image which is a standard level 2A product, captured in May 2009 (Figure 6.29).
3. A DTM which was derived from an archived medium scale topographic map (scale 1:5 000, contours interval: 4m), which was compiled in 1970s with photogrammetric stereo-restitution (Figure 6.30).

The study site is located in the greater north-eastern region of Athens, Greece. The area has steep mountainous terrain and it is generally covered by sparse vegetation. Kalamos and Markopoulo Oropou, are two communities localised in the area.

Metallic pillars appear in all data sets (Figure 6.31).

6.4.2 Application and results

The georeferencing of the optical image was done using Ground Control Linear Features (GCLFs) through ICP-based (Iterative Closest Point algorithm) matching (Section 2.8) while the georeferencing of the TerraSAR-X image was done using science orbit data without using Ground Control Information (Section 3.2). The computed projective transformations were used to project the 3D nodes of the TIN to the 2D image spaces (the optical and the SAR) independently.

The proposed method was used to fuse the optical and SAR images. The new, fused, image is shown in Figure 6.33. The geometric and radiometric characteristics of the SAR image are maintained and at the same time the SAR image is enhanced with the descriptive optical colours, avoiding loss of radiometric quality. In Figure 6.32 (magnified view of Figure 6.33), one can notice that objects, such as metallic pillars, appear more clearly in the fused image.

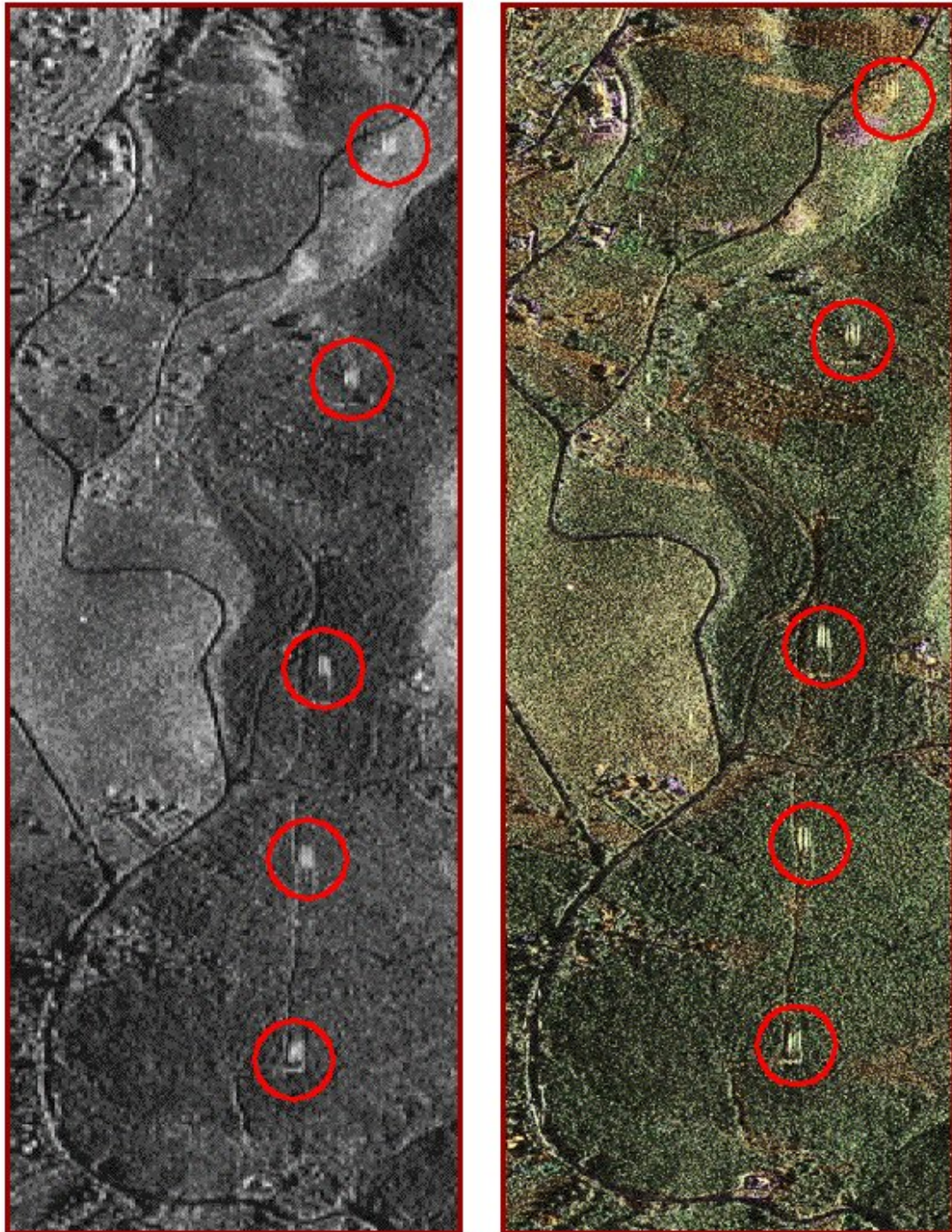


Figure 6.32: Metallic pillars. Left: SAR image. Right: fused SAR image.

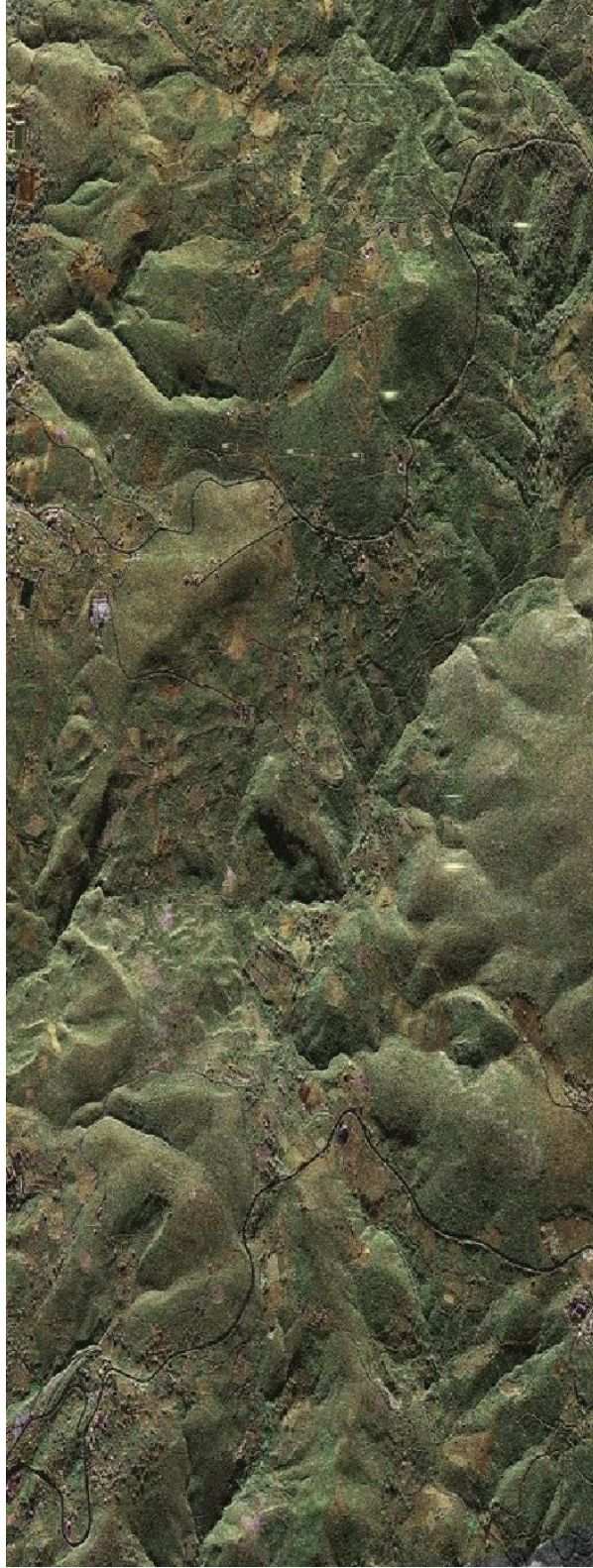


Figure 6.33: Optical and SAR images fused in slant range geometry.

The fusion of the optical and SAR images in slant range SAR geometry maintains and enhances the available information of the SAR image, which is lost when the images are geometrically corrected. The method does not need (or create) geometrically corrected images, also avoiding the loss of the radiometric quality introduced by the geometric correction process. The method can also be used to create simulated SAR images.

6.5 Rapid geometric correction of SAR images

Satellite remote sensing data is especially useful in crisis management as it allows the review and the evaluation of the situation, as well as the means for planning assistance and support. In-situ presence to the area of interest is usually difficult, as is the collection of Ground Control Points (GCPs) in order to establish the relationship of the image with the object space and the DEM collection for the geometric correction. In some cases GCPs and DEM are taken from remote sensing and geospatial data archives. In many cases though, data archives do not exist, or if they do exist time is usually too short to recover and exploit them. Furthermore, if the crisis happens during days with cloud cover or during the night, the usefulness of optical images is little, as they illustrate the clouds or a dark and shadowy surface of the Earth. In such cases the use of SAR data is the best solution. SAR sensors are active microwave sensors with all-weather and day-and-night capabilities which are able to provide information about the properties of the Earth's surface, its geometry and its evolution over time. Additionally, modern satellite SAR sensors are able to illustrate the Earth's surface with high resolution imaging technology.

In this Section a process for the rapid geometric correction of slant range (SSC) TerraSAR-X images is presented and evaluated. The geometric correction consists of two steps: i) the establishment of the relationship of the 2D SAR image with the 3D object space and ii) the geometric correction of the image. The establishment of the relationship of the 2D SAR image with the 3D object space is usually computed with GCPs which are hard or time consuming to collect. In contrast, the GCPs are completely bypassed in this Section, using the direct georeferencing method (Vassilaki et al. [2011b] - Section 3.2) which is based only on orbital data and other metadata provided by TerraSAR-X's operator. The geometric correction of the slant range SAR image is usually computed using DEM collected for this purpose, which is also hard or time consuming to collect. Here two global DEMs are used instead, which are freely available on nearly global scale and can be obtained before any crisis happens: i) the interferometrically produced DEM by the Shuttle Radar Topography Mission (SRTM), which has nominal accuracy of 16 m and offers 80% coverage of the Earth's

surface Bamler [1999], ii) the photogrammetrically produced DEM by the Advanced Space-borne Thermal Emission and Reflection Radiometer (ASTER) on Terra spacecraft, which has nominal accuracy of 20 m and offers 99% coverage of the Earth's surface (ASTER GDEM Validation Team [2009]). The geometric correction is performed by applying backward projection Mikhail et al. [2001]. Each pixel of the orthoimage is projected to the DEM and from there it is back-projected to the slant range image using the physical sensor model established by the direct georeferencing step.

In order to implement this two-step process, the reference systems used by the satellite sensor and the global DEM must be taken into account. The orbital data of the sensor is given in geocentric coordinates of the World Geodetic System 84 (WGS84) ellipsoid, which correspond to ellipsoid (geometric) elevations. On the other hand the global DEMs provide orthometric elevations. To convert between geometric and orthometric elevations the geoid undulation is necessary. Among the numerous global geoid undulation models, the Earth Gravitational Model 2008 (EGM2008) Pavlis et al. [2008], which is used in this Section, and the EIGEN-6C2 Förste et al. [2012] are considered the most accurate, according to the evaluation of the International centre for Global Earth Models (ICGEM).

An additional advantage of this two-step process is its flexibility: i) if a local DEM, which is usually more accurate than the global ones, is readily available it can be used instead of the global DEM and ii) if a local geoid, which is usually more accurate than the global ones, is readily available it can be used instead of the global geoid.

The process is applied over a sub-urban hilly area, northeast of Athens using an experimental 300 MHz high resolution spotlight SSC TerraSAR-X image. The accuracy of the geometric correction is evaluated by independent check points (CPs), collected from other available data.

6.5.1 Coordinate systems

In order to perform the geometric correction of SAR images, various coordinate systems must be taken into account:

1. The 2D image space coordinate system of the not geometrically corrected SSC SAR image.
2. The 3D object space coordinate system of the global DEM.
3. The 2D image space coordinate system of the orthoSAR image.
4. The 3D object space coordinate system of the orthoSAR map.

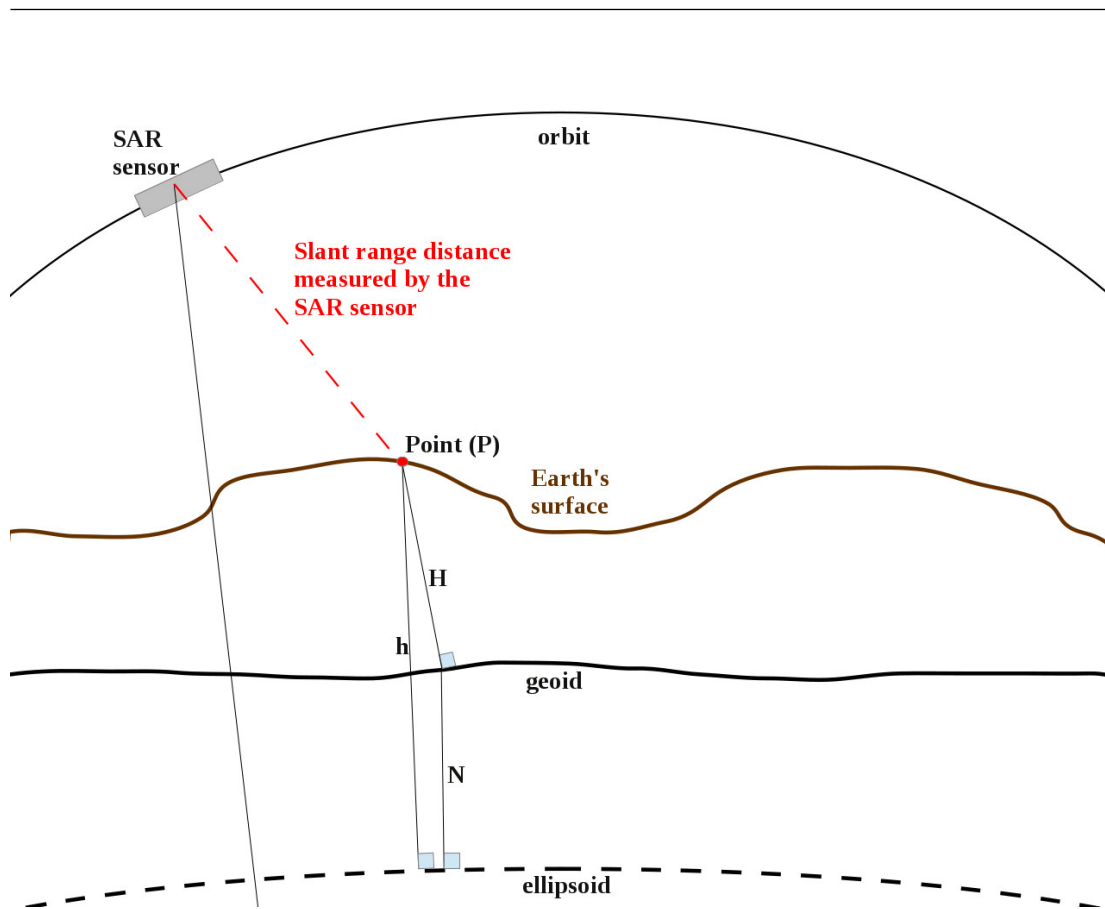


Figure 6.34: The geoid undulation.

The 2D SSC image coordinate system is defined by two axes (x_s, y_s) in pixel units. The y_s axis represents time which roughly represents the position of the sensor along its orbit. The x_s axis represents the slant range distance (perpendicular to the orbit) between the sensor and a point on the Earth's surface. The 3D object coordinate system of the global DEM is in the form of ellipsoid geodetic coordinates and orthometric elevation (λ, ϕ, H) . The coordinates are converted later to geocentric coordinates (X, Y, Z) needed by the physical model of the TerraSAR-X sensor. The 3D object coordinate system of the orthoSAR map is in the form of Easting-Northing coordinates and orthometric elevation (E, N, H) of a map projection such as the Transverse Mercator (projection coordinates). The 2D orthoSAR image coordinate system is defined by two axes (x_o, y_o) in pixel units and is essentially the projection coordinate system translated and scaled.

6.5.2 The method

The two-step geometric correction method of slant range (SSC) TerraSAR-X images consists of 2 steps:

1. The georeferencing of the SAR image.
2. The geometric correction of the SAR image.

The georeferencing used in this Section is the TerraSAR-X sensor's physical model (Section 3.2), the parameters of which are taken by science orbit data and other metadata given in the XML file that accompanies the SAR image (Section 3.2.2). The geometric correction process is a special case of the general geometric fusion described in Section 3.3.1. The intensity (gray shade) of a pixel of the orthoSAR image is computed as the bicubic interpolation of the intensities of the pixels of the SSC SAR image, which surround the position of the back-projection of the orthoSAR pixel to the SSC SAR image (Section 3.3.2).

However a lot of transformations between different coordinate systems are needed (Figure 6.35):

$$\begin{array}{c}
 (x_o, y_o) \xrightarrow{f_1} (E, N) \xrightarrow{\text{Redfearn}} (\lambda, \phi) \xrightarrow{\text{DEM}} H \xrightarrow{\text{geoid}} h \\
 \xrightarrow{f_2} (X, Y, Z) \xrightarrow[\text{georeferencing}]{\text{direct}} x_s, y_s
 \end{array}$$

The transformations are described in the following subsections.

6.5.3 Computation of projection coordinates (f_1)

Assuming that the origin of the orthoSAR image is E_A, N_A and its scale is s , the projection coordinates of a pixel x_o, y_o is given by:

$$\begin{aligned}
 E &= E_A + s \cdot x_o \\
 N &= N_A + s \cdot y_o
 \end{aligned} \tag{6.13}$$

The translation and scale are computed by the user selected scale and resolution of the orthoSAR image, as well as by the area which spans the SAR image and which is taken from the SAR metadata XML file.

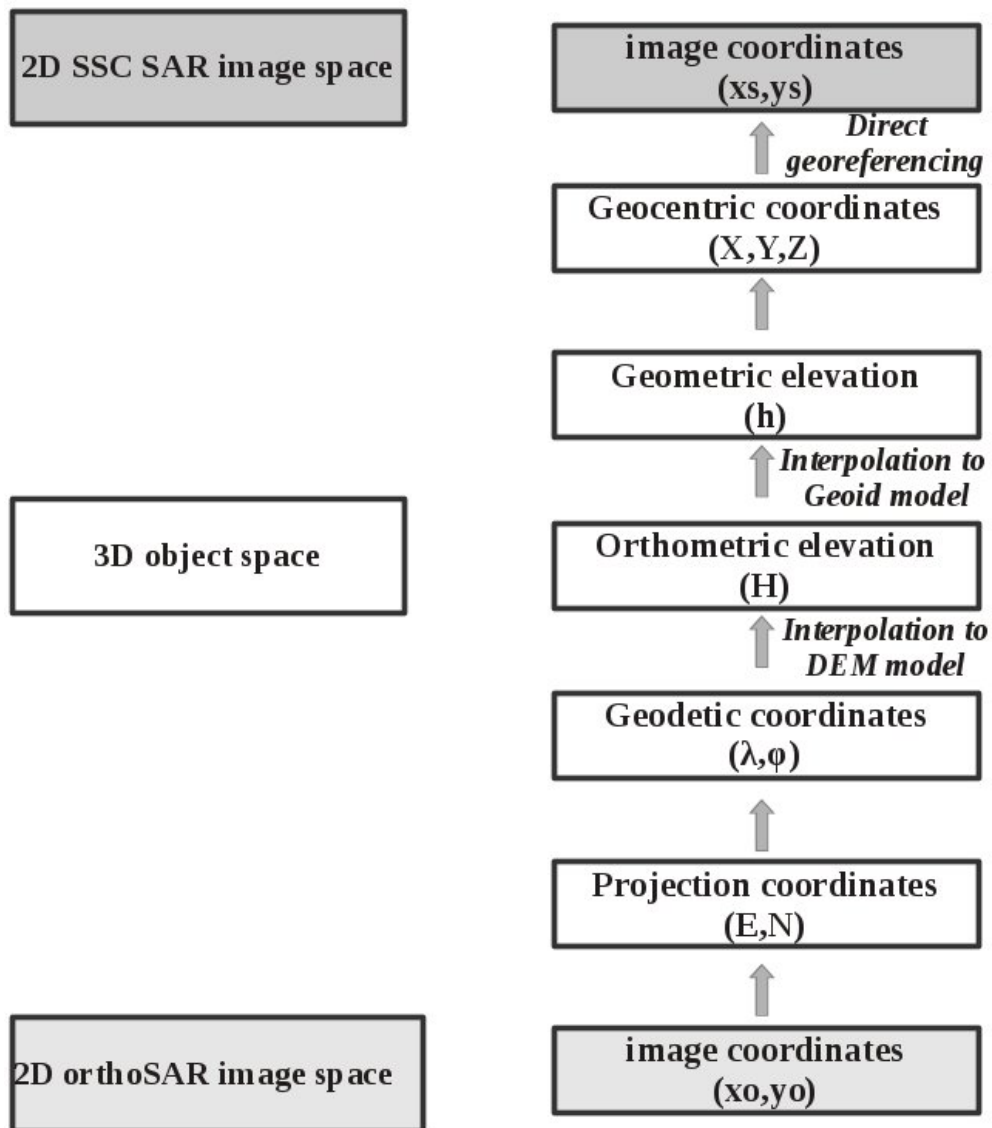


Figure 6.35: Transformations of coordinate systems.

6.5.4 Computation of geodetic coordinates (Redfearn series)

The transformation from Easting, Northing to geodetic coordinates of a Transverse Mercator projection is given by the Redfearn series (Redfearn [1948]):

$$\begin{aligned}\lambda &= \lambda_0 + \frac{x^1 V_1}{1! c_1 (k_0 v_1)^1} - \frac{x^3 V_3}{3! c_1 (k_0 v_1)^3} - \frac{x^5 V_5}{5! c_1 (k_0 v_1)^5} - \frac{x^7 V_7}{7! c_1 (k_0 v_1)^7} \\ \phi &= \phi_1 - \frac{x^2 \beta_1 t_1 U_2}{2! (k_0 v_1)^2} - \frac{x^4 \beta_1 t_1 U_4}{4! (k_0 v_1)^4} - \frac{x^6 \beta_1 t_1 U_6}{6! (k_0 v_1)^6} - \frac{x^8 \beta_1 t_1 U_8}{8! (k_0 v_1)^8}\end{aligned}\quad (6.14)$$

The parameters of the Transverse Mercator projection are:

$$x = E - E_0, \quad y = N - N_0$$

$$V_1 = 1$$

$$V_3 = \beta_1 + 2t_1^2$$

$$V_5 = 4\beta_1^3(1 - 6t_1^2) - \beta_1^2(9 - 68t_1^2) - 72\beta_1 t_1^2 - 24t_1^4$$

$$V_7 = 61 + 662t_1^2 + 1320t_1^4 + 720t_1^6$$

$$U_2 = 1$$

$$U_4 = 4\beta_1^2 - 9\beta_1(1 - t_1^2) - 12t_1^2$$

$$U_6 = 8\beta_1^4(11 - 24t_1^2) - 12\beta_1^3(21 - 71t_1^2) + 15\beta_1^2(15 - 98t_1^2 + 15t_1^4) + 180\beta_1(5t_1^2 - 3t_1^4) + 360t_1^4$$

$$U_8 = -1385 - 3633t_1^2 - 4095t_1^4 - 1575t_1^6$$

$$\beta_1 = \frac{v_1}{\rho_1}, \quad t_1 = \tan(\phi_1), \quad c_1 = \cos(\phi_1)$$

$$v_1 = \frac{a}{\sqrt{1 - e^2 \sin^2(\phi_1)}}, \quad \rho_1 = \frac{1 - e^2}{a^2} v_1^3, \quad e^2 = \frac{a^2 - b^2}{a^2}$$

$$\phi_1 = \mu + D_2 \sin(2\mu) + D_4 \sin(4\mu) + D_6 \sin(6\mu) + D_8 \sin(8\mu)$$

$$D_2 = \frac{3}{2}n - \frac{27}{32}n^3, \quad D_4 = \frac{21}{16}n^2 - \frac{55}{32}n^4$$

$$D_6 = \frac{151}{96}n^3, \quad D_8 = \frac{1097}{512}n^4$$

$$n = \frac{a - b}{a + b}, \quad \mu = \frac{\pi y}{2m_p k_0}$$

$$m_p = \frac{\pi B_0}{2}, \quad B_0 = b\left(1 + n + \frac{5}{4}n^2 + \frac{5}{4}n^3\right)$$

where a and b are the semi-major and semi-minor axis of the ellipsoid, λ_0 is the longitude of the central meridian, k_0 is the scale factor on the central meridian and E_0, N_0 are the false Easting and false Northing of the Transverse Mercator projection.

6.5.5 Computation of orthometric elevation (DEM)

The orthometric elevation H is computed by interpolation to the global DEM. Should a local DEM be available, the elevation is computed using it. If the local DEM fails to compute the elevation of a point, the computation falls back to the global DEM.

6.5.6 Computation of geometric elevations (geoid)

The geometric elevation h is computed by the orthometric elevation and the undulation N :

$$h = H + N \tag{6.15}$$

The undulation (Figure 6.34) is computed with the EGM2008 geoid model, using the self-contained suite of coefficient files, FORTRAN software, and pre-computed geoid grids provided by Pavlis et al. [2008]. The software uses a $1' \times 1'$ grid (in geodetic coordinates λ, ϕ) and 6×6 2D spline to interpolate the undulation.

Two optimisations were done to the FORTRAN code. First, the original code padded 7 columns and rows each time it was run in order to account for the fact that the Earth is round in both directions. These rows and columns were embedded into the grid in order to make the process faster. Second, in the vast majority of all cases the undulation is computed locally and thus it is unnecessary to read the whole grid (about 1 GB). The code was modified to input only the part of the grid that is actually needed, improving the computation time and the memory consumption.

Should a local geoid model be available, the undulation is computed using it. If the local geoid fails to compute the undulation of a point, the computation falls back to the EGM2008.

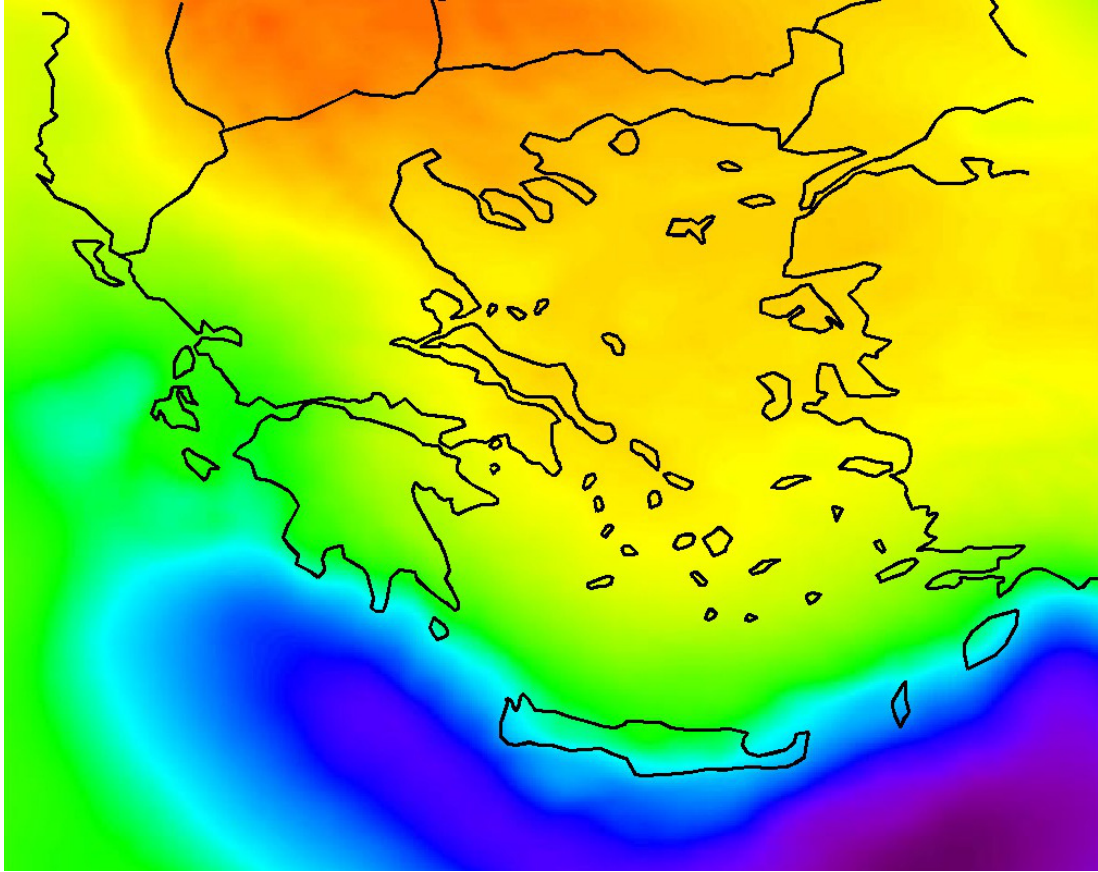


Figure 6.36: Geoid undulation over the country according to EGM2008.

6.5.7 Computation of geocentric coordinates (f_2)

The geocentric coordinates are computed from the geodetic coordinates λ, ϕ and the geometric elevation h :

$$\begin{aligned} X &= (N' + h) \cdot \cos(\phi) \cdot \cos(\lambda) \\ Y &= (N' + h) \cdot \cos(\phi) \cdot \sin(\lambda) \\ Z &= [(1 - e^2)N' + h] \cdot \sin(\phi) \end{aligned} \quad (6.16)$$

where, N' is the prime vertical radius of curvature at latitude ϕ and e is the eccentricity of the ellipsoid:

$$N' = \frac{a}{\sqrt{1 - e^2 \cdot \sin^2(\phi)}}, \quad e^2 = \frac{a^2 - b^2}{a^2}$$

6.5.8 Computation of SSC image coordinates (direct georeferencing)

The SSC image pixel coordinates are computed using direct georeferencing (Section 3.2). No GCPs are necessary as the translation and scale parameters R_0 , ΔR , t_0 , Δt_{AZ} of the physical model of the sensor are taken or are computed from the SAR metadata XML file (Section 3.2.2):

$$x_s = \frac{R_P - R_0}{\Delta R}, \quad y_s = \frac{t_P - t_0}{\Delta t_{AZ}} \quad (6.17)$$

The distance R_P from the sensor to the target point P, and the time t_P of the point acquisition are computed from the geocentric coordinates X, Y, Z of point P, and orbital data taken from XML file.

6.5.9 Application of the method

The study area is in the greater north-eastern region of Athens, Greece. It has steep mountainous terrain, with average elevation 270 m and it is generally covered by sparse vegetation. It also includes two small urban regions. The data used is:

1. A whole scene of a Single Look Slant Range (SSC) TerraSAR-X product which was captured in 2009 with 300 MHz High Resolution SpotLight imaging mode. The scene covers an area of about 50 Km² (5x10 Km) (Figure 6.42). The polarisation is HH and the scene centre incidence angle is 53°. The projected spacing values for range and azimuth are 0.45 m and 0.87 m, respectively.
2. The EGM2008 global geoid model (Figure 6.36).
3. The tiles of the SRTM-CGIAR (Figure 6.37) and the ASTER (Figure 6.38) global DEMs over the test site. The nominal absolute vertical accuracy of the used global DEMs is 16 m and 20 m respectively.
4. Two local, more accurate, DEMs one archived (Figure 6.39) and one recent (Figure 6.40). The nominal absolute vertical accuracy of the both local DEMs is 4 m. The archived local DEM is available in the form of paper maps with contours of 4 m interval while the recent local DEM is available in digital form with 5 m pixel size. Preprocessing was performed in order to convert the archived DEM in digital form (geodetic reference system transformations and resampling, digitisation of the contours and computation of the Delaunay triangulation).

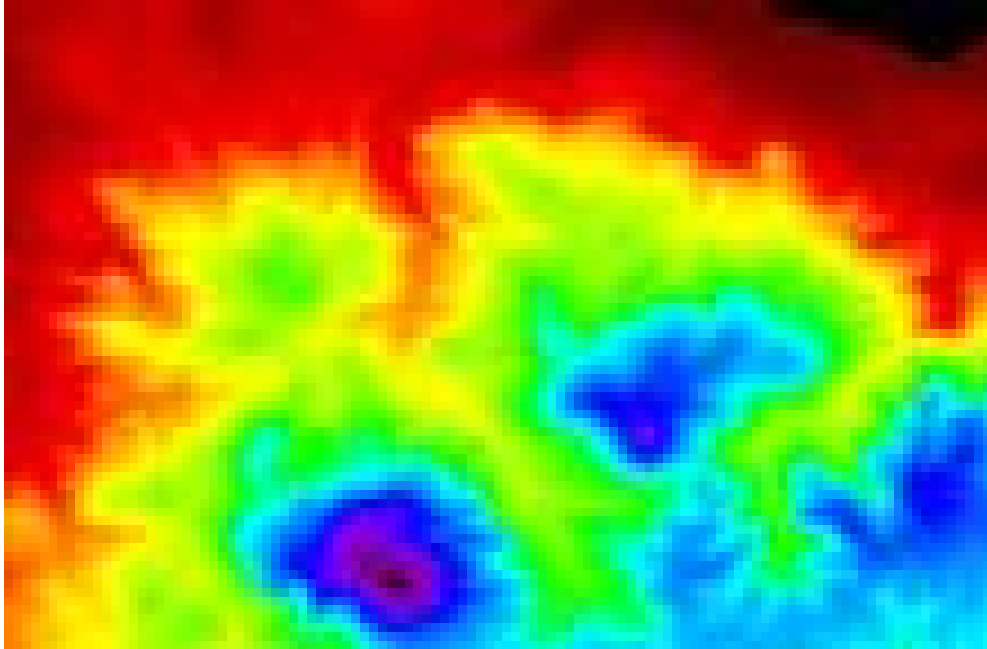


Figure 6.37: The global SRTM DEM over the test site.

5. A recent optical orthoimage which has been produced using the recent DEM. Its pixel size is 0.5 m and it is of nominal absolute planar accuracy 2.5 m.

The objective is to geometrically correct (georeferencing and geometric correction) the SSC SAR image. Four independent orthoSAR images were computed using the four available DEMs:

1. The SRTM DEM.
2. The ASTER DEM.
3. The archived local DEM.
4. The recent local DEM.

In all four cases the georeferencing of the SSC SAR image was computed using the direct georeferencing method (Section 3.2), without using any form of ground control information. The geometric correction was based on back-projecting as stated before and the proposed process was implemented in FORTRAN and was embedded into an open source CAD Stamos [2007] for convenience and usability (Figure 6.41).

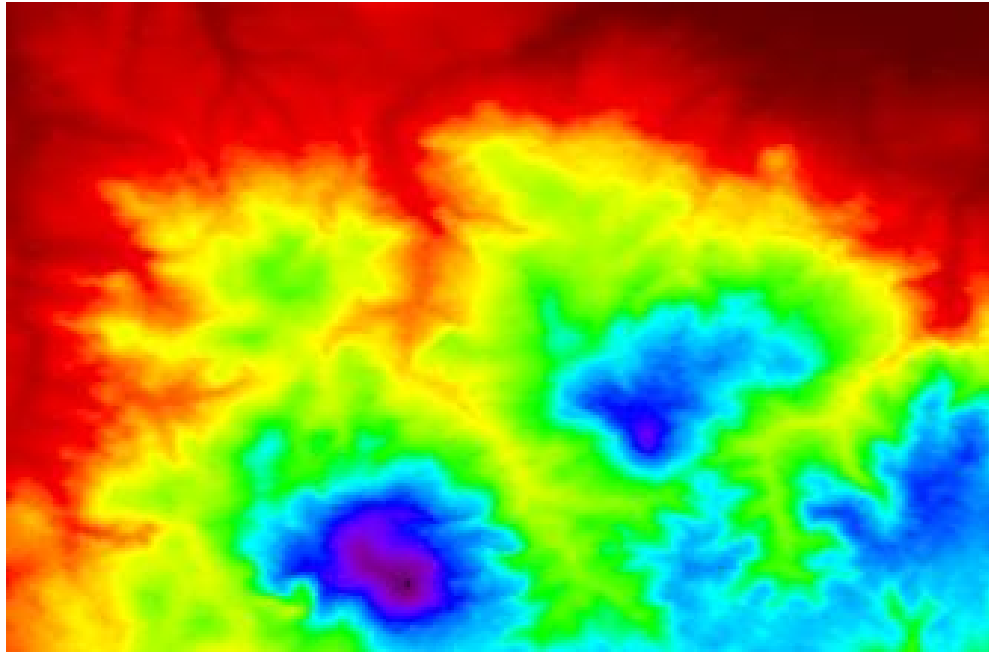


Figure 6.38: The global ASTER DEM over the test site.

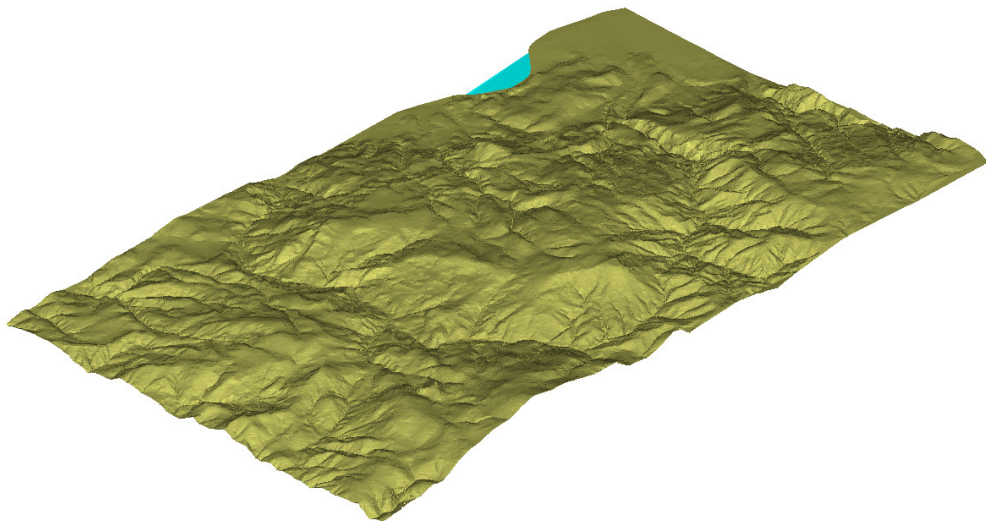


Figure 6.39: The archived local DEM over the test site.

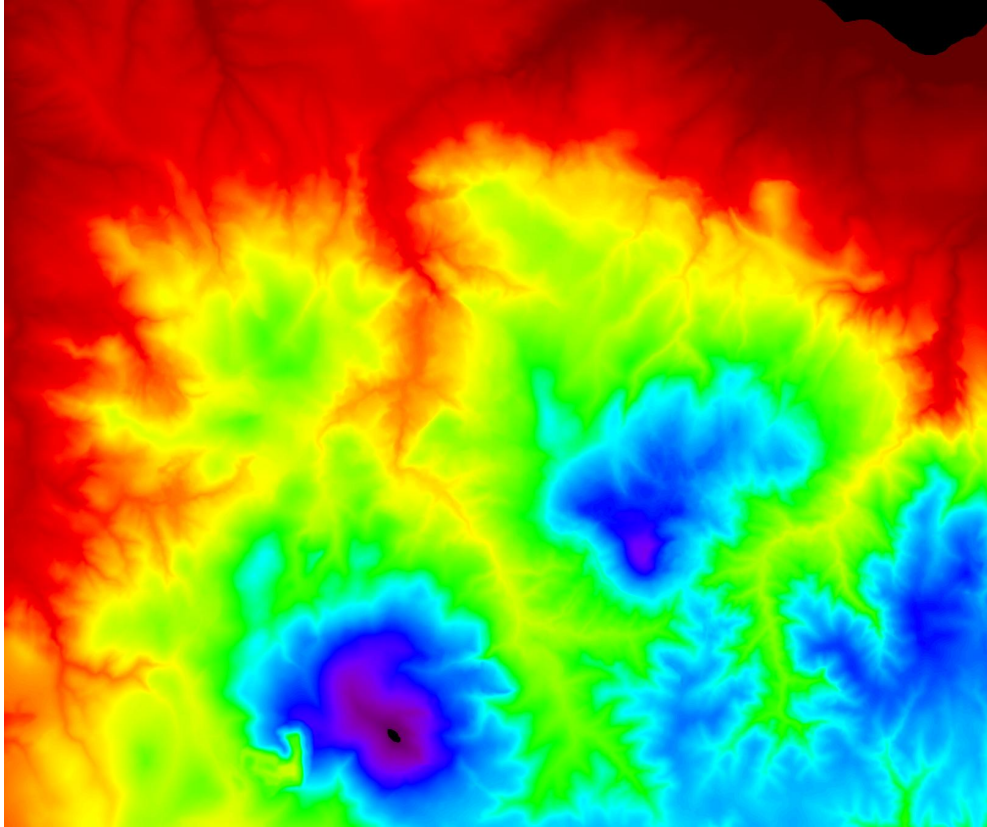


Figure 6.40: The recent local DEM over the test site.

The accuracy of the geometric correction was evaluated using 108 independent CPs. The points were collected independently on the four 2D geometrically corrected SAR images. The same points were also collected in the 3D object space using the recent optical orthoimage and the corresponding recent local DEM. Figure 6.42 shows the distribution of the CPs on the SSC SAR image. The planar residuals of each point between the measured coordinates in the 3D object space and the measured coordinates in the 2D geometrically corrected SAR images were then computed. The minimum and the maximum residuals as well as the RMSE in meters are shown in Table 6.5 for the SRTM, the ASTER, the archived and the recent DEMs.

The objective of this study is not the analysis of error, but at first sight the planar accuracies computed using both global DEMs are surprisingly good (RMSE 7.6 m and 3.8 m for the SRTM and ASTER respectively). According to DEMs' nominal vertical accuracy (16 m and 20 m respectively) the expected planar accuracies, or errors, are 13 m or more, as computed by the the sensors'

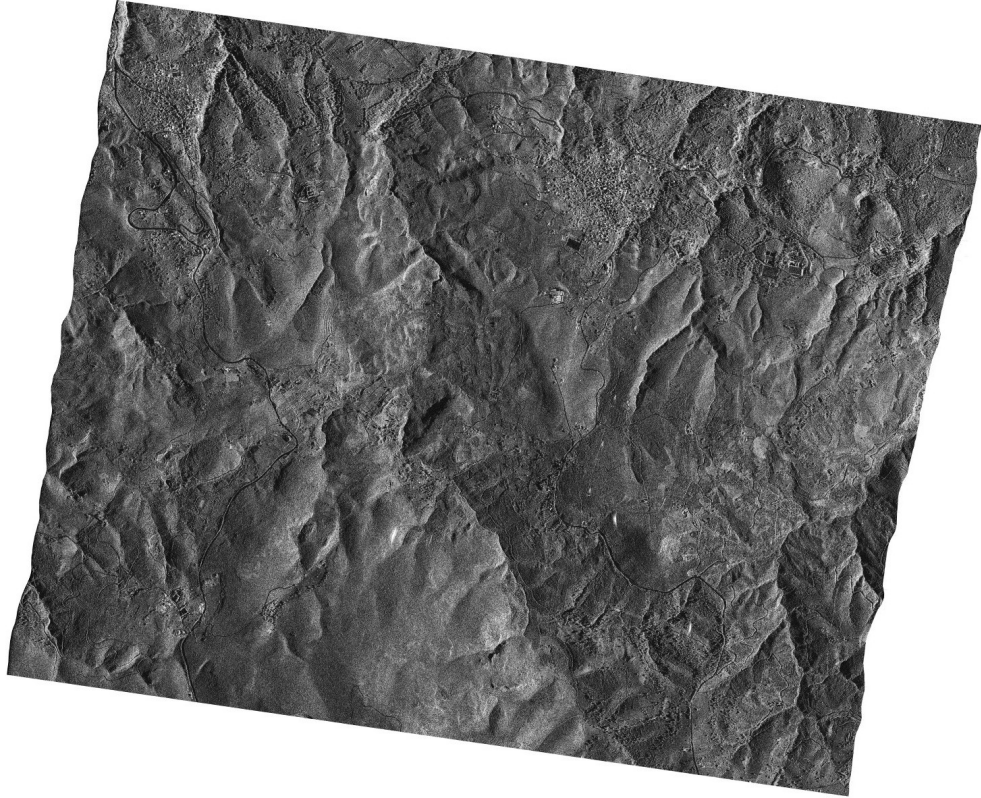


Figure 6.41: The geometrically corrected image using the ASTER DEM.

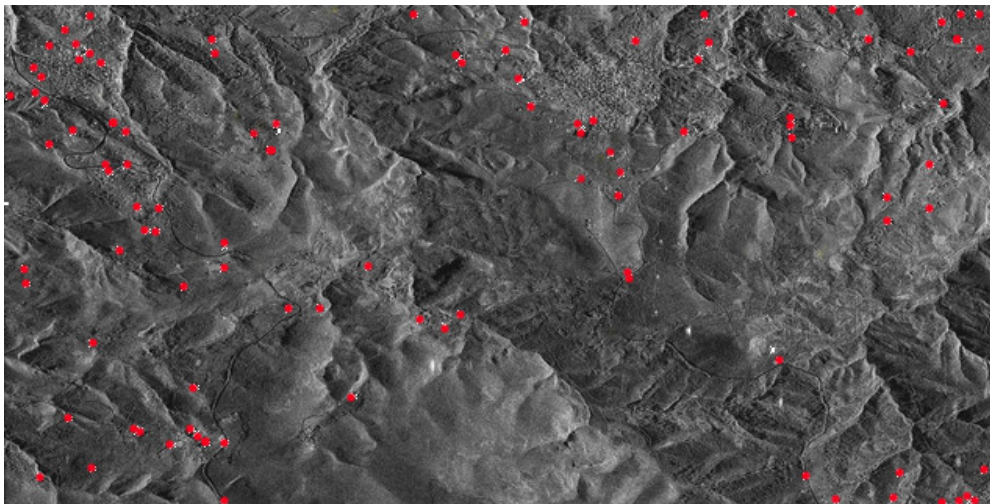


Figure 6.42: The distribution of the CPs on the SSC TerraSAR-X image.

Table 6.5: The CPs errors.

DEM	Error	X (m)	Y(m)	Planar (m)	Z(m)
SRTM	min	0.0	0.5	0.5	-19.7
	max	9.7	-2.1	9.9	9.9
	RMSE	7.2	2.4	7.6	7.4
ASTER	min	0.1	0.2	0.2	-9.5
	max	-8.4	-1.4	8.5	9.8
	RMSE	3.0	2.4	3.8	5.9
Archived	min	-0.1	0.1	0.2	-7.8
	max	2.7	-8.0	8.5	9.2
	RMSE	2.8	2.4	3.7	2.0
Recent	min	0.8	0.1	0.8	n/a
	max	1.9	-7.5	7.7	n/a
	RMSE	3.0	2.4	3.9	n/a

specifications Fritz et al. [2007] and by the analytic computation of the error propagation from the 3D object space to the 2D orthoSAR image space (Section 6.1.4). The expected errors are shown in Figure 6.43 and Table 6.6.

However, the analytic computation of the error assumes that the vertical accuracy is 3/2 of the planar accuracy, which is not the case here. Since direct georeferencing is used, the planar error is the nominal planar error of the georeferencing which is 1–2 m (Bresnahan [2009], Roth et al. [2004]), while the vertical error of the global DEMs is much higher (16 m and 20 m for the SRTM and ASTER respectively). Using the analytic formulas of Section 6.1.4 taking into account these errors, the expected planar errors are 9.5 m and 12 m, which are closer to the computed RMSE.

Furthermore, in Europe the vertical accuracy is better than the nominal (Rodriguez et al. [2006]), and in fact, in the test site, the vertical errors are by chance even smaller (7.4 m and 5.9 m), as computed by the CPs (Table 6.5). Using the analytic formulas taking into account these vertical errors, the expected errors are 4.6 m and 3.6 m, which are even closer to the computed RMSE (Table 6.5).

The high accuracy computed in the present test site, though not unique (Rodriguez et al. [2006]), does not generally represent other areas of the world. For example the computed planar RMSE of the 2D ortho SAR image produced using the ASTER DEM is 3.8 m, while in the general case it should be about 12 m.

Table 6.6: The expected planar error (m) for incidence angle 50° .

DEM elev. error	Expected error sensor's specifications	Expected error analytic computation
2	1.7	1.8
6	4.9	5.3
8	7.0	7.0
16	13.0	14.0

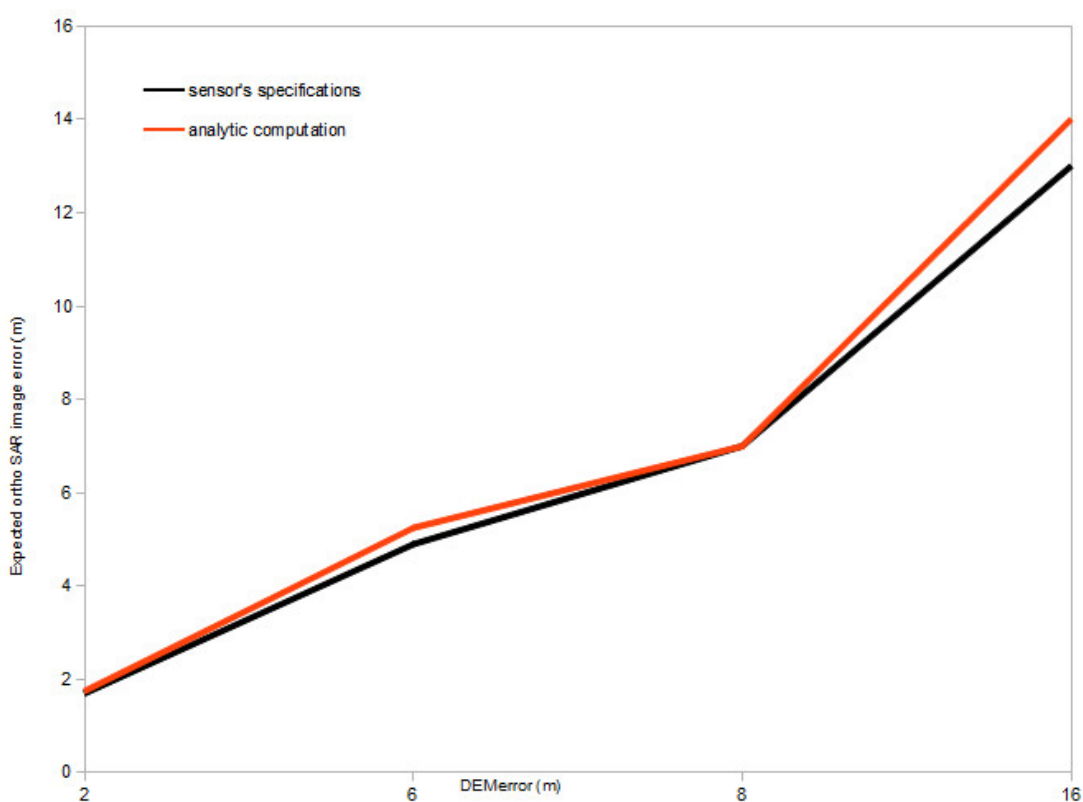


Figure 6.43: Expected planar error according to the sensor's specifications (in black) and according to analytical equations (in red).

6.6 Overview and contribution

In this Chapter (*Chapter 6*) new specific methods were developed, based on the the novel general methods described in Chapters 2 and 3. Each one of the specific methods is a separate contribution:

- The registration (or georeferencing) of not geometrically corrected SAR

images to geometrically corrected unitemporal and multitemporal maps and optical images and the corresponding DEM.

- The registration (or georeferencing) of not geometrically corrected optical images to geometrically corrected SAR images and the corresponding DEM.
- The co-registration of not geometrically corrected optical and SAR images.
- The pixel-based fusion of not geometrically corrected SAR and multispectral optical images in slant range SAR imaging geometry.
- The rapid geometric correction of slant range TerraSAR-X SSC images using global DEMs and global geoid models.

Chapter 7

Contribution, conclusions and outlook

The general objective of this dissertation was two fold:

1. To research the potential of the combined use of high resolution satellite SAR data with heterogeneous data (multimodal and multitemporal remote sensing and geospatial data).
2. To research the use of linear features as an alternative to solitary points for reference information for the registration of HR satellite SAR data with heterogeneous data and vice-versa.

The specific objective of this dissertation was to, in contrast to previous research, face the following:

1. HR satellite SAR data.
2. Not geometrically corrected data.
3. Linear features of arbitrary geometry.
4. Terrain of arbitrary form, not necessarily flat.
5. Greater areas of the Earth's surface, not just small patches.
6. Metric exploitation of HR satellite data for topographic applications.

The general and specific objectives of this dissertation (Chapter 1) were met. The newly introduced methods succeed to:

-
1. Perform the registration, the georeferencing and the fusion of not geometrically corrected high resolution SAR data with heterogeneous (multimodal and multitemporal) remote sensing and geospatial data, and vice-versa, over greater areas of the Earth's surface with arbitrary terrain type.
 2. Use FFLFs as an alternative to solitary points for reference information for registration problems on multiview, multitemporal, multimodal and scene to model analysis, in order to achieve better accuracy than or equal accuracy to results with point-based methods.

This dissertation developed methods and processes which exploit metric information of SAR data for topographic applications. The methods bring closer modern, state-of-the-art, SAR sensors to existing mapping technologies and to existing (multimodal and multitemporal) remote sensing and geospatial data. They enable the integration and the interoperability of SAR data and other data types. More specifically, the contribution of this dissertation with respect to the objectives and the state-of-the-art (Chapter 1) is the following new general and specific methods:

1. The automated ICP-based method for global matching of single pairs of heterogeneous FFLFs of the same (2D-2D, 3D-3D) or of different dimensionality (3D-2D) which is accompanied by the automated computation of the initial approximation by using physical or statistical properties of the FFLFs (Chapter 2).
2. The automated method for global matching of networks (multiple pairs) of heterogeneous FFLFs of the same (2D-2D, 3D-3D) or of different dimensionality (3D-2D) which is accompanied by the automated identification of FFLFs correspondences and the unified Least Squares Adjustment for all the FFLFs of the networks (Chapter 2).
3. The robust and automatic computation of homologous points of a pair of FFLFs. The method is computationally intensive and can be accelerated by divide and conquer and/or parallel programming (Chapter 2).
4. The method to automatically compute the initial approximation required by the ICP algorithm. The method exploits physical properties of the whole FFLF such as the length and the centroid, to compute an initial similar transformation which brings the FFLFs close (Chapter 2).
5. The method to automatically compute the initial approximation required by the ICP algorithm, when the distortions of the sensor are severe and can not be approximated by rigid transformations. The method exploits

statistical properties of the whole FFLF such as the average and higher order moments, to compute an initial 1st order polynomial transformation which brings the FFLFs close (Chapter 2).

6. The concept of using FFLFs as GCI (GCLFs) (Chapter 3).
7. The concept of the co-registration of not geometrically corrected SAR images with other data types through 3D-2D projective scene-to-model co-registration (not simply 2D-2D image-to-image transformations) (Chapter 3).
8. The direct georeferencing of TerraSAR-X images using orbital data and other meta data provided by the operator and without using any kind of GCI (Chapter 3).
9. The geometric correlation of not-geometrically-corrected heterogeneous images (Chapter 3).
10. The radiometric merging of not-geometrically-corrected heterogeneous images (Chapter 3).

Based on these general methods, a multitude of new methods were developed to solve real world problems with real world data (Chapter 5).

Based on the general methods as well as on other principles, methods, and data sets of surveying engineering, the following new specific methods were developed for the synergy of SAR and heterogeneous data:

11. The registration (or georeferencing) of not geometrically corrected SAR images to geometrically corrected unitemporal and multitemporal maps and optical images and the corresponding DEM (Chapter 6).
12. The registration (or georeferencing) of not geometrically corrected optical images to geometrically corrected SAR images and the corresponding DEM (Chapter 6).
13. The co-registration of not geometrically corrected optical and SAR imagery (Chapter 6).
14. The pixel-based fusion of not geometrically corrected SAR and multispectral optical images in slant range SAR imaging geometry (Chapter 6).
15. The rapid geometric correction of slant range TerraSAR-X SSC images using global DEMs and global geoid models (Chapter 6).

All the general and specific methods are published in international journals and international conference proceedings (Chapter 1). The research performed in this dissertation has drawn many conclusions which are discussed in details in the corresponding Sections and publications. The key conclusions are:

- Linear features and specifically linear features of arbitrary geometry (FFLFs) are a viable alternative form of reference information to solitary points for reference system transformation of the same (2D-2D, 3D-3D) and of different dimensionality (3D-2D). They can be used as reliable matching primitives for co-registration and georeferencing.
- FFLFs can compute very accurate results, within an ICP-based matching scheme. They can compute more accurate results than solitary points in multimodal and multitemporal data analysis including the co-registration of SAR and heterogeneous data. They tend to persist over time and are easily identifiable in data sets of different spectral and geometric characteristics.
- Modern SAR data can easily, accurately and practically be georeferenced using GCLFs or direct georeferencing. GCLFs can be extracted from medium scale mapping products (or better) and the accuracy is that of the mapping products. Archived multimodal and multitemporal mapping products can also be utilised, without loss of accuracy.
- Modern SAR data has compatible resolution (less than double pixel size of optical images) and equivalent relative accuracy with optical images, but much better absolute geolocation accuracy.
- Modern SAR data can be used in real world practical topographic applications. Specifically it can be used as source of ground control information (either GCLFS or GCPs) for the georeferencing of satellite optical images. Combined with global geoid models and global DEMs, it can be used for rapid and accurate geometric correction in crisis management.

As a general conclusion, modern SAR data with the developed methods is a considerable tool in the tool-box of the surveying engineer, and encourages further research. Topics of future research could be:

- Automatic extraction of linear features coupled with partial matching of FFLFs. Although this is of great significance, it was not discussed in this dissertation because there are no general approaches for the identification and the extraction of linear features. Different kinds of data demand different approaches which are not always complete or correct, especially in real-world complex scenes. The extension of the developed methods to

handle poorly segmented images is a challenging topic for future research, which could be based on the limited partial matching introduced in this dissertation.

- SAR image analysis such as feature extraction and classification, in slant range SAR imaging geometry. The conducted research shows that the slant range imaging geometry reveals details of the Earth's surface which are not present in other data types, and which degenerate, or completely lost, when the SAR images are geometrically corrected.

References

- M. Abramowitz and I. Stegun. *Handbook of mathematical functions*. Dover Publishing Inc., New York, 9th edition, 1970. ISBN 0-486-61272-4. 32
- A. Akav. *Determination of Relative Orientation with Linear Features*. PhD thesis, Technion Institute of Technology, Israel, 2008. 89
- A. Akav, G.H. Zalmanson, and Y. Doytsher. Linear feature based aerial triangulation. *ISPRS - International Archives of Photogrammetry and Remote Sensing*, 35(B3):7–12, 2004. 7, 154
- Z. Ali, G. Kroupnik, G. Matharu, J. Graham, I. Barnard, P. Fox, and G. Raimondo. RADARSAT-2 space segment design and its enhanced capabilities with respect to RADARSAT-1. *Canadian Journal of Remote Sensing*, 30(3):235–245, 2004. 1
- ASTER GDEM Validation Team. ASTER global DEM validation. Summary report, 28 p., METI/ERSDAC, NASA/LPDAAC, USGS/EROS, 2009. 170
- R. Bamler. The SRTM mission: A world-wide 30 m resolution DEM from SAR interferometry in 11 days. In *Photogrammetric Week*, pages 145–154, 1999. 170
- A. Bartoli and P. Sturm. Structure-from-motion using lines: Representation, triangulation, and bundle adjustment. *Computer Vision and Image Understanding*, 100(3):416–441, 2005. 7
- A. Bellman and O. Hellwich. *Sensor and data fusion contest: Information for mapping from airborne SAR and optical imagery (phase 1)*. EuroSAR Projects, Official Publication No. 50, Frankfurt, Germany, 2006. 89, 153
- J.A. Benediktsson, P.H. Swan, and O.K. Ersoy. Neural network approaches versus statistical methods in classification of multisource remote sensing data. *IEEE Transactions on Geoscience and Remote Sensing*, 28(4):540–552, 1990. 3

REFERENCES

- P.J. Besl and N.D. McKay. A method for registration of 3-D shapes. *IEEE Transactions on Pattern Analysis and Machine Intelligence*, 14(2):239–256, 1992. 7, 19
- X. Blaes, L. Vanhalle, and P. Defourny. Efficiency of crop identification based on optical and SAR image time series. *Remote Sensing of Environment*, 96(3–4):352–365, 2005. 3
- H. Breit, T. Fritz, U. Balss, M. Lachaise, A. Niedermeier, and M. Vonavka. TerraSAR-X SAR processing and products. *IEEE Transactions on Geoscience and Remote Sensing*, 48(2):727–740, 2010. 1, 55
- P. Bresnahan. Absolute geolocation accuracy evaluation of TerraSAR-X spotlight and stripmap imagery - study results. In *Civil Commercial Imagery Evaluation Workshop*, USGS, Fairfax Virginia, USA, 31 March – 2 April 2009. 182
- G.J. Briem, J.A. Benediktsson, and J.R. Sveinsson. Multiple classifiers applied to multisource remote sensing data. *IEEE Transactions on Geoscience and Remote Sensing*, 40(10):2291–2299, 2002. 3
- L.G. Brown. A survey of image registration techniques. *ACM Computing Surveys*, 24(1992):326–376, 1992. 3, 5
- D. Brunner, G. Lemoine, and L. Bruzzone. Earthquake damage assessment of buildings using VHR optical and SAR imagery. *IEEE Transactions on Geoscience and Remote Sensing*, 48(5):2403–2420, 2010. 3
- M. Butenuth, v.G. Gössele, M. Tiedge, C. Heipke, U. Lipeck, and M. Sester. Integration of heterogeneous geospatial data in a federated database. *ISPRS Journal of Photogrammetry and Remote Sensing*, 62(5):328–346, 2007. 2, 7, 89
- V. Castelli, C.D. Elvidge, C.S. Li, and J.J. Turek. *Classification-based change detection: Theory and applications to the NALC data set*, volume Remote Sensing Change Detection: Environmental Monitoring Methods and Applications, pages 53–74. MI: Ann Arbor Press, 1998. Lunetta,R.S. and Elvidge,C.D. Eds. 103
- L. Changno and J.S. Bethel. Extraction, modelling, and use of linear features for restitution of airborne hyperspectral imagery. *ISPRS Journal of Photogrammetry and Remote Sensing*, 58(5–6):289–300, 2004. 89
- H.M. Chen, P.K. Varshney, and M.K. Arora. Performance of mutual information similarity measure for registration of multitemporal remote sensing images. *IEEE Transactions on Geoscience and Remote Sensing*, 41(11 Part I):2445–2454, 2003. 103

REFERENCES

- Y. Chen and G. Medioni. Object modelling by registration of multiple range images. *Image Vision Computing*, pages 145–155, 1991. 7, 19
- M. Chini, N. Pierdicca, and W. J. Emery. Exploiting SAR and VHR optical images to quantify damage caused by the 2003 bam earthquake. *IEEE Transactions on Geoscience and Remote Sensing*, 47(1):145–152, 2009. 3
- L. Coulter, D. Stow, and S. Baer. A frame centre matching technique for precise registration of multitemporal airborne frame imagery. *IEEE Trans. on Geoscience and Remote Sensing*, 41(11):2436–2444, 2003. 89
- F. Covello, F. Battazza, A. Coletta, E. Lopinto, C. Fiorentino, L. Pietranera, G. Valentini, and S. Zoffoli. COSMO-SkyMed an existing opportunity for observing the earth. *Journal of Geodynamics*, 49(3-4):171–180, 2010. 1
- M. Crespi, P. Capaldo, F. Fratarcangeli, A. Nascetti, and F. Pieralice. DSM generation from very high optical and radar sensors: Problems and potentialities along the road from the 3D geometric modelling to the surface model. In *IEEE International Geoscience and Remote Sensing Symposium*, pages 3596–3599, 2010. 140
- M. Crosetto. *Interferometric SAR for DEM Generation: Validation of an Integrated Procedure Based on Multisource Data*. PhD thesis, Politecnico di Milano, Geodetic and Surveying Sciences, Milano, Italy, 1998. 153
- X. Dai. The effects of image misregistration on the accuracy of remotely sensed change detection. *IEEE Transactions on Geoscience and Remote Sensing*, 36(5):1566–1577, 1998. 3, 103
- P. Dare and I. Dowman. An improved model for automatic feature-based registration of SAR and SPOT images. *ISPRS Journal of Photogrammetry and Remote Sensing*, 56(1):13–28, 2001. 3, 6, 89, 143
- Digital Globe, 2013. URL <http://www.digitalglobe.com>. 147
- I. Dowman and J. Dollof. An evaluation of rational function for photogrammetric restitution. *ISPRS - International Archives of Photogrammetry and Remote Sensing*, 33(B3):254–266, 2000. 126
- I. Dowman, K. Jacobsen, G. Konecny, and R. Sandau. *High Resolution Optical Satellite Imagery*. Whittles Publishing, 2012. 50, 147, 148
- M. Ehlers. Multisensor image fusion techniques in remote sensing. *ISPRS Journal of Photogrammetry and Remote Sensing*, 46(1):19–30, 1991. 50, 165

REFERENCES

- M. Ehlers and D. Tomowski. *On Segment Based Image Fusion*, volume Object-Based Image Analysis: Spatial Concepts for Knowledge-Driven Remote Sensing Applications of *Lecture Notes in Geoinformation and Cartography*, pages 735–754. Springer, Berlin, 2008. Blaschke, T. and Lang, S. and Hay, G.J. Eds. 3
- M. Eineder, N. Adam, R. Bamler, N. Yague-Martinez, and H. Breit. Spaceborne spotlight SAR interferometry with TerraSAR-X. *IEEE Transactions on Geoscience and Remote Sensing*, 47(5):1524–1535, 2009. 1, 131, 153
- L.M.G. Fonseca and B.S. Manjunath. Registration techniques for multisensor remotely sensed imagery. *Photogrammetric Engineering and Remote Sensing*, 62(9):1049–1056, 1996. 4
- G. Forkert. Die lösung photogrammetrischer orientierungs- und rekonstruktion-saufgaben mittels allgemeiner kurven- förmiger elemente. Heft 41, Technische Universität Wien, 1994. 7
- C. Förste, S. Bruinsma, F. Flechtner, J.-C. Marty, J.-M. Lemoine, C. Dahle, O. Abrikosov, K.H. Neumayer, R. Biancale, F. Barthelmes, and G. Balmino. A preliminary update of the direct approach GOCE processing and a new release of EIGEN-6C. In *Fall Meeting*, number Abstract No. G31B-0923, San Francisco, USA, 3–7 Dec 2012. 170
- J. E. S. Fransson, G. Smith, J. Askne, and H. Olsson. Stem volume estimation in boreal forest using ERS-1/2 coherence and SPOT XS optical data. *International Journal of Remote Sensing*, 22(14):2777–2791, 2001. 3
- T. Fritz, M. Eineder, M. Lachaise, A. Roth, H. Breit, B. Schättler, and M. Huber. *TerraSAR-X Ground Segment Level 1b Product Format Specification*. DLR, Germany, 2007. 54, 55, 182
- F. Galland, F. Tupin, J. . Nicolas, and M. Roux. Registering of synthetic aperture radar and optical data. In *International Geoscience and Remote Sensing Symposium (IGARSS)*, volume 5, pages 3513–3516, 2005. 2
- A.A. Goshtasby and S. Nikolov. Image fusion: Advances in the state of the art. *Information Fusion*, 8(1):114–118, 2007. 50
- A. Habib and D. Kelley. Single-photo resection using the Modified Hough Transform. *Photogrammetric Engineering and Remote Sensing*, 67(8):909–914, 2001. 154
- A. Habib, M. Morgan, E.M. Kim, and R. Cheng. Linear features in photogrammetric activities. *International Archive of Photogrammetry and Remote Sensing*, 35(B2):610–615, 2004. 6

REFERENCES

- A.F. Habib and R.I. Al-Ruzouq. Line-based modified Iterated Hough Transform for automatic registration of multi-source imagery. *Photogrammetric Record*, 19(105):5–21, 2004. 89
- A.F. Habib and R.I. Al-Ruzouq. Semi-automatic registration of multi-source satellite imagery with varying geometric resolutions. *Photogrammetric engineering & remote sensing*, 71(3):325–332, 2005. 3
- A.F. Habib, Y. Lee, and M. Morgan. Automatic matching and three-dimensional reconstruction of free-form linear features from stereo images. *Photogrammetric Engineering and Remote Sensing*, 69(2):189–197, 2003a. 7
- A.F. Habib, H.T. Lin, and M.F. Morgan. Line-Based Modified Iterated Hough Transform for Autonomous Single-Photo Resection. *Photogrammetric Engineering and Remote Sensing*, 69(12):1351–1357, 2003b. 7
- R.M. Haralick and Y.H. Chu. Solving camera parameters from perspective projection of a parameterised curve. *Pattern Recognition*, 17(6):637–645, 1984. 7
- J. Heikkila. Use of linear features in digital photogrammetry. *Photogrammetric Journal of Finland*, 12(2):40–56, 1991. 6
- F.M Henderson and A.J. Lewis, editors. *Principles and Applications of Imaging Radar*, volume 2 of *Manual of Remote Sensing*. John Wiley & Sons, Inc., New York, Chichester, Weinheim, Brisbane, Singapore, Toronto, third edition, 1998. 2
- H. Holmström and J. E. S. Fransson. Combining remotely sensed optical and radar data in kNN-estimation of forest variables. *Forest Science*, 49(3):409–418, 2003. 3
- T.D. Hong and R.A. Schowengerdt. A robust technique for precise registration of radar and optical satellite images. *Photogrammetric Engineering and Remote Sensing*, 71(5):585–593, 2005. 3, 143
- M. Honikel. Improvement of InSAR DEM accuracy using data and sensor fusion. In *International Geoscience and Remote Sensing Symposium (IGARSS)*, volume 5, pages 2348–2350, 1998. 153
- X. Huang, N. Paragios, and D. Metaxas. Shape registration in implicit spaces using information theory and free form deformations. *IEEE Transactions on Pattern Analysis and Machine Intelligence*, 28(8):1303–1318, 2006. 89

REFERENCES

- J. Inglada and A. Giros. On the possibility of automatic multisensor image registration. *IEEE Transactions on Geoscience and Remote Sensing*, 42(10): 2104–2120, 2004. 3, 4, 89, 153
- Intermap, 2013. URL <http://www.intermap.com>. 144
- C. Ioannidis and D.I. Vassilaki. Combined use of spaceborne optical and SAR data-incompatible data sources or a useful procedure? *FIG proceedings: FIG Working Week 2008 in Stockholm, Sweden*, June 14–19:cd, 2008. 1
- J.J. Jaw and N.H. Perny. Line feature correspondence between object space and image space. *Photogrammetric Engineering and Remote Sensing*, 74(12):1521–1528, 2008. 7
- M. Karjalainen. Geocoding of synthetic aperture radar images using digital vector maps. *IEEE Geoscience and Remote Sensing Letters*, 4(4):616–620, 2007. 6, 143
- M. Karkee, M. Kusanagi, and B.L. Steward. Fusion of optical and InSAR DEMs: Improving the quality of free data. In *ASAE Annual Meeting*, number 061172, 2006. 153
- T. Kasetkasem and P.K. Varshney. An image change detection algorithm based on Markov Random Field Models. *IEEE Trans. Geoscience and Remote Sensing*, 40:1815–1823, 2002. 103
- B. Kieler, W. Huang, J.H. Haunert, and J. Jiang. *Matching River Datasets of Different Scales*, volume Advances in GIScience of *Lecture Notes in Geoinformation and Cartography*, pages 135–154. Springer-Verlang, Berlin Heidelberg, 2009. 89
- H. Kimura and N. Ito. ALOS/PALSAR: the japanese second-generation spaceborne SAR and its applications. In *Proceedings of SPIE - The International Society for Optical Engineering*, volume 4152, pages 110–119, 2000. 2
- J. Koskinen, S. Metsämäki, J. Grandell, S. Jänne, L. Matikainen, and M. Halikainen. Snow monitoring using radar and optical satellite data. *Remote Sensing of Environment*, 69(1):16–29, 1999. 3
- K. Kubik. Relative and absolute orientation based on linear features. *ISPRS Journal of Photogrammetry and Remote Sensing*, 46(1):199–204, 1988. 89
- E.F. Lambin and A.H. Strahler. Indicators of land-cover change for change-vector analysis in multitemporal space at coarse spatial scales. *International Journal of Remote Sensing*, 15:2099–2119, 1994. 103

REFERENCES

- S.L. Le Hegarat-Mascle, I. Bloch, and D. Vidal-Madjar. Application of Dempster-Shafer evidence theory to unsupervised classification in multisource remote sensing. *IEEE Transactions on Geoscience and Remote Sensing*, 35(4):1018–1031, 1997. 3
- J. Le Moigne, W.J. Campbell, and R.F. Crompt. An automated parallel image registration technique of multiple source remote sensing data. *IEEE Transactions on Geoscience and Remote Sensing*, 40(8):1849–1864, 2002. 89
- F. Leberl. *Radargrammetric image processing*. Artech House, Norwood, 1991. 2, 53
- W.H. Lee and K. Yu. Bundle block adjustment with 3d natural cubic splines. *Sensors*, 9(12):9629–9665, 2009. 7, 89
- B.H. Li, G.M. Han, and H.A. Mang. A new method for evaluating singular integrals in stress analysis of solids by the direct Boundary Element Method. *International Journal of Numerical methods in engineering*, 21(21):2071–2098, 1985. 61
- H. Li, B. Manjunath, and S. Mitra. A contour-based approach to multi-sensor image registration. *IEEE Transactions on Image Processing*, 4(3):320–334, 1995. 6
- J. Li and W. Chen. A rule-based method for mapping Canada’s wetlands using optical, radar and DEM data. *International Journal of Remote Sensing*, 26(22):5051–5069, 2005. 3, 60
- X. Liu and R.G. Lathrop. Urban change detection based on an artificial neural network. *International Journal of Remote Sensing*, 23:2513–2518, 2002. 103
- Y. Liu, T.S. Huang, and O.D. Faugeras. Determination of camera locations from 2d to 3d line and point correspondence. *IEEE Transactions on Pattern Analysis and Machine Intelligence*, 12(1):28–37, 1990. 7
- T. Macri-Pellizzeri, C.J. Oliver, and P. Lombardo. Segmentation-based joint classification of SAR and optical images. *IEEE Radar Sonar Navigation*, 149(6):281–296, 2002. 3
- J.B.A. Maintz and M.A. Viergever. A survey of medical image registration. *Med. Image Analysis*, 2:1–36, 1998. 89
- H. Maitre. *Processing of synthetic aperture radar SAR images*. ISTE - John Wiley & Sons, London, 2010. 2, 53

REFERENCES

- G.D. Manolis and D.D. Beskos. *Boundary Element Methods in elastodynamics*. Unwin Hyman, London, 1988. 60
- J.F. Mas. Monitoring land-cover changes: A comparison of change detection techniques. *International Journal of Remote Sensing*, 20:139–152, 1999. 103
- S.E. Masry. Digital mapping using entities: a new concept. *Photogrammetric Engineering and Remote Sensing*, 48(11):1561–1599, 2008. 7
- D. Massonnet and J. Souyris. *Imaging with Synthetic Aperture Radar*. EFPL Press 2008, Lausanne, Switzerland, 2010. ISBN 978-0-8493-8239-0. 2
- B. Mercer. National and regional scale DEMs created from airborne InSAR. *ISPRS - International Archives of Photogrammetry, Remote Sensing and Spatial Information Sciences*, 36(3/W49B):113–117, 2007. 144
- E. Mikhail. Linear features for photogrammetric restitution and object completion integrating photogrammetric techniques with scene analysis and machine vision. *SPIE proceedings*, 1944:16–30, 1993. 154
- E.M. Mikhail, J.S. Bethel, and J.C. McGlone. *Introduction to modern photogrammetry*. John Wiley & Sons, New York, 2001. 16, 65, 118, 170
- M. Moghaddam, J. L. Dungan, and S. Acker. Forest variable estimation from fusion of SAR and multispectral optical data. *IEEE Transactions on Geoscience and Remote Sensing*, 40(10):2176–2187, 2002. 3
- M. S. Moran, A. Vidal, D. Troufleau, J. Qi, T. R. Clarke, P. J. Pinter Jr., T. A. Mitchell, Y. Inoue, and C. M. U. Neale. Combining multifrequency microwave and optical data for crop management. *Remote Sensing of Environment*, 61(1):96–109, 1997. 3
- D.C. Mulawa and E.M. Mikhail. Photogrammetric treatment of linear features. *ISPRS - International Archives of Photogrammetry and Remote Sensing*, 27(B10):383–393, 1988. 7, 89
- P.R.T. Newby. Photogrammetric terminology: Second edition. *The Photogrammetric Record*, 27(139):360–386, 2012. 3
- W. Niblack. *An introduction to digital image processing*. Strandberg Publishing Company, Denmark, 1985. 60, 64
- T. Nonaka, Y. Ishizuka, N. Yamane, T. Shibayama, S. Takagishi, and T. Sasagawa. Evaluation of the geometric accuracy of TerraSAR-X. *ISPRS - International Archives of Photogrammetry, Remote Sensing and Spatial Information Sciences*, 37(B7):135–140, 2008. 140

REFERENCES

- J.K. Nowak Da Costa and A. Walczynska. Geometric quality testing of the WorldView-2 Image Data Acquired over the JRC Maussane Test Site using ERDAS LPS, PCI Geomatics and Keystone digital photogrammetry software packages - Initial Findings with ANNEX. Technical Report JRC 64624, Institute for Environment and Sustainability, European Commission, Joint Research Centre, 2011. 147, 150, 152
- A.O. Ok, J.D. Wegner, C. Heipke, F. Rottensteiner, U. Sörgel, and V. Toprak. Matching of straight line segments from aerial stereo images of urban areas. *ISPRS Journal of Photogrammetry and Remote Sensing*, 74:133–152, 2012. 7
- K. Okamoto and H. Kawashima. Estimation of rice-planted area in the tropical zone using a combination of optical and microwave satellite sensor data. *International Journal of Remote Sensing*, 20(5):1045–1048, 1999. 3
- F. Orsomando, P. Lombardo, M. Zavagli, and M. Costantini. SAR and optical data fusion for change detection. In *Urban Remote Sensing Joint Event*, pages 1–9, 2007. 153
- N.K. Pavlis, S.A. Holmes, S.C. Kenyon, and J.K. Factor. An earth gravitational model to degree 2160: EGM2008. In *General assembly of the European Geosciences Union*, Vienna, Austria, 13–18 April 2008. 170, 175
- E. Petsa. *Photogrammetry with straight lines. Development, Research and Testing of Photogrammetric Algorithms with Straight Lines for Contemporary Digital Applications*. PhD thesis, National Technical University of Athens, Greece, 1995. 89
- E. Petsa and P. Patias. Formulation and assessment of straight line based algorithms for digital photogrammetry. *ISPRS - International Archives of Photogrammetry, Remote Sensing and Spatial Information Sciences*, 30(5):310–317, 1994. 7
- C. Pohl and Van.J.L. Genderen. Multisensor image fusion in remote sensing: concepts, methods and applications. *International Journal of Remote Sensing*, 19(5):823–854, 1998. 50, 89, 165
- W.H. Press, B.P. Flannery, S.A. Teukolsky, and W.T. Vetterling. *Numerical Recipes in FORTRAN: The Art of Scientific Computing*. Cambridge University Press, Cambridge, 2nd edition, 1992. ISBN 0-521-43064-X. 13, 18, 32, 45, 58
- A. Raouf and J. Lichtenegger. Integrated use of SAR and optical data for coastal zone management, 1997. URL <http://earth.esa.int/workshops/ers97/papers/lichtenegg>. Accessed 13 Apr. 2009. 153

REFERENCES

- J.C.B. Redfearn. Transverse mercator formulae. *Survey Review*, 9(69):318–322, 1948. 174
- P. Redweik, D. Roque, A. Marques, R. Matildes, and F. Marques. Triangulating the past - recovering portugal’s aerial images repository. *Photogrammetric Engineering and Remote Sensing*, 76(9):1007–1018, 2010. 111, 116
- P. Reinartz, R. Muller, P. Schwind, S. Suri, and R. Bamler. Orthorectification of VHR optical satellite data exploiting the geometric accuracy of TerraSAR-X data. *ISPRS Journal of Photogrammetry and Remote Sensing*, 66(1):124–132, 2011. 50, 143
- J.F. Reinoso. An algorithm for automatically computing the horizontal shift between homologous contours from DTMs. *ISPRS Journal of Photogrammetry and Remote Sensing*, 66(3):272–286, 2011. 84
- B. Rezaie and M. D. Srinath. Algorithms for fast image registration. *IEEE Transactions on Aerospace and Electronic Systems*, AES-20(6):716–728, 1984. ISSN 0018-9251. doi: 10.1109/TAES.1984.310454. 5
- E. Rodriguez, C.S. Morris, and J.E. Belz. A global assessment of the SRTM performance. *Photogrammetric Engineering and Remote Sensing*, 72(3):249–260, 2006. 182
- A. Rosenqvist, M. Shimada, N. Ito, and M. Watanabe. ALOS PALSAR: A pathfinder mission for global-scale monitoring of the environment. *IEEE Transactions on Geoscience and Remote Sensing*, 45(11):3307–3316, 2007. 2
- A. Roth, M. Huber, and D. Kosmann. Geocoding of TerraSAR-X data. *ISPRS - International Archives of Photogrammetry, Remote Sensing and Spatial Information Sciences*, 35(3):840–845, 2004. 182
- T. Schenk. From point-based to feature-based aerial triangulation. *ISPRS Journal of Photogrammetry and Remote Sensing*, 58(5–6):315–329, 2004. 6, 89
- A.H. Schistad, T. Taxt, and A.K. Jain. A Markov Random Field Model for Classification of Multisource Satellite Imagery. *IEEE Transactions on Geoscience and Remote Sensing*, 34(1):100–113, 1996. 3
- S.B. Serpico and F. Roli. Classification of multisensor remote-sensing images by structured neural networks. *IEEE Transactions on Geoscience and Remote Sensing*, 33(3):562–578, 1995. 3

REFERENCES

- R. Shibasaki, Y. Osawa, K. Toda, H. Wakabayashi, T. Hamazaki, and H. Takamatsu. Advanced land observing satellite (ALOS): Mission objectives and payloads. In *Proceedings of SPIE - The International Society for Optical Engineering*, volume 2957, pages 200–207, 1997. 2
- G. Simone, A. Farina, F.C. Morabito, S.B. Serpico, and L. Bruzzone. Image fusion techniques for remote sensing applications. *Information Fusion*, 3(1): 3–15, 2002. 50
- A. Singh. Digital change detection techniques using remotely-sensed data. *International Journal of Remote Sensing*, 10(6):989–1003, 1989. 3
- L. A. Soderblom, R. L. Kirk, J. I. Lunine, J. A. Anderson, K. H. Baines, J. W. Barnes, J. M. Barrett, R. H. Brown, B. J. Buratti, R. N. Clark, D. P. Cruikshank, C. Elachi, M. A. Janssen, R. Jaumann, E. Karkoschka, S. L. Mouélic, R. M. Lopes, R. D. Lorenz, T. B. McCord, P. D. Nicholson, J. Radebaugh, B. Rizk, C. Sotin, E. R. Stofan, T. L. Sucharski, M. G. Tomasko, and S. D. Wall. Correlations between Cassini VIMS spectra and RADAR SAR images: Implications for Titan’s surface composition and the character of the Huygens Probe Landing Site. *Planetary and Space Science*, 55(13):2025–2036, 2007. 3
- U. Sörgel, E. Cadario, A. Thiele, and U. Thönnessen. Feature extraction and visualisation of bridges over water from high-resolution InSAR data and one orthophoto. *IEEE Journal of Selected Topics in Applied Earth Observations and Remote Sensing*, 1(2):147–153, 2008. 3, 89, 153
- H. Sportouche, F. Tupin, and L. Denise. Extraction and three-dimensional reconstruction of isolated buildings in urban scenes from high-resolution optical and SAR spaceborne images. *IEEE Transactions on Geoscience and Remote Sensing*, 49(10 PART 2):3932–3946, 2011. 2
- A.A. Stamos. Thancad: a 2dimensional cad for engineers. In *Europython 2007*, Vilnius, Lithuania, 9–11 July 2007. 90, 178
- A.A. Stamos, D.I. Vassilaki, and C. Ioannidis. Speed enhancement of free-form curves matching with Parallel Fortran 2008. In *1st International Conference on Parallel, Distributed and Grid Computing for Engineering*, pages 11.1–14.10, Pecs, Hungary, 6–8 April 2009. 23
- S. Stramondo, C. Bignami, M. Chini, N. Pierdicca, and A. Tertulliani. Satellite radar and optical remote sensing for earthquake damage detection: Results from different case studies. *International Journal of Remote Sensing*, 27(20): 4433–4447, 2006. 3

REFERENCES

- S. Suri and P. Reinartz. Mutual-information-based registration of TerraSAR-X and Ikonos imagery in urban areas. *IEEE Transactions on Geoscience and Remote Sensing*, 48(2):939–949, 2010. 3
- S. Suri, S. Türmer, P. Reinartz, and U. Stilla. Registration of high resolution sar and optical satellite imagery in urban areas. *ISPRS - International Archives of the Photogrammetry, Remote Sensing and Spatial Information Sciences*, XXXVIII-1-4-7/W5:cd, 2009. 3
- M.A. Taverna. Cnes, asi to join on military/government satellite project. *Aviation Week and Space Technology (New York)*, 171(23), 2009. 2
- A. Thiele, J.D. Wegner, E. Cadario, K. Schulz, and U. Sörgel. Segmentation and fusion of building features based on InSAR and optical data. In *Proceedings of SPIE - The International Society for Optical Engineering*, volume 7478, 2009b. 2
- A. M. G. Tommaselli and J. Marcato Jr. Bundle block adjustment of CBERS-2B HRC imagery combining control points and lines. *Photogrammetrie, Fernerkundung, Geoinformation*, 2012(2):129–139, 2012. 6
- A.M.G. Tommaselli, N.G. Medeiros, T. Nonaka, Y. Ishizuka, N. Yamane, T. Shibayama, S. Takagishi, and T. Sasagawa. Determination of the indirect orientation of orbital pushbroom images using control straight lines. *Photogrammetric Record*, 25(130):159–179, 2010. 7
- T. Toutin. Multisource data fusion with an integrated and unified geometric modelling. *EARSeL Journal: Advances in Remote Sensing*, 4(2):118–129, 1995. 3
- T. Toutin. Review paper: Geometric processing of remote sensing images: models, algorithms and methods. *International Journal of Remote Sensing*, 25(10):1893–1924, 2004. 16, 50, 53, 126, 127, 147, 148
- P. A. Townsend and S.J. Walsh. Modelling floodplain inundation using an integrated GIS with radar and optical remote sensing. *Geomorphology*, 21(3–4):295–312, 1998. 3
- J.R.G. Townshend, C.O. Justice, C. Gurney, and J. McManus. The impact of misregistration on change detection. *IEEE Transactions on Geoscience and Remote Sensing*, 30(5):1054–1060, 1992. ISSN 0196-2892. doi: 10.1109/36.175340. 3, 103

REFERENCES

- E. Trouve, G. Vasile, M. Gay, L. Bombrun, P. Grussenmeyer, T. Landes, J. Nicolas, P. Bolon, I. Petillot, A. Julea, L. Valet, J. Chanussot, and M. Koehl. Combining airborne photographs and spaceborne SAR data to monitor temperate glaciers: Potentials and limits. *IEEE Transactions on Geoscience and Remote Sensing*, 45(4):905–922, 2007. 3
- F. Tupin. Fusion of interferometric and optical data for 3d reconstruction. In *International Geoscience and Remote Sensing Symposium (IGARSS)*, number 4242077, pages 3627–3630, 2006. 153
- F. Tupin and M. Roux. Detection of building outlines based on the fusion of SAR and optical features. *ISPRS Journal of Photogrammetry and Remote Sensing*, 58(1–2):71–82, 2003. 2
- D.I. Vassilaki. Matching and evaluating free-form linear features for georeferencing space-borne SAR imagery. *Photogrammetrie - Fernerkundung - Geoinformation*, 2012(4):408–419, 2012. 6, 10, 11, 143
- D.I. Vassilaki and C. Ioannidis. Georeference of high resolution TerraSAR-X images with RPFs. *EARSeL Symposium Proceeding: Remote Sensing for Science, Education, and Natural and Cultural Heritage in Paris, France*, May 31 – June 3:573–580, 2010. 110, 140
- D.I. Vassilaki, C. Ioannidis, and A.A. Stamos. Computation of the closest points for matching curves of different dimensionality. In *3rd International Conference: From Scientific Computing to Computational Engineering in Athens, Greece*, page cd, 9–12 July 2008a. 10, 11
- D.I. Vassilaki, C. Ioannidis, and A.A. Stamos. Registration of 2d free-form curves extracted from high resolution imagery using Iterative Closest Point Algorithm. In *EARSeL Workshop proceedings: Remote Sensing: New challenges of high resolution in Bochum, Germany*, pages 141–152, 5–7 March 2008b. 10, 11
- D.I. Vassilaki, C. Ioannidis, and A.A. Stamos. Geospatial data integration using automatic global matching of free-form curves. *Digital Earth Summit on Geoinformatics: Tools for Global Change Research*, Wichmann Verlag, Heidelberg: 195–200, 2008c. 10, 11
- D.I. Vassilaki, C. Ioannidis, and A.A. Stamos. Multitemporal data registration through global matching of networks of free-form curves. *FIG proceedings: FIG Working Week 2009 in Eilat, Israel*, May 3–8:cd, 2009a. 10, 11
- D.I. Vassilaki, C. Ioannidis, and A.A. Stamos. Registration of unrectified optical and SAR imagery over mountainous areas through automatic free-form

REFERENCES

- features global matching. *ISPRS - International Archives of the Photogrammetry, Remote Sensing and Spatial Information Sciences*, XXXVIII-1-4-7/W5:cd, 2009b. 10, 11, 101, 143
- D.I. Vassilaki, C. Ioannidis, and A.A. Stamos. Enhanced first approximation for ICP-based global matching of free-form curves in side-looking radar geometry. *ISPRS - International Archives of the Photogrammetry, Remote Sensing and Spatial Information Sciences*, XXXVIII part 3A:85–90, 2010. 10, 11
- D.I. Vassilaki, C. Ioannidis, and A.A. Stamos. Fusion of optical and SAR images in slant range SAR geometry. *EARSeL Symposium Proceeding: Remote Sensing and Geoinformation not only for Scientific Cooperation, in Prague, Czech Republic*, May 30 – June 2:552–560, 2011a. 10, 11
- D.I. Vassilaki, C. Ioannidis, and A.A. Stamos. Georeference of TerraSAR-X images using science orbit data. *EARSeL Symposium Proceeding: Remote Sensing and Geoinformation not only for Scientific Cooperation in Prague, Czech Republic*, May 30 – June 2:472–480, 2011b. 11, 16, 143, 169
- D.I. Vassilaki, C. Ioannidis, and A.A. Stamos. Georeferencing of TerraSAR-X images using networks of ground control linear features. *ISPRS - International Archives of the Photogrammetry, Remote Sensing and Spatial Information Sciences*, XXXVIII-4/W19:cd, 2011c. 10, 11
- D.I. Vassilaki, C. Ioannidis, and A.A. Stamos. Recovery of the geometry of historical aerial photos associating self-calibration with ground control linear features. *1st EARSeL Workshop on Temporal Analysis of Satellite Images*, pages 202–207, May 23–25 2012a. 10, 11, 116
- D.I. Vassilaki, C. Ioannidis, and A.A. Stamos. Automatic ICP-based global matching of Free-Form Linear Features. *Photogrammetric Record*, 27(139):311–329, 2012b. 10, 11, 20
- D.I. Vassilaki, C. Ioannidis, and A.A. Stamos. High resolution TerraSAR-X data as source of ground control information. In *5. Terrasar-X/4. TanDEM-X Science Team Meeting*, German Aerospace Centre (DLR), Oberpfaffenhofen, Germany, June 10–12 2013a. 11
- D.I. Vassilaki, C. Ioannidis, and A.A. Stamos. Evaluation of SAR data as source of ground control information: First results. *ISPRS - International Archives of the Photogrammetry, Remote Sensing and Spatial Information Sciences*, XL-1/W1:363–367, May 21–24 2013b. 11

REFERENCES

- D.I. Vassilaki, A.A. Stamos, and C. Ioannidis. Automatic georeferencing and orthorectification of slant range TerraSAR-X images using globally available data. In *4th Advanced Training Course in Land Remote Sensing*, Athens, Greece, July 1–5 2013c. 11
- D.I. Vassilaki, A.A. Stamos, and C. Ioannidis. Rapid geometric correction of SSC TerraSAR-X images using direct georeferencing, global DEMs and global geoid models. *ISPRS - International Archives of the Photogrammetry, Remote Sensing and Spatial Information Sciences*, XL-1/W1:357–362, 2013d. doi: 10.5194/isprsarchives-XL-1-W1-357-2013. 11
- A. Vidal and M. R. Moreno. Change detection of isolated housing using a new hybrid approach based on object classification with optical and TerraSAR-X data. *International Journal of Remote Sensing*, 32(24):9621–9635, 2011. 3
- C. Wang, A. Stefanidis, A. Croitoru, and P. Agouris. Map registration of image sequences using linear features. *Photogrammetric Engineering and Remote Sensing*, 74(1):25–38, 2008. 50, 89, 154
- B. Waske and J.A. Benediktsson. Fusion of support vector machines for classification of multisensor data. *IEEE Transactions on Geoscience and Remote Sensing*, 45(12):3858–3866, 2007. 3
- B. Waske and S. van der Linden. Classifying multilevel imagery from SAR and optical sensors by decision fusion. *IEEE Transactions on Geoscience and Remote Sensing*, 46(5):1457–1466, 2008. 3
- J. Wegner, J. Inglada, and C. Tison. Automatic fusion of SAR and optical imagery based on line features. In *7th European Conference on Synthetic Aperture Radar*, volume 1, pages 171–174, 2008. 153
- J. D. Wegner, R. Hansch, A. Thiele, and U. Sörgel. Building detection from one orthophoto and high-resolution InSAR data using Conditional Random Fields. *IEEE Journal of Selected Topics in Applied Earth Observations and Remote Sensing*, 4(1):83–91, 2011. 2
- J.D. Wegner. Automatic fusion of sar and optical imagery. Accomplished at the Centre National d’études Spatiales (CNES) Toulouse, France, 2007. Thesis in partial fulfilment of requirements for the degree of Dipl.-Ing. 3
- J.D. Wegner. *Detection and height estimation of buildings from SAR and optical images using conditional random fields*. PhD thesis, Fakultät für Bauingenieurwesen und Geodäsie der Gottfried Wilhelm Leibniz Universität Hannover, Hannover, Germany, 2011. 2, 3

REFERENCES

- J.D. Wegner, U. Sörgel, and A. Thiele. Building extraction in urban scenes from high resolution InSAR data and optical imagery. *2009 Joint Urban Remote Sensing Event in Shanghai, China*, May 20–22, 2009. 2
- J. Weng, T.S. Huang, and N. Ahuja. Motion and structure from line correspondences closed-form solution, uniqueness and optimisation. *IEEE Transactions on Pattern Analysis and Machine Intelligence*, 14(3):318–336, 1992. 7
- R. Werninghaus and S. Buckreuss. The TerraSAR-X mission and system design. *IEEE Transactions on Geoscience and Remote Sensing*, 48(2):606–614, 2010. 1
- D. Xiong and J. Sperling. Semiautomated matching for network database integration. *ISPRS Journal of Photogrammetry and Remote Sensing*, 59(1–2):35–46, 2004. 89
- Y.T. Yoon, M. Eineder, N. Yague-Martinez, and N. Montenbruck. TerraSAR-X precise trajectory estimation and quality assessment. *IEEE Transactions on Geoscience and Remote Sensing*, 47(6):1859–1868, 2009. 51, 55, 108
- H.G. Zalmanson. Hierarchical recovery of exterior orientation from parametric and natural 3-D curves. *ISPRS - International Archives of Photogrammetry and Remote Sensing*, XXXIII,partB2:610–617, 2000. 7, 89, 154
- L. Zhang, X. He, T. Balz, X. Wei, and M. Liao. Rational function modelling for spaceborne SAR datasets. *ISPRS Journal of Photogrammetry and Remote Sensing*, 66(1):133–145, 2011. 126
- Q. Zhang, M. Simantov, J. de Vries, S. Griffiths, and B. Mercer. Assigning elevations to 2d road networks based on IfSAR-derived DEMs. *ISPRS - International Archives of Photogrammetry, Remote Sensing and Spatial Information Sciences*, 36(1), 2010. 144, 149
- Y. Zhang. Highlight article: Understanding image fusion. *Photogrammetric Engineering and Remote Sensing*, 70(6):657–661, 2004. 50
- Y. Zhang, J. Pulliainen, S. Koponen, and M. Hallikainen. Application of an empirical neural network to surface water quality estimation in the Gulf of Finland using combined optical data and microwave data. *Remote Sensing of Environment*, 81(2–3):327–336, 2002. 3
- Z. Zhang. Iterative point matching for registration of free-form curves and surfaces. *International Journal of Computer Vision*, 13(2):119–152, 1994. 7, 19

REFERENCES

- H. Zielinski. *Object Reconstruction with Digital Line Photogrammetry*. PhD thesis, Royal Institute of Technology, 1993. 89
- O.C. Zienkiewicz. *The Finite Element Method*. McGraw-Hill, London, third edition, 1988. 60
- B. Zitova and J. Flusser. Image registration methods: A survey. *Image and Vision Computing*, 21(11):977–1000, 2003. 3, 4, 5, 89, 153

Curriculum Vitae

Personal information

Name: Dimitra Vassilaki

Place of birth: Heraklion, Crete

Citizenship: Greek

Occupational field

Surveying Engineering

Work Experience

Freelance surveyor engineer (1998 onwards)

Education and training

Engineer Diploma (1998)

School of Rural and Surveying Engineering

National Technical University of Athens

Master Diploma (2004)

School of Science and Technology

Hellenic Open University